

AFRL-PR-WP-TR-1998-2118

Aerodynamic Effects on Mistuned Response of a
High-Speed, Low Aspect Ratio Fan

James A. Kenyon

Technology Evaluation Branch
Turbine Engine Division



Sanford Fleeter

Department of Mechanical Engineering
Purdue University
West Lafayette, IN

October 1998

Final Report for 12/1/96-5/9/98

Approved for public release; distribution is unlimited.

Propulsion Directorate
Air Force Research Laboratory
Air Force Materiel Command
Wright-Patterson AFB, OH 45433-7251

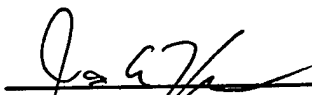
19990317 037


NOTICE

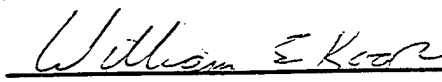
USING GOVERNMENT DRAWINGS, SPECIFICATIONS, OR OTHER DATA INCLUDED IN THIS DOCUMENT FOR ANY PURPOSE OTHER THAN GOVERNMENT PROCUREMENT DOES NOT IN ANY WAY OBLIGATE THE US GOVERNMENT. THE FACT THAT THE GOVERNMENT FORMULATED OR SUPPLIED THE DRAWINGS, SPECIFICATIONS, OR OTHER DATA DOES NOT LICENSE THE HOLDER OR ANY OTHER PERSON OR CORPORATION; OR CONVEY ANY RIGHTS OR PERMISSION TO MANUFACTURE, USE, OR SELL ANY PATENTED INVENTION THAT MAY RELATE TO THEM.

THIS REPORT IS RELEASABLE TO THE NATIONAL TECHNICAL INFORMATION SERVICE (NTIS). AT NTIS, IT WILL BE AVAILABLE TO THE GENERAL PUBLIC, INCLUDING FOREIGN NATIONS.

THIS TECHNICAL REPORT HAS BEEN REVIEWED AND IS APPROVED FOR PUBLICATION.


JAMES A. KENYON
Aerospace Engineer
Technology Evaluation Branch


ROBERT J. ALLEN
Acting Chief.
Technology Evaluation Branch
Turbine Engine Division
Propulsion Directorate


WILLIAM E. KOOP
Chief of Technology
Turbine Engine Division
Propulsion Directorate

Do not return copies of this report unless contractual obligations or notice on a specific document requires its return.

REPORT DOCUMENTATION PAGE			Form Approved OMB No. 0704-0188	
<small>Public reporting burden for this collection of information is estimated to average 1 hour per response, including the time for reviewing instructions, searching existing data sources, gathering and maintaining the data needed, and completing and reviewing the collection of information. Send comments regarding this burden estimate or any other aspect of this collection of information, including suggestions for reducing this burden, to Washington Headquarters Services, Directorate for Information Operations and Reports, 1215 Jefferson Davis Highway, Suite 1204, Arlington, VA 22202-4302, and to the Office of Management and Budget, Paperwork Reduction Project (0704-0188), Washington, DC 20503.</small>				
1. AGENCY USE ONLY (Leave blank)		2. REPORT DATE OCTOBER 98		3. REPORT TYPE AND DATES COVERED FINAL: 12/1/96 - 5/9/98
4. TITLE AND SUBTITLE AERODYNAMIC EFFECTS ON MISTUNED RESPONSE OF A HIGH-SPEED, LOW ASPECT RATIO FAN			5. FUNDING NUMBERS PE 62203 PR 3066 TA 17 WU Y8	
6. AUTHOR(S) JAMES A. KENYON SANFORD FLEETER (PURDUE UNIVERSITY)				
7. PERFORMING ORGANIZATION NAME(S) AND ADDRESS(ES) PROPULSION DIRECTORATE AIR FORCE RESEARCH LABORATORY AIR FORCE MATERIEL COMMAND WRIGHT PATTERSON AFB OH 45433-7251			8. PERFORMING ORGANIZATION REPORT NUMBER	
9. SPONSORING/MONITORING AGENCY NAME(S) AND ADDRESS(ES) PROPULSION DIRECTORATE AIR FORCE RESEARCH LABORATORY AIR FORCE MATERIEL COMMAND WRIGHT PATTERSON AFB OH 45433-7251 POC: JAMES A. KENYON AFRL/PRTE (937)255-6802 EXT 243			10. SPONSORING/MONITORING AGENCY REPORT NUMBER AFRL-PR-WP-TR-1998-2118	
11. SUPPLEMENTARY NOTES PREPARED IN COOPERATION WITH THE DEPARTMENT OF MECHANICAL ENGINEERING, PURDUE UNIVERSITY, WEST LAFAYETTE, IN 47907				
12a. DISTRIBUTION AVAILABILITY STATEMENT APPROVED FOR PUBLIC RELEASE; DISTRIBUTION IS UNLIMITED.			12b. DISTRIBUTION CODE	
13. ABSTRACT (Maximum 200 words) BLADE RESPONSE TO AN INLET TOTAL PRESSURE DISTORTION WAS MEASURED IN AN INTEGRALLY BLADED DISK, OR BLISK. BLADE-TO-BLADE VARIATIONS IN BLADE RESONANT FREQUENCIES, KNOWN AS MISTUNING, AND HOW THESE VARIATIONS ARE RELATED TO VIBRATORY STRESS AMPLITUDE AND VISCOUS DAMPING VARIATIONS WERE INVESTIGATED. IN ADDITION, A REDUCED-ORDER ANALYTICAL MODEL WAS USED TO PREDICT THE BLADE RESONANT STRESS VARIATIONS BASED ON THE FREQUENCY VARIATION MEASURED IN THE BLISK. THE MEASURED STRESS VARIATIONS WERE FOUND TO BE STRONGLY INFLUENCED BY UNSTEADY AERODYNAMIC COUPLING. BLADE STRUCTURAL MISTUNING AND MECHANICAL COUPLING THROUGH HUB MOTION WERE DETERMINED TO HAVE ONLY A MINOR INFLUENCE ON BLADE-TO-BLADE STRESS VARIATIONS. STRESS DISTRIBUTION PATTERNS AT RESONANCE AND AT CONSTANT SPEEDS ABOVE AND BELOW RESONANCE SUGGESTED A RELATIONSHIP BETWEEN STRESS VARIATIONS AND UNSTEADY AERODYNAMICS. TO SUPPORT THIS, AERODYNAMIC DAMPING VARIATIONS MEASURED AT RESONANCE WERE SHOWN TO ROUGHLY CORRESPOND TO STRESS VARIATIONS. EXPERIMENTAL RESULTS WERE COMPARED TO THE PREDICTED VARIATIONS FROM THE REDUCED-ORDER MODEL. RESULTS FROM THE MODEL INDICATED THAT UNSTEADY AERODYNAMIC COUPLING PLAYED AN IMPORTANT ROLE IN THE MISTUNED RESPONSE OF THE BLISK.				
14. SUBJECT TERMS MISTUNING, MISTUNED RESPONSE, COMPRESSORS, FANS, AERODYNAMICS			15. NUMBER OF PAGES 171	
			16. PRICE CODE	
17. SECURITY CLASSIFICATION OF REPORT UNCLASSIFIED	18. SECURITY CLASSIFICATION OF THIS PAGE UNCLASSIFIED	19. SECURITY CLASSIFICATION OF ABSTRACT UNCLASSIFIED	20. LIMITATION OF ABSTRACT UL	

TABLE OF CONTENTS

	Page
LIST OF TABLES	v
LIST OF FIGURES	vi
NOMENCLATURE	xii
1.0 INTRODUCTION AND BACKGROUND	1
1.1 Previous Studies	2
1.2 Previous Tests on Current Test Article	4
1.3 Problem Statement and Technical Approach	5
2.0 DESCRIPTION OF EXPERIMENT	9
2.1 Test Facility	9
2.2 Experimental Configuration	11
2.2.1 Test Rotor	11
2.2.2 Downstream Airfoils	14
2.2.3 Distortion Screen	15
2.3 Instrumentation and Data Acquisition	18
2.4 Experimental Procedure	22
3.0 DATA REDUCTION AND ANALYSIS	25
3.1 Steady-State Data Reduction	25
3.2 Steady-State Analysis	25
3.3 Transient Data Reduction	32
3.4 Transient Analysis	32
4.0 EXPERIMENTAL RESULTS	37
4.1 Off-Resonant Mistuning Effects	37
4.1.1 Blade Stress Variations	37
4.1.2 Ensemble Averages	42
4.1.3 Summary of Off-Resonant Results	45
4.2 Mistuning Effects at Resonance	45
4.2.1 Evaluation of Structural Mistuning	46
4.2.2 Hub Participation and Aerodynamic Mistuning Effects	46

	Page
4.2.3 Damping Effects on Stress Variations.....	51
4.2.4 Summary of Resonant Results	55
5.0 REDUCED-ORDER MODELING	60
5.1 Reduced-Order Modeling Technique	60
5.2 Blisk Structural Model	61
5.2.1 Finite Element Modeling.....	62
5.2.2 Structural Mistuning Effects.	62
5.3 Aerodynamic Coupling	64
5.3.1 Development of Aerodynamic Model.....	64
5.3.2 Coupling Strength.	66
6.0 SUMMARY AND CONCLUSIONS.....	69
6.1 Summary of Results	69
6.2 Conclusions	71
7.0 REFERENCES.....	73
APPENDICES	
APPENDIX A: Aft Blade Row Campbell Diagrams	76
APPENDIX B: Strain Gage Specifications and Uncertainty	80
APPENDIX C: On-line Campbell Diagrams	84
APPENDIX D: Tabulated Experimental Data	148
APPENDIX E: Comparison of Campbell Diagrams and Recorded Data	154

LIST OF TABLES

Table	Page
2.1: Rotor 1 geometric parameters.	13
2.2: Rotor 1 performance at the design and test conditions.	13
2.3: Tape log from 3/rev 1F resonant crossing.	22
2.4: Estimated corrected mass flows of compressor operating lines.	23
5.1: LINSUB input parameters.	65
B.1: Dynamic strain gage specifications and signal conditioning.	80
B.2: Signal conditioning gains.	82
D.1: Off-resonant steady-state strain gage data, 8100 rpm mechanical speed.	148
D.2: Off-resonant steady-state strain gage data, 9100 rpm mechanical speed.	149
D.3: Strain gage data at resonance, WOD.	150
D.4: Strain gage data at resonance, NOL.	151
D.5: Strain gage data at resonance, PE.	152
D.6: Strain gage data at resonance, NS.	153
E.1: Natural frequency statistical comparison.	154
E.2: Resonant stress statistical comparison.	155

LIST OF FIGURES

Figure	Page
1.1: Rotor 1 predicted Campbell diagram.	7
2.1: CRF test chamber schematic.	10
2.2: Profile schematic of test article.	12
2.3: 3/rev distortion screen pattern.	16
2.4: Circumferential map of inlet total pressure field (mean of 5 radial immersions).	17
2.5: Inlet total pressure frequency distribution (based on mean of 5 radial immersions).	17
2.6: Interaction of 3/rev distortion screen and inlet struts.	19
2.7: Rotor 1 strain gage location.	21
2.8: Test summary.	24
3.1: PSD of steady-state strain gage signal (NOL, Blade 2 strain gage, 8100 rpm)	27
3.2: Ensemble average of strain gage signal (PE, Blade 9 strain gage, 9100 rpm).	29
3.3a: Time history of clean steady-state strain gage signal (WOD, Blade 8 strain gage, 9100 rpm).	31
3.3b: Time history of contaminated steady-state strain gage signal (WOD, Blade 3 strain gage, 9100 rpm).	31
3.4: Half power method for determining damping from Campbell diagrams.	33
3.5: PSD of transient strain gage signal (NS, Blade 15 strain gage).	35
3.6a: Time history of clean transient strain gage signal (NS, Blade 15 strain gage).	36

Figure	Page
3.6b: Time history of contaminated transient strain gage signal (NS, Blade 3 strain gage).....	36
4.1: Blade-to-blade stress variations, 8100 rpm mechanical speed.....	38
4.2: Blade-to-blade stress variations, 9100 rpm mechanical speed.....	39
4.3: Rotor 1 velocity triangle.....	41
4.4: Ensemble averages of strain gage response, 8100 rpm mechanical speed.....	43
4.5: Ensemble averages of strain gage response, 9100 rpm mechanical speed.....	44
4.6a: Comparison of blade natural frequencies and peak stresses (WOD and NOL).	47
4.6b: Comparison of blade natural frequencies and peak stresses (PE and NS).	48
4.7: Circumferential peak stress distribution.....	50
4.8: Throttle effects on resonant response.....	52
4.9a: Relationship between total damping and stress amplitude at resonance (WOD and NOL).....	53
4.9b: Relationship between total damping and stress amplitude at resonance (PE and NS).....	54
4.10: Circumferential total damping distribution.....	56
4.11a: Comparison of blade natural frequencies and total damping (WOD and NOL).....	57
4.11b: Comparison of blade natural frequencies and total damping (PE and NS).....	58
5.1: Finite element models of single hub-blade sector.....	63
5.2: Predicted magnification factors for various aerodynamic coupling strengths.	67

Figure	Page
A.1: Rotor 2 Campbell diagram.	76
A.2: Stator 1 strut Campbell diagram.....	77
A.3: Stator 1 flap Campbell diagram.	78
A.4: Stator 2 Campbell diagram.....	79
C.1: Blade 1 Campbell diagram, WOD.	84
C.2: Blade 2 Campbell diagram, WOD.	85
C.3: Blade 3 Campbell diagram, WOD.	86
C.4: Blade 4 Campbell diagram, WOD.	87
C.5: Blade 5 Campbell diagram, WOD.	88
C.6: Blade 6 Campbell diagram, WOD.	89
C.7: Blade 7 Campbell diagram, WOD.	90
C.8: Blade 8 Campbell diagram, WOD.	91
C.9: Blade 9 Campbell diagram, WOD.	92
C.10: Blade 10 Campbell diagram, WOD.	93
C.11: Blade 11 Campbell diagram, WOD.	94
C.12: Blade 12 Campbell diagram, WOD.	95
C.13: Blade 13 Campbell diagram, WOD.	96
C.14: Blade 14 Campbell diagram, WOD.	97
C.15: Blade 15 Campbell diagram, WOD.	98
C.16: Blade 16 Campbell diagram, WOD.	99
C.17: Blade 1 Campbell diagram, NOL.....	100

Figure	Page
C.18: Blade 2 Campbell diagram, NOL.....	101
C.19: Blade 3 Campbell diagram, NOL.....	102
C.20: Blade 4 Campbell diagram, NOL.....	103
C.21: Blade 5 Campbell diagram, NOL.....	104
C.22: Blade 6 Campbell diagram, NOL.....	105
C.23: Blade 7 Campbell diagram, NOL.....	106
C.24: Blade 8 Campbell diagram, NOL.....	107
C.25: Blade 9 Campbell diagram, NOL.....	108
C.26: Blade 10 Campbell diagram, NOL.....	109
C.27: Blade 11 Campbell diagram, NOL.....	110
C.28: Blade 12 Campbell diagram, NOL.....	111
C.29: Blade 13 Campbell diagram, NOL.....	112
C.30: Blade 14 Campbell diagram, NOL.....	113
C.31: Blade 15 Campbell diagram, NOL.....	114
C.32: Blade 16 Campbell diagram, NOL.....	115
C.33: Blade 1 Campbell diagram, PE.	116
C.34: Blade 2 Campbell diagram, PE.	117
C.35: Blade 3 Campbell diagram, PE.	118
C.36: Blade 4 Campbell diagram, PE.	119
C.37: Blade 5 Campbell diagram, PE.	120
C.38: Blade 6 Campbell diagram, PE.	121

Figure	Page
C.39: Blade 7 Campbell diagram, PE.	122
C.40: Blade 8 Campbell diagram, PE.	123
C.41: Blade 9 Campbell diagram, PE.	124
C.42: Blade 10 Campbell diagram, PE.	125
C.43: Blade 11 Campbell diagram, PE.	126
C.44: Blade 12 Campbell diagram, PE.	127
C.45: Blade 13 Campbell diagram, PE.	128
C.46: Blade 14 Campbell diagram, PE.	129
C.47: Blade 15 Campbell diagram, PE.	130
C.48: Blade 16 Campbell diagram, PE.	131
C.49: Blade 1 Campbell diagram, NS.	132
C.50: Blade 2 Campbell diagram, NS.	133
C.51: Blade 3 Campbell diagram, NS.	134
C.52: Blade 4 Campbell diagram, NS.	135
C.53: Blade 5 Campbell diagram, NS.	136
C.54: Blade 6 Campbell diagram, NS.	137
C.55: Blade 7 Campbell diagram, NS.	138
C.56: Blade 8 Campbell diagram, NS.	139
C.57: Blade 9 Campbell diagram, NS.	140
C.58: Blade 10 Campbell diagram, NS.	141
C.59: Blade 11 Campbell diagram, NS.	142

Figure	Page
C.60: Blade 12 Campbell diagram, NS.....	143
C.61: Blade 13 Campbell diagram, NS.....	144
C.62: Blade 14 Campbell diagram, NS.....	145
C.63: Blade 15 Campbell diagram, NS.....	146
C.64: Blade 16 Campbell diagram, NS.....	147
E.1: Resonant frequencies from recorded signals and experimental Campbell diagrams.	156
E.2: Peak stress amplitudes from recorded signals and experimental Campbell diagrams.	157

NOMENCLATURE

Symbols

1F	first flex mode
1T	first torsion mode
1-2S	first 2-stripe mode
2F	second flex mode
2T	second torsion mode
e	electrical potential in strain gage circuit
f	non-dimensional frequency
f_{max}	highest frequency at which stress amplitude equals σ_{rms}
f_{min}	lowest frequency at which stress amplitude equals σ_{rms}
f_{res}	frequency at peak resonance
k	index of sample in x , or blade index, or gage factor
m	index of components of X_m
x	vector of discrete data samples
x_k	k th data sample in x
v_k	modified data set, inverse of V_m
w_k	weighting factor for Hanning windows
A	a constant
\mathbf{A}	aerodynamic coupling matrix
\mathbf{A}^k	diagonal element of \mathbf{A}
AC	alternating current
A/D	analog-to-digital
C	number of upstream wakes or hub nodal diameters
CRF	Compressor Research Facility
E	total energy in the discrete signal x_k , or modulus of elasticity
FFT	fast Fourier transform

G	total gain
G_{AD}	A/D converter gain
G_{FILTER}	filter gain
G_{PAC}	Pacific amplifier gain
$G_{PRESTON}$	Preston amplifier gain
G_{REC}	analog recorder gain
I	excitation current through strain gage circuit
L	length of strain gage test area
M	Hanning window length, or number of cantilevered blades analyzed
N	number of discrete samples in x , or number of blades on rotor
NOL	nominal operating line
N_p	number of components in zero-padded FFT
NS	near stall operating line
N_z	number of zeros inserted into zero-padded FFT
PE	peak efficiency operating line
P_m	PSD of x
PSD	power spectral density function
R	resistance across strain gage
R1	rotor 1
R2	rotor 2
S	stress uncertainty
S1	stator 1
S2	stator 2
U	wheel speed
V	axial flow velocity
V_m	zero-padded FFT
V_T	potential change resulting from transducer
W	blade relative flow velocity
WOD	wide open discharge operating line

X	FFT component at a specific frequency f
X_m	m th component of FFT of x
Z	number of interpolated points between real data points
ε	strain
σ	stress
σ_B	interblade phase angle
σ_k	interblade phase angle of k th blade
σ_{max}	stress half amplitude at resonance, or estimated maximum stress in blade
σ_{rms}	root-mean-square value of resonant stress half amplitude
ζ	blade total damping coefficient
Δe	change in e
ΔL	change in L
ΔR	change in R
∂	partial differential operator

1.0 INTRODUCTION AND BACKGROUND

Advancements in technology and new materials have led to the evolution of high cycle fatigue (HCF) as a major design consideration. HCF affects modern gas turbine engines currently in service as well as those still under development. A more thorough understanding of HCF is needed before it can be effectively controlled. Mistuning in a compressor rotor contributes to engine high cycle fatigue as it can significantly increase individual blade vibratory stress amplitudes, which in turn decreases the number of cycles to failure for subject blades. Mistuning can occur in any periodic system but has received a great deal of recent attention in the context of axial flow turbomachine rotors.

Periodic systems feature spatial repetition over time. In a machine, this generally takes the form of harmonic oscillations in which some component repeatedly passes through the same physical position. Either type of motion may be described in the time domain using harmonic functions which define both the amplitude and the frequency of the oscillation. Resonant modes and mode shapes are the natural response of the machine to excitations of different frequencies. These depend on natural frequencies, which in turn depend on geometry, materials, and manufacturing tolerances. When excited at a natural frequency, the amplitude of the oscillation increases dramatically. This condition is known as resonance and is an important design and operational consideration as operation at resonance can lead to accelerated fatigue or failure. Thus, a thorough understanding of resonance and its effects are crucial in the design and operation of rotating machinery.

The concept of a periodic system may be extended to involve a number of identical periodic subsystems which are dynamically coupled. A blade row in an ideal modern turbomachine is such an arrangement. A number of identical blades are mounted around a circumferentially homogeneous disk in a manner that is indistinguishable from blade-to-blade. This arrangement is characterized by mode shapes which extend throughout the system since all parts of the system respond similarly at resonance. Such a system is an idealization and generally does not occur. Instead, minor variations rising

from a range of possible sources including material anisotropy, manufacturing defects, and wear, result in some degree of nonuniformity or mistuning. These lead to spatially localized mode shapes, which are characterized by strong vibrations in a small region of the rotor, with amplitude decay away from this region. Localization means that prediction, measurement, and control of resonance become more complex. It can also increase stress amplitude in comparison to a tuned response during resonance. In a turbomachine, the effect on vibration amplitude is seen as significant variations from blade-to-blade with particular blades responding more vigorously than the mean response.

Modern compressor rotors often utilize a blisk design. A blisk is an integrally bladed disk in which the disk and blades are machined from one continuous piece of material, which often results in a higher degree of tuning in the rotor. However, it has been experimentally found that significant blade-to-blade variations in stress amplitude occur in these rotors, suggesting that something other than structural differences between blades is responsible for the differences in blade response. Unsteady aerodynamic effects and disk modes are potential reasons for these variations, but little experimental work has been accomplished to investigate these blade stress amplitude variations in blisks.

1.1 Previous Studies

Turbomachine rotors tend to exhibit mode localization, and therefore have been the subject of many studies. Wagner [1] attached a vibration exciter to a blade on a static rotor and observed large responses in blades well away from the excited blade. He found that amplitude variations between blades were due to structural variations as reflected by natural frequencies, and that disk motion provided mechanical energy transfer between blades on the rotor. This coupling in turn reduced stresses in blades with low damping by allowing some of the vibrational energy of one blade to be absorbed by other blades. Whitehead [2] studied aerodynamic coupling by treating blades as oscillators connected only by aerodynamic forces. He reasoned that mechanical intercoupling would be analogous to aerodynamic effects and established a theoretical maximum for the ratio of mistuned response to tuned response at $1/2(1+\sqrt{N})$, where N is the number of blades in a

bladed-disk assembly. Dye and Henry [3] followed with a lumped parameter model which predicted local stress increases greater than 35 percent. They used certain parameters, obtained from vibration tests of an actual rotor disk and blades excited electromagnetically, to determine the effects that various types and magnitudes of frequency variation have on blade stress variations. El-Bayoumy and Srinivasan [4] developed a model to compare to the predicted and measured results of Ewins [5]. In it, they treated the disk as an axisymmetric plate of variable thickness and replaced the blades with single degree-of-freedom oscillators. They found that the amount of overstressing depends on the frequency distribution and the deviation of blade frequencies from the mean. Ewins [6] conducted a number of studies, the most comprehensive of which involved tuning the individual blades in a bladed-disk assembly to measure the relationship between natural frequency mistuning and stress amplitude variations. Once again, the rotor was excited electromagnetically.

More recent studies have attempted to examine mistuning in a rotor under more realistic circumstances. Many of these studies view mistuning as a random phenomenon and take a statistical approach to predict its results. Sinha, individually [7] and with Chen [8], developed statistical models and compared their results with numerical simulations from previous models. Mignolet and Lin [9] published a perturbation model which they validated in a similar manner. Other approaches have attempted to more closely model real system dynamics. Most finite element models for analysis of rotors employ cyclic symmetry, thereby eliminating the possibility of mistuning. However, some models have been developed to investigate mistuning, though they tend to be computationally cumbersome [10, 11]. Pierre, et al. [12, 13], developed a reduced-order model which introduced random variations into the computations for cyclically symmetric models to yield mistuning effects, thereby reducing computational requirements. This model included both free vibrations and forced response.

Mistuning studies have included little experimental work on an operating rotor. Griffin [14] measured mistuning for a bladed disk assembly using strain gages, focusing particularly on probabilistic results which he correlated with analytical results from a

statistical model developed in the same study. He found that the largest stress amplitudes occurred for blades which vibrated near the tuned disk frequency, which he defined as the frequency at which the bladed disk would respond if the blades were all tuned.

These studies have generally focused on bladed disk assemblies rather than monolithic blisks. Because of this, the common assumption that blade stress amplitude variations result from blade mistuning may not necessarily apply to modern rotors which utilize the blisk design. The reduced-order technique of Pierre, et al. [12, 13], is an exception to this, but still relies to some extent on blade mistuning to yield stress variations. Thus further investigation of mistuning in a blisk configuration is vital to understanding its effects in a modern compressor rotor.

1.2 Previous Tests on Current Test Article

The blisk studied for this report has been previously tested under several programs. The first of these was the Fan Durability Assessment (FDA) Program, which was initiated to provide an experimental basis for evaluating and improving existing analysis techniques for predicting the forced response and flutter characteristics of advanced fan stages. It used total pressure distortion screens to experimentally simulate inlet distortions experienced by modern military aircraft in flight, a technique which has been refined for the current study. During FDA, the rotor was instrumented with strain gages on each blade, and an extensive set of data was obtained for response frequencies and stress amplitudes [15]. Datko and O'Hara [16] noted that the blades resonated at nearly identical frequencies during this test but showed significant variations in stress amplitude. However, they did not investigate why this occurred.

A second program, Augmented Damping of Low Aspect Ratio Fans (ADLARF), attempted to further characterize this test rotor aerodynamically and structurally. One portion of the ADLARF program mapped the inlet flow field produced by the total pressure distortions. These distortions produced an aerodynamic forcing function effective in driving resonance in the blisk [17]. However, much of the blade-mounted instrumentation intended to measure unsteady blade loading and response failed during

testing, and a comprehensive data set was not obtained [18, 19]. A third program focusing on the GE Swept Fan Assessment Rig (GESFAR) was run, but only select blades were instrumented [20]. Thus, data were not acquired to quantify mistuning effects during either of these programs.

The current investigation is part of the Compressor Research Facility Experimental Rig (CRFER) program. Minkiewicz and Russler [21] provided an analysis of a portion of the data obtained during this experiment. Their study showed that the 3/rev pressure distortion propagated through the rotor intact and characterized the on-blade pressures as tones superimposed on broadband noise. This study also provided a limited account of mistuning for the test rotor. It asserts that unsteady aerodynamics may be involved in mistuning but did not further investigate this possibility.

1.3 Problem Statement and Technical Approach

Although not investigated in the previous experiments, the test rotor has shown significant stress amplitude variation at resonance while the blades responded at nearly identical frequencies. This result is inconsistent with the findings of the previously cited mistuning studies of bladed-disk assemblies, which have shown a correlation between stress amplitude and natural frequency variations. The objective of this report is to provide a comprehensive account of natural frequency and vibration amplitude variations for a blisk so this observation can be verified and better understood.

Dynamic strain gages were mounted to be sensitive in bending on the root of each of the 16 blades on the blisk. The blades were a low aspect ratio, high speed design. The rotor was accelerated through its first resonant blade mode, the first flex (1F) mode, which was excited by a 3/rev inlet total pressure distortion. The 1F mode is essentially a pure bending blade mode for the test rotor. Data from the strain gages quantified resonant frequencies, vibratory stress amplitudes, and damping so that blade-to-blade variations in these parameters could be evaluated. The variations found for each of these parameters were compared to determine the dependence between them and to gain insight into why they occurred. Finally, the test blisk was analyzed using the reduced-order

model of Pierre, et al. [12, 13], with the results compared to experimental data to evaluate the nature of the blade stress amplitude variations.

One way to quantify blade response as a function of rotor speed is with a Campbell diagram. The predicted Campbell diagram for the blisk studied here is shown in Figure 1.1. This diagram is the predicted response for the rotor used in this investigation. It shows an original finite element prediction, which was adjusted to match bench tests at zero speed [15]. The nearly horizontal lines represent the natural frequencies of the blades. The lines which intersect at the origin represent engine order excitations, or the frequencies of external forcing functions which are integer multiples of the engine rotational frequency. Resonance occurs at the intersection of these lines.

During testing, experimental Campbell diagrams were obtained from strain gages on the blades. These Campbell diagrams are produced using fast Fourier transform (FFT) techniques. Data are sampled and analyzed in real time to determine the frequency components of the response. Each frequency component is plotted horizontally across the Campbell diagram as a function of rotor speed with the amplitude of the response indicated. Response frequencies, peak stress amplitudes, and total damping were determined directly from the Campbell diagrams.

Raw strain gage signals were also recorded on analog tape. The recorded data were analyzed using FFT techniques similar to those used in producing the Campbell diagrams. Recorded signals were used for off-resonant analysis since Campbell diagrams provide little information away from a resonant response. Analog data at resonance were used to validate the techniques involved in production of the Campbell diagrams. However, recording limitations prevented recording data from all gages, so Campbell diagrams were the primary resource for this report.

The analytical model used to predict mistuning in the test rotor creates reduced-order models of bladed disks from finite element modal analysis results. Motion of the blade is assumed to consist of disk-induced static motion and cantilevered blade elastic motion. This is consistent with previous structural mistuning models because it allows coupling between natural frequency and stress amplitude variations through the flexibility

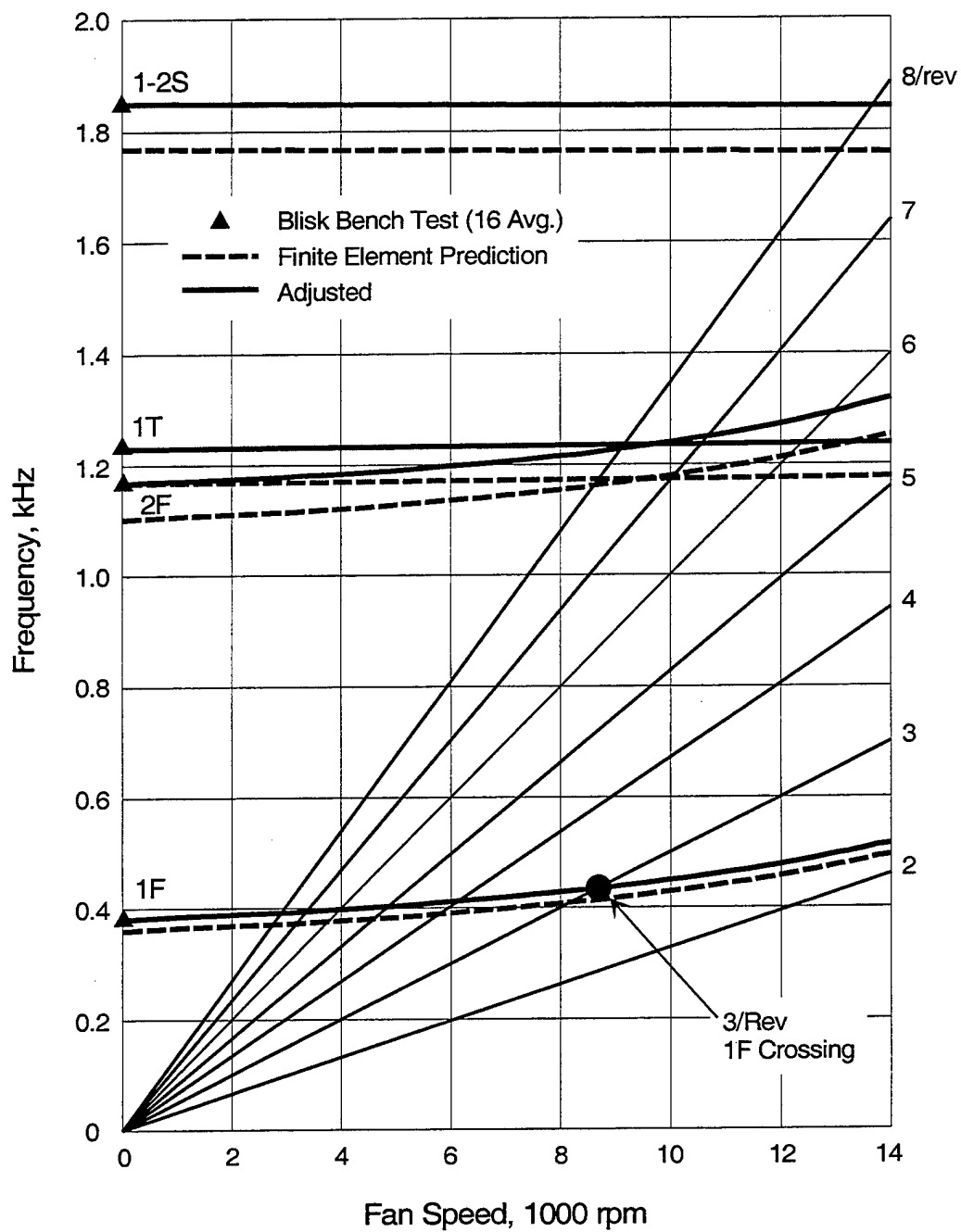


Figure 1.1: Rotor 1 predicted Campbell diagram.

of the disk. The output of the reduced-order model consists of finite element normalized displacements. Because the blade motion is assumed to be elastic, these displacements are linearly related to stresses through Hooke's Law. Therefore, predicted percent displacement variations for each blade are equivalent to stress variations.

2.0 DESCRIPTION OF EXPERIMENT

A high speed, low aspect ratio compressor fan was tested to determine mistuning effects at resonance. Testing was conducted under the CRFER (Compressor Research Facility Experimental Rig) program at the Compressor Research Facility (CRF) located at Wright Patterson Air Force Base, Ohio. The facility, test configuration, instrumentation, experimental procedure, and data acquisition are described in the following sections.

2.1 Test Facility

The CRF supports the experimental efforts of the Turbine Engine Research Center (TERC) of the Propulsion Directorate of the Air Force Research Laboratory. It provides the means for testing the steady-state and transient behavior of full-scale, multistage, single-spool compressors and small fans.

The CRF test chamber is an open cycle system in which the test article provides the sole power for moving air through the facility. The test compressor is mounted inside a 20-foot diameter test chamber. The compressor draws filtered air from the atmosphere into the test chamber plenum through an array of five inlet control valves which can be used to regulate inlet pressure. A 10-foot diameter flow conditioning barrel is mounted inside the test chamber plenum with screens and flow straighteners to minimize distortions at the test compressor inlet. A discharge valve is used to control the compressor mass flow. Discharge air passes into a collector and then into ducting which directs the flow into an acoustically treated atmospheric discharge stack. A schematic diagram of the test facility is shown in Figure 2.1.

The compressor is powered through two speed-increasing gearboxes by either of two 30,000 horsepower synchronous electric-drive motors. Various gearbox and drive motor combinations allow for various compressor speed and power ranges. The speed is controlled by varying the frequency of the electric power to the selected drive motor. Auxiliary support systems include hydraulics, test article lube oil, service air, cooling

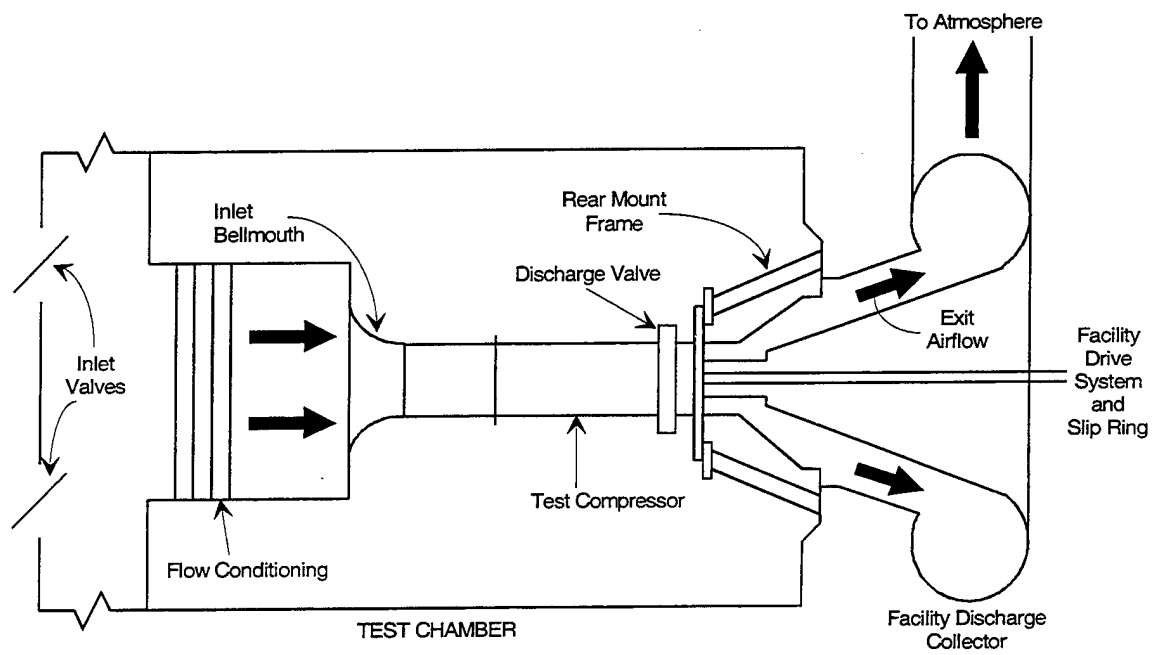


Figure 2.1: CRF test chamber schematic.

water, and fire protection. A network of computers provides control, monitoring, data acquisition, and data reduction/analysis for the facility.

2.2 Experimental Configuration

The experiment investigated a two stage compressor as shown schematically in Figure 2.2. Both the first and second stage rotors were mounted on the main shaft, with thrust loads removed by a thrust bearing system. The aft end of the main shaft was attached to the facility drive system through a series of flexible couplings capable of accommodating normal misalignment and thermal differential expansion between the vehicle and the facility [15]. The forcing function used to drive the 3/rev resonant test condition was produced by an inlet total pressure distortion created by a meshed screen mounted in the compressor inlet flow field, as shown in the figure. The inlet distortion was measured approximately one rotor radius upstream of the compressor face using distortion rakes instrumented with total pressure probes. These rakes were removed prior to obtaining the strain gage data presented here to eliminate any blade response due to the additional distortion that could be generated from the rakes.

2.2.1 Test Rotor

The first stage rotor of the compressor was evaluated for mistuning effects in the experiment described in this report. It was a blisk configuration with 16 airfoils and an integral stub shaft constructed of Ti-6-4 titanium. The blisk was an advanced design comprised of low aspect ratio blades as described by the geometric parameters shown in Table 2.1 [15].

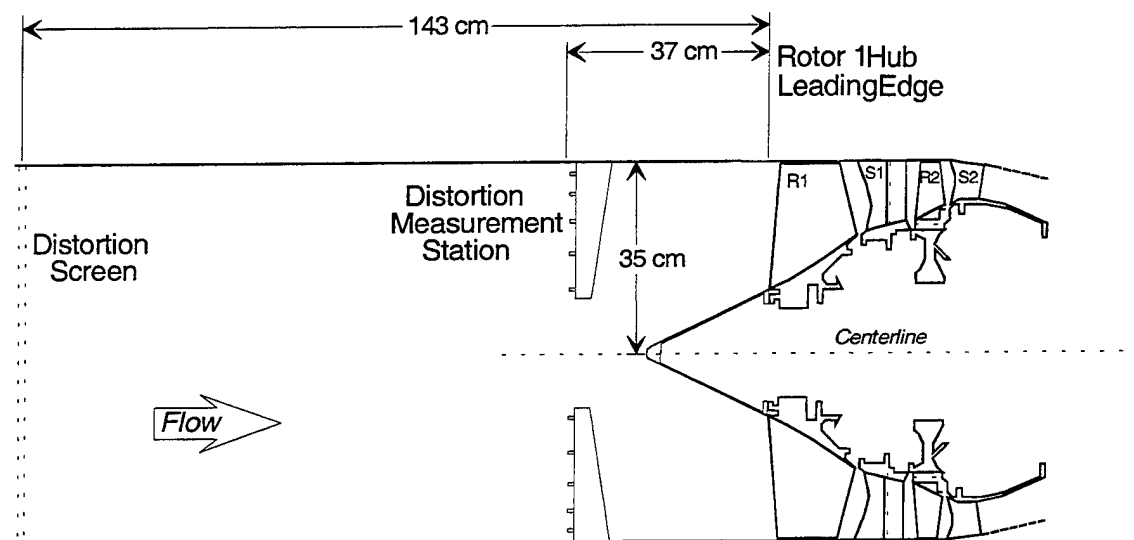


Figure 2.2: Profile schematic of test article.

Table 2.1: Rotor 1 geometric parameters.

Parameter	Value
Aspect Ratio, Root	1.1
Average Aspect Ratio	1.22
Rotor Tip Radius (cm)	35.24
Solidity, Tip	1.5
Solidity, Hub	2.67
Tip Chord (cm)	17.45
Hub Chord (cm)	20.75
Max. Thickness/Chord, Tip	0.028
Max. Thickness/Chord, Hub	0.087

The aerodynamic design pressure ratio and mass flow for rotor 1 occur at a mechanical speed in excess of 13,000 rpm. Testing took place at rotor speeds ranging from 8100 rpm to 9100 rpm. The performance parameters of the rotor at design condition and at the test condition of this study are shown in Table 2.2 [21]. At the design point, the rotor relative air flow is supersonic at 45 percent span for inlet temperatures near 300 K. For the test condition investigated in this report, the flow was subsonic throughout.

Table 2.2: Rotor 1 performance at the design and test conditions.

Parameter	Design Condition	Test Condition
Adiabatic Efficiency (%)	88.9	81.6
Total Pressure Ratio	2.5	1.59
Total Temperature Ratio	1.30	1.18
Tip Speed (m/s)	483.5	335.8
Mass Flow (kg/s)	71.8	45.9

For this experiment, mistuning effects were evaluated at the first blade resonant crossing, known to occur at a mechanical speed near 8700 rpm with a 3/rev disturbance and to exhibit the 1F mode shape at a frequency of approximately 435 Hz, as indicated

previously by Figure 1.1. Additional blade resonant crossings occur at approximately 1200 Hz (2F/1T) and 1850 Hz (1-2S). Higher order modes also exist, but fall outside of the normal operating range of the compressor. Blisk modes include a zero-nodal mode at 380 Hz and two-nodal diameter modes at 1350 Hz and 1780 Hz identified during the FDA program using holographic techniques with the rotor in a static fixture [15].

2.2.2 Downstream Airfoils

The aeromechanical response of blade and vane rows aft of Rotor 1 did not affect the response of the test rotor within the range of compressor speeds tested. Thus the measured response of the test rotor at its 1F mode was isolated. The additional blade rows aft of Rotor 1 have been characterized during previous test programs to determine potential resonant conditions, and Campbell diagrams for each are shown in APPENDIX A [22].

Rotor 2 was a bladed-disk assembly consisting of 40 blades and was linked directly to the test rotor through the compressor main shaft. Therefore, resonant conditions in Rotor 2 could impact the response of Rotor 1 if these were present at frequencies near the rotor 1 first blade mode. The 1F mode for Rotor 2 existed at a frequency of approximately 600 Hz, which was not excited by any engine order disturbances within the operating range under consideration in this experiment. The rotor had a 1T mode at approximately 1700 Hz which likewise was not excited by any engine order excitations in this operating range. Higher order modes at frequencies in excess of 2000 Hz had no significant impact on this study.

Stator 1 was comprised of 41 vanes consisting of a strut and a trailing edge flap to adjust flow turning in the stage. In the operating range of this experiment, the stator strut had a 1F resonance at approximately 1700 Hz. Higher order resonant conditions existed at frequencies in excess of 2500 Hz. The stator flap had a 1F resonance at approximately 1000 Hz as well as a 1T resonance at 1100 Hz. These crossings had no significant effect on Rotor 1 response since the stator is not connected to the rotor. Because the flow is subsonic at the test operating speed, upstream propagating potential disturbances from

this stator could excite Rotor 1. However, this resonant crossing at 40/rev was well out of the operating range examined in this report.

The compressor exit stator consisted of 60 vanes. It had a 1F mode at approximately 4000 Hz and could only be excited in the test operating speed range by engine order excitations between 24/rev and 32/rev. Furthermore, the location and installation of Stator 2 prevented it from directly affecting the test rotor. Upstream propagating potential waves from this stator did not excite Rotor 2 within the operating range of interest.

2.2.3 Distortion Screen

The forcing function used to drive the 3/rev resonant test condition was produced by an inlet total pressure distortion introduced using a meshed screen mounted in the compressor inlet flow field. The porosity of the screen was equally incremented around the compressor circumference to produce a roughly sinusoidal forcing function. A diagram of the screen showing this mesh density can be seen in Figure 2.3. The distortion pattern was mapped forward of the compressor face using a distortion rake consisting of a total pressure probe at five radial immersions in the flow. The five radial positions were at the centers of equal areas in the inlet. The distortion screen was rotated with the rake fixed so that a circumferential pressure distribution was measured at each immersion. A sector of approximately 10° was not mapped, but sufficient data were obtained to characterize the inlet forcing function. The mean of pressure fields measured by the probes is shown in Figure 2.4. The screen produced a maximum total pressure variation of approximately ± 2.5 percent of the circumferential mean.

Although the primary frequency component of the inlet distortion was the intended 3/rev pattern, additional components were present as well. Figure 2.5 shows the frequency content of the inlet flow field with the frequency expressed per revolution. Besides the 3/rev component, drivers were present at 1/rev, 9/rev, and 15/rev. The 9/rev driver excited a resonance in rotor 1 at the low end of the operating range of interest. At 8100 rpm, the excitation frequency of this pressure component was 1215 Hz, which was

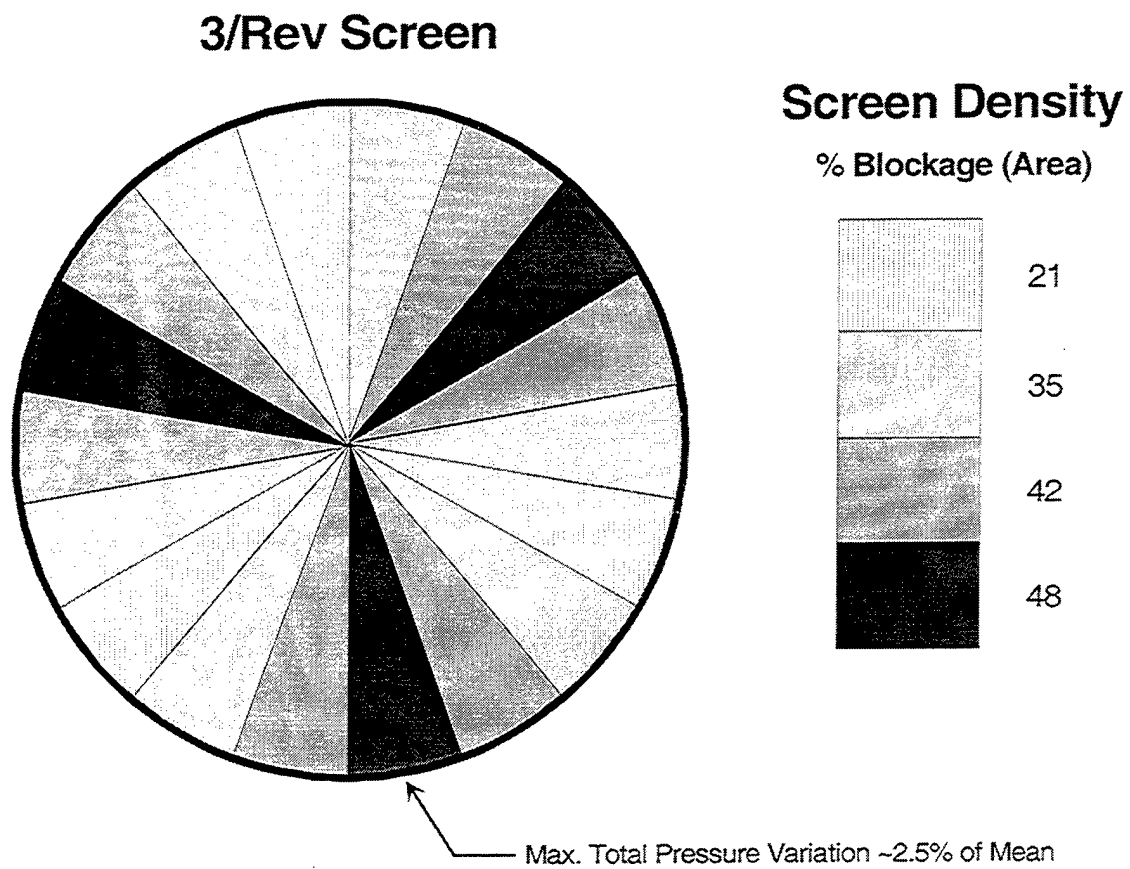


Figure 2.3: 3/rev distortion screen pattern.

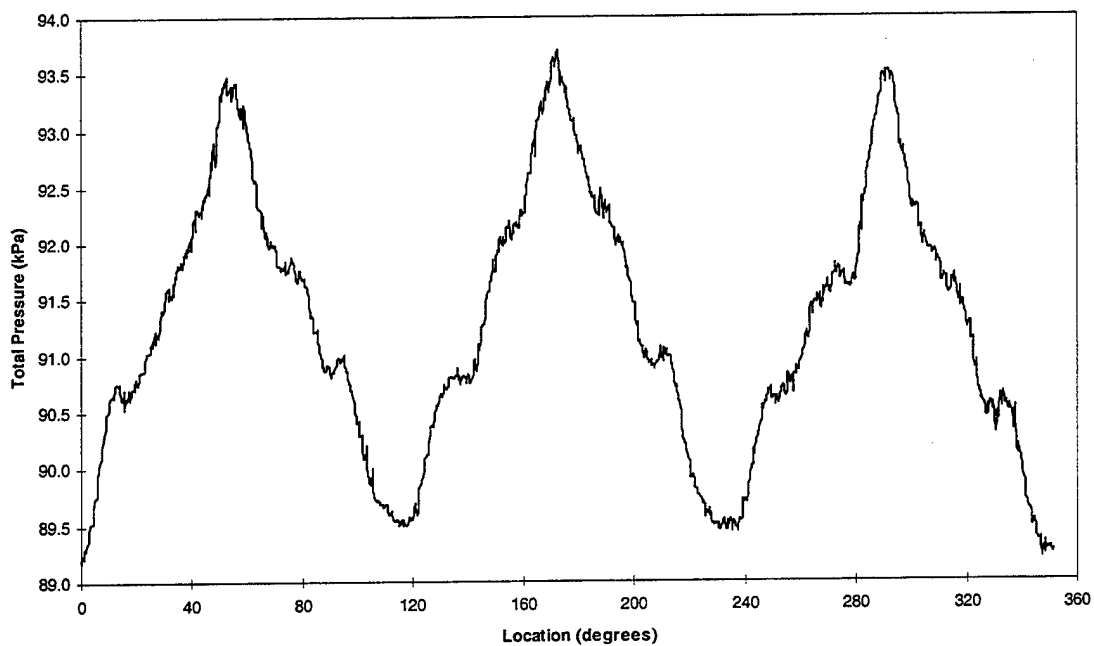


Figure 2.4: Circumferential map of inlet total pressure field (mean of 5 radial immersions).

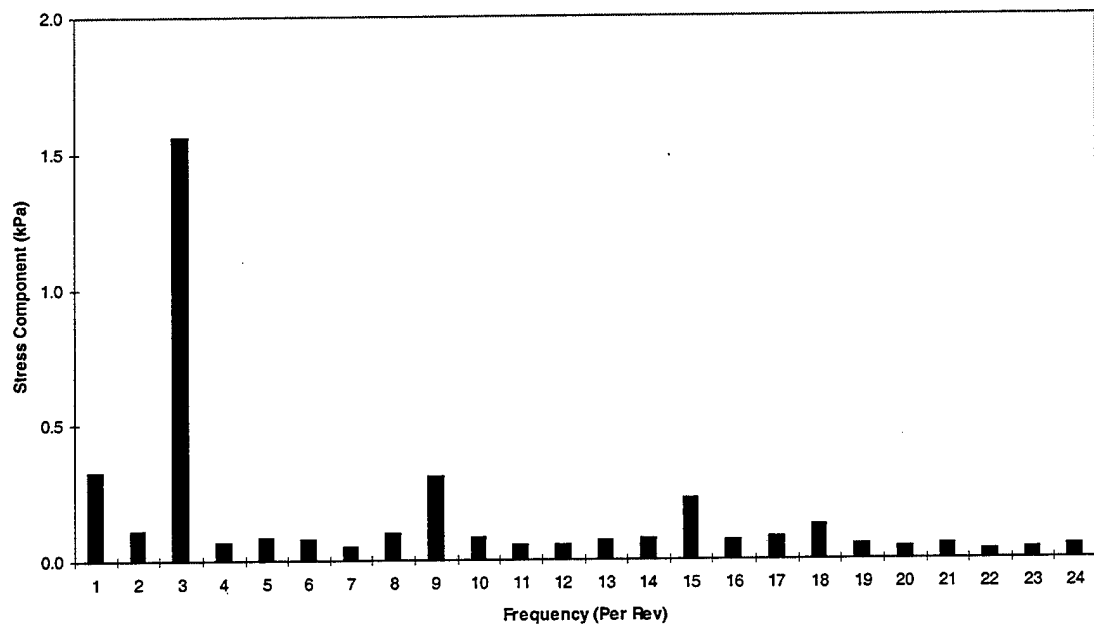


Figure 2.5: Inlet total pressure frequency distribution (based on mean of 5 radial immersions).

near the 2F/1T natural frequencies of the blades. This driver was caused by interaction between the screen and a set of struts mounted forward of the screen in the compressor inlet, Figure 2.6. It shows the struts overlaid on the 3/rev screen pattern, with numbered sectors of the screen corresponding to the circumferential location of the numbered regions in the pressure field diagram. The pressure field was measured at approximately half the compressor radius from the center. Each sector in the screen caused a step change in the pressure, with a peak at the center of the sector and away from the joints between sectors as the joints caused some additional blockage. The heavy mesh densities at Sectors 6, 12, and 18 resulted in these peaks being small in comparison to others. Furthermore, Sectors 2 and 4 had the same screen mesh density, but the character of the step change was different because Sector 2 was unobstructed while Sector 4 had a strut blocking its centerline. Sectors 1 and 5 had a similar situation in which one sector was blocked by a strut while the other was free of obstruction. However, the higher screen density washed out this effect to some degree so that the differences in the step change between sectors were not as pronounced. These relationships between sectors repeated circumferentially. Therefore, the step changes at odd-numbered locations in the figure were the most prominent. Examination of the distribution of these locations reveals the 9/rev pattern in the pressure field.

The strength of the resonant response was not sufficient to prevent operation at that speed, and data analysis techniques allowed decomposition of the response into frequency components, thereby minimizing any detrimental effects on the experiment from this resonant condition. The 1/rev and 15/rev were of little significance during this experiment.

2.3 Instrumentation and Data Acquisition

Strain instrumentation consisted of ED-DY-062AP-350E dynamic strain gages produced by Micro-Measurements. The uncertainty of these gages in stress amplitude measurement was estimated at approximately 6 percent. Strain gage specifications and details of the uncertainty analysis are provided in APPENDIX B. A strain gage was

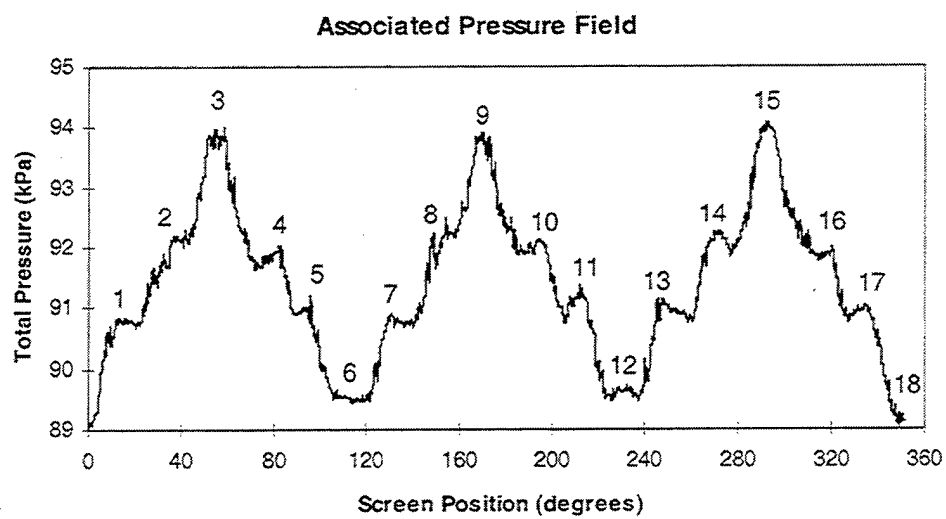
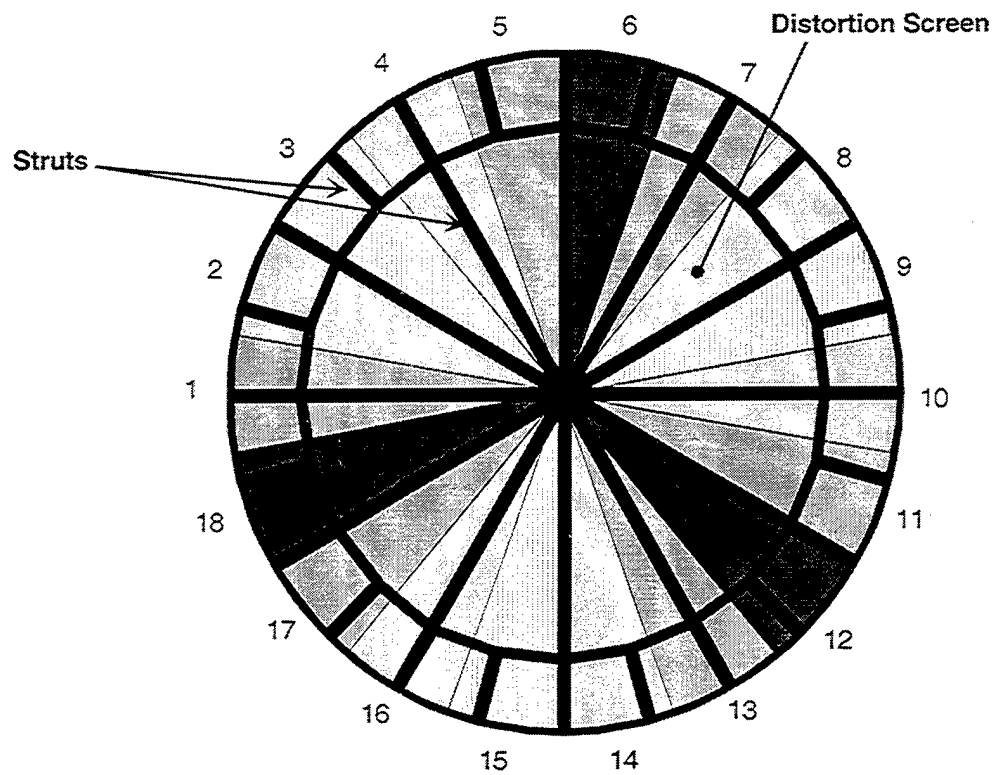


Figure 2.6: Interaction of 3/rev distortion screen and inlet struts.

applied at the root of each of the 16 blades. The location of the gage on each blade is shown in Figure 2.7. The strain gages were connected to a slip ring located at the drive end of the test compressor which linked them to the stationary data acquisition system.

The strain gage signals were all AC coupled, which effectively high pass filtered them at approximately 5 Hz. This removed voltage offset and allowed transient signals to be recorded using the full range of the recording system, which in turn reduced post-processing errors associated with the recording device and the A/D conversion.

Campbell diagrams were generated on-line for all strain gages during accelerations through resonance. A brief description of the process used to produce these Campbell diagrams is given in Chapter 3. The Campbell diagrams from the root strain gages at the 1F resonance are included in APPENDIX C. In addition to Campbell diagrams, signals from blade-mounted strain gages were recorded on analog tape for post-test processing. The tape, number AR2619, is stored in the CRF tape library. Table 2.3 shows the tape log from the portion of the experiment pertinent to this report. Operating lines are defined in the next section. The tape speed was 15 inches per second, which allowed signals with frequency content up to 10 kHz to be recorded. Signal corruption from the recorder prevented use of the signal from the strain gage on Blade 3. The gage on Blade 4 failed at the beginning of the experiment. In addition, signals from Blades 10 and 11 were not recorded. However, the responses of 75 percent of the blades were obtained on tape.

Additional instrumentation during the experiment included leading and trailing edge strain gages on 6 blades and Kulite high-frequency response pressure transducers on two blades. Detailed information on this instrumentation is not included in this report since these were not used in the subject mistuning study. Additional information is given in ref. 21.

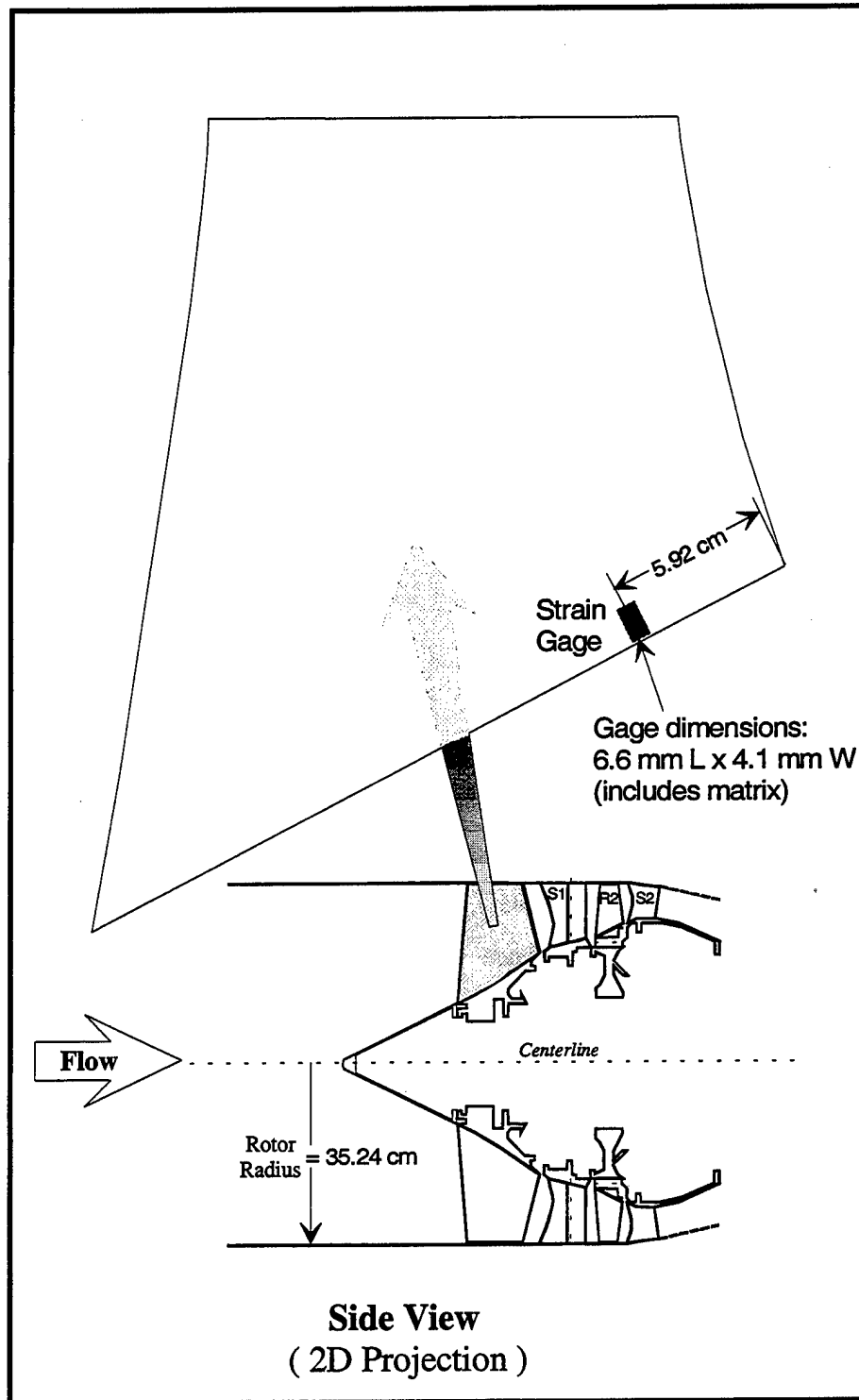


Figure 2.7: Rotor 1 strain gage location.

Table 2.3: Tape log from 3/rev 1F resonant crossing.

Operating Line	Rotor Speed	Time
WOD	8100 rpm	006:19:39:00-41:00
NOL	8100 rpm	006:19:42:30-44:30
PE	8100 rpm	006:19:45:20-47:20
NS	8100 rpm	006:19:49:00-51:00
WOD	9100 rpm	006:19:53:00-55:00
NOL	9100 rpm	006:19:55:45-57:45
PE	9100 rpm	006:20:01:00-03:00
NS	9100 rpm	006:20:03:55-05:55
WOD	accel	006:19:51:55-52:40
NOL	accel	006:20:09:20-10:00
PE	accel	006:20:11:35-12:10
NS	accel	006:20:13:50-14:30

2.4 Experimental Procedure

Although the objective of this experiment was to investigate mistuning effects on rotor resonant response, the rotor could not be operated at resonance for long periods. However, steady-state data were necessary to quantify the blade forcing function. Therefore, data were acquired during steady operation both above and below resonance, i.e. 8100 rpm and 9100 rpm, respectively. These operating speeds were chosen to come as close as possible to peak resonance without damaging the blisk. Transient data quantifying the peak resonant conditions were also acquired as the rotor speed was increased through resonance from 8100 rpm to 9100 rpm. These speed increases were executed at a rate of approximately 30 rpm/second, which was rapid enough to avoid damaging the rotor but still allowed the acquisition of useful peak resonance data.

The steady-state and transient data were acquired along four different operating lines as defined by corrected compressor mass flow. These throttle conditions consisted of Wide Open Discharge (WOD), the Nominal Operating Line (NOL), Peak Efficiency (PE), and Near Stall (NS). Inlet total pressure probes were not installed during the test to prevent extraneous drivers in the inlet flow field. Therefore, actual mass flows could only be estimated based on the discharge flow area, which is defined by the discharge valve (DV) position. This value represents the percentage of the compressor annulus

which is open for air flow at the DV. Estimated mass flows for the operating lines are shown in Table 2.4. They are useful in examining relative steady blade loading. Data points, operating lines, and accelerations through resonance for this experiment are summarized in Figure 2.8.

Table 2.4: Estimated corrected mass flows of compressor operating lines.

Operating Line	DV Setting	Mass Flow (kg/s)	
		8100 rpm	9100 rpm
WOD	60.0	40.28	48.40
NOL	57.0	39.79	48.13
PE	55.4	38.97	47.44
NS	53.3	36.31	45.61

During testing, the compressor was started and accelerated with the discharge valve in its wide open position to 8100 rpm, where a settling time of 2 minutes was allowed for passage of flow transients, and then data were recorded for approximately 2 minutes. Once this was completed, the discharge valve was closed to attain NOL. A 30-second settling time was allowed, and data were recorded at this condition. This procedure was repeated at constant speed for the PE and NS conditions. When data had been recorded at 8100 rpm for all throttle positions, the discharge valve was fully opened and the compressor was accelerated to 9100 rpm, where the same procedure was repeated for all four operating conditions. At completion, the discharge valve was opened and the rotor was decelerated back to 8100 rpm. The rotor was then accelerated up to 9100 rpm on the WOD line with data being recorded. The compressor was decelerated back to 8100 rpm, and the discharge valve was closed to reach NOL. The compressor was accelerated at this throttle condition to 9100 rpm, and then decelerated to 8100 rpm without adjusting the throttle. This procedure was repeated for the PE and NS operating lines. When testing was completed, the discharge valve was opened and the rotor was brought to full stop.

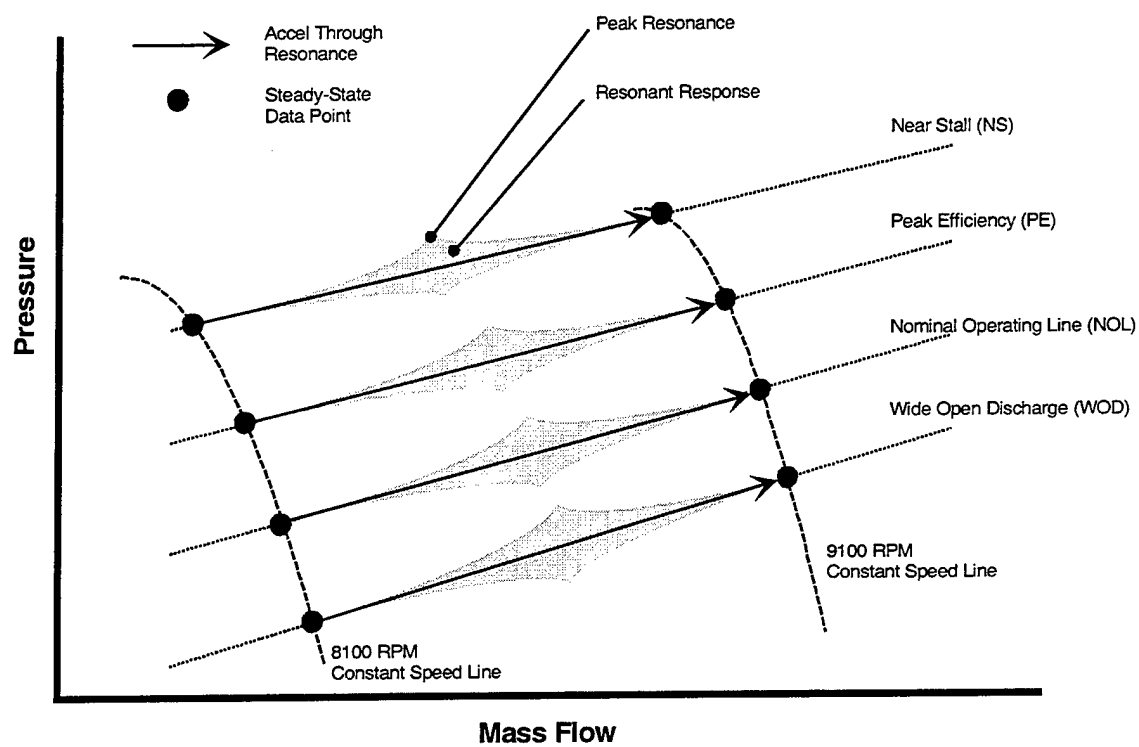


Figure 2.8: Test summary.

3.0 DATA REDUCTION AND ANALYSIS

To verify tuning of the test rotor and to investigate blade-to-blade stress and damping variations, response frequencies, stress amplitudes, and total damping were determined. To facilitate this, data from the experiment were reduced and analyzed as described in the following sections.

3.1 Steady-State Data Reduction

The analog signals on tape were digitized and stored electronically. This was accomplished by passing the signal from the tape through a low-pass filter with a cutoff frequency of 10 kHz to reduce signal aliasing and through a 12-bit analog-to-digital (A/D) converter. A sampling rate of 2.5 kHz was used. This minimized electronic storage requirements but allowed for resolution of frequencies near the 1F resonance at 435 Hz. This sampling rate also allowed for resolution of stress amplitudes for the steady-state data. Ten seconds of steady-state data were sampled on each operating line at 8100 rpm and at 9100 rpm. The result was an array of raw data for each condition including digital signals for each root strain gage except Blades 10 and 11. Digital data were imported into the Lab Work Bench computer software package and stored as an ASCII format file [23].

3.2 Steady-State Analysis

Steady-state data for conditions above and below resonance were examined for frequency response and blade-to-blade stress variations. The frequency response of each strain gage signal was analyzed by determining the power spectral density function (PSD) of the signal, which is derived from its FFT. An FFT is used to transform an ordered sequence of data samples, usually from the time domain into the frequency domain. For a vector x , of length N , consisting of discrete samples x_k , the FFT of the vector may be expressed as:

$$X_m = \sum_{k=0}^{N-1} x_k e^{-j(2\pi km/N)}, \quad m = 0, 1, \dots, N-1. \quad (3.1)$$

The FFT is thus a series of N components, with each component corresponding to a discrete frequency equivalent to multiplying the sampling rate by m/N . Each component is generally a complex number, with its amplitude being its absolute value.

The power density spectrum is defined as the squared magnitude of the fast Fourier transform, usually scaled by N . Thus the PSD of a sampled signal is defined mathematically as:

$$P_m = \frac{1}{N} |X_m|^2, \quad m = 0, 1, \dots, N-1. \quad (3.2)$$

The total energy in a signal can be written in terms of the fast Fourier transform, or the PSD, in an expression known as Parseval's relationship.

$$E[x_k^2] = \frac{1}{N^2} \sum_{m=0}^{N-1} |X_m|^2 = \frac{1}{N} \sum_{m=0}^{N-1} P_m \quad (3.3)$$

Thus the PSD, Figure 3.1, is qualitatively the distribution of the total energy in a signal over its frequency range [24]. A peak in the PSD of a signal indicates a strong response at the frequency where it occurs, generally due to a forcing function or resonance. Response at harmonics of a given frequency may also be observed in this manner, though the response tends to be smaller than at the fundamental frequency. From this analysis, which used an FFT length N of 1024 derived from non-overlapping Hanning windows, the frequency of the 3/rev forcing function was determined at off-resonant speeds.

Hanning windows separate a data array into shorter sequences to improve the accuracy of FFT analysis. With this technique, a weighting factor is multiplied by the terms in the sequence to eliminate end effects on the signal. For a Hanning window of length M , this weighting factor, w_k , is:

$$w_k = \frac{1}{2} \left(1 - \cos \frac{2k\pi}{M-1} \right), \quad 0 \leq k \leq M-1 \quad (3.4)$$

To calculate the amplitude of the steady-state response, the amplitude of the complex Fourier coefficient of the signal at the frequency of the forcing function was found. This was accomplished by an application of the FFT. A specific component, X_m , of the FFT may be determined by specifying m . If the component for a specific frequency is desired, the following substitution may be made.

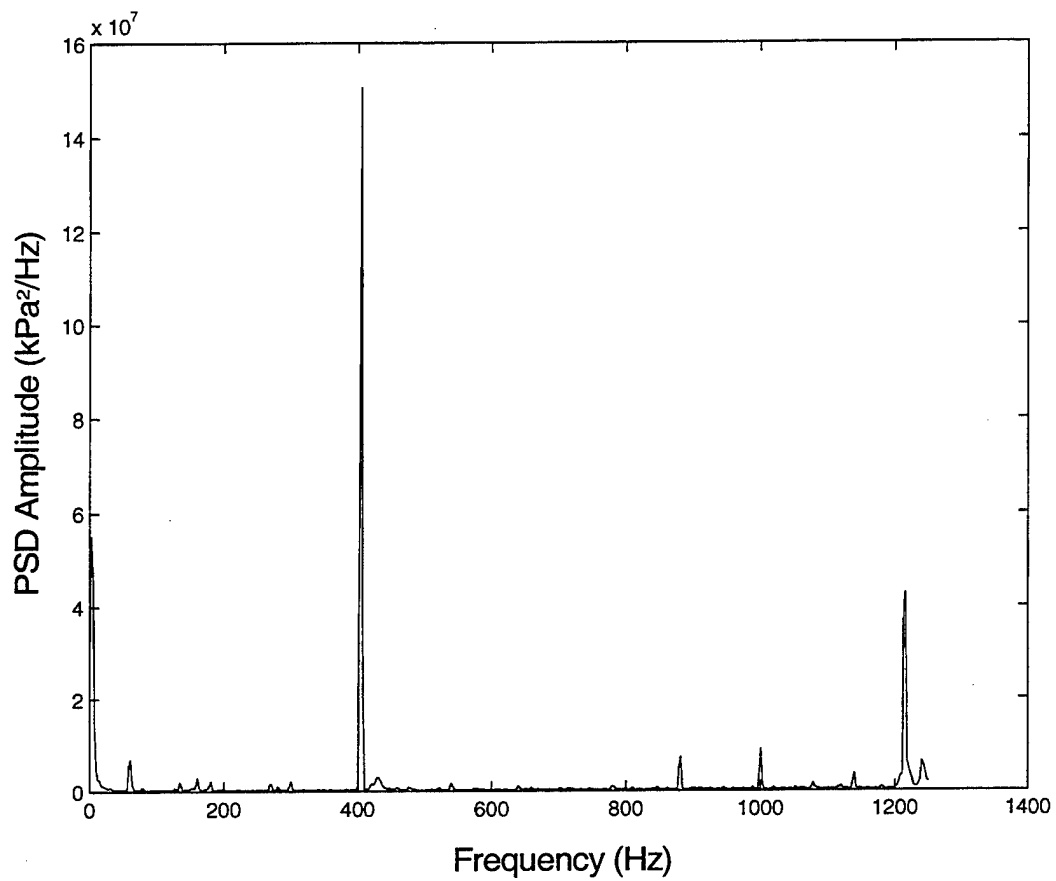


Figure 3.1: PSD of steady-state strain gage signal (NOL, Blade 2 strain gage, 8100 rpm).

$$f = \frac{m}{N} \quad (3.5)$$

To maintain consistent units, the frequency f in this expression is in Hz-s, and is found by dividing the desired frequency by the sampling rate used in obtaining the data sequence. Using this in Equation 3.1, the expression for a specific component X of the FFT of a given signal is:

$$X = \sum_{k=0}^{N-1} x_k e^{-j(2\pi kf)} \quad (3.6)$$

This method works well when the amplitude of the signal does not change quickly. Therefore, it was used to determine the steady-state stress amplitudes above and below resonance.

In addition to the frequency and amplitude response of the steady-state data, ensemble averaging was employed to determine the stress on the blade as a function of circumferential location. An example of such an ensemble average is shown in Figure 3.2, which displays the normalized average stress over a single rotor revolution. Ensemble averaging divides a vector of data into smaller sets containing an equal number of samples such that each small data set includes the same number of periods from a signal. Corresponding points from all of the smaller data sets are then averaged to find the mean of the signal over the number of periods specified. In turbomachinery analysis, ensemble averages often determine a mean over one rotor revolution.

Ensemble averaging between data points was improved using a zero-padding technique. This technique allows nonlinear interpolation to produce a curve fit while maintaining the spectral character of the original signal. To accomplish this, the FFT, X_m , of the signal is determined. This FFT contains the same number of discrete points, N , as the digital signal being analyzed. If Z denotes the number of interpolated points desired between each real data point, then the number of points, N_p , in the padded FFT will be:

$$N_p = N(Z + 1). \quad (3.7)$$

Zeros are then inserted into the FFT of the signal, with the number of added zeros, N_z , depending on whether N is even or odd.

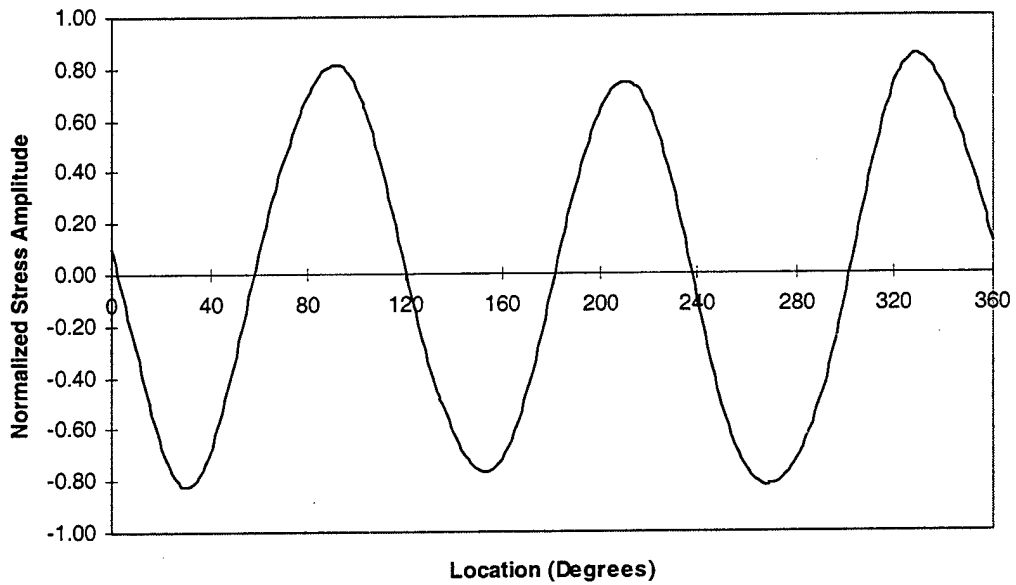


Figure 3.2: Ensemble average of strain gage signal (PE, Blade 9 strain gage, 9100 rpm).

$$N_z = N_p - N - 1, N \text{ even} \quad (3.8a)$$

$$N_z = N_p - N, N \text{ odd} \quad (3.8b)$$

This yields a modified FFT, V_m , with the same spectral content as the original.

$$[V_m] = \left[X_0, X_1, \dots, \frac{X_{N/2}}{2}, (\text{zeros}), \frac{X_{N/2}}{2}, \dots, X_{N-1} \right], N \text{ even} \quad (3.9a)$$

$$[V_m] = \left[X_0, X_1, \dots, X_{(N-1)/2}, (\text{zeros}), X_{(N+1)/2}, \dots, X_{N-1} \right], N \text{ odd} \quad (3.9b)$$

The inverse FFT of V_m results in a new set of data, v_k , of length N_p which preserves the wave form of the original signal. This technique was applied to the ensemble average of each signal, producing eight interpolated points between real data points. The additional data points enhanced the signal so its characteristics could be more readily observed.

The average from each blade was shifted by an appropriate angle so that the averages overlapped and the mean stress distribution around the circumference of the rotor could be determined. The maximum value of this mean stress distribution for all operating lines was used as the normalizing factor.

To assist in verifying the quality of the strain gage signals, time histories of the strain gage output were plotted. These indicated if a large amount of noise was present or if the signal was completely contaminated. A sample of both a clean signal and a contaminated signal are shown in Figure 3.3. Corrupted signals were determined to be caused by the recorder and not strain gage failures.

Steady-state stress and frequency data were analyzed to examine blade-to-blade stress variations away from resonance at the frequency of the inlet forcing function. In particular, the circumferential mean stress component at the forced frequency and variations from this mean were determined. Although the structural nature of each blade could not be considered through this type of analysis, it showed whether stress variations could occur at a common frequency without a direct resonant response.

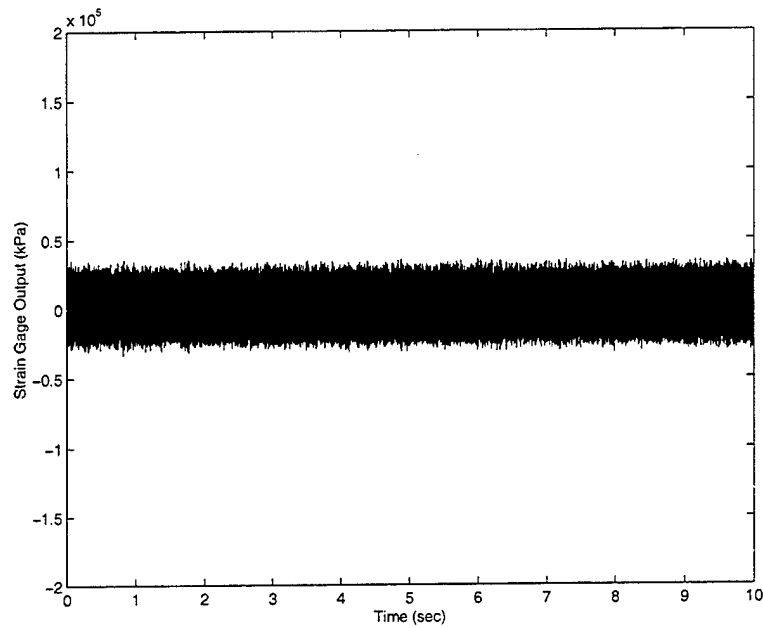


Figure 3.3a: Time history of clean steady-state strain gage signal (WOD, Blade 8 strain gage, 9100 rpm).

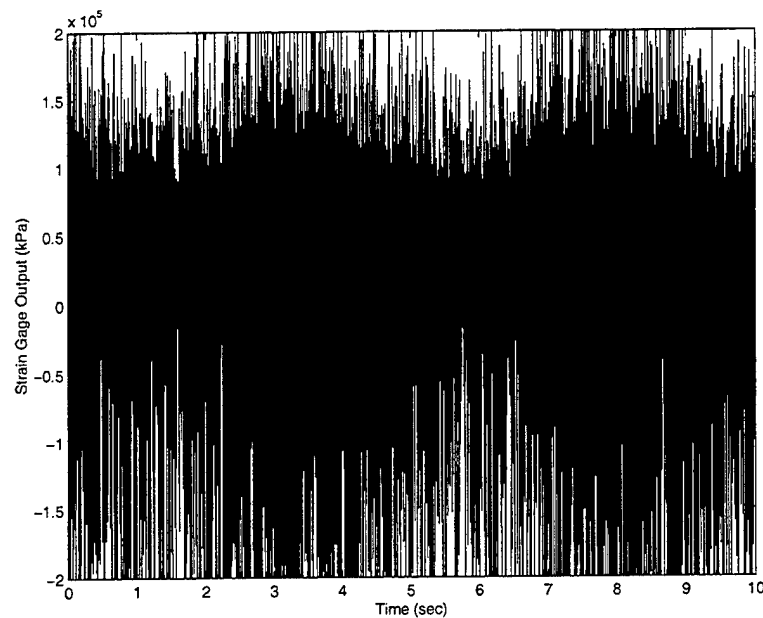


Figure 3.3b: Time history of contaminated steady-state strain gage signal (WOD, Blade 3 strain gage, 9100 rpm).

3.3 Transient Data Reduction

Campbell diagrams were generated for all of the strain gages on-line during accelerations through resonance. The diagrams were stored as Post Script graphics files. The Campbell diagrams from all strain gages are provided in APPENDIX C. The processor sampled data at a rate of 30 kHz and performed an FFT on each signal to determine the frequency response of the strain gage and the amplitude of each frequency component. Hanning windows were used to separate the data into sequences consisting of 1024 samples for each FFT. The frequencies and corresponding stress amplitudes were plotted on the Campbell diagram as a function of rotor mechanical speed.

Analog transient signals were reduced similarly to steady-state signals. However, the sampling rate was not sufficient to accurately determine resonant stress amplitudes from the transient data so that blade-to-blade relative stress distributions could be discerned but actual amplitudes could not be computed [25]. Accurate amplitude resolution was not necessary due to the use of Campbell diagrams. A time window of 40 seconds was chosen for the transient data to insure that the entire resonance was captured.

3.4 Transient Analysis

Campbell diagrams were available from more strain gages than those recorded. Therefore, resonant frequencies, peak stress amplitudes, and total damping for each blade were determined directly from the Campbell diagrams. The peak response was selected from the diagram and its amplitude was measured and compared to a scale on the diagram to determine the peak-to-peak stress amplitude at resonance. The frequency at which the peak response occurred was also extracted from the diagram. Damping was determined from the Campbell diagram using the half power method, as shown in Figure 3.4. This method uses the frequency, f_{res} , at peak resonance as well as the stress half amplitude, σ_{max} , at that point to estimate damping. The root-mean-square value of the stress half amplitude, σ_{rms} , is calculated.

$$\sigma_{rms} = \frac{\sigma_{max}}{\sqrt{2}} \quad (3.10)$$

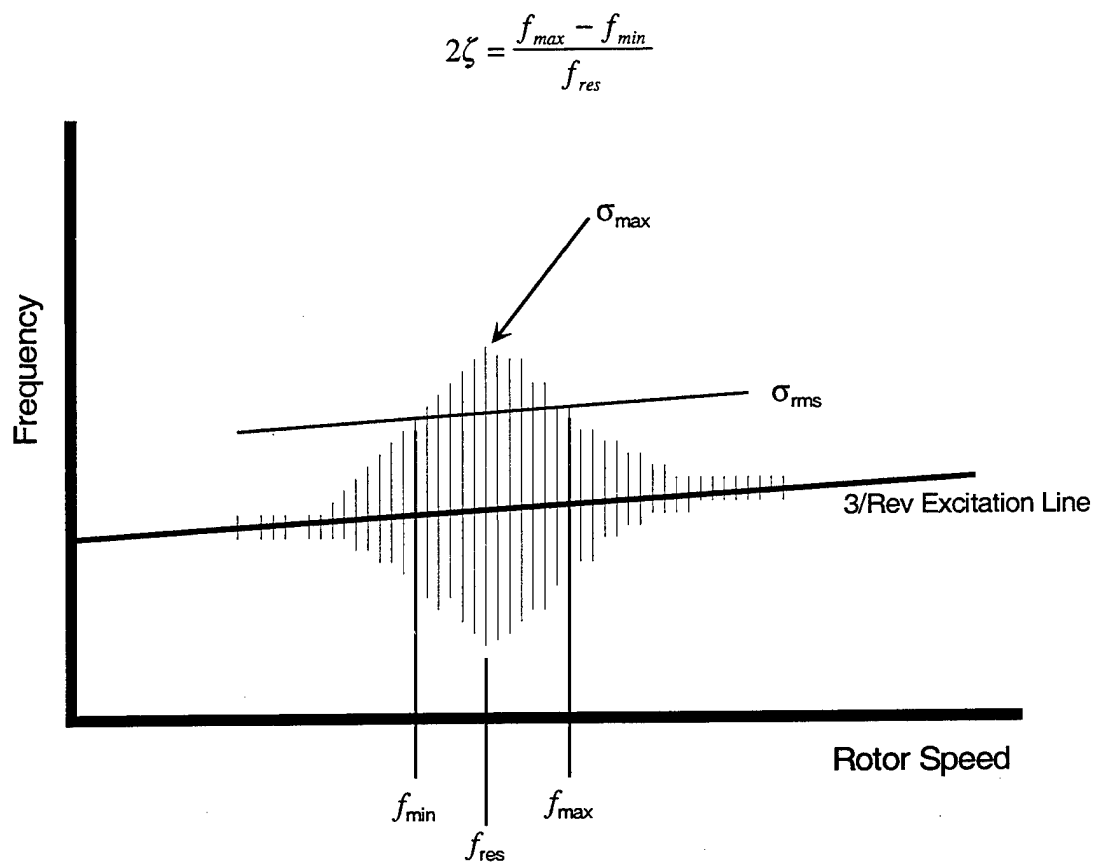


Figure 3.4: Half power method for determining damping from Campbell diagrams.

This value is marked on the Campbell diagram, and a line is drawn through this point parallel to the engine order excitation line. This line crosses the response blossom on the Campbell diagram in two locations, and the frequencies, f_{max} and f_{min} , at those locations are determined. The engine mechanical speed may be used for all of the frequencies in this method. From this information, the total damping coefficient ζ of the blade may be estimated.

$$\zeta = \frac{f_{max} - f_{min}}{2f_{res}} \quad (3.11)$$

Once the resonant frequency, peak amplitude, and damping coefficient for each blade were determined, blade-to-blade variations in these parameters were examined. This included finding the mean, the maximum percent deviation from the mean, and the standard deviation for all three.

Spectral analysis of the recorded signals was used to verify the results obtained from the Campbell diagrams. The resonant frequency of each blade was determined in the same manner that the forcing frequency was determined from the steady-state data. The power spectral density function of the signal was computed. Since most of the energy in the system was concentrated at the resonant frequency, the strongest response in the frequency spectrum occurred at resonance. Because the data arrays from accelerations through resonance were long, only 30 percent of the data were used to improve the signal-to-noise ratio from the signal. The data retained for analysis included peak resonance and pre- and post-peak data based upon a plotted time history of the signal. The PSD of one of the strain gage signals is shown in Figure 3.5. This analysis used an FFT length of 1024 with non-overlapping Hanning windows. The stress amplitude at resonance was estimated from the peak in the PSD using Equation 3.2. As for the steady-state data, plotted time histories of the strain gage output were used to examine the integrity of each signal. Examples of clean and corrupt signals are shown in Figure 3.6. Because the poor quality of the signal for Blade 3 was caused by the analog recorder, the Campbell diagram for this blade was not affected.

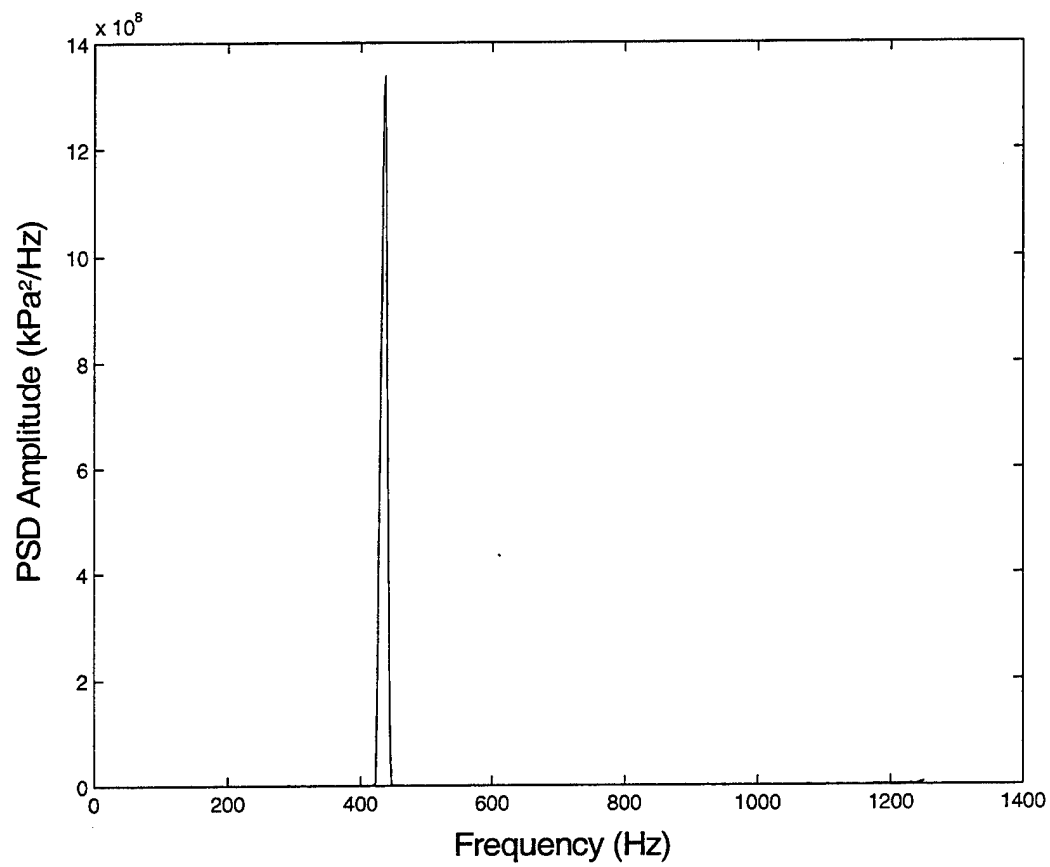


Figure 3.5: PSD of transient strain gage signal (NS, Blade 15 strain gage).

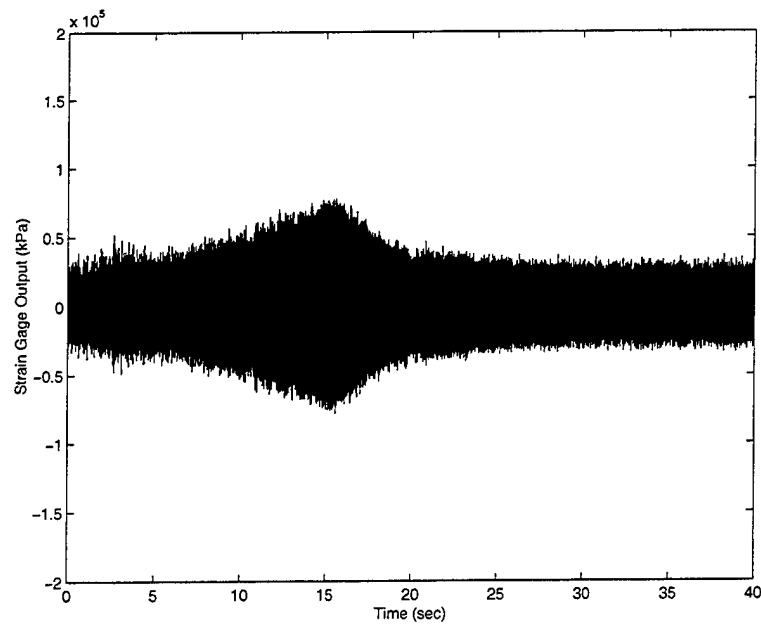


Figure 3.6a: Time history of clean transient strain gage signal (NS, Blade 15 strain gage).

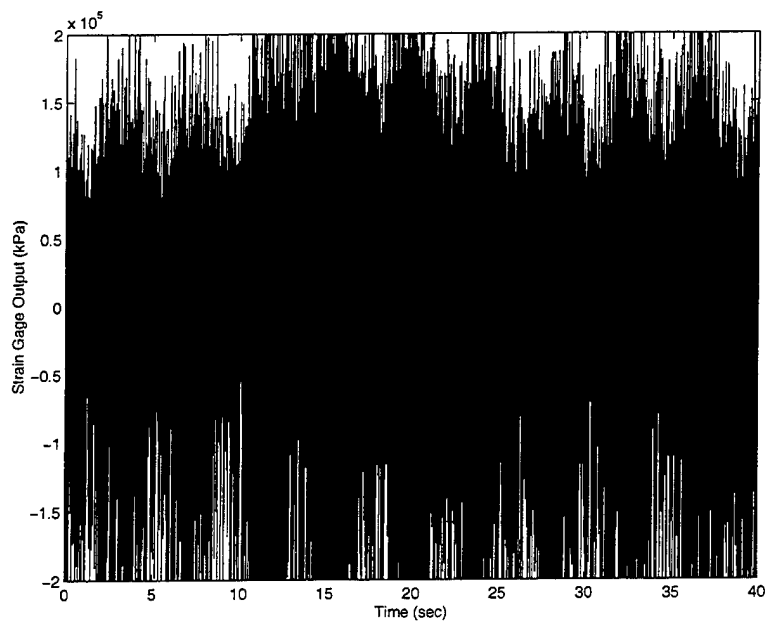


Figure 3.6b: Time history of contaminated transient strain gage signal (NS, Blade 3 strain gage).

4.0 EXPERIMENTAL RESULTS

Variations in response frequency, stress amplitude, and total damping were studied to characterize the nature of mistuning effects in a blisk. The experimental data used for this are tabulated in APPENDIX D. Response frequencies and resonant stress amplitudes were also determined from recorded signals to verify the Campbell diagrams. A comparison of the data obtained from the Campbell diagrams and recorded signals is contained in APPENDIX E. The implications of the experimental data are discussed in this chapter.

4.1 Off-Resonant Mistuning Effects

The PSD of each strain gage signal indicated the frequency of the forcing function at the steady-state operating points away from resonance. This frequency was 405 Hz for all blades at 8100 rpm mechanical speed and 455 Hz at 9100 rpm. The amplitudes of the stress components were calculated at these frequencies. As previously mentioned, results were not available from Blades 3 and 4 as well as from Blades 10 and 11.

4.1.1 Blade Stress Variations

The mean stress amplitude around the rotor was calculated for each operating condition, and the percent deviation from this mean in the response of each blade found. The results of this analysis are shown in Figure 4.1 for all four throttle conditions at 8100 rpm. Although the response at the common excitation frequency was measured for each blade, the amplitude of this response varied significantly from blade-to-blade. The stresses varied by as much as 17 percent of the mean stress on the PE operating line, and the standard deviation ranged from 6.7 percent on NOL to 8.7 percent on the PE line. Figure 4.2 shows similar results at 9100 rpm, though the variation was greater. The stress amplitude at the forcing frequency varied by up to 21 percent of the mean while operating near stall, with the standard deviation ranging from 9.8 percent at WOD to 13.7 percent at NS. No correlation to variations in structural properties of the blades can be made

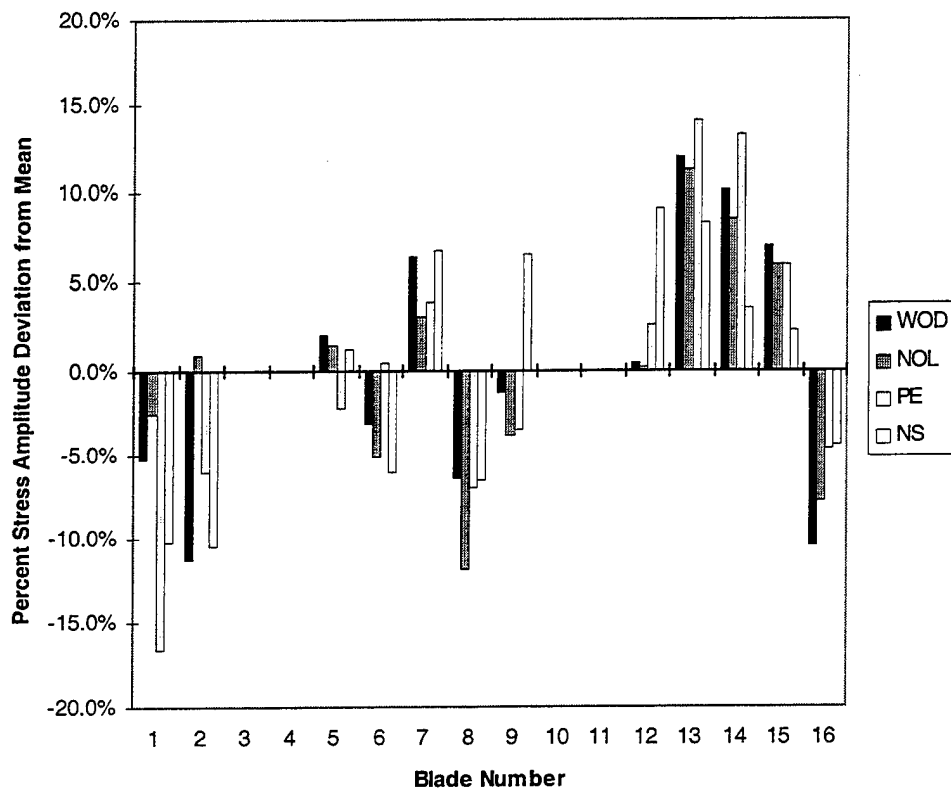


Figure 4.1: Blade-to-blade stress variations, 8100 rpm mechanical speed.

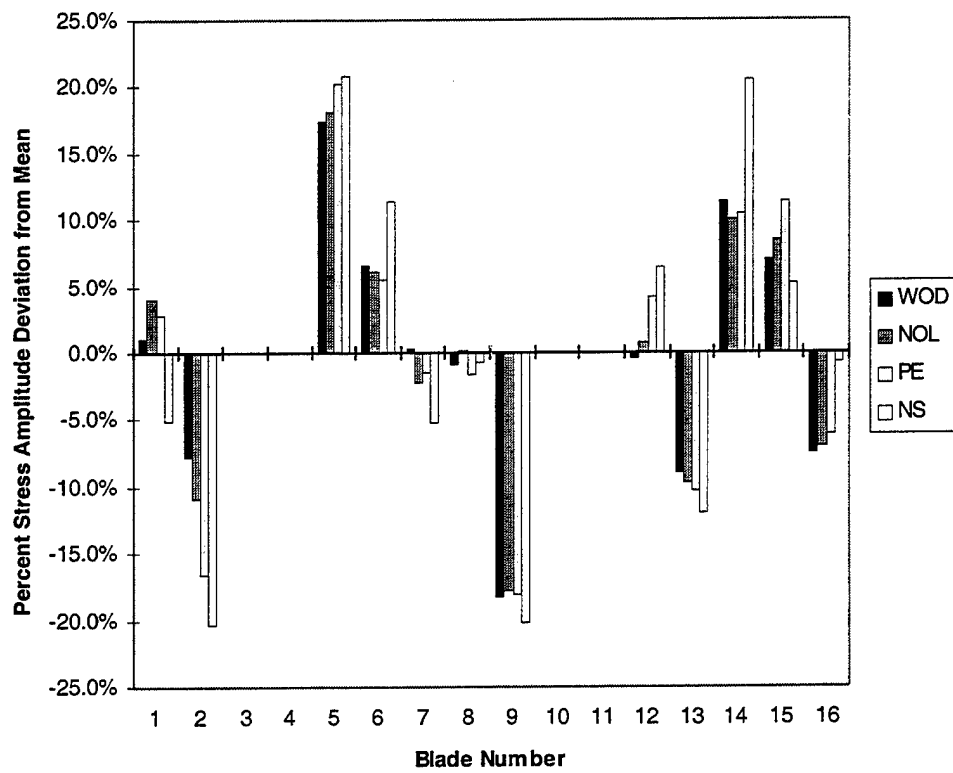


Figure 4.2: Blade-to-blade stress variations, 9100 rpm mechanical speed.

because the response was not determined at a natural frequency. However, since these stresses were measured at a common frequency away from resonance, the variations cannot be attributed to mistuning.

Both figures show similar patterns between operating lines at the same speed. The general stress pattern at 8100 rpm around the circumference of the rotor changes quantitatively, but is qualitatively the same for all four throttle conditions, and the same holds true at 9100 rpm. However, the fundamental pattern changes considerably from one speed to the other, thus indicating a relationship between speed and circumferential stress distribution. This observation provides important insight into the nature of the stress variations, suggesting that blade aerodynamic loading may be strongly involved.

A typical velocity triangle for the rotor is shown in Figure 4.3. The triangle assumes no preswirl in the inlet flow. The unsteady aerodynamic load on each blade will vary slightly due to small differences in angle of attack, blade curvature, and surface roughness which do not appreciably affect blade structure. These differences can account for the variation in blade response around the rotor.

At constant speed, either 8100 rpm or 9100 rpm, the wheel speed component U remains constant for all throttle conditions. As the throttle is closed, however, the inlet flow velocity V changes, though this change is generally small. V is approximately 30 percent of U . Since V is the smaller of the two components that comprise the relative velocity W , and because the changes in V are small, throttling the compressor causes only small changes in W , which can be seen in Figures 4.1 and 4.2 as the minor differences between operating lines that do not fundamentally alter the pattern around the rotor. Moreover, the blade shape remains similar for all throttle conditions at constant speed. In particular, the blade relative angle of attack does not change since the blade does not untwist at constant speed. Therefore, the aerodynamic characteristics of the blades do not change appreciably. As rotor speed is increased from 8100 rpm to 9100 rpm, more noticeable changes occur. The wheel speed U increases significantly, which causes a substantial modification in W . In addition, the blades untwist with additional centrifugal stiffening at higher speed, altering the aerodynamic characteristics of the blades. This

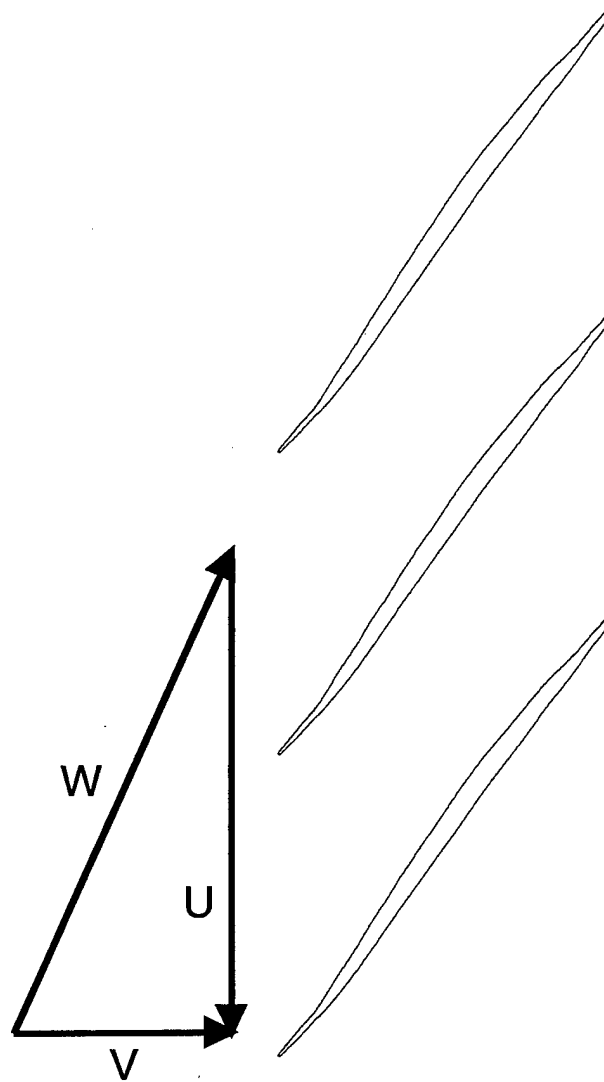


Figure 4.3: Rotor 1 velocity triangle.

fundamentally modifies the blade-to-blade aerodynamics of the rotor and accounts for the overall change in the stress distribution pattern seen between the two speeds. This argument will be discussed in more detail later.

4.1.2 Ensemble Averages

Ensemble averages were used to determine both the normalized mean stress distribution around the rotor circumference for each blade and the rotor mean stress distribution by averaging the individual blade results. Figure 4.4 shows the rotor mean stress distribution as well as the ensemble averages for Blades 2 and 13 at 8100 rpm on the NOL and NS operating lines. Blades 2 and 13 were chosen as representative examples of all blades on the rotor.

The ensemble averages show several interesting features. The 3/rev forcing function is verified, particularly in the rotor mean stress distribution. An additional response is seen as a 9/rev harmonic superimposed on the 3/rev fundamental. This 9/rev component is the response of the blades to the 9/rev driver previously shown to exist in the inlet flow field. At 8100 rpm, this driver yields a frequency of 1215 Hz, which corresponds to the 2F blade resonance of the rotor. This response can also be seen in the steady-state PSD in Figure 3.1 and in the on-line Campbell diagrams in APPENDIX C at 8100 rpm. The amplitude of this resonant response was not strong enough to prevent prolonged operation at this speed. Furthermore, the FFT techniques used during data analysis separated the response into frequency components, so the additional response at 1215 Hz does not affect the response at 405 Hz used to determine stress variations, assuming that the response is linear and the components can be superimposed. Thus, the 2F resonant response at 8100 rpm has no impact on the results presented here.

Similar ensemble averages at 9100 rpm are shown in Figure 4.5. Once again, the 3/rev forcing function is verified. The averages at this speed do not show the same frequency content as those at 8100 rpm because the 9/rev driver at 1365 Hz is no longer near a blade natural frequency. This can be verified in the Rotor 1 predicted Campbell diagram, Figure 1.1, as well as the on-line Campbell diagrams, APPENDIX C.

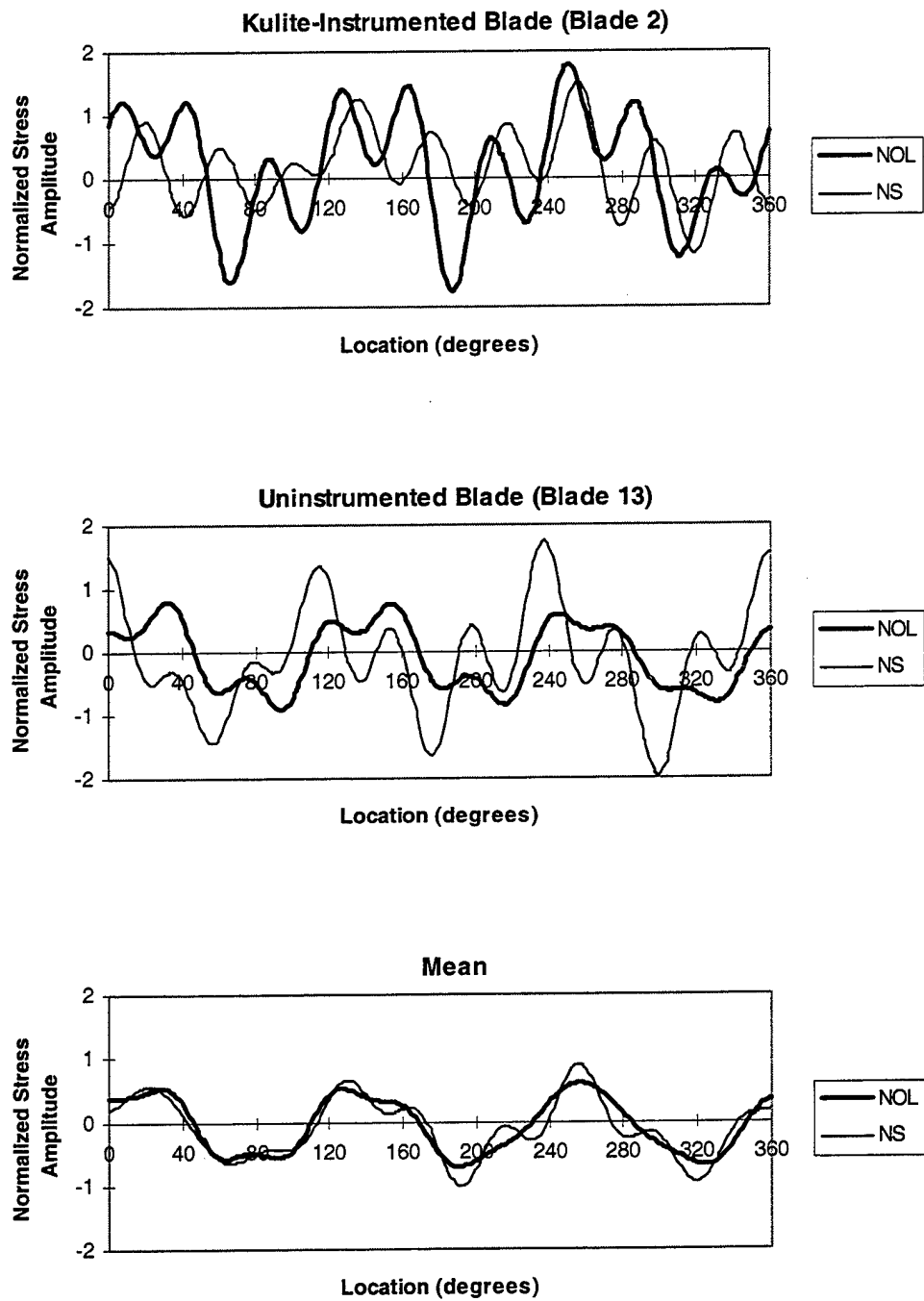


Figure 4.4: Ensemble averages of strain gage response, 8100 rpm mechanical speed.

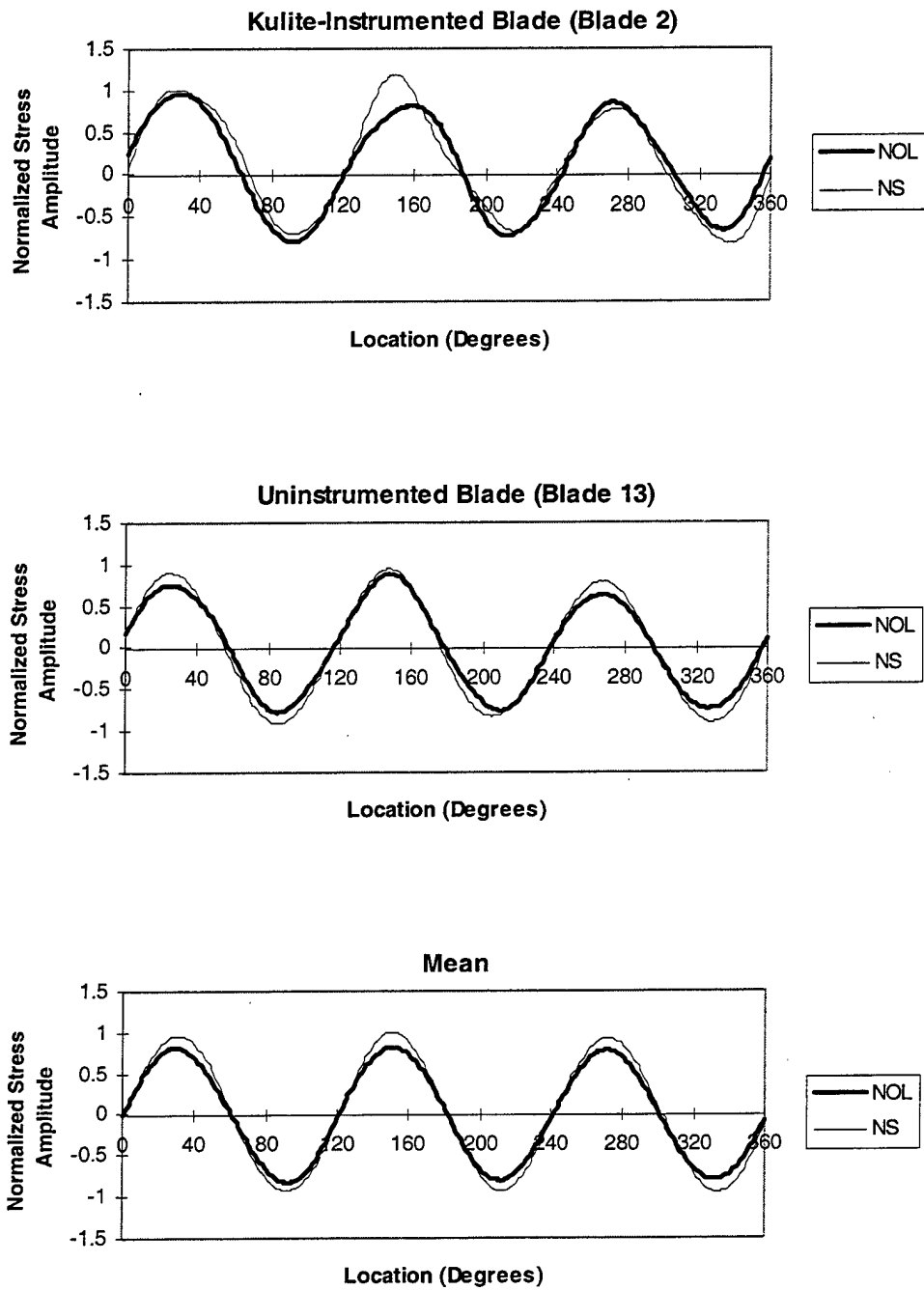


Figure 4.5: Ensemble averages of strain gage response, 9100 rpm mechanical speed.

The ensemble averages in both figures were phase shifted so that the blades could be directly compared. However, phase has important implications in the response of each blade. Interblade phase angle σ_B can be expressed mathematically as:

$$\sigma_B = -360^\circ \left(\frac{C}{N} \right), \quad (4.1)$$

where N is the number of blades on the rotor, and C represents the number of upstream wakes for an aerodynamic disturbance or the number of nodal diameters in a hub mode. The negative sign indicates a backward traveling wave, which occurs in a stable system such as the test rotor.

Raw signals from adjacent blades were compared to determine the phase angle between them. The interblade phase angle at both constant speeds was determined to be approximately -67° for all blades, which corresponds to the interblade phase angle for a 3/rev upstream aerodynamic disturbance, $\sigma_B = -67.5^\circ$, showing that the responses observed away from resonance were strictly blade response to the primary aerodynamic forcing function.

4.1.3 Summary of Off-Resonant Results

Results off-resonance indicate that blade-to-blade stress variations involve factors other than structural mistuning. The response at the common forcing frequency varied significantly between blades at steady operating points above and below resonance. The circumferential stress distribution patterns at these speeds suggest that differences in individual blade unsteady aerodynamic loading account for the stress variations. Ensemble averages and phase analysis verified that the measured blade stresses were in response to the 3/rev aerodynamic disturbance as opposed to structural coupling as reflected by disk motion.

4.2 Mistuning Effects at Resonance

Blade-to-blade variations in resonant response frequencies, peak stress amplitudes, and total damping were examined to characterize the effects of mistuning at

resonance. This allowed evaluation of blade structural mistuning as well as a more detailed investigation of aerodynamic and mechanical coupling.

4.2.1 Evaluation of Structural Mistuning

Examination of response frequencies and peak stresses at resonance allowed for evaluation of structural mistuning in the blisk. Figure 4.6a shows the circumferential peak stress distribution compared to related resonant frequencies for WOD and NOL, and Figure 4.6b shows the same information for PE and NS. The mean stresses and frequencies for each operating line are also shown so that variations from the mean can be observed. The ordinate axes for frequencies and stresses have different scales with regard to the amount of variation from the indicated mean.

The figures show that the blisk is essentially tuned. The frequency varied by less than 0.7 percent of the mean for all blades on all operating lines. However, the peak stresses varied by up to 26 percent of the mean at NOL, with standard deviations ranging from 11.4 percent at WOD to 12.4 percent at NOL. Closer examination also shows that the distribution patterns around the rotor circumference are not the same for frequency and stress, thus showing a lack of correlation between these parameters. Blades which respond below the mean frequency do not show a tendency for either higher or lower than mean peak stress. Since natural frequency is a direct measurement of blade structure, this lack of correlation indicates that the blade-to-blade variations in stress are not related to blade structural mistuning, supporting the results from off-resonant analysis.

4.2.2 Hub Participation and Aerodynamic Mistuning Effects

As with the off-resonant stresses, a distinct pattern in the circumferential peak stress distribution exists at resonance for all operating lines. While these stresses were not measured at a constant speed, resonance occurred at nearly the same operating speed for each throttle condition. The mean response frequency changed by 1 Hz from WOD to NS, which corresponds to a maximum speed difference of 20 rpm between operating lines. In terms of the velocity triangle in Figure 4.3, this yields only a small change in U .

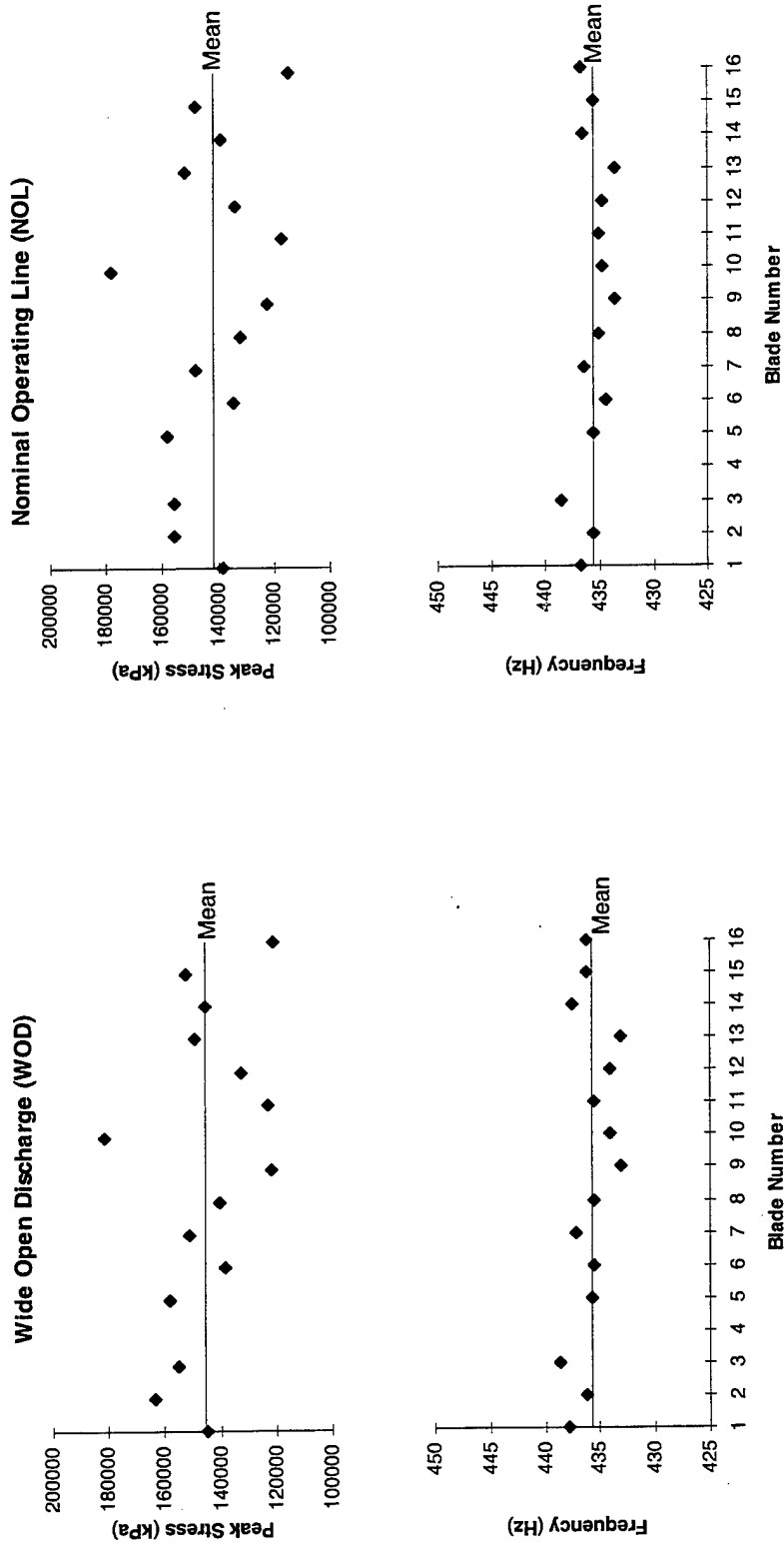


Figure 4.6a: Comparison of blade natural frequencies and peak stresses (WOD and NOL).

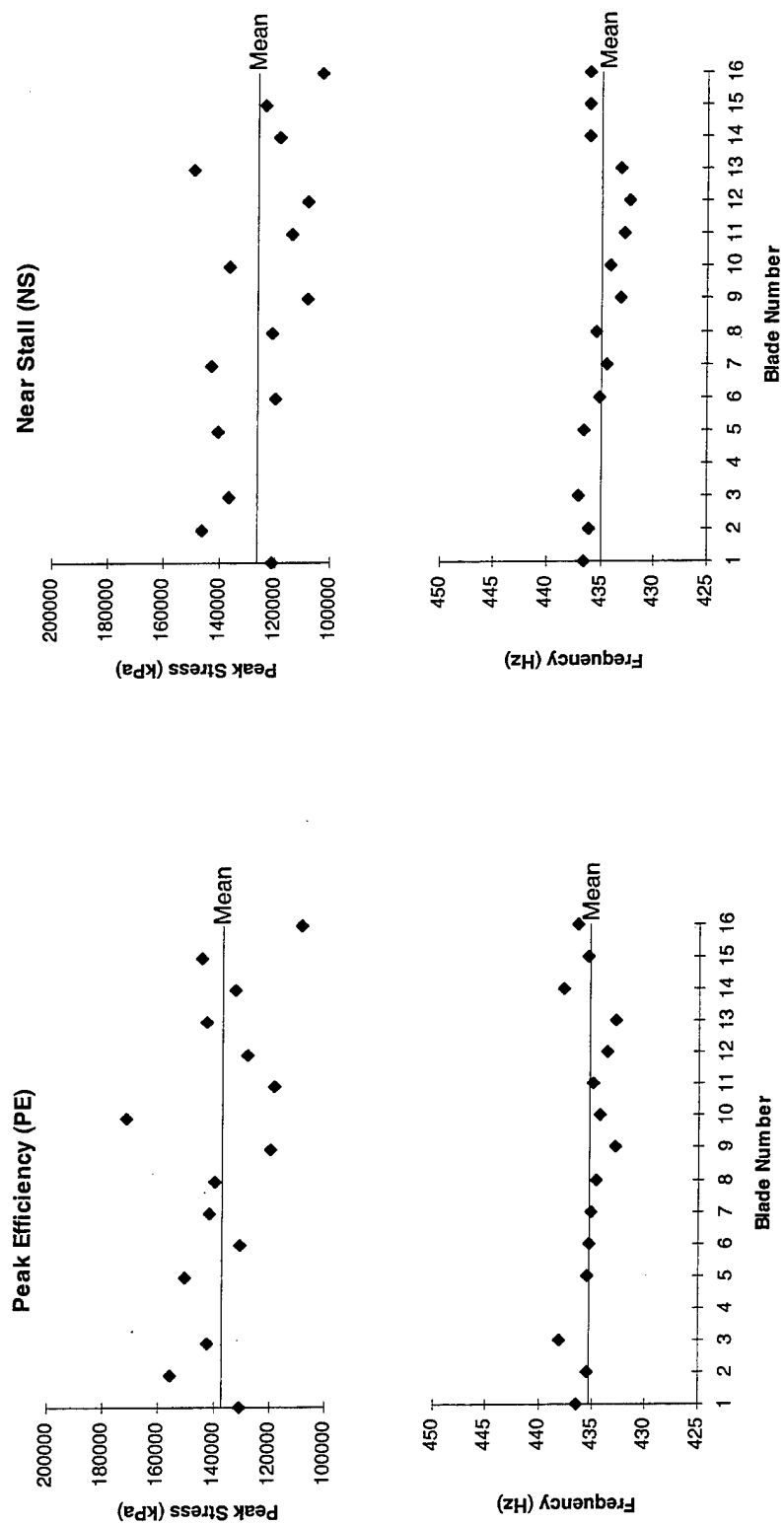


Figure 4.6b: Comparison of blade natural frequencies and peak stresses (PE and NS).

This range in wheel speed will not significantly impact blade untwist. Therefore, the resonant conditions for each operating line may be assumed to occur at essentially constant speed, comparable to the off-resonant constant speed conditions. Therefore, the existence of a fundamental pattern at the resonant speed with only small changes between operating lines is consistent with the previous results, and again supports the notion of an aerodynamic driver yielding the blade stress variations.

Further investigation of the stress distribution yields significant information. A spatial FFT of the peak stresses from each operating line is shown in Figure 4.7. The spatial FFT is expressed by Equation 3.1, with m representing each diametric distribution component expressed per revolution. Data for Blade 4 was interpolated using the mean of the other 15 blades to yield 16 samples around the rotor. This number of samples allowed for content up to 8/rev in the pattern to be determined. The addition of the interpolated point had little impact on the results shown. The most significant aspect of this analysis is the 6/rev component in the stress distribution for all operating lines, particularly since this is an integer multiple of the resonant driver.

Two possible explanations for the 6/rev pattern exist. The first is a 6-nodal diameter hub mode interacting with the blade 1F mode at this frequency. However, this is unlikely. At low frequencies such as the 1F blade frequency, high nodal diameter response is blade-dominated such that the distinct 6/rev pattern would not be evident. Previous holographic testing of the test rotor has indicated that no hub modes of this nature occur at frequencies near the 1F blade mode [15]. Moreover, phase data from this experiment does not indicate the presence of a hub mode. From Equation 4.1, a 6-nodal diameter hub mode would yield an interblade phase angle of -135° . The phase measured from recorded signals between a pair of adjacent blades was approximately -67° , indicating a backward traveling 3-nodal wave typical of a 3/rev inlet forcing function. Thus, hub modal participation probably was not a significant factor in the resonant response at this crossing.

An unsteady aerodynamic driver due to the interaction of the inlet forcing function and the blade resonant response would account for the 6/rev pattern. The blade passage

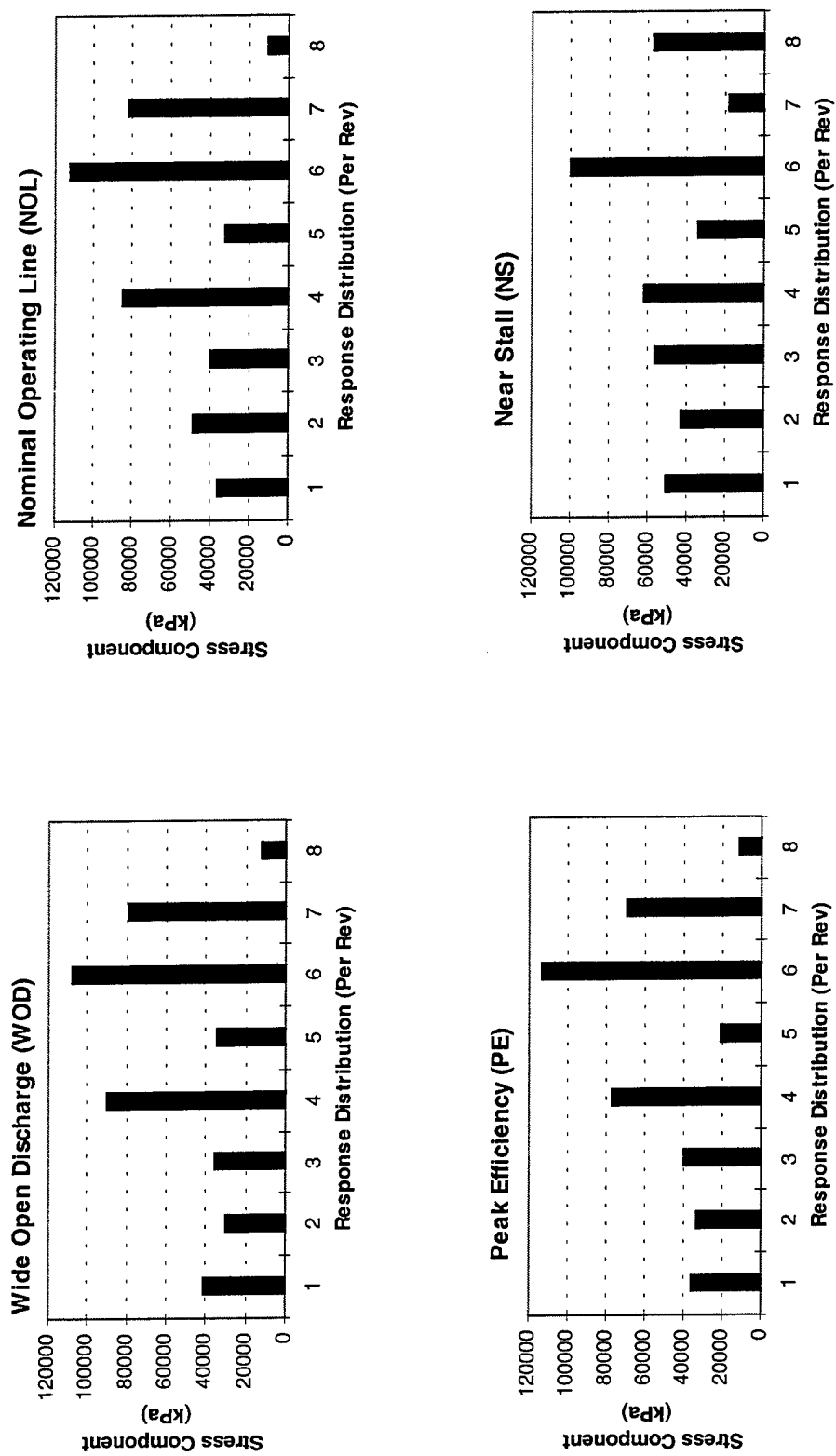


Figure 4.7: Circumferential peak stress distribution.

flow field at this condition is complex, and investigation of the flow field is beyond the scope of this study. However, the existence of the pattern at this condition and not away from resonance makes this explanation feasible, especially when considered in regard to previous discussion on velocity triangles and blade untwist.

An FFT analysis of the resonant frequency distribution around the rotor did not yield results comparable to those seen for the stress distribution. No distinct diametric component could be seen in the mistuning pattern around the rotor circumference. This further demonstrates that blade stress variations are decoupled from structural parameters of the blisk, and supports the notion of an unsteady aerodynamic driver.

The effect of throttle position on blade resonant response can be seen in Figure 4.8. The overall stress on the rotor blades as indicated by the circumferential mean decreases as blade loading is increased toward stall. This is likely to be caused by an increase in aerodynamic damping, though the total damping measured during the experiment do not show any notable effect from compressor throttling. The figure also shows that peak stress amplitude variations are not significantly affected by throttle position except at NS. The magnitude of the variations at that condition was significantly smaller than at the other operating conditions, showing that the higher blade loading actually reduced mistuning effects.

4.2.3 Damping Effects on Stress Variations

Total damping is compared to resonant stresses in Figure 4.9a for WOD and NOL and in Figure 4.9b for PE and NS. The ordinate axes have been scaled to display approximately the same percent variation from the mean for both peak stress and total damping so that a direct comparison of mistuning effects may be made. Total damping varied as much as 46 percent of the mean damping ratio at PE, with the standard deviation ranging from 18 percent at WOD to 26 percent at NOL. More importantly, comparison of peak stress and total damping shows that high total damping generally corresponds to low peak stress and the converse, denoting an inverse relationship between these parameters.

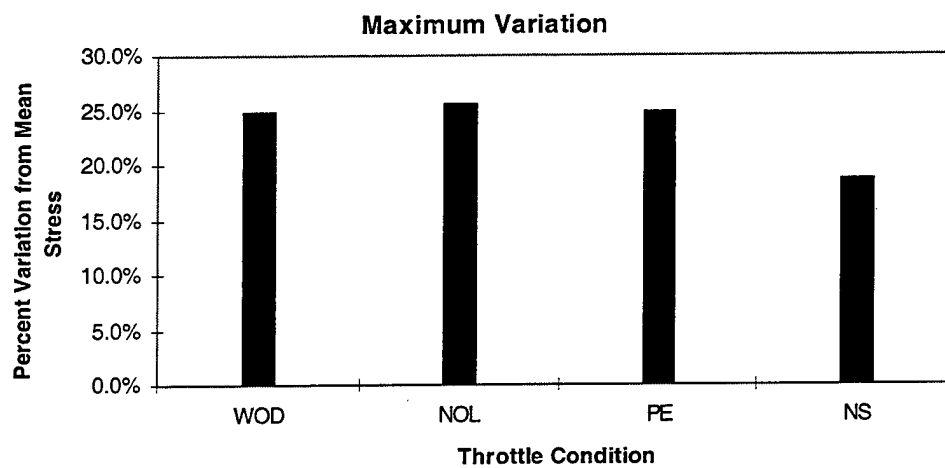
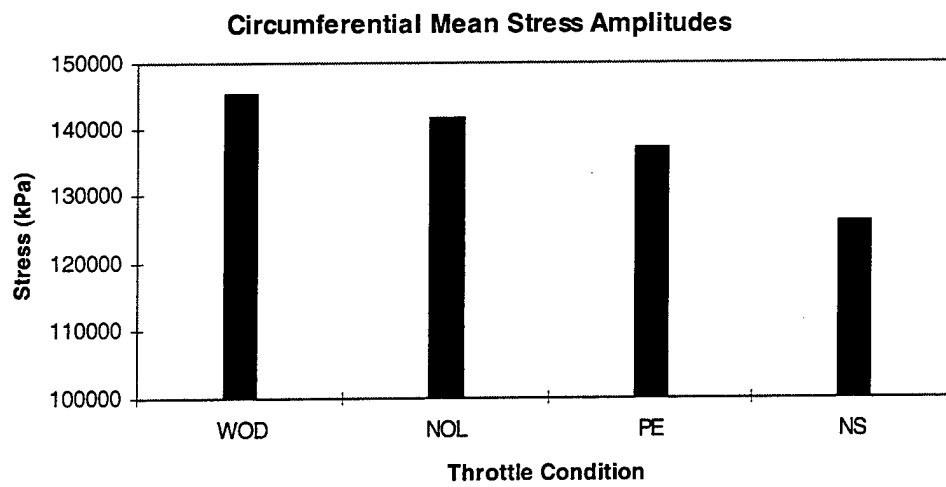


Figure 4.8: Throttle effects on resonant response.

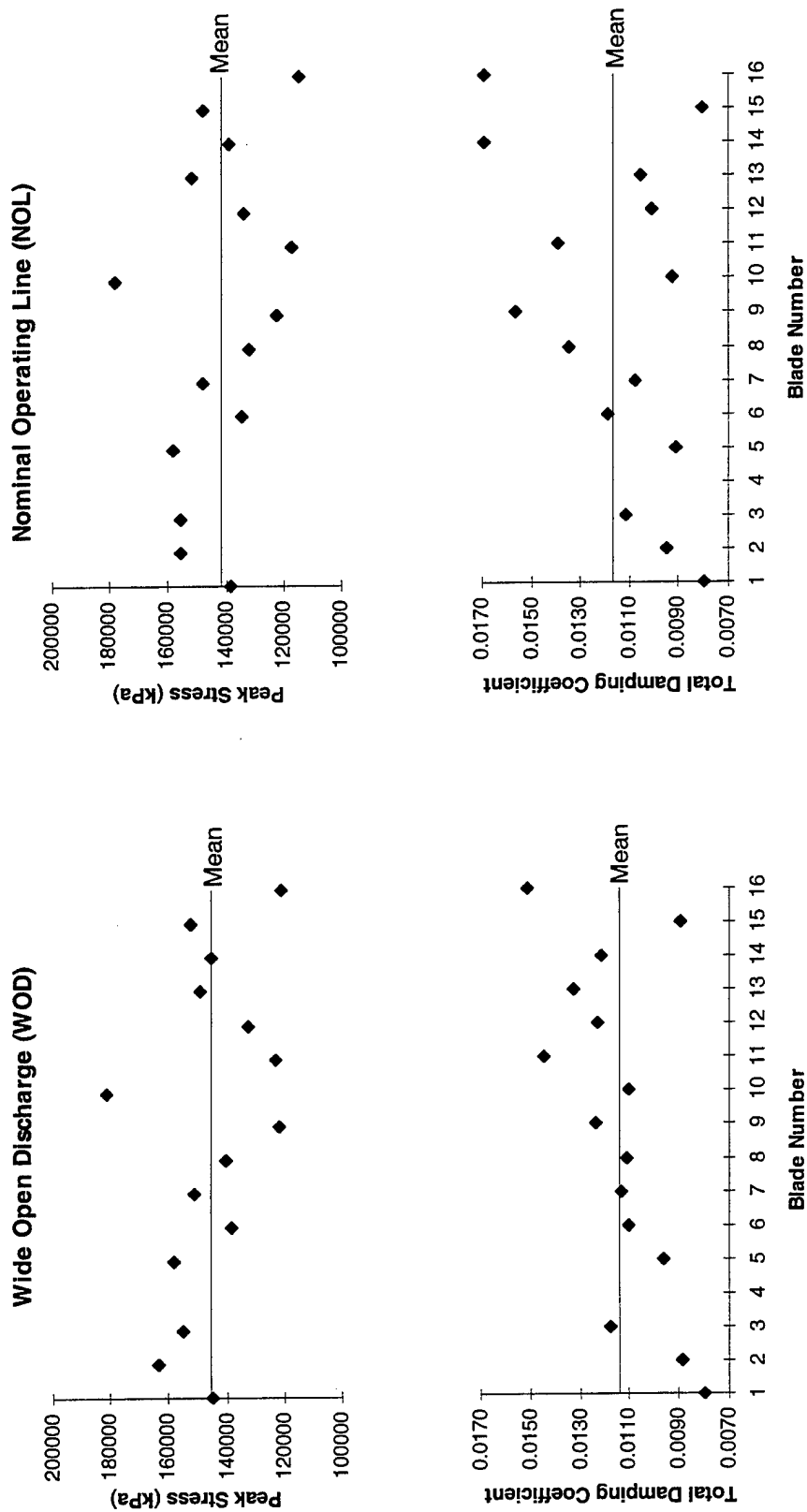


Figure 4.9a: Relationship between total damping and stress amplitude at resonance (WOD and NOL).

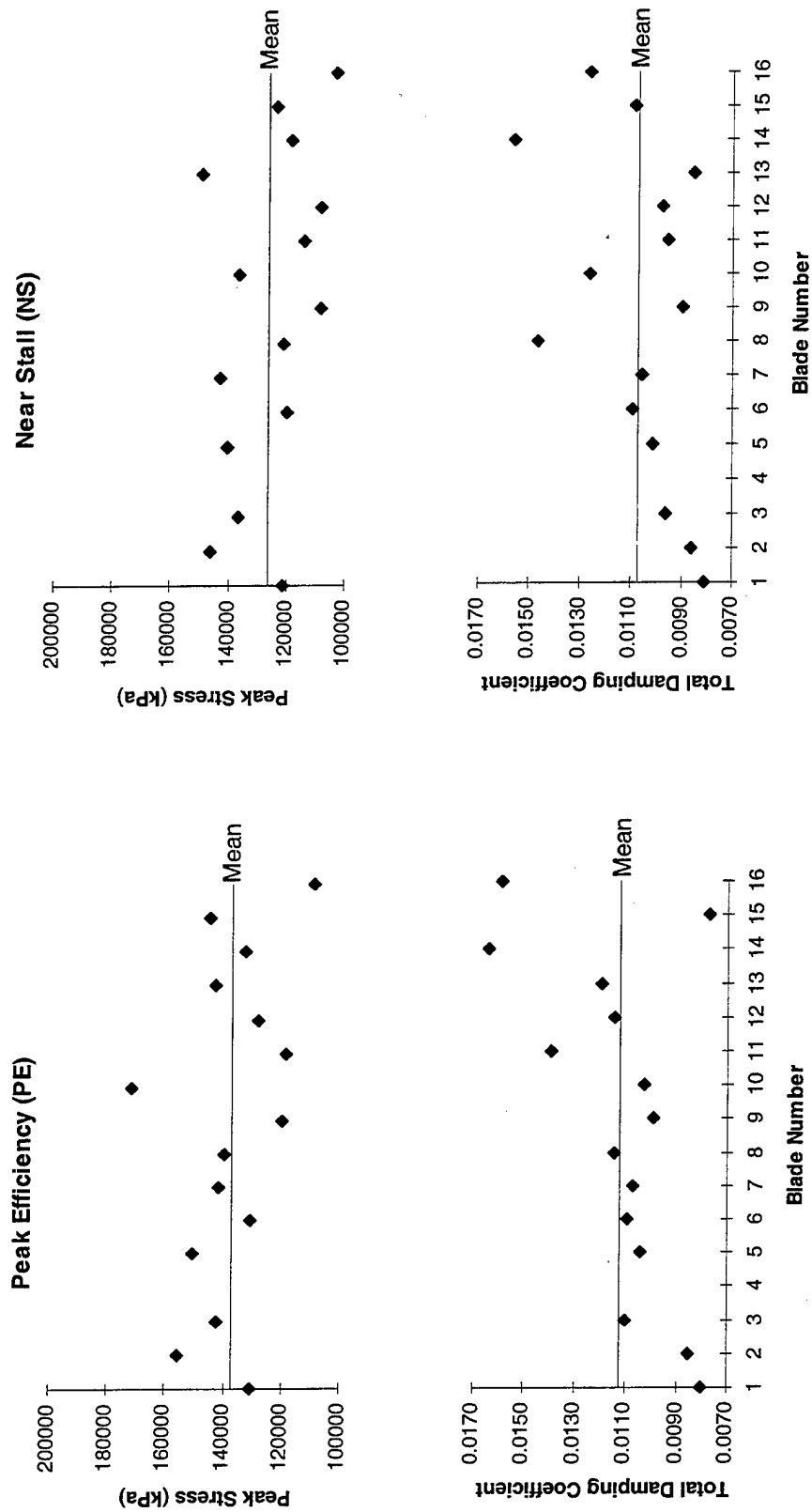


Figure 4.9b: Relationship between total damping and stress amplitude at resonance (PE and NS).

A spatial FFT of the circumferential total damping distribution for each operating line is shown in Figure 4.10 to further define this relationship. A 6/rev component is present in the damping distribution for all throttle conditions except NS. Comparing this result to Figures 4.9a and 4.9b shows that the correlation between stress and total damping is weakest at NS. For the other operating lines, the 6/rev component in the damping data is not as distinct as that for stress. Therefore, the blade-to-blade damping variations are a factor in the observed stress variations, serving primarily to highlight the role of unsteady aerodynamic loading as will be shown shortly.

The inverse relationship between total damping and resonant stress amplitude is typical of most mechanical systems. However, it becomes significant with regard to the role of blade structure. It has been shown in Figures 4.6a and 4.6b that blade peak stresses are not related to blade structure. Figure 4.11a shows total damping variations compared to frequency variations for WOD and NOL, and Figure 4.11b displays the same information for PE and NS. The scale of the variations are not comparable for damping and frequency. From the figures, it can be seen that the measured total damping variations are likewise not associated with structure. Significant variations in total damping occur with little variation in natural frequency, and no correlation exists between damping and frequency distributions. Total damping consists of two components, mechanical damping due to viscous energy dissipation in the structure and aerodynamic damping due to energy dissipation into the surrounding fluid. Since damping is decoupled from blade structure in the blisk, the rough relationship to blade resonant stress must be related to aerodynamic coupling. This observation further supports the idea that the blade peak stress variations are caused by variations in the flow field of each blade passage.

4.2.4 Summary of Resonant Results

Three possible causes for the measured blade-to-blade resonant stress variations exist. The first is blade structure, which is exhibited in natural frequency variations and is thus the source of classical mistuning. However, the blisk is tuned, decoupling blade

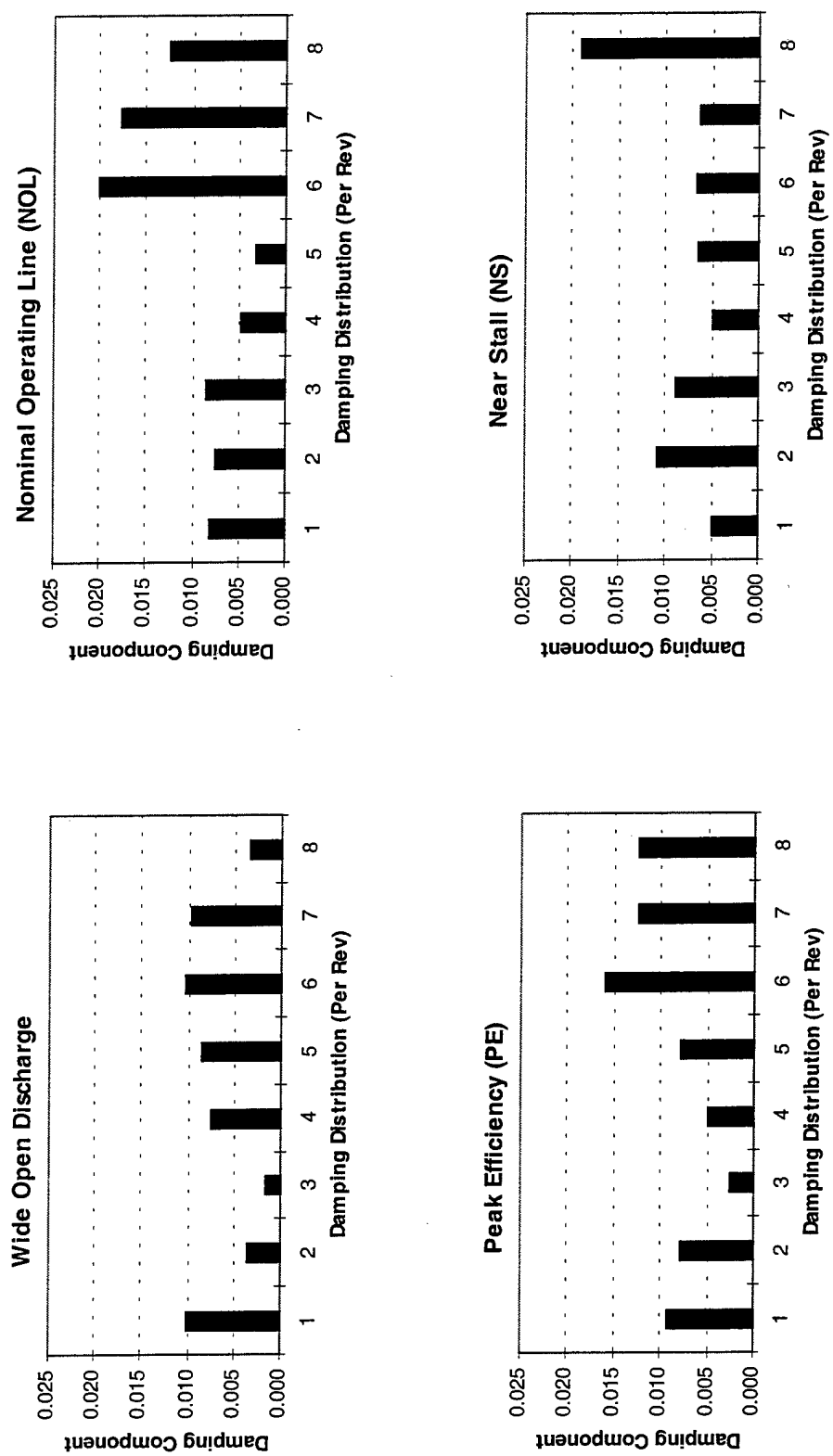


Figure 4.10: Circumferential total damping distribution.

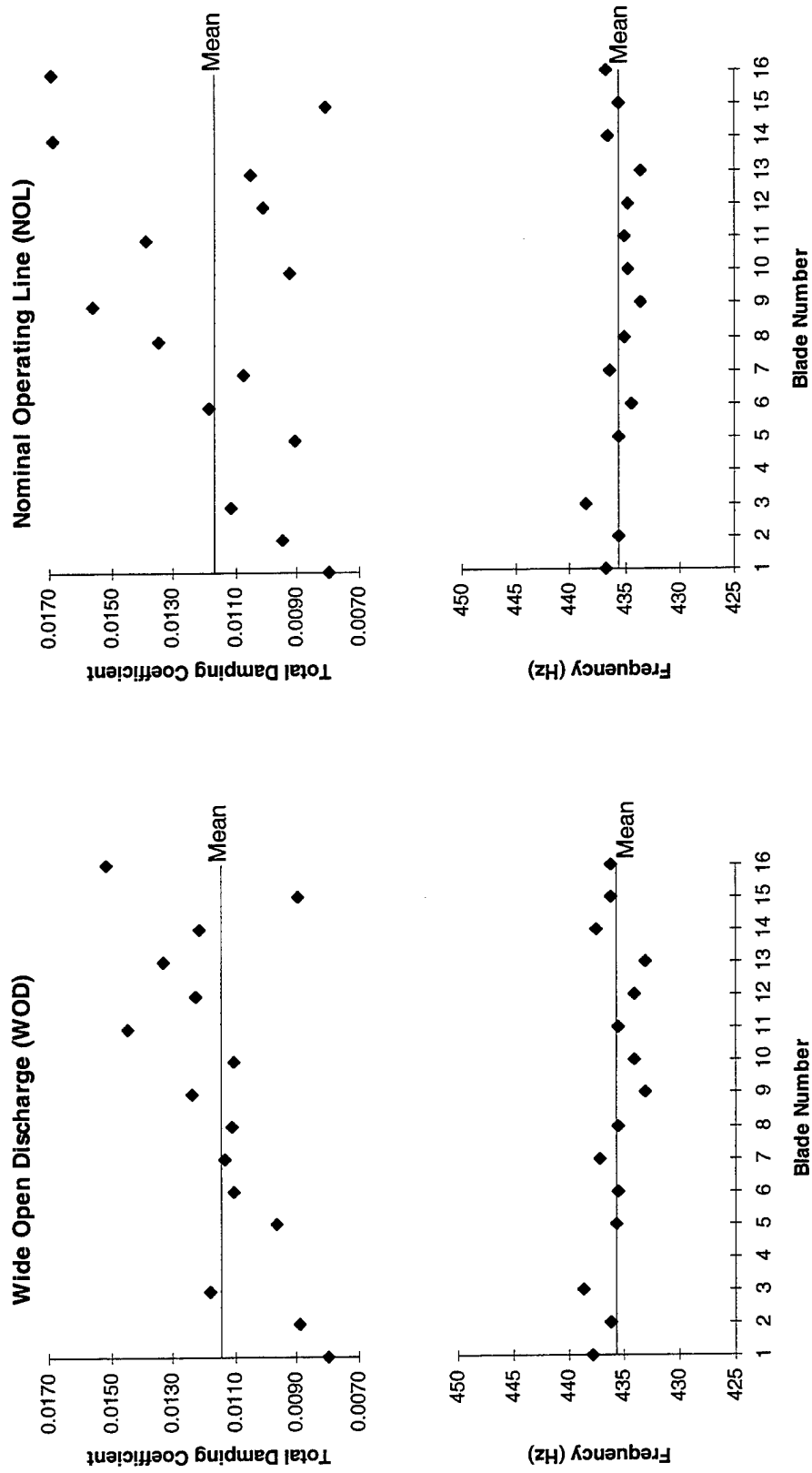


Figure 4.11a: Comparison of blade natural frequencies and total damping (WOD and NOL).

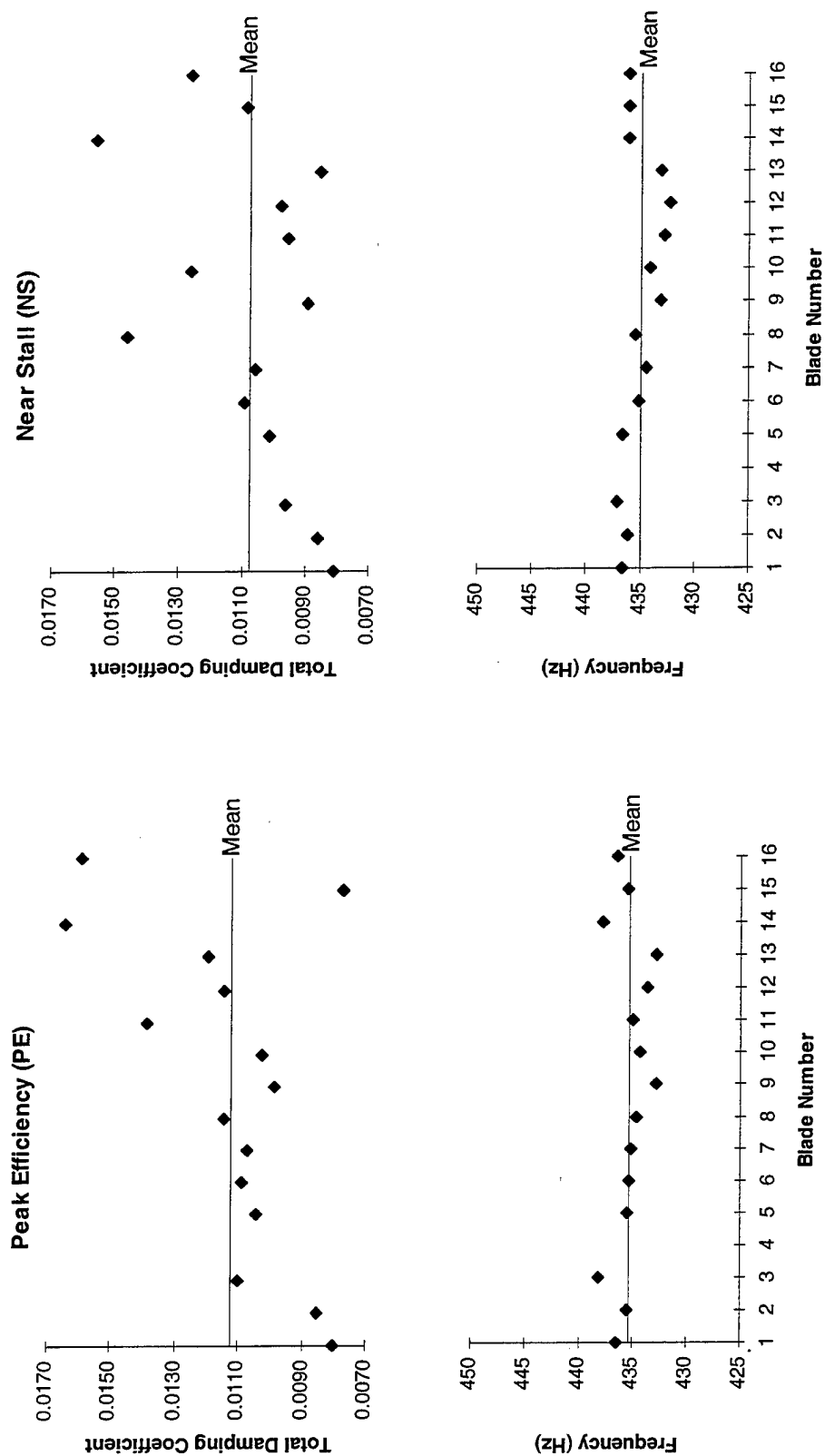


Figure 4.11b: Comparison of blade natural frequencies and total damping (PE and NS).

structure from the stress variations. A second potential cause is hub modal participation, but this is rendered unlikely both by historical tests on the blisk and by phase data obtained during this experiment which indicate that a substantial diametric hub mode does not exist at the blade 1F frequency. Analyses of blade passage aerodynamics and unsteady pressures on blade surfaces are beyond the scope of this study. However, the results of the experiment at resonance indicate that blade-to-blade variations in unsteady aerodynamic loads account for the observed peak stress variations. This is consistent with off-resonant results and shows that unsteady aerodynamics play a particularly significant role in mistuning effects for modern compressor fans utilizing a blisk design.

5.0 REDUCED-ORDER MODELING

The effects of mechanical energy transfer through the hub and motion-dependent aerodynamic coupling were investigated with the reduced-order method developed by Pierre, et al. [12, 13]. This method uses modal response from finite element analyses as well as aerodynamic parameters to predict mistuning effects in a bladed disk with minimal computation time. The output of the model is a normalized resonant displacement for each blade. Normalization is based on finite element coordinates. Since the model is assumed to be linear, the displacements are proportional to stress, and percent deviations from the circumferential mean displacement can be directly correlated to percent deviations from the mean stress determined experimentally. The following sections describe how this method was applied to study the test rotor. The results from studying the blisk were compared to experimental results to provide additional insight into nature of blade-to-blade peak stress variations.

5.1 Reduced-Order Modeling Technique

Reduced-order modeling employs a component mode technique with components consisting of disk-induced motion and cantilevered blade motion, allowing individual mistuning of each blade. Blade motion consists of blade finite element mode shapes, with the blade cantilevered at its interface with the disk, superimposed on the motion of the disk. Disk motion is described by finite element mode shapes of the disk with massless blades attached. Finite element modeling of a single disk-blade sector is required to obtain mode shapes. These mode shapes are used to build a reduced-order model of the entire rotor with a reduced number of degrees of freedom in comparison to a complete finite element model. Monte Carlo simulations provide a statistical analysis of frequency variations, which are assumed to be random, and the resulting displacement variations.

Monte Carlo simulations are an alternative method for solving probability density functions. A mistuning pattern for one realization of a mistuned assembly is obtained

from a random number generator. An incremental frequency sweep is performed, with the forced response problem for each unit of the assembly solved at each frequency increment. The largest resonant response for each unit is determined from its frequency response. The largest resonant amplitude constitutes one sample, and the process is repeated until some convergence criterion is met. Post-processing of all the samples acquired yields an approximation of the response statistics, which is equivalent to the probability density function. The number of solutions required by this method is expensive in terms of computation time. Thus, the reduced number of degrees of freedom necessary for reduced-order modeling provides significant advantages [12, 26].

The reduced-order technique was used in this study to analyze the forced response of the blisk at its first blade mode with and without motion-dependent aerodynamic coupling. The forced response portion of the program has been validated against a full finite element model of an industrial turbomachine rotor. Aerodynamic coupling has not been compared to any benchmark [27]. Formulation of the reduced-order modeling technique is not provided in this study. However, details of the finite element modeling and determination of aerodynamic coupling parameters are described.

5.2 Blisk Structural Model

The reduced-order modeling program used the output from finite element analyses to create a structural model of the blisk. Separate finite element models determined the mode shapes of the hub, including the blade interface, and of the blade alone. The motion of the blade root was retained from the hub model, and these nodes were matched to the nodes from the blade model. The blade mode shape was superimposed on the motion of the blade root to determine the overall response of each blade. The purely structural analysis allowed for determination of mistuning effects in the test rotor without aerodynamic coupling, forming a baseline for aerodynamic analysis.

5.2.1 Finite Element Modeling

The reduced-order structural model of the blisk was based on two finite element models. The first consisted of a single hub-blade sector, as shown in Figure 5.1, and determined the hub contribution to blade response. The blade portion was comprised of 1200 brick elements and 1764 nodes, and the hub was created using 1098 elements and 1630 nodes. The blade elements were assigned no mass by specifying zero density in the material properties of those elements, and the blade was fixed to the hub surface by multi-point constraints. The attach points of the hub to the compressor main shaft were fixed by single point constraints on all displacement degrees of freedom.

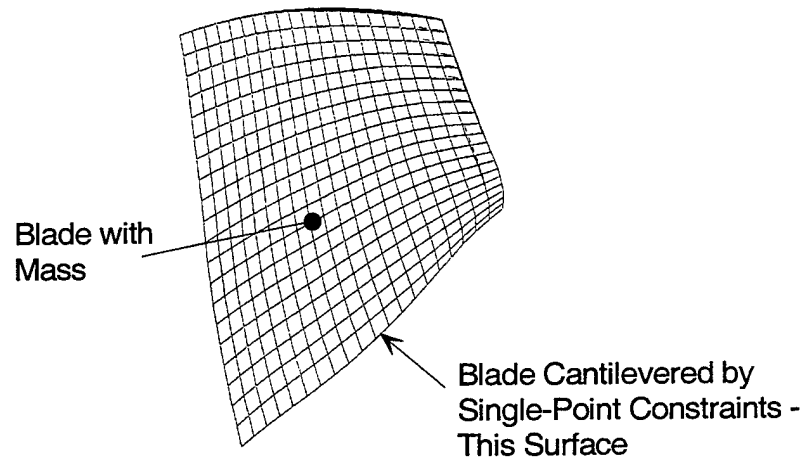
The reduced-order model requires the use of cyclic symmetry in the hub model, which is based on linear superposition. This precludes direct consideration of centrifugal stiffening, which requires a nonlinear analysis. To account for this, the hub modulus of elasticity was adjusted to reflect centrifugal stiffening. The original modulus was 16.5 Mpsi, and the adjusted modulus was 22.1 Mpsi.

The second finite element model consisted of the blade alone, cantilevered at its root to solve for the blade mode shapes. The hub elements were removed from this model, and the blade root was fixed using single point constraints on all displacement degrees of freedom. A nonlinear modal analysis was accomplished, which yielded blade frequencies and mode shapes with centrifugal stiffening at speed. The predicted blade response frequency in the first mode was 435.5 Hz, which agrees with experimental results and predicted Campbell diagrams. This model was also used to determine blade mass and stiffness matrices for the reduced-order model.

5.2.2 Structural Mistuning Effects

Blade-to-blade resonant stress variations caused by the weak blade mistuning present in the blisk and mechanical energy transfer through the hub were predicted with the structural mistuning model. The magnification factors from 20 Monte Carlo simulations were obtained. Magnification factor is the ratio of the maximum single-blade response to the rotor nominal, or "tuned," response. This is equivalent to the ratio of the

BLADE MODEL WITHOUT HUB



HUB MODEL WITH MASSLESS BLADE

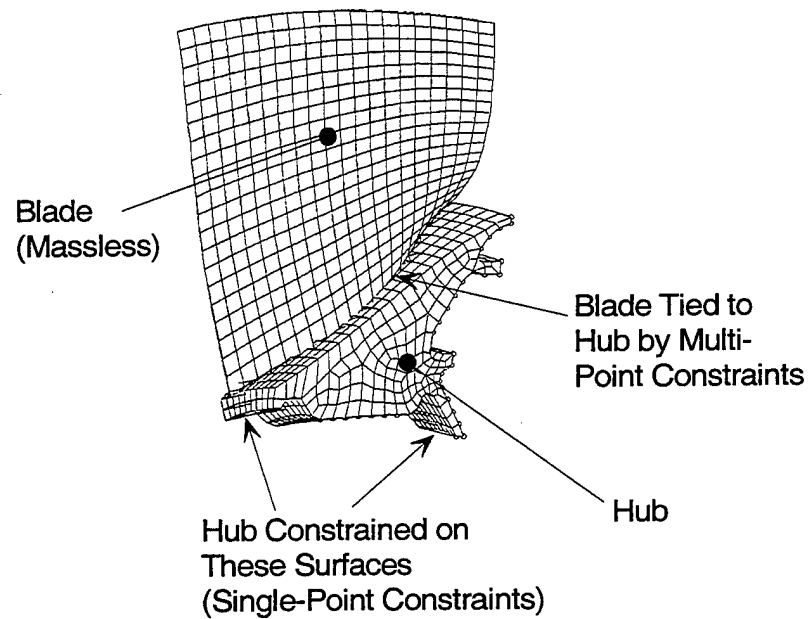


Figure 5.1: Finite element models of single hub-blade sector.

maximum response to the rotor mean response in experimental analysis. Nearly all of the Monte Carlo simulations predicted magnification factors much greater than those observed during the experiment. The mean predicted magnification factor over 20 simulations was 1.56, indicating a maximum resonant stress variation of 56 percent. This is more than double the maximum variation measured in the blisk, which averaged 24 percent over the four throttle conditions for a magnification factor of 1.24. In addition, the structural model predicted a correlation between response frequency and amplitude, which is not consistent with experiment.

The reduced-order model predictions with a purely structural model thus suggest that weak blade mistuning and interaction through the hub play a role in the blade-to-blade stress variations observed in the test rotor. However, the magnitude of the variations and the observed relationship to natural frequency indicate that significant aerodynamic influence is likely.

5.3 Aerodynamic Coupling

The reduced-order model allows addition of motion-dependent aerodynamic coupling between blades to the structural model. Using the structural model as a baseline, this provides a means for directly examining the effects of unsteady aerodynamics on blade-to-blade stress variations.

5.3.1 Development of Aerodynamic Model

Motion-dependent aerodynamic coupling in the reduced-order model is introduced in the form of a matrix of dimensional unsteady aerodynamic terms.

$$\mathbf{A} = \begin{bmatrix} \mathbf{A}^1 & \mathbf{0} & \dots & \mathbf{0} \\ \mathbf{0} & \mathbf{A}^2 & \ddots & \vdots \\ \vdots & \ddots & \ddots & \mathbf{0} \\ \mathbf{0} & \dots & \mathbf{0} & \mathbf{A}^N \end{bmatrix} \quad (5.1)$$

This matrix is block diagonal and in general non-symmetric. Each element \mathbf{A}^k corresponds to a blade at the k th interblade phase angle, σ_k :

$$\sigma_k = \frac{2\pi(k-1)}{N}, \quad k = 1, \dots, N, \quad (5.2)$$

where N is the total number of blades on the rotor. Each block on the diagonal is an $M \times M$ matrix, where M is the number of cantilevered blade modes used in the analysis. Since only the 1F mode is being investigated, $M = 1$ for this analysis, with the coefficient representing unsteady lift in the bending mode for each blade [28].

A nondimensional unsteady lift coefficient for each blade was obtained from the LINSUB program developed by Whitehead [29]. For simplicity, the program assumes a flat plate, which is a reasonable approximation for this study given the high speed design of the blades with a thin airfoil and little camber over the most heavily loaded portion of the blade span. Formulation of the LINSUB program is not included here. Input parameters, summarized in Table 5.1, were based on airfoil geometry and conditions at 85 percent span and 8700 rpm wheel speed. This span location has been used for aerodynamic analyses of the test rotor for a number of studies [15, 19, 21]. It was initially chosen because it served as a reference used in the original design of the rotor and because it is located on a heavily loaded portion of the blade while remaining out of tip effects [18]. Reduced frequency was based on blade chord and relative flow velocity. The elastic axis was approximated at 50 percent chord because the blade is integrally fixed to the hub. Using the LINSUB program, a complex non-dimensional lift coefficient was obtained for each interblade phase angle as described by Equation 5.2.

Table 5.1: LINSUB input parameters.

Parameter	Value
Reduced Frequency	0.63
Mach Number	0.88
Spacing/Chord Ratio (Solidity)	0.63
Stagger Angle (degrees)	52.0
Elastic Axis (Fraction of Chord)	0.50

The resulting non-dimensional coefficients reflect the relative unsteady lift on the blades, but the reduced-order model requires dimensional input in the form of an effective stiffness between blades. Thus, the coefficients were dimensionalized by the lowest eigenvalue from the cantilevered blade finite element model to obtain lift terms consistent with the reduced-order model. The resulting unsteady lift terms were reduced by weighting factors of $1/180$, $1/60$, and $1/36$ to consider weak, moderate, and strong aerodynamic coupling, respectively. This follows the convention of the authors of the reduced-order program [27].

5.3.2 Coupling Strength

The three aerodynamic coupling strengths were studied to determine the strength of the coupling in the test rotor. Twenty simulations were performed for each coupling strength to determine the mean predicted magnification factor. Figure 5.2 shows the results of this study along with the magnification factor from the structural model with no aerodynamic coupling. Coupling strengths are expressed as percentages. The parabolic curve is a second-order polynomial curve fit to facilitate comparison to the results of Ottarsson and Pierre [26], which will be described in the next paragraph. The experimental magnification factor averaged over all operating lines is provided as a reference.

The figure shows that the displacement variations increase in the blisk with aerodynamic coupling strength to a maximum and then begin to decline. This result is not surprising. A similar trend was determined to generally occur for mistuned systems in a study by Ottarsson and Pierre [26]. They reasoned that a mostly localized response could yield significant variation from blade-to-blade, as seen by the result for no aerodynamic coupling. As coupling increases, energy is exchanged between blades, which allows a single blade to absorb the energy of its neighbors and vibrate more vigorously, illustrated by the peak in the maximum magnification factor shown in the figure. However, increasing coupling further can actually reduce mistuned response because so much energy is shared between blades that the response is no longer localized.

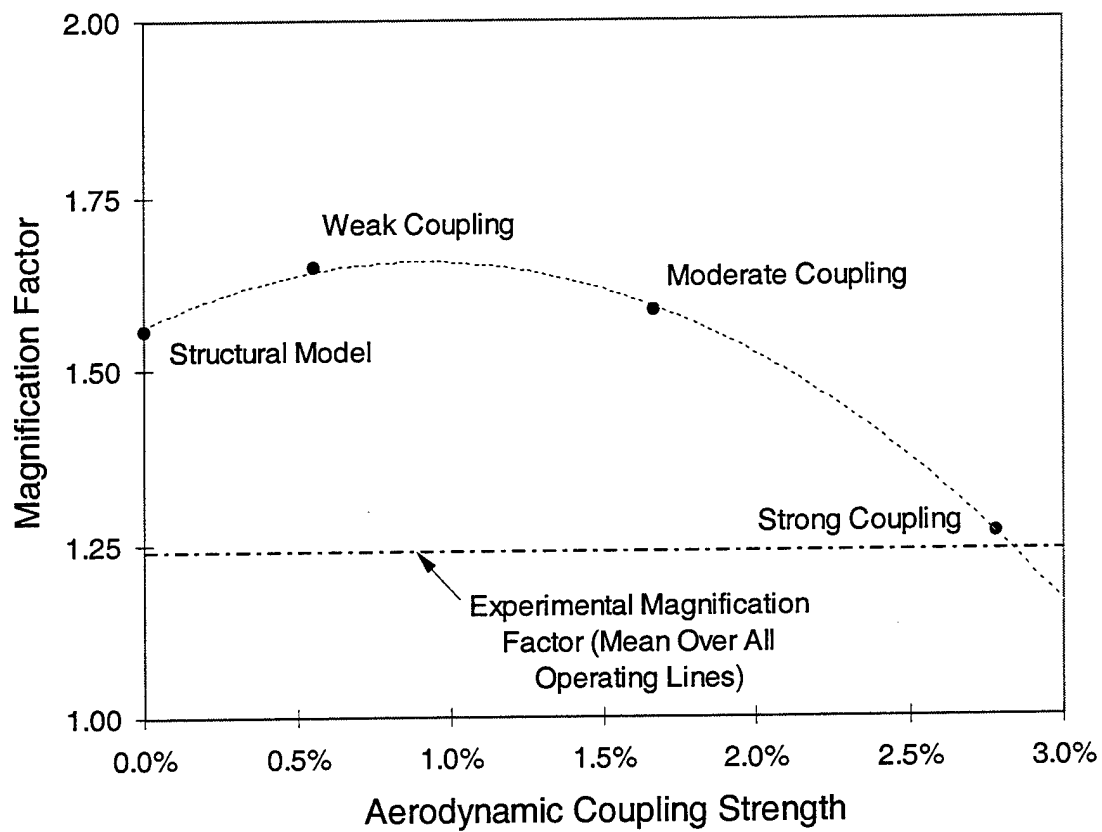


Figure 5.2: Predicted magnification factors for various aerodynamic coupling strengths.

Instead, the entire rotor begins to respond as a system. The test rotor at its 3/rev 1F mode falls on the declining portion of the curve, where strong aerodynamic coupling has reduced localization from its possible maximum. The reduced maximum stress variation at NS shown previously in Figure 4.8 supports this observation. Unsteady blade loading, and thus aerodynamic coupling, is strongest at that throttle condition and decreases the localized response of the blades. The predicted magnification factor for strong aerodynamic coupling agrees with experimental data, indicating that aerodynamic coupling was strong for the blisk during the experiment. Comparison to the structural model demonstrates that motion-dependent aerodynamic coupling dominates structural mistuning and mechanical energy transfer through the hub in the test rotor at its 3/rev 1F blade mode.

6.0 SUMMARY AND CONCLUSIONS

Blade-to-blade variations in response frequency, stress amplitude, and total damping were investigated in the response of high speed, low aspect ratio compressor fan to a 3/rev inlet total pressure distortion. Dynamic strain gage data acquired for steady compressor operation at speeds above and below the blade 1F resonance, as well as for acceleration through this resonance, were studied to characterize the nature and causes of these variations. In addition, a reduced-order model was used to predict blade-to-blade stress variations in the rotor. A purely structural model was examined to determine the effects of weak blade mistuning and mechanical energy transfer through the rotor hub, providing a baseline for aerodynamic analysis. Motion-dependent unsteady aerodynamic coupling was incorporated to investigate how it affects these variations based on the strength of the coupling. The results from the reduced-order model were used to gain further insight into experimental findings.

6.1 Summary of Results

Dynamic strain gage data were studied to characterize mistuning and its effects in a modern compressor blisk. Analysis of this data yielded a number of significant results:

- During steady operation above and below resonance, blade response at the excitation frequency provided by the inlet total pressure distortion was determined. The response at the common forcing frequency varied significantly between blades. The circumferential stress distribution patterns at these speeds suggest that differences in individual blade aerodynamic loading account for the stress variations.
- Ensemble averages verified that the measured blade stresses were in response to the 3/rev aerodynamic disturbance as opposed to structural coupling through hub motion.
- Resonant response of the rotor demonstrated that the blisk was essentially tuned, thus decoupling blade structure from measured blade-to-blade stress variations. This

finding is particularly important since such stress variations are classically attributed to blade mistuning.

- Interblade phase angle measured at resonance indicated that hub motion was not a significant factor in the measured stress variations. Phase analysis showed that blade motion was due to a 3/rev aerodynamic driver upstream from the rotor.
- Circumferential stress distribution patterns at resonance supported the observation that the blade-to-blade peak stress variations are caused by unsteady aerodynamic loading. Total damping comparisons to resonant frequencies and blade stresses were in agreement.

A reduced-order structural model investigated weak blade mistuning and mechanical energy transfer through the hub, providing a baseline for aerodynamic analysis. Aerodynamic coupling added to the model determined the influence of unsteady lift on blade-to-blade stress variations. Nondimensional unsteady coefficients were generated based on interblade phase angle. These coefficients were dimensionalized using different coupling strengths to determine the strength of motion-dependent aerodynamic coupling in the test rotor. The results from this model were compared to experimental results.

- The structural model showed that weak blade mistuning could produce significant blade-to-blade resonant stress variations. However, the magnitude of these variations was approximately double what was observed in the test rotor. The model also predicted that stress amplitude variations were related to blade structure, which is inconsistent with experimental results.
- Analysis of aerodynamic coupling strengths suggested that strong motion-dependent aerodynamic coupling was present during the experiment on the blisk. This coupling strength was shown to actually reduce localization in the rotor such that blade-to-

blade stress variations were less than their possible maximum, which would occur with weaker coupling.

Experimental analysis and reduced-order modeling together show that the mistuned response of the test blisk at its 1F mode is governed primarily by unsteady aerodynamic loading. This is important because blade-to-blade stress variations such as those measured in the blisk are classically attributed to blade structural mistuning. However, in an essentially tuned system comparable to the test rotor, outside factors that are normally dominated by structural mistuning become prominent. For a blisk in a gas turbine engine, one of these factors is motion-dependent aerodynamic coupling.

6.2 Conclusions

Previous studies, both analytical and experimental, have considered blade structural mistuning as the primary source of blade-to-blade stress amplitude variations. Stress amplitudes were shown to be related to blade natural frequency, which is determined by the structural properties of the blade. Blades on a rotor were also shown to be coupled through disk motion. The test rotor used for this experiment was known to exhibit significant blade stress variations at the 1F blade mode although it was essentially tuned in terms of blade response frequency. Therefore, this experiment was accomplished to quantify these variations and to determine their nature.

The results of the experiment indicate that the observed blade-to-blade stress variations are dominated by unsteady aerodynamic coupling. Experimental results were compared to the predicted variations from a reduced-order model. Although weak blade mistuning and mechanical coupling produced stress variations, the model showed that the stress variations in the test rotor are governed primarily by aerodynamic coupling.

In a traditional bladed-disk assembly, mistuning leads to blade-to-blade stress variations. However, the use of blisks in modern compressor fan design leads to systems that are more tuned than traditional bladed-disk assemblies. As a result, unsteady blade loads that are typically outweighed by mistuning effects become significant. More consideration must be given to the role of unsteady aerodynamics in mistuned rotor

response, especially as rotor designs continue to advance. However, blade-to-blade energy transfer through unsteady aerodynamic loading is not well understood. This investigation shows that an improved understanding of the complex flow field in the blade passage, and particularly how this facilitates coupling between blades, is necessary to fully account for blade response variations. More complete comprehension of these variations can lead to refined predictive models and ultimately better fan designs to reduce high cycle fatigue.

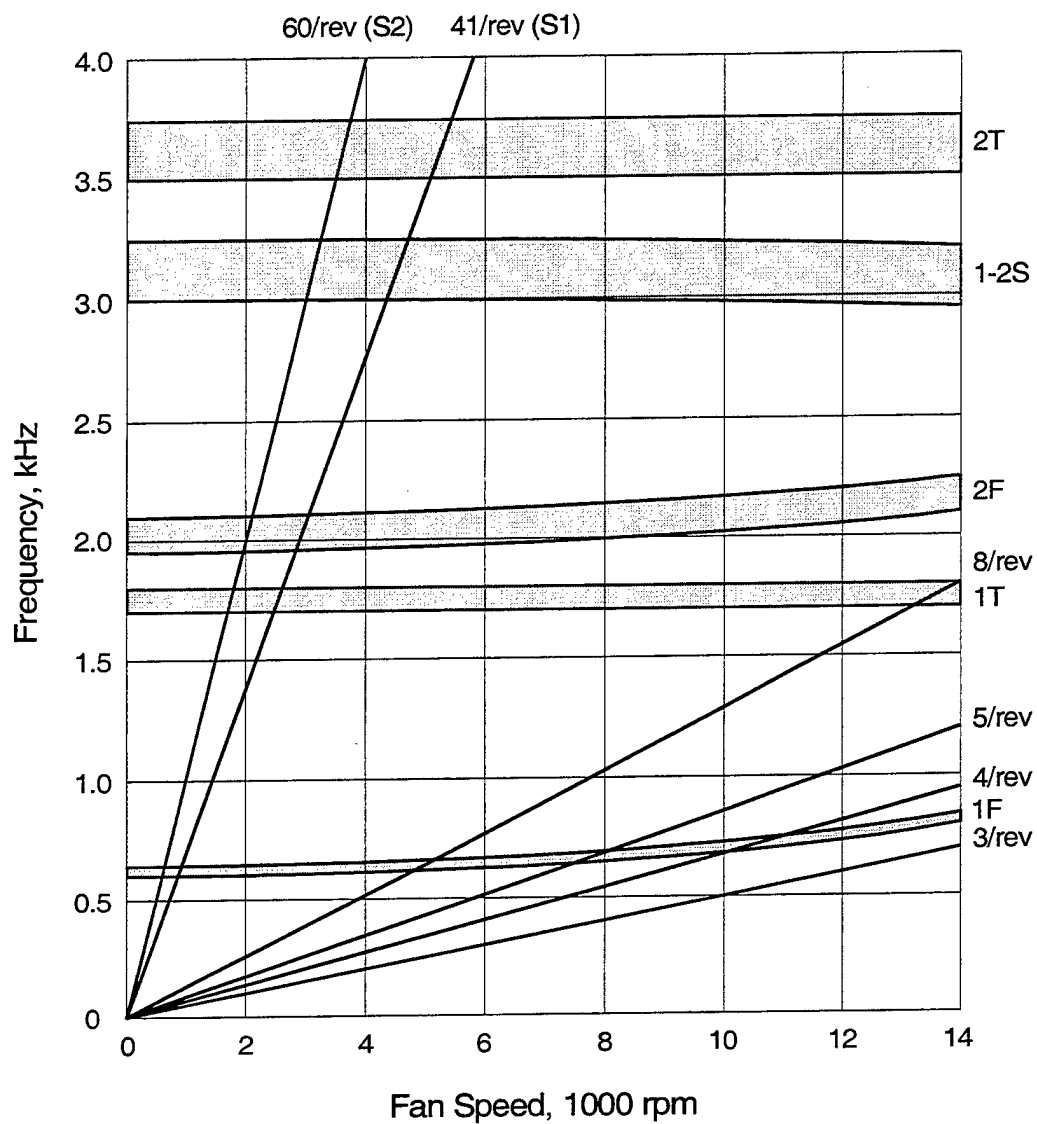
7.0 REFERENCES

1. Wagner, J.T., 1967, "Coupling of Turbomachine Blade Vibrations Through the Rotor," *ASME Journal of Engineering for Power*, Series A, Vol. 89, No. 4, pp. 502-513.
2. Whitehead, D.S., 1966, "Effect of Mistuning on the Vibration of Turbomachine Blades Induced by Wakes," *Journal of Mechanical Engineering Science*, Vol. 8, No. 1, pp. 15-21.
3. Dye, R.C.F., and Henry, T.A., 1969, "Vibration Amplitudes of Compressor Blades Resulting from Scatter in Blade Natural Frequencies," *Transactions of the ASME, Journal of Engineering for Power*, Vol. 91, pp. 182-188.
4. El-Bayoumy, L.E., and Srinivasan, A.V., 1975, "Influence of Mistuning on Rotor-Blade Vibrations," *AIAA Journal*, Vol. 13, No. 4, pp. 460-464.
5. Ewins, D.J., 1972, "A Study of the Vibration Modes of a Bladed Turbine Wheel," *Conference on Vibrations in Rotating Systems*, Institution of Mechanical Engineers, London, pp. 170-184.
6. Ewins, D.J., 1976, "Vibration Modes of Mistuned Bladed Disks," *ASME Journal of Engineering for Power*, pp. 349-355.
7. Sinha, A., 1986, "Calculating the Statistics of Forced Response of a Mistuned Bladed Disk Assembly," *AIAA Journal*, Vol. 24, No. 11, pp. 1797-1801.
8. Sinha, A., and Chen, S., 1989, "A Higher Order Technique to Compute the Statistics of Forced Response of a Mistuned Bladed Disk," *Journal of Sound and Vibration*, Vol. 130, pp. 207-221.
9. Mignolet, M.P., and Lin, C.C., 1993, "The Combined Closed Form - Perturbation Approach to the Analysis of Mistuned Bladed Disks," *Journal of Turbomachinery*, Vol. 115, pp. 771-780.
10. Ottarsson, G.S., and Pierre, C., 1993, "Vibration Localization in Mono- and Bi-Coupled Bladed Disks - A Transfer Matrix Approach," *Proceedings of the 34th AIAA/ASME/ASCE/AHS/ASC Structures, Structural Dynamics and Materials Conference*, La Jolla, California, Vol. 6, pp. 3683-3697.

11. Kaza, K.R.V., and Kielb, R.E., 1984, "Effects of Structural Coupling on Mistuned Cascade Flutter and Response," *ASME Journal of Engineering for Gas Turbines and Power*, Vol. 106, No. 1, pp. 17-24.
12. Ottarsson, G.S., Castanier, M.P., and Pierre, C., 1994, "A Reduced-Order Modeling Technique for Mistuned Bladed Disks," *Proceedings of the 35th AIAA/ASME/ASCE/AHS/ASC Structures, Structural Dynamics and Materials Conference*, Hilton Head, South Carolina.
13. Kruse, M.J., and Pierre, C., 1996, "Reduced-Order Modeling Technique for Mistuned Bladed Disks Part II: Forced Vibrations," *Proceedings of the 37th AIAA/ASME/ASCE/AHS/ASC Structures, Structural Dynamics, and Materials Conference*, Salt Lake City, Utah.
14. Griffin, J.H., 1988, "On Predicting the Resonant Response of Bladed Disk Assemblies," *Journal of Engineering for Gas Turbines and Power*, Vol. 110, pp. 45-50.
15. Fost, R.B., and Niskode, P.M., 1987, "Joint Technology Demonstrator Engine Fan Durability Assessment Program," AFWAF-TR-86-2067.
16. Datko, J.T., and O'Hara, J.A., 1987, "The Aeromechanical Response of an Advanced Transonic Compressor to Inlet Distortion," ASME Paper 87-GT-189.
17. Rabe, D., Bolcs, A., and Russler, P., 1995, "Influence of Inlet Distortion on Transonic Compressor Blade Loading," AIAA Paper 95-2461.
18. Russler, P.M., 1995, "Acquisition and Reduction of Blade-Mounted Pressure Transducer Data from a Low Aspect Ratio Fan," WL-TR-95-2021.
19. Manwaring, S.R., Rabe, D.C., Lorence, C.B., and Wadia, A.R., 1996, "Inlet Distortion Generated Forced Response of a Low Aspect Ratio Transonic Fan," ASME Paper 96-GT-376.
20. Fost, R.B., 1997, "General Electric Swept Fan Assessment Rig (GESFAR) Aeromechanics Test Report," WL-TR-97-2076.
21. Minkiewicz, G., and Russler, P., 1997, "Dynamic Response of Low Aspect Ratio Blades in a Two Stage Transonic Compressor," AIAA Paper 97-3284.
22. Cardinale, V.M., McKay, R.A., and Oldakowski, T.J., 1985, High Tip Speed Compressor GE/USAF Program Review, Aeromechanical Summary, Compressor Research Facility, Wright Patterson Air Force Base, Ohio.

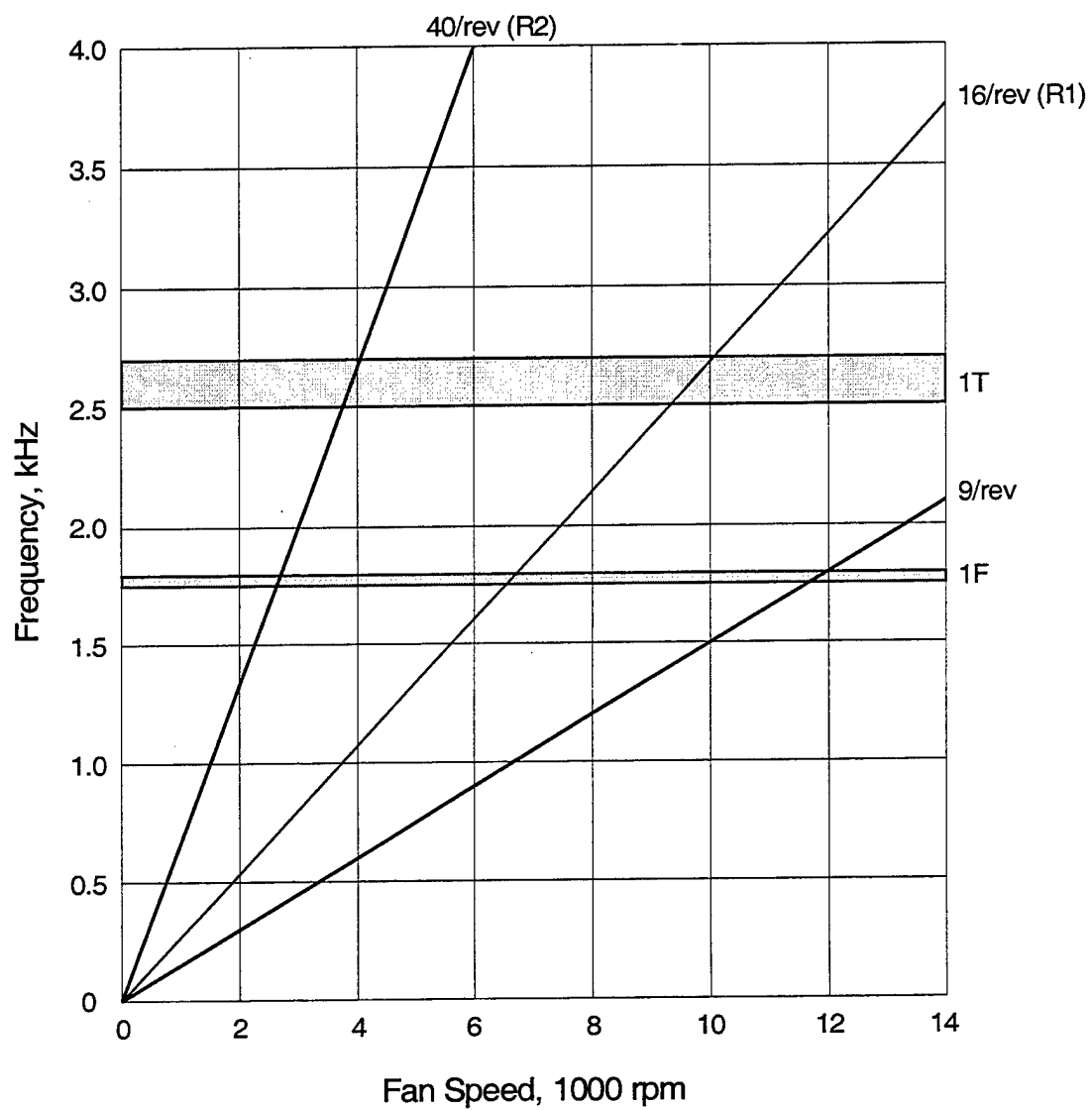
23. Laboratory Workbench User's Guide, Masscomp.
24. Kreyszig, E., 1993, Advanced Engineering Mathematics, 7th Ed., John Wiley & Sons, New York, 1993.
25. Stearns, S.D. and David, R.A., 1996, Signal Processing Algorithms in MATLAB, Prentice Hall, New Jersey.
26. Ottarsson, G., and Pierre, C., 1995, "On the Effects of Interblade Coupling on the Statistics of Maximum Forced Response Amplitudes in Mistuned Bladed Disks," AIAA Paper 95-1494.
27. Kruse, M.J., and Pierre, C., 1996, "Dynamic Response of an Industrial Turbomachine Rotor," *Proceedings of the 32nd AIAA/ASME/SAE/ASEE Joint Propulsion Conference and Exhibit*, Lake Buena Vista, Florida.
28. Pierre, C., Castanier, M.P., and Bladh, R., 1997, REDUCE Version 2.1 User's Manual, Department of Mechanical Engineering and Applied Mechanics, University of Michigan, Ann Arbor, Michigan.
29. Whitehead, D.S., 1987, "Classical Two-Dimensional Methods," *AGARD Manual on Aeroelasticity in Axial Flow Turbomachines, Volume 1: Unsteady Turbomachine Aerodynamics*, AGARD-AG-298, Vol. 1, Chapter III.
30. Nichol, K.L., 1998, "Numerical Strain Gage Representation," *Proceedings of the 39th AIAA/ASME/ASCE/AHS/ACS Structures, Structural Dynamics and Materials Conference* (to be published), Long Beach, California.

APPENDIX A: Aft Blade Row Campbell Diagrams



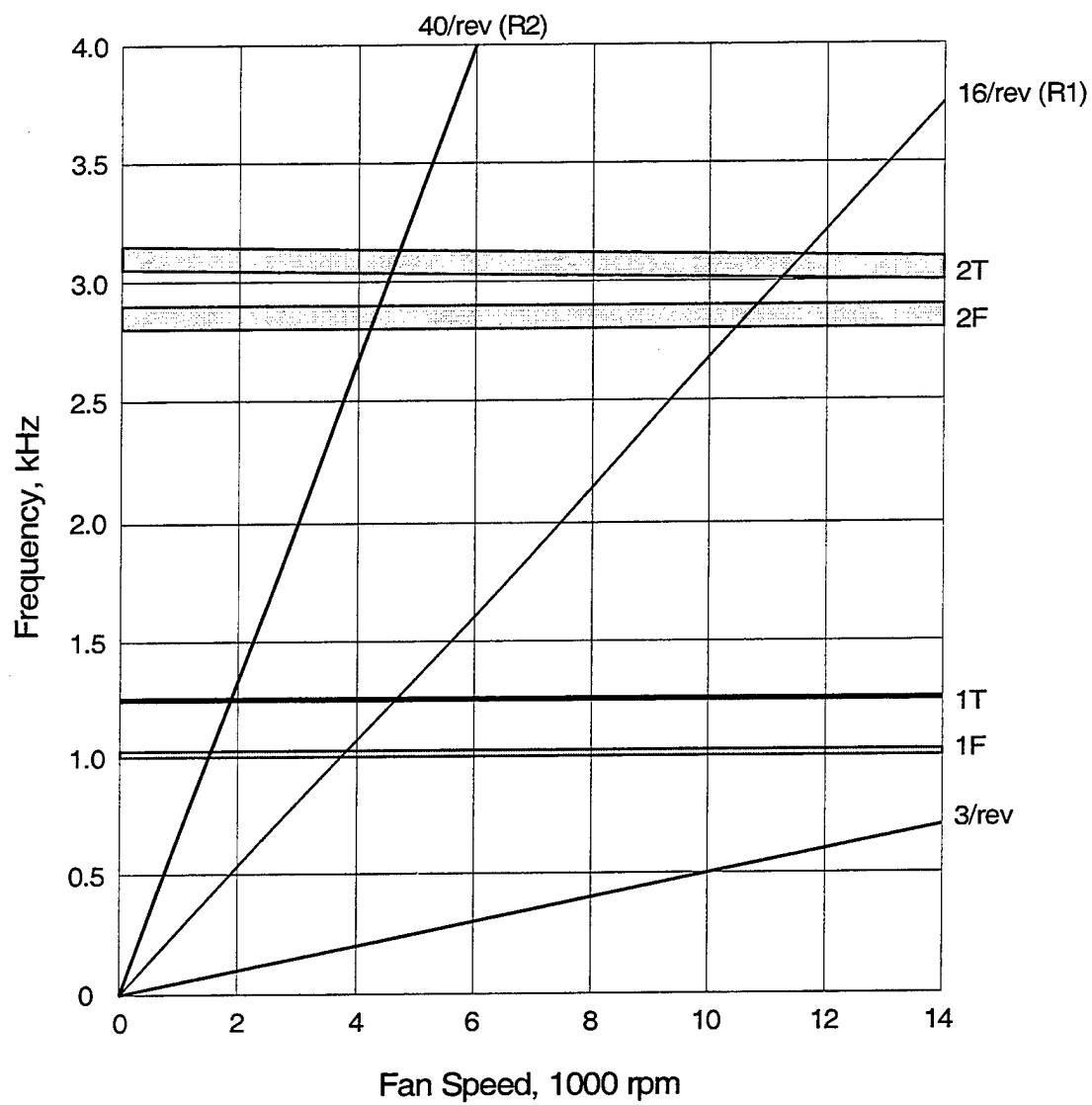
(NOTE: Ranges based on bench test data.)

Figure A.1: Rotor 2 Campbell diagram.



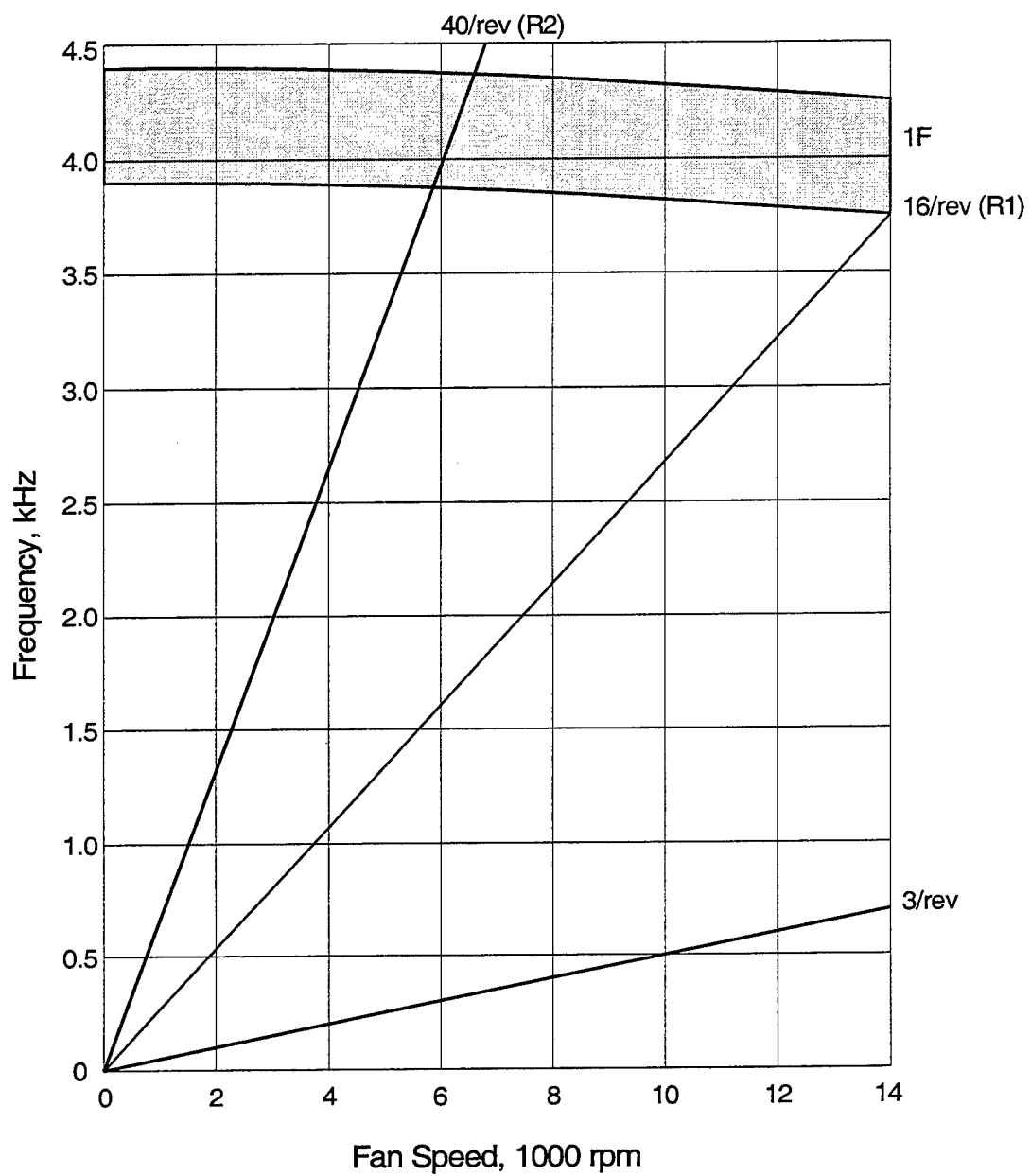
(NOTE: Ranges based on bench test data.)

Figure A.2: Stator 1 strut Campbell diagram.



(NOTE: Ranges based on bench test data.)

Figure A.3: Stator 1 flap Campbell diagram.



(NOTE: Ranges based on bench test data.)

Figure A.4: Stator 2 Campbell diagram.

APPENDIX B: Strain Gage Specifications and Uncertainty

Strain instrumentation used in this experiment consisted of 28 ED-DY-062AP-350E dynamic strain gages produced by Micro-Measurements. Gages were applied at the roots of all 16 blades of the rotor. In addition, gages were placed at the leading and trailing edges of blades 1 through 6. Only data from the root strain gages were used for the mistuning analysis. Strain gage and signal conditioning specifications are listed in Table B.1.

Table B.1: Dynamic strain gage specifications and signal conditioning.

Model	ED-DY-062AP-350E
Gage Factor	3.27
Gage Resistance	351.7 Ω \pm 0.32%
Gage + Lead Resistance	357.7 Ω \pm 0.62%
Ground Resistance	∞
Young's Modulus	16.55 Mpsi
Temperature Range	200 $^{\circ}$ F
Max. Stress Level	40 kpsi
Corrected Gage Factor	3.337
Filter	Wide Band
Coupling	AC
Excitation	15 mA

Stress measurement uncertainty for the strain gages was estimated. These gages actually measure strain, which is defined as:

$$\varepsilon = \frac{\Delta L}{L} \quad (\text{B.1})$$

The term L denotes the length of the application area and ΔL a small change in this length. Small wires in the strain gage elongate or compress when strain occurs in the test specimen, leading to a change in the resistance of the wire. Thus for a gage factor k and resistance R , strain may be rewritten as:

$$\varepsilon = \frac{1}{k} \frac{\Delta R}{R} \quad (\text{B.2})$$

The potential e in the electrical circuit is defined in terms of the resistance R and the excitation current I through the circuit.

$$e = IR \quad (\text{B.3})$$

This can be rewritten in terms of changes in potential and resistance.

$$\Delta e = I \Delta R \quad (\text{B.4})$$

Solving this for ΔR and substituting into Equation B.2 yields an expression for strain in terms of changes in electrical potential across the circuit, which can be directly measured.

$$\varepsilon = \frac{\Delta e}{kRI} \quad (\text{B.5})$$

For a linearly elastic material, stress σ is related to strain by the modulus of elasticity E of the material through a relation known as Hooke's Law.

$$\sigma = E\varepsilon \quad (\text{B.6})$$

Solving for ε and substituting into Equation B.5 gives an expression for stress in terms of electrical potential changes.

$$\sigma = \frac{E\Delta e}{kRI} \quad (\text{B.7})$$

To account for uncertainties arising from signal conditioning, changes in electrical potential are defined in terms of a potential change from the transducer, V_T , and a gain, G .

$$\Delta e = V_T G \quad (\text{B.8})$$

The gain G is the product of the gains of all components used in signal conditioning.

$$G = G_{PAC} G_{REC} G_{FILTER} G_{A/D} G_{PRESTON} \quad (\text{B.9})$$

The source of each gain is listed in Table B.2 along with its value and published uncertainty.

Table B.2: Signal conditioning gains.

Gain	Source	Value	Uncertainty
G_{PAC}	Pacific Model 8255 Amplifier	157.4	0.10%
G_{REC}	3700J Wideband Analog Recorder	0.2	0.16%
$G_{PRESTON}$	Preston Model MX-G1 Amplifier	5	0.02%
G_{FILTER}	Wavetec System 816 Multi-Channel Low-Pass Filter	1	0.10%
$G_{A/D}$	ADA Masscomp Concurrent AD12V26 A/D Converter	1	0.26%

For simplicity, constants are combined into one term A .

$$A = \frac{E}{kI} \quad (B.10)$$

Substituting Equations B.8 through B.10 into Equation B.7 results in a final expression for stress in terms of strain gage and signal conditioning parameters.

$$\sigma = \frac{A}{R} V_T G_{PAC} G_{REC} G_{FILTER} G_{A/D} G_{PRESTON} \quad (B.11)$$

The uncertainty S of the stress measurements is defined as:

$$S = \frac{\partial \sigma}{\partial R} + \frac{\partial \sigma}{\partial V_T} + \sqrt{\left(\frac{\partial \sigma}{\partial G_{PAC}}\right)^2 + \left(\frac{\partial \sigma}{\partial G_{REC}}\right)^2 + \left(\frac{\partial \sigma}{\partial G_{FILTER}}\right)^2 + \left(\frac{\partial \sigma}{\partial G_{A/D}}\right)^2 + \left(\frac{\partial \sigma}{\partial G_{PRESTON}}\right)^2} \quad (B.12)$$

The first two terms in this expression are bias errors because they result in voltage offsets, and are thus summed directly in the uncertainty analysis. The other terms are variable depending on the amplitude of the signal, so the root-mean-square values of these terms are summed in the uncertainty expression.

An example of one of the derivatives in Equation B.12 is:

$$\frac{\partial \sigma}{\partial R} = -\frac{A}{R^2} \frac{\partial R}{\partial R} V_T G_{PAC} G_{REC} G_{FILTER} G_{A/D} G_{PRESTON} \quad (B.13)$$

The partial derivative of R with respect to itself is the uncertainty of the resistance. Similar expressions are derived for each term in Equation B.12.

This analysis gives the uncertainty as a stress based on the expected maximum stress range during testing. The percent uncertainty may be estimated by dividing by the maximum expected stress. A maximum stress, σ_{max} , of 206.8 MPa was specified based on a previous test program [15]. From this, the maximum transducer output V_T was calculated.

$$V_T = \frac{kRI\sigma_{max}}{EG_{PAC}} \quad (B.14)$$

Based on this analysis and the specifications provided in the tables, the strain gage uncertainty due solely to instrumentation and signal conditioning was determined to be 1.85 percent. However, additional uncertainty due to strain gage application must be included. A location sensitivity analysis was performed using the methods of Nichol [30] to determine uncertainty based on tolerances held during application. From this analysis, uncertainty due to horizontal and vertical location was estimated at 3 percent each, and uncertainty due to angular orientation was 4 percent. The total uncertainty of the strain gage measurements is the root-mean-squared sum of each of the precision uncertainties, location, orientation, and electronic. This results in an overall uncertainty of approximately 6 percent in stress amplitude measurements.

APPENDIX C: On-line Campbell Diagrams

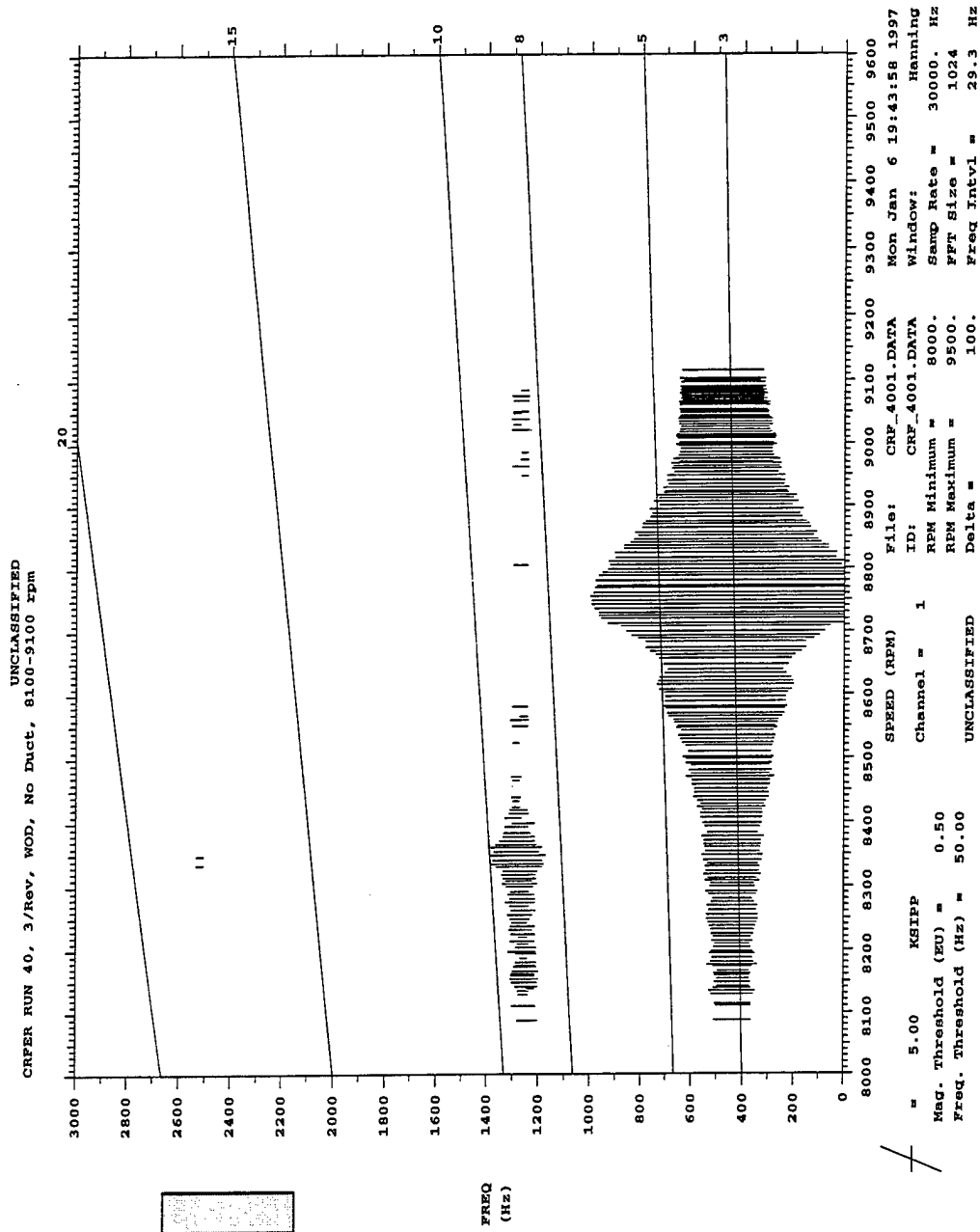


Figure C.1: Blade 1 Campbell diagram, WOD.

CRFER RUN 40, 3/rev, WOD, NO Duct, 8100-9100 rpm

UNCLASSIFIED

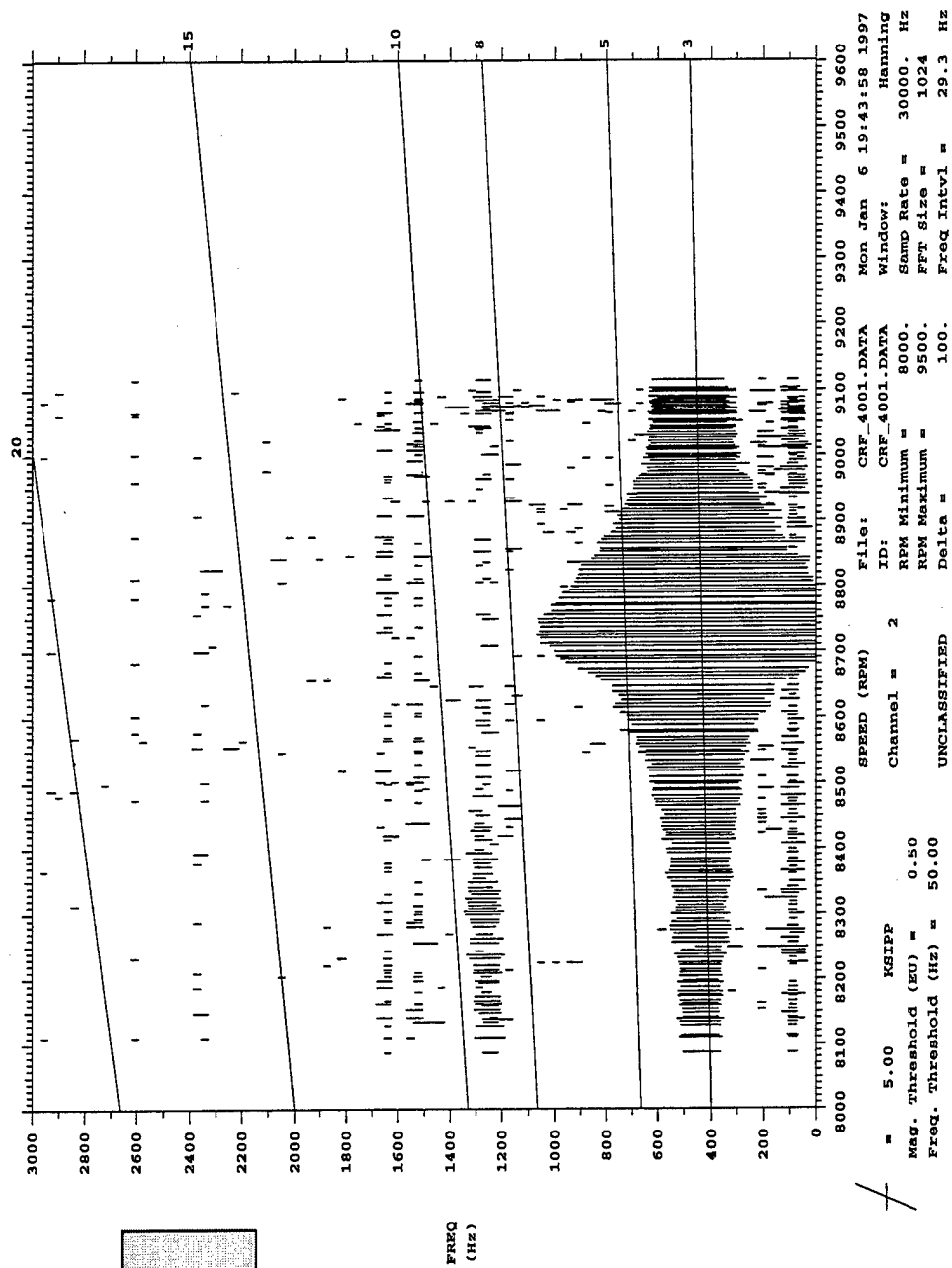


Figure C.2: Blade 2 Campbell diagram, WOD.

UNCLASSIFIED
CRFR RUN 40, 3/Rev, WOD, No Duct, 8100-9100 rpm

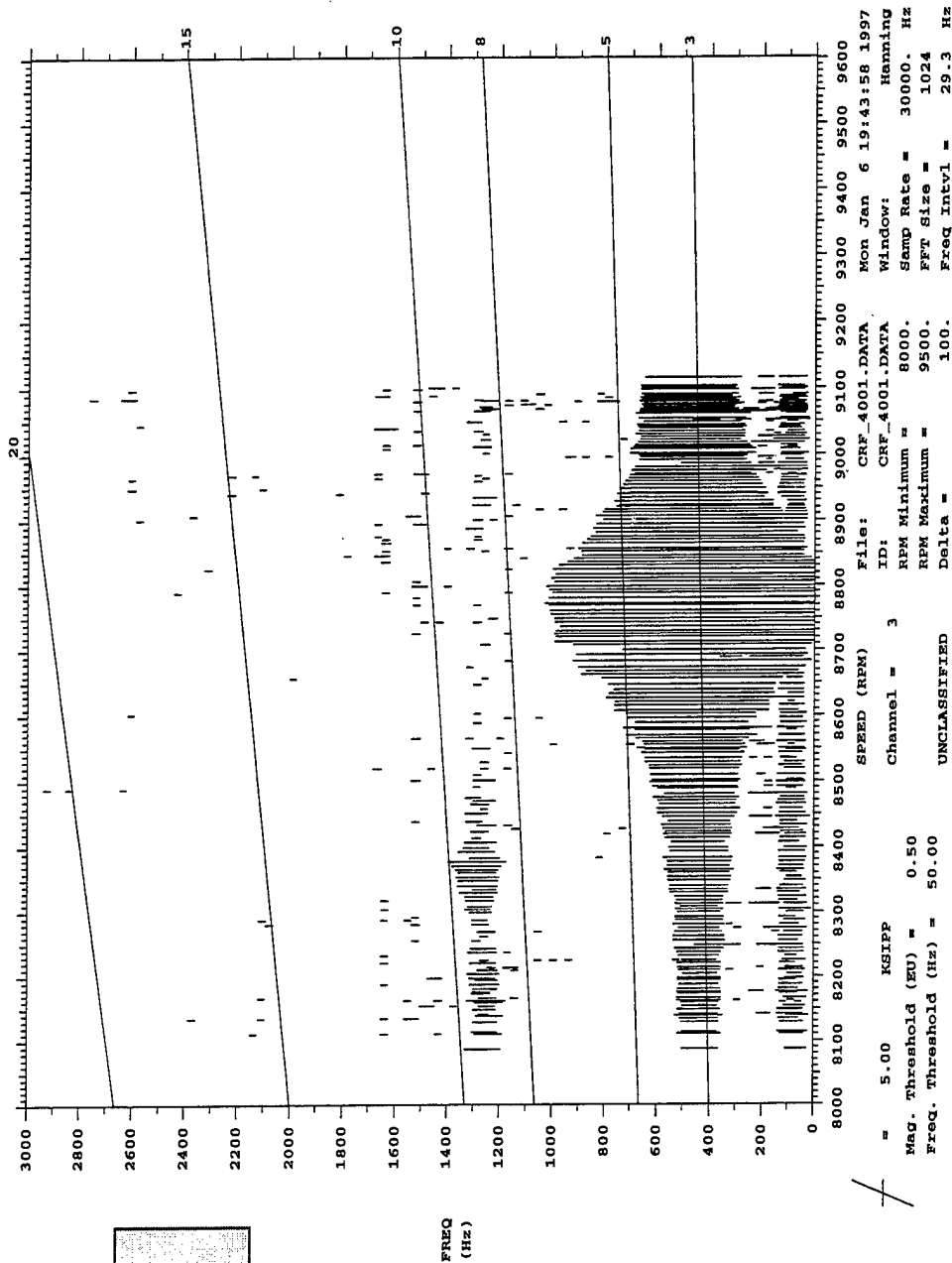


Figure C.3: Blade 3 Campbell diagram, WOD.

UNCLASSIFIED
CRFER RUN 40, 3/Rev, WOD, No Duct, 8100-9100 rpm

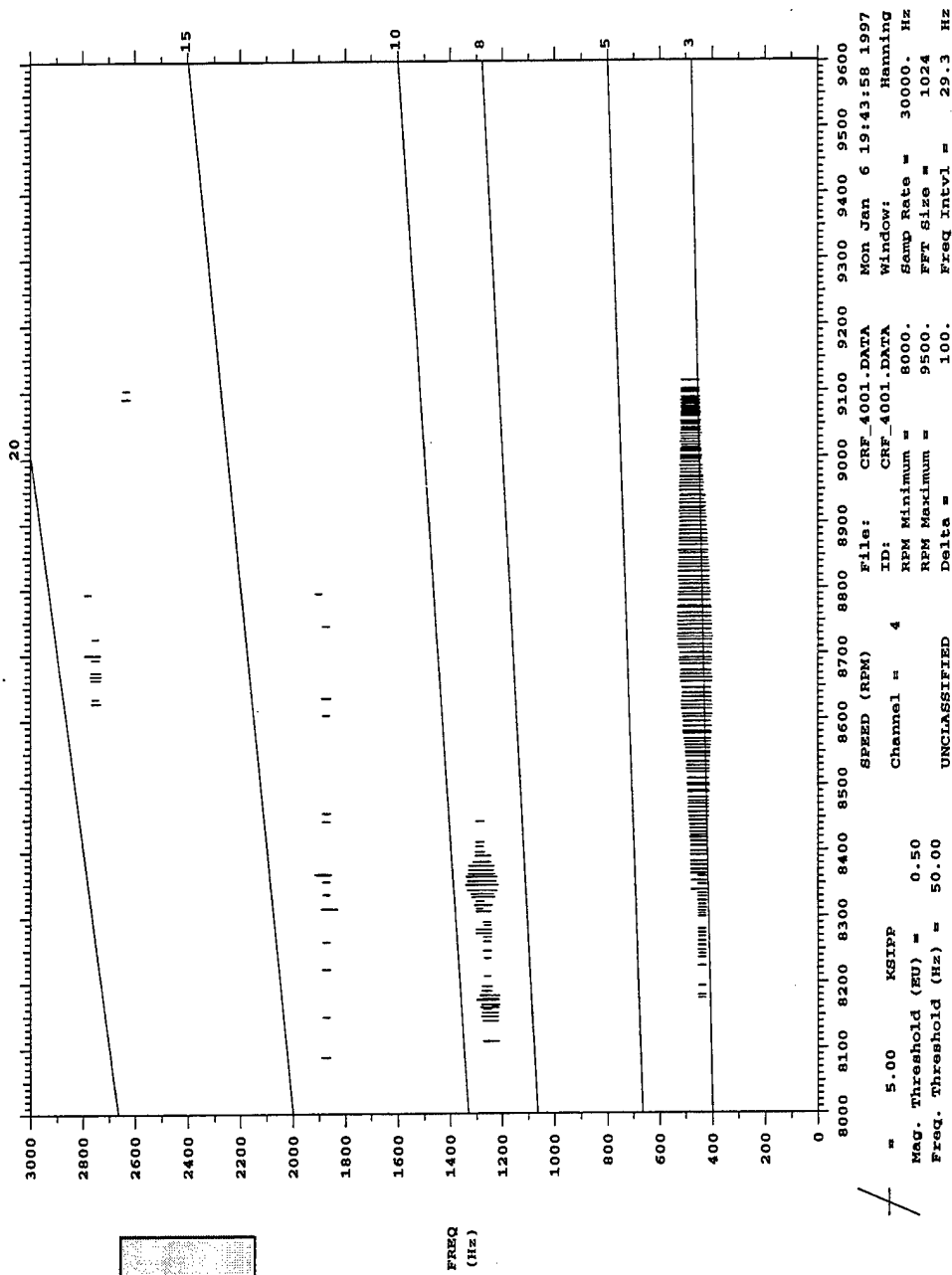


Figure C.4: Blade 4 Campbell diagram, WOD.

UNCLASSIFIED
 CRFER RUN 40, 3/Rev, WOD, No Duct, 8100-9100 rpm

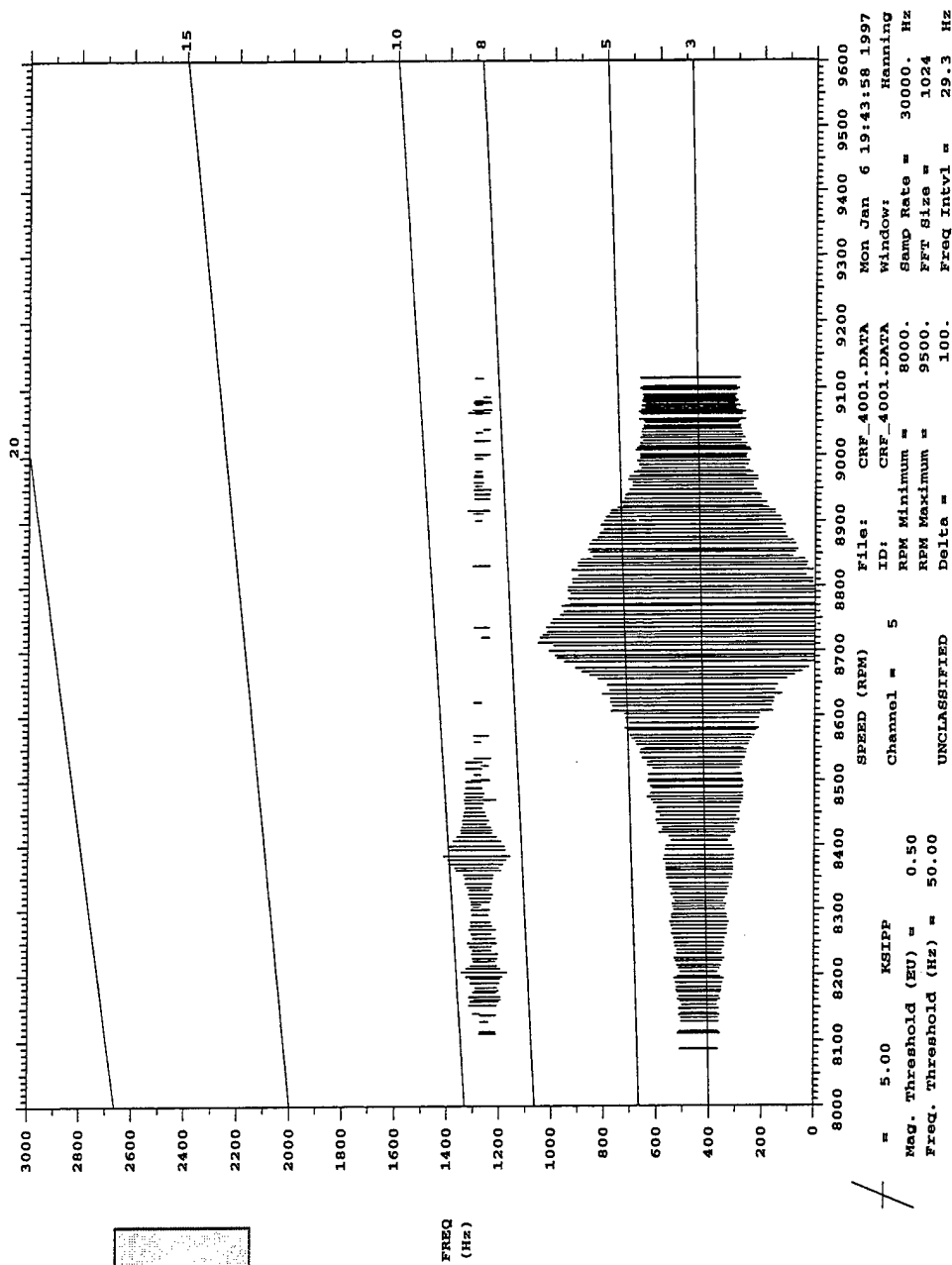


Figure C.5: Blade 5 Campbell diagram, WOD.

UNCLASSIFIED
 CREER RUN 40, 3/rev, WOD, NO Duct, 8100-9100 rpm

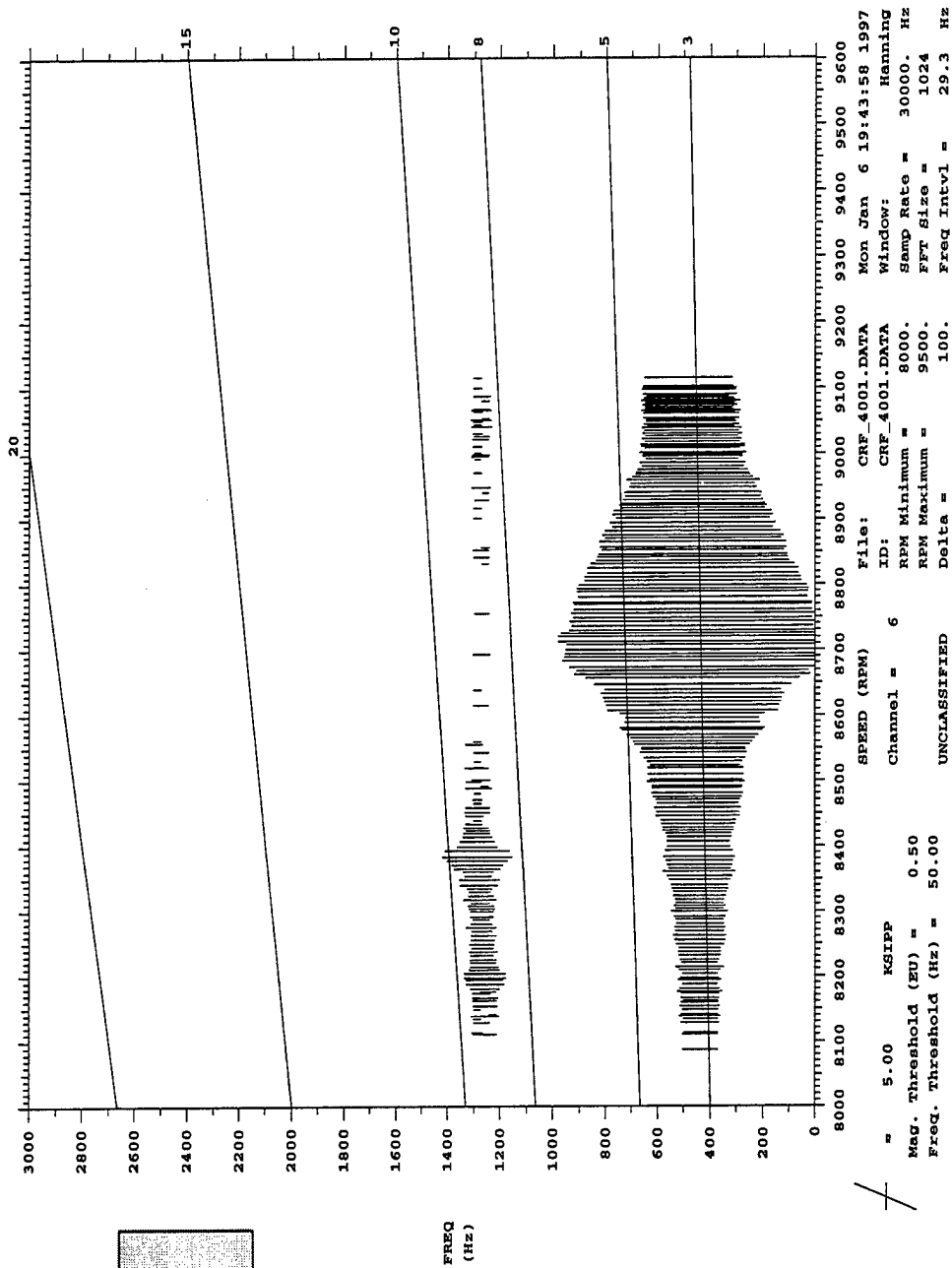


Figure C.6: Blade 6 Campbell diagram, WOD.

UNCLASSIFIED
CRFR RUN 40, 3/Rev, WOD, No Duct, 8100-9100 rpm

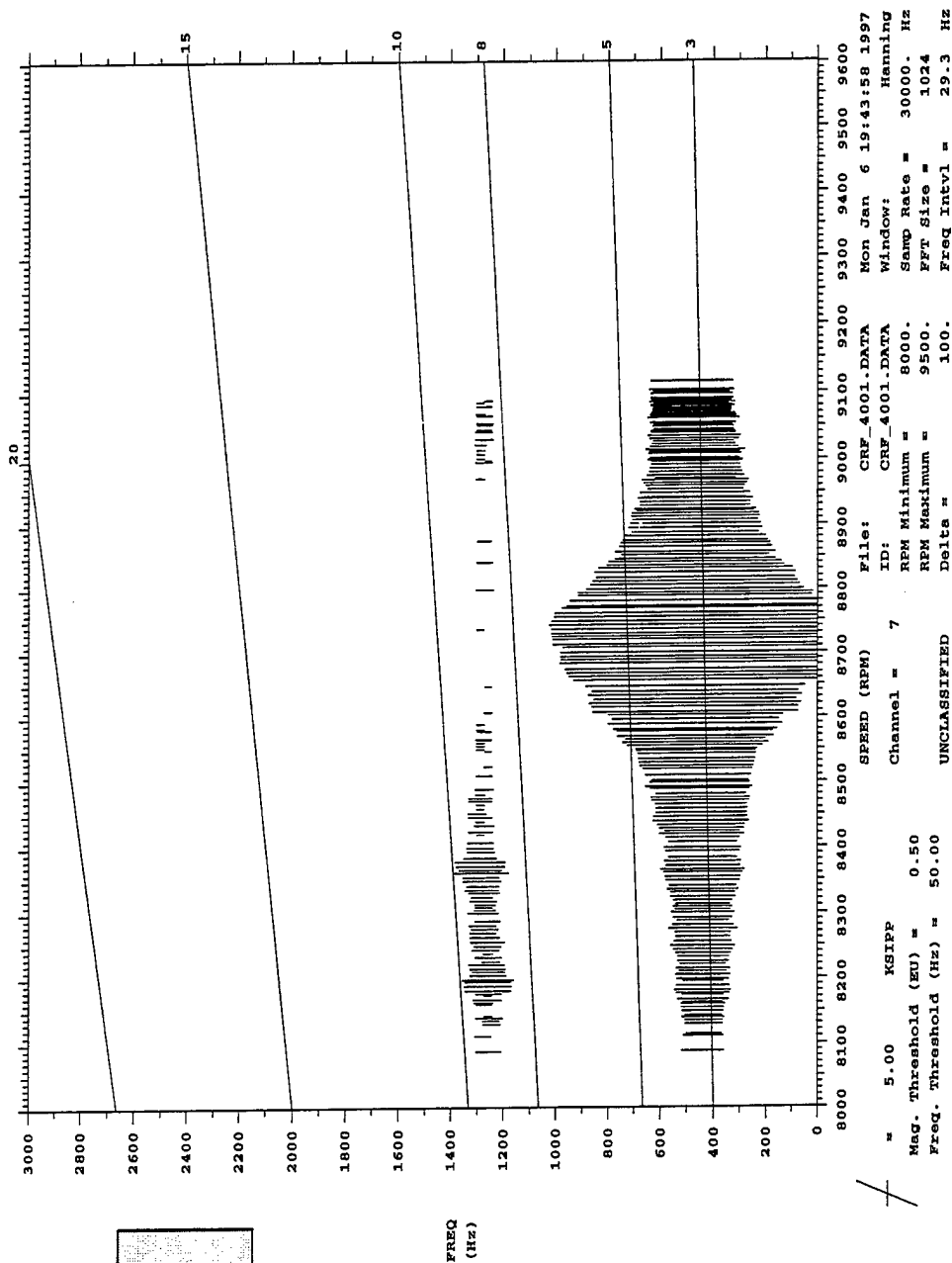


Figure C.7: Blade 7 Campbell diagram, WOD.

UNCLASSIFIED
CRFER RUN 40, 3/rev, WOD, No Duct, 8100-9100 rpm

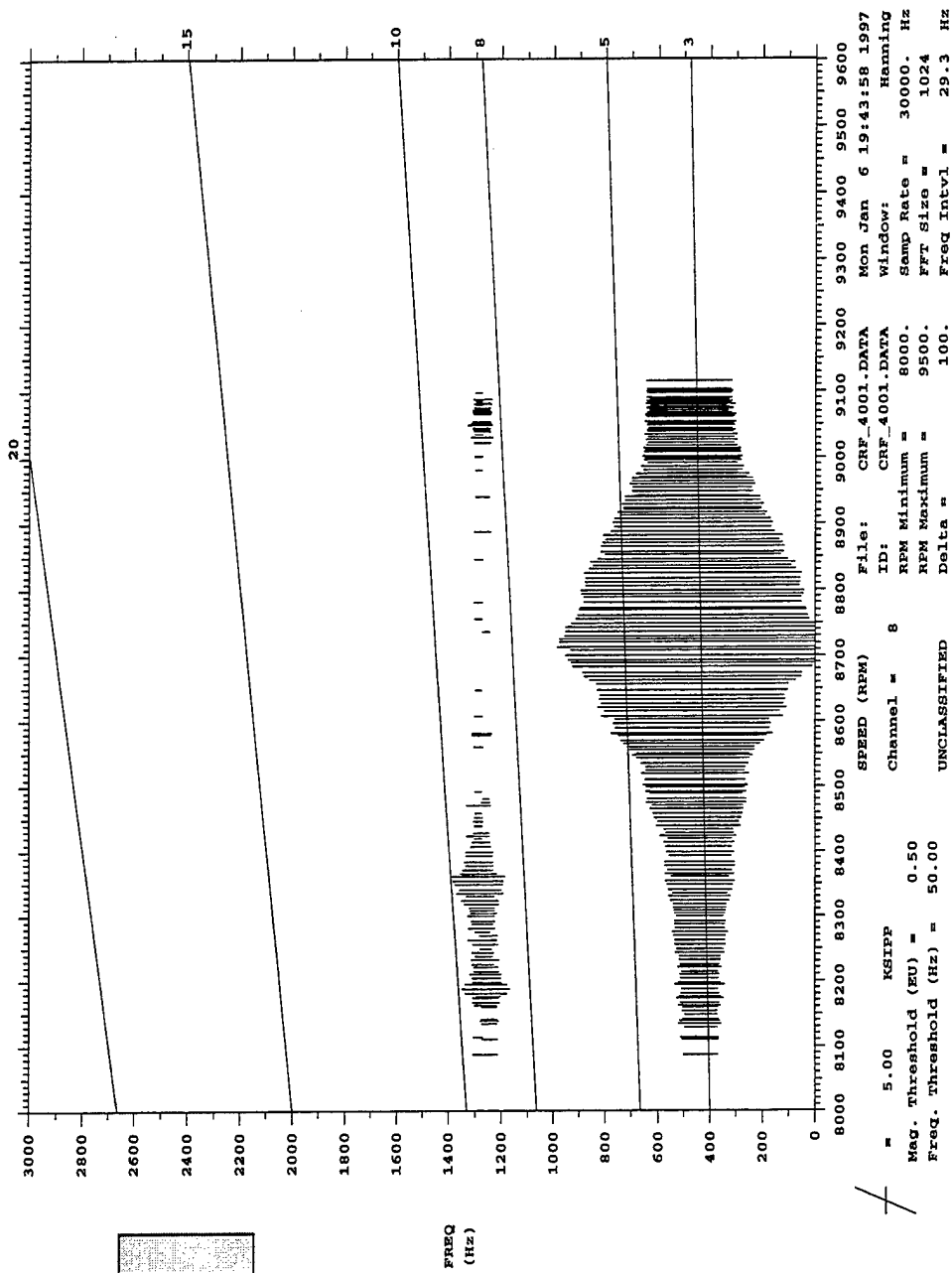


Figure C.8: Blade 8 Campbell diagram, WOD.

UNCLASSIFIED
CRFER RUN 40, 3/Rev, WOD, No Duct, 8100-9100 rpm

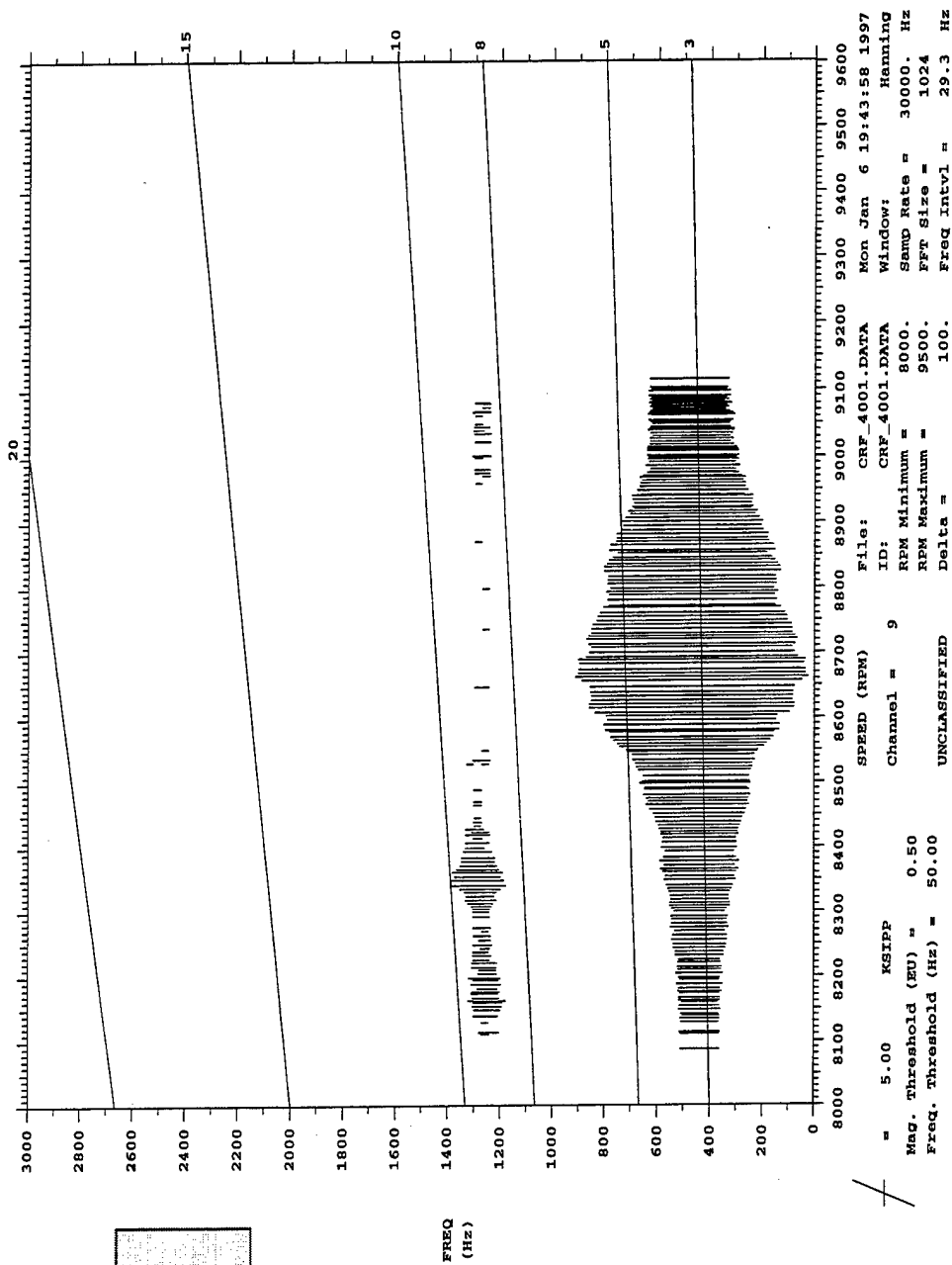


Figure C.9: Blade 9 Campbell diagram, WOD.

CRFER RUN 40, 3/rev, WOD, No Duct, 8100-9100 RPM

UNCLASSIFIED

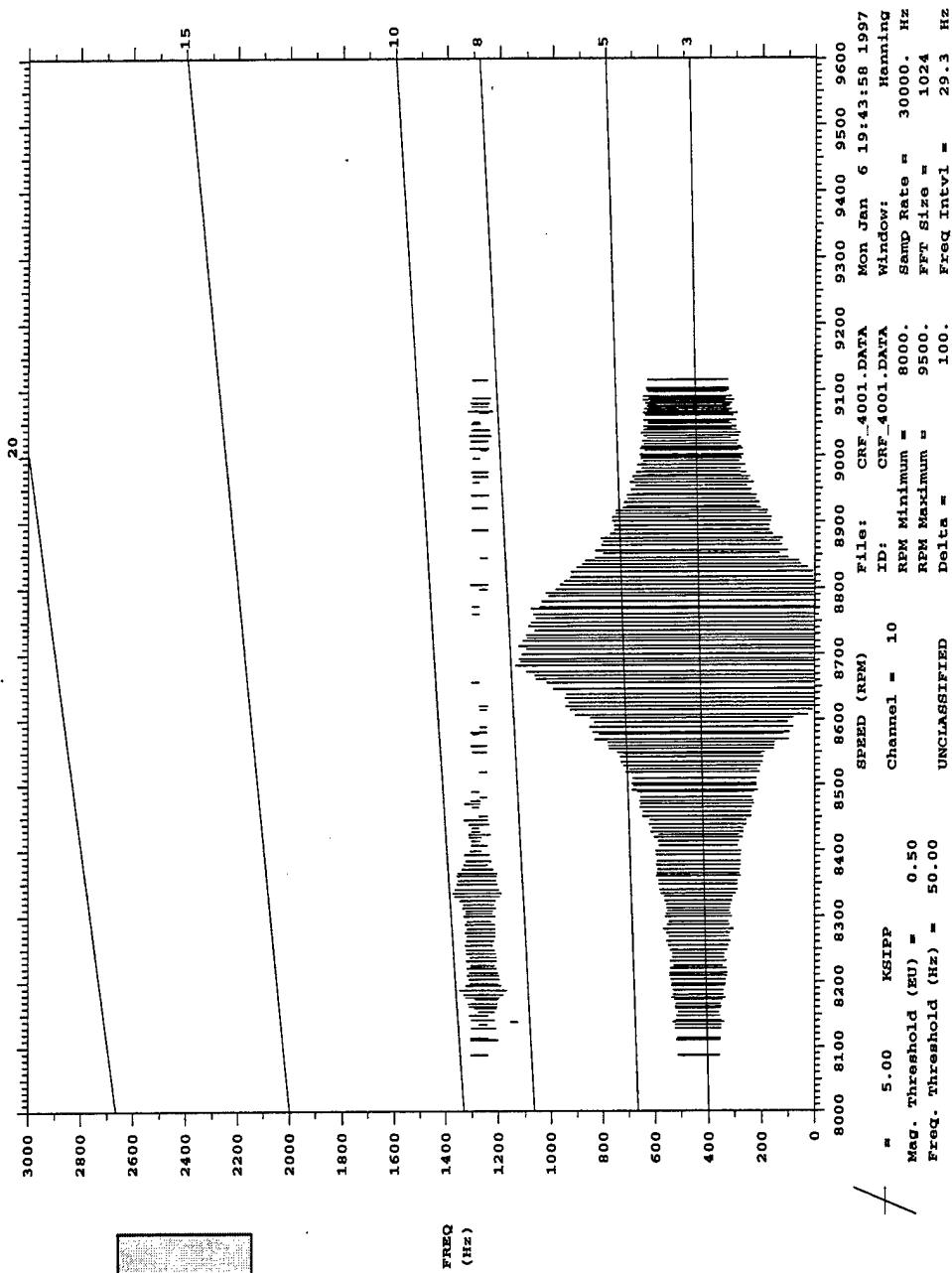


Figure C.10: Blade 10 Campbell diagram, WOD.

UNCLASSIFIED
 CRFER RUN 40, 3/Rev, WOD, No Duct, 8100-9100 rpm

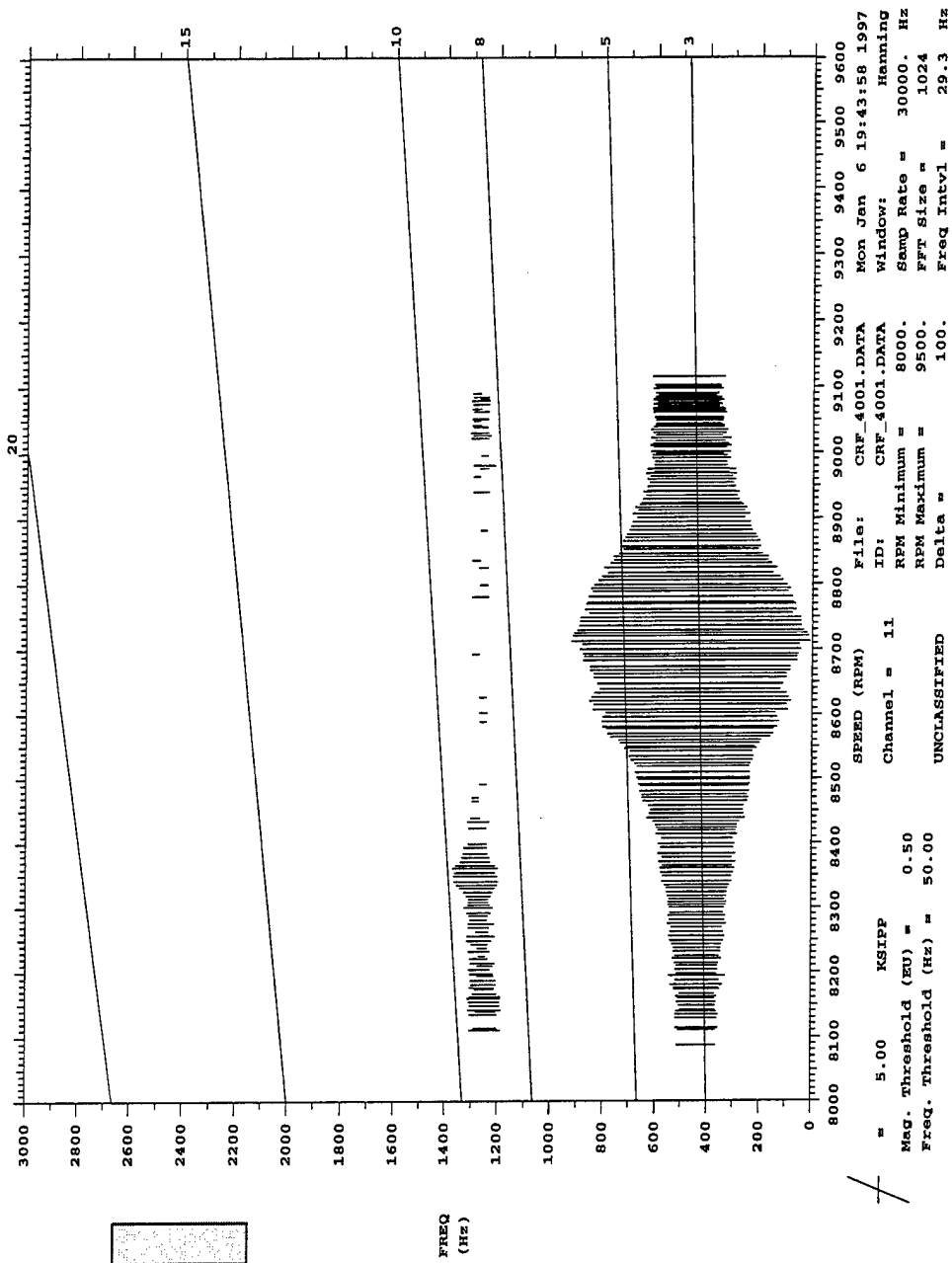


Figure C.11: Blade 11 Campbell diagram, WOD.

UNCLASSIFIED
CRFER RUN 40, 3/rev, WOD, No Duct, 8100-9100 rpm

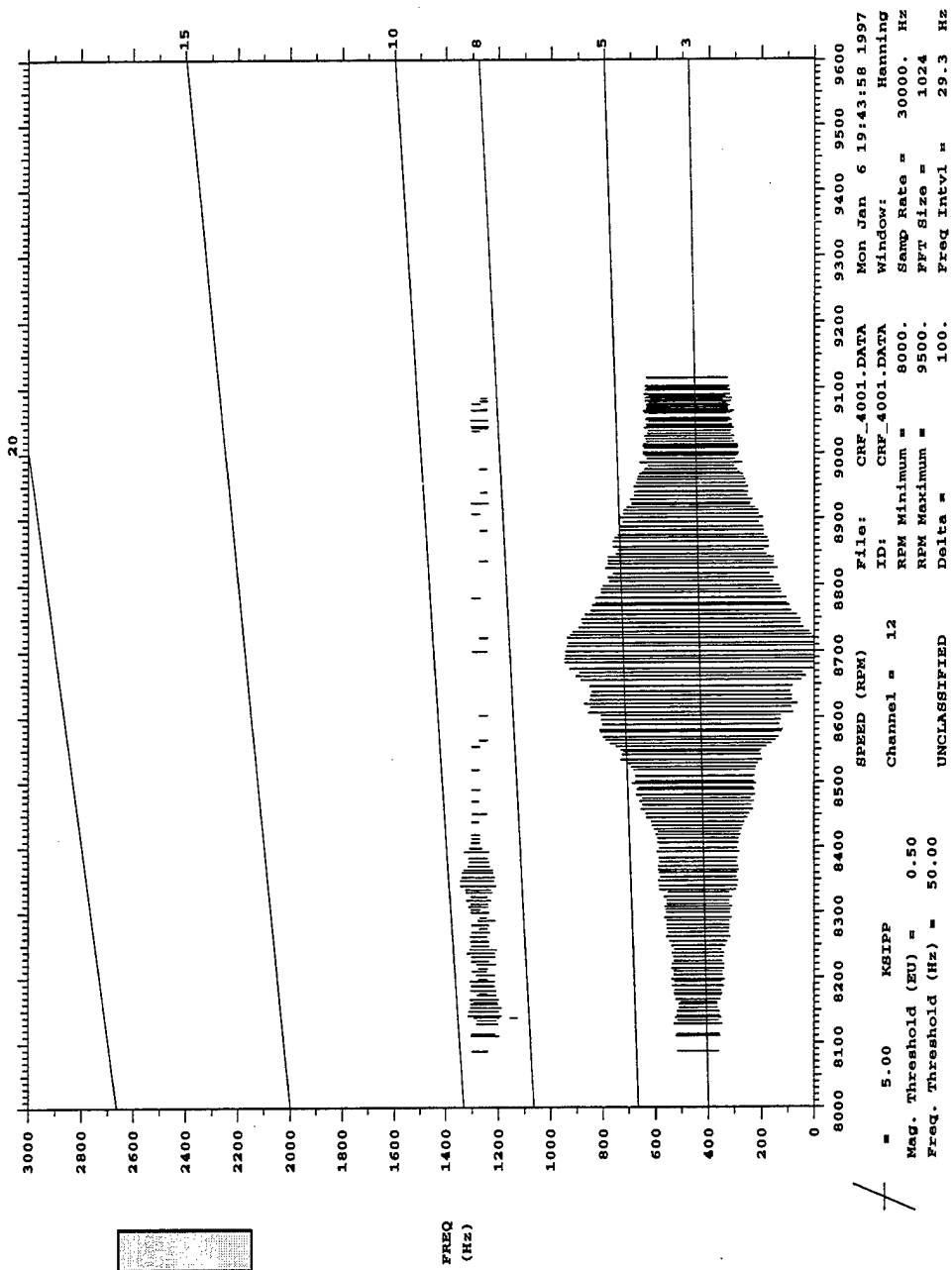


Figure C.12: Blade 12 Campbell diagram, WOD.

CRFR RUN 40, 3/rev, WOD, No Duct, 8100-9100 rpm

UNCLASSIFIED

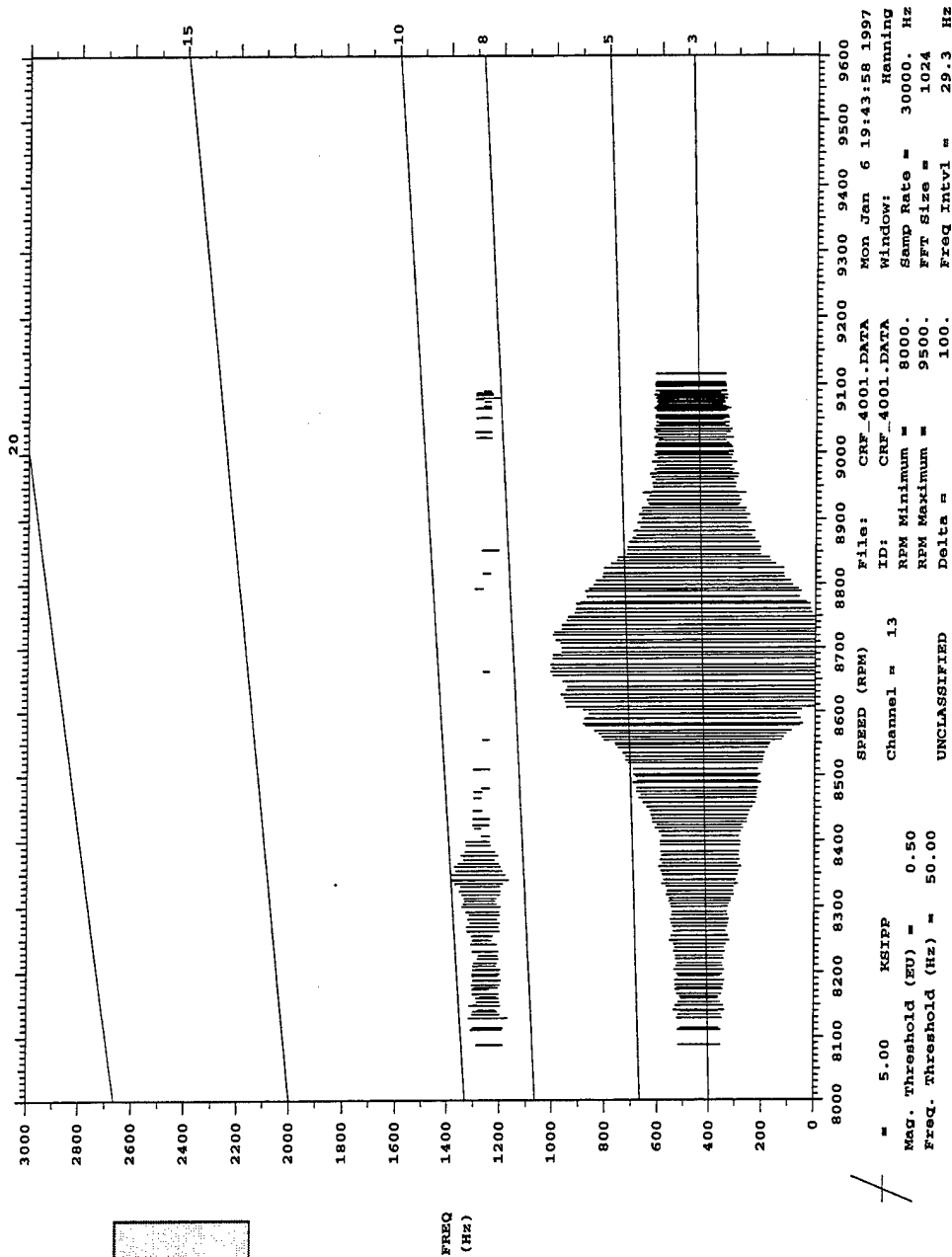


Figure C.13: Blade 13 Campbell diagram, WOD.

UNCLASSIFIED
 CRFR RUN 40, 3/rev, WOD, NO DUCT, 8100-9100 RPM

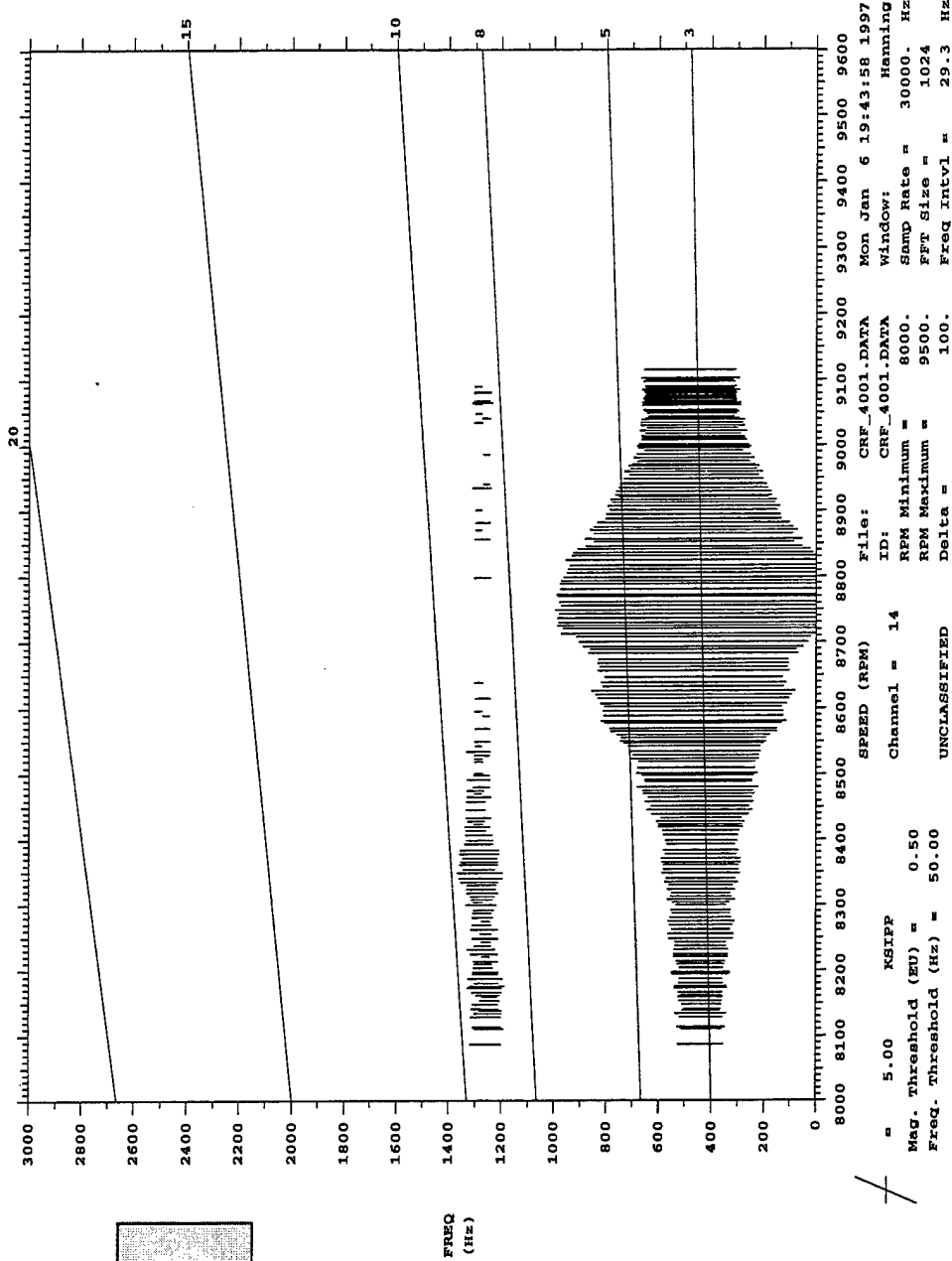


Figure C.14: Blade 14 Campbell diagram, WOD.

UNCLASSIFIED
 CREER RUN 40, 3/Rev, WOD, No Duct, 8100-9100 rpm

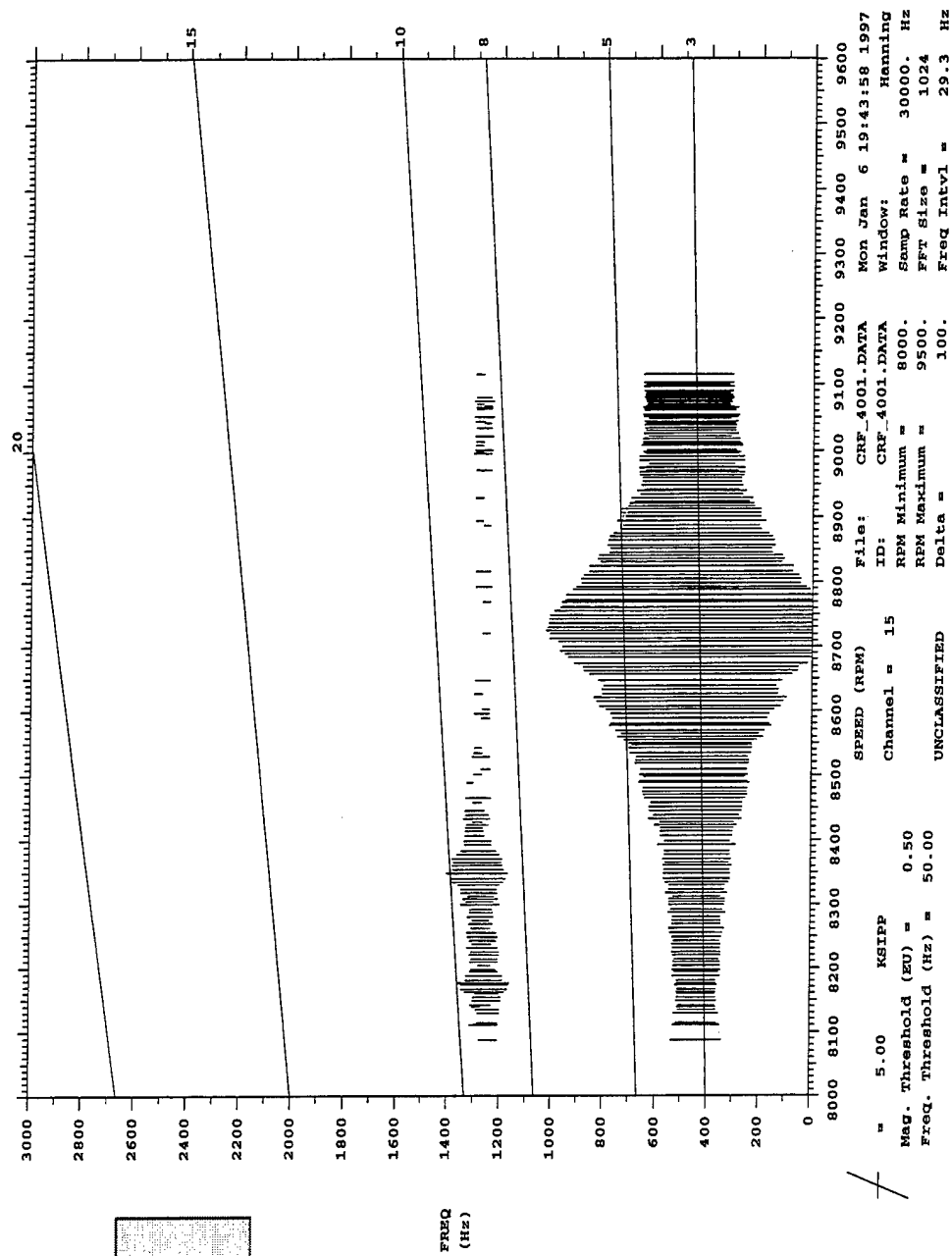


Figure C.15: Blade 15 Campbell diagram, WOD.

UNCLASSIFIED
 CREER RUN 40, 3/Rev, WOD, No Duct, 8100-9100 rpm

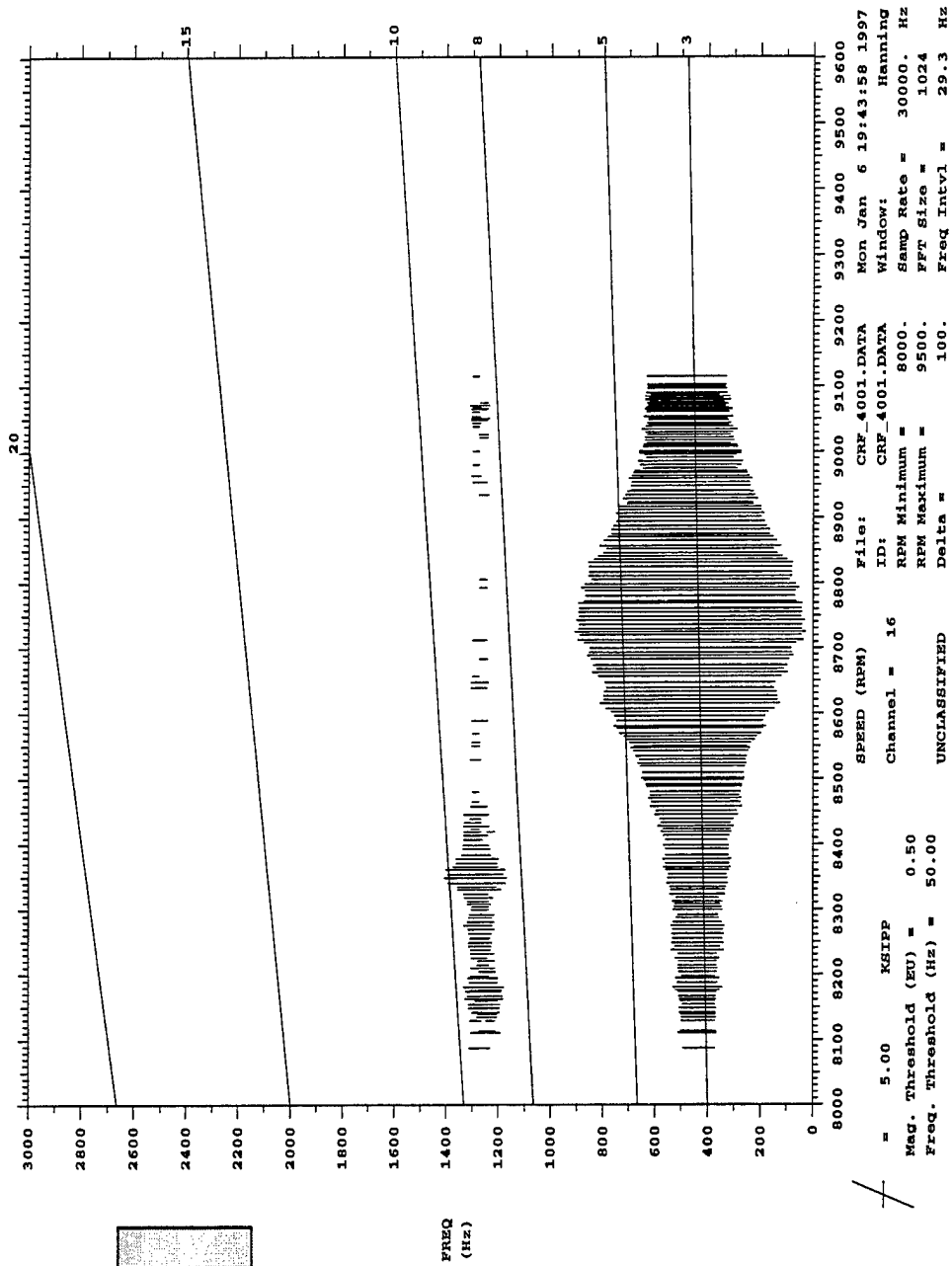


Figure C.16: Blade 16 Campbell diagram, WOD.

CRFR RUN 40, 3/rev, NOL, No Duct, 8100-9100 rpm

UNCLASSIFIED

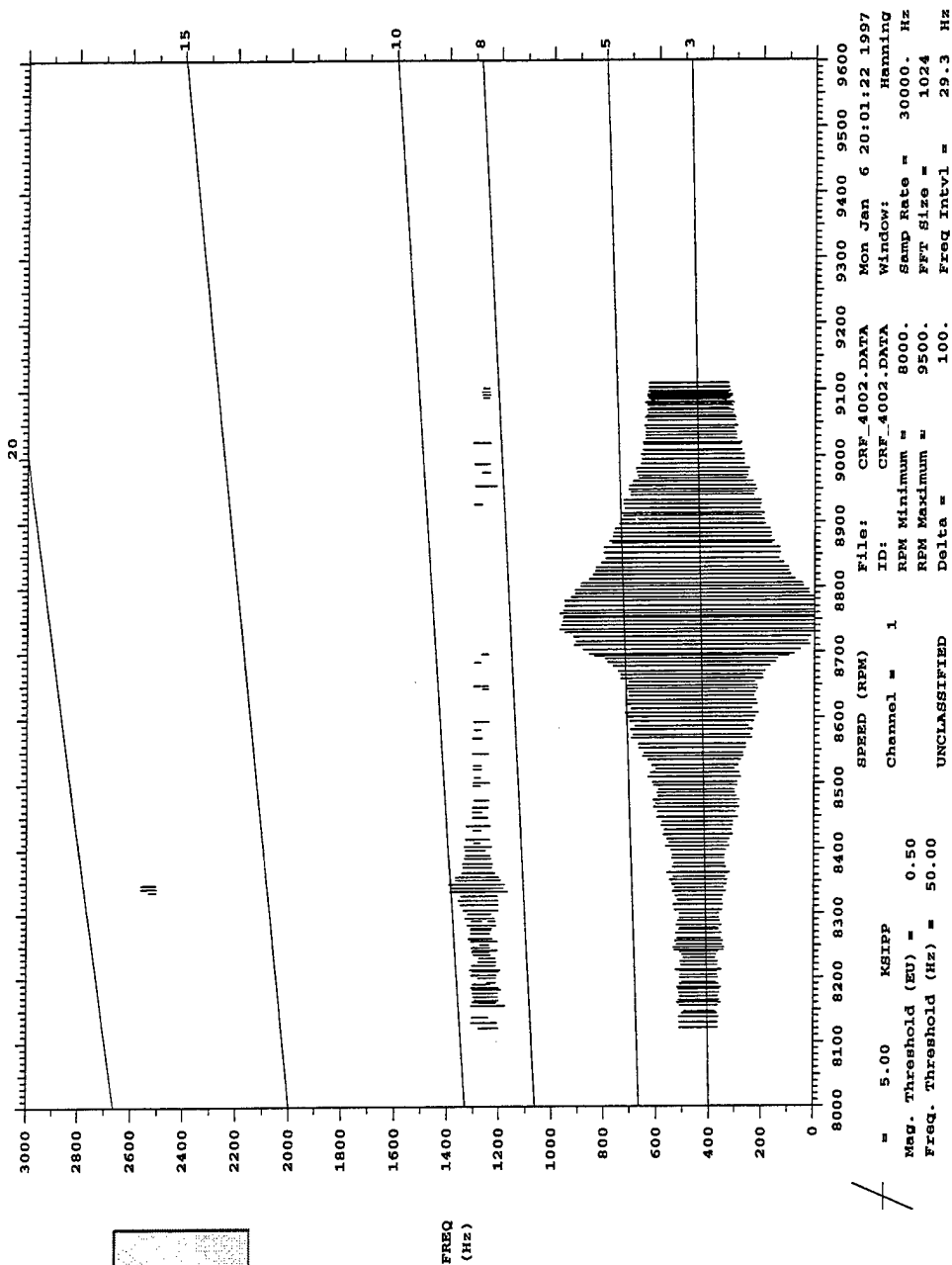


Figure C.17: Blade 1 Campbell diagram, NOL.

CRFER RUN 40, 3/rev, NOL, No Duct, 8100-9100 rpm

UNCLASSIFIED

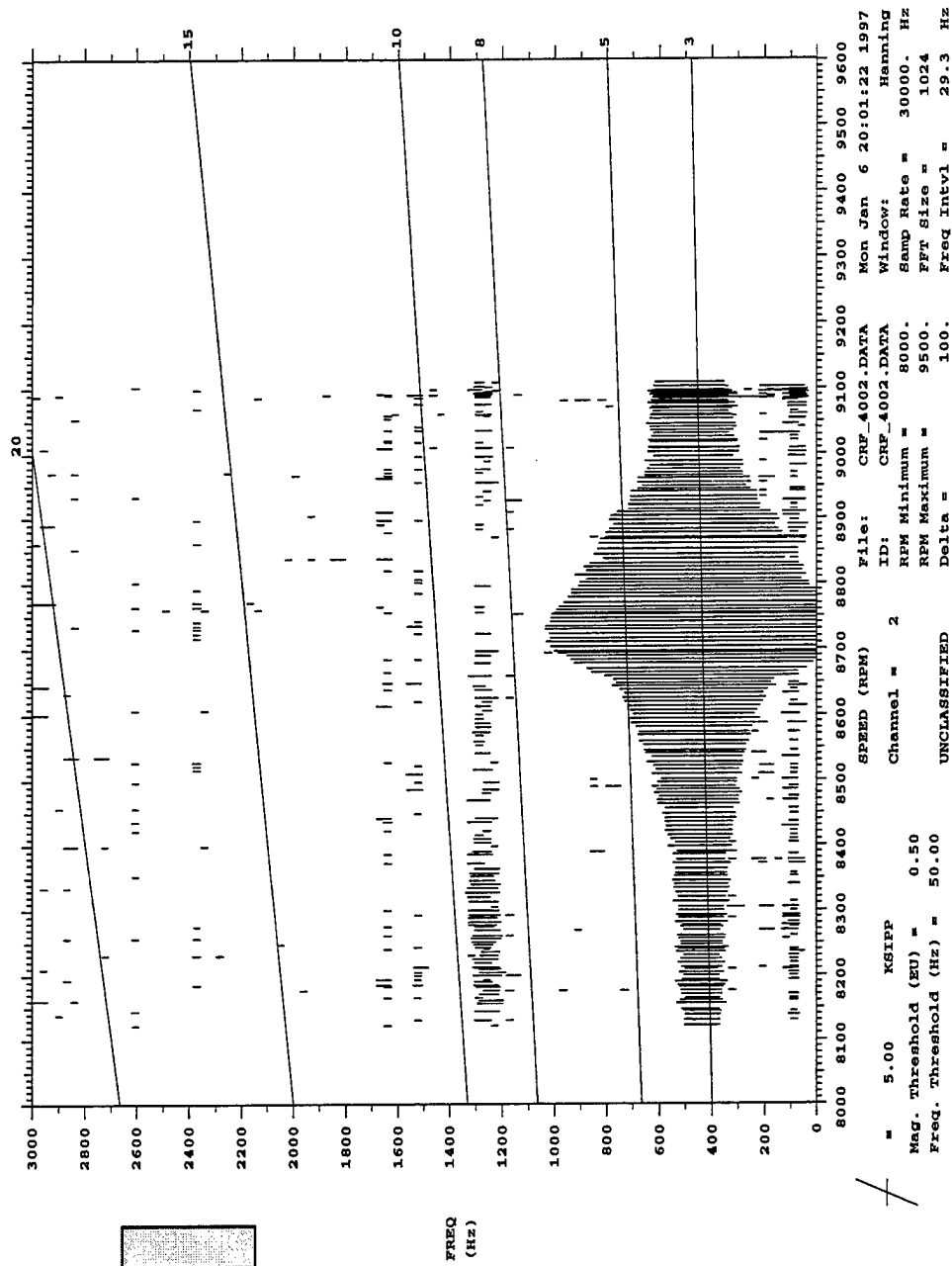


Figure C.18: Blade 2 Campbell diagram, NOL.

UNCLASSIFIED
CRFR RUN 40, 3/Rev, NOL, No Duct, 8100-9100 rpm

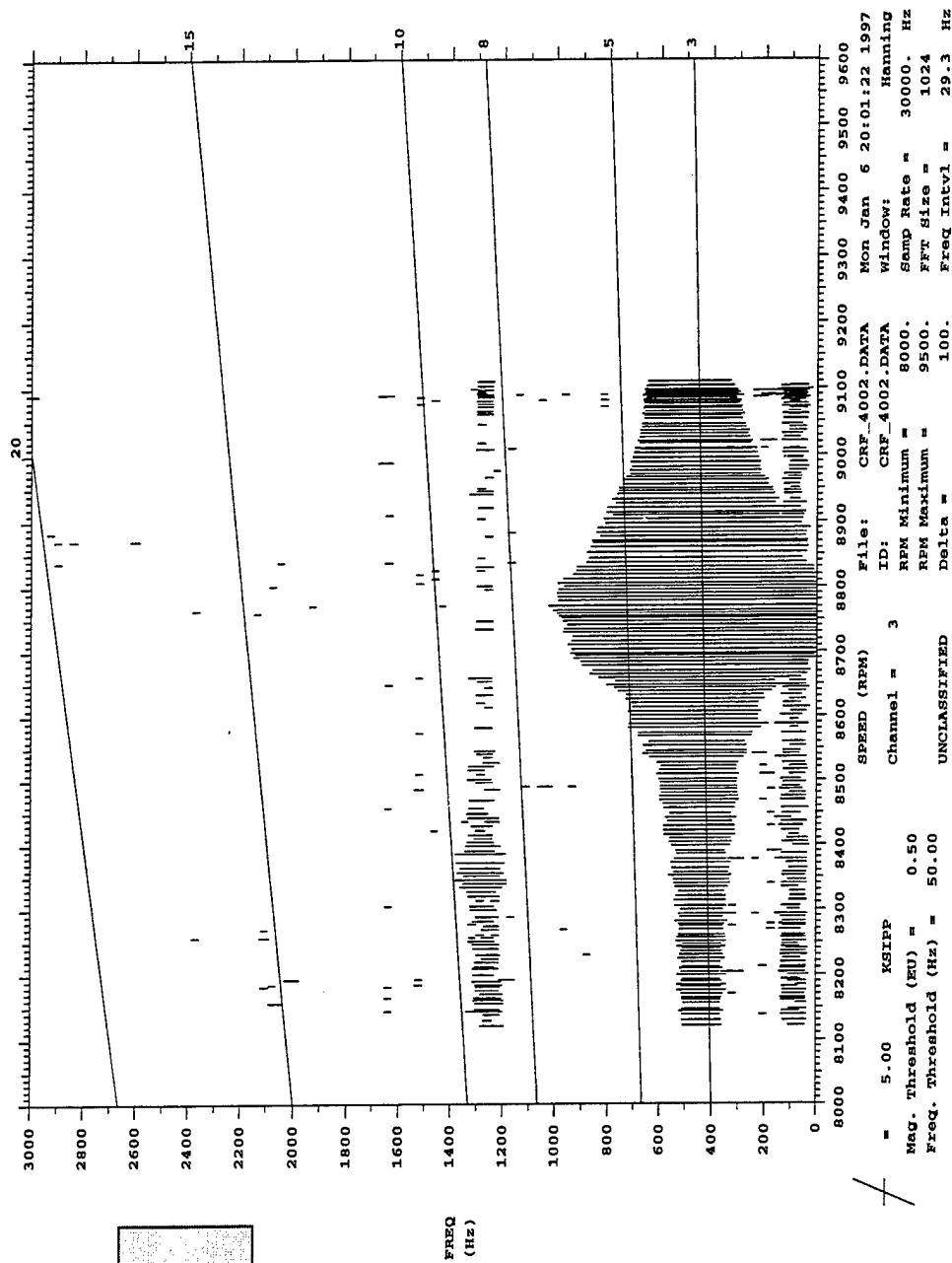


Figure C.19: Blade 3 Campbell diagram, NOL.

CRFER RUN 40, 3/Rev, NOL, No Duct, 8100-9100 rpm UNCLASSIFIED

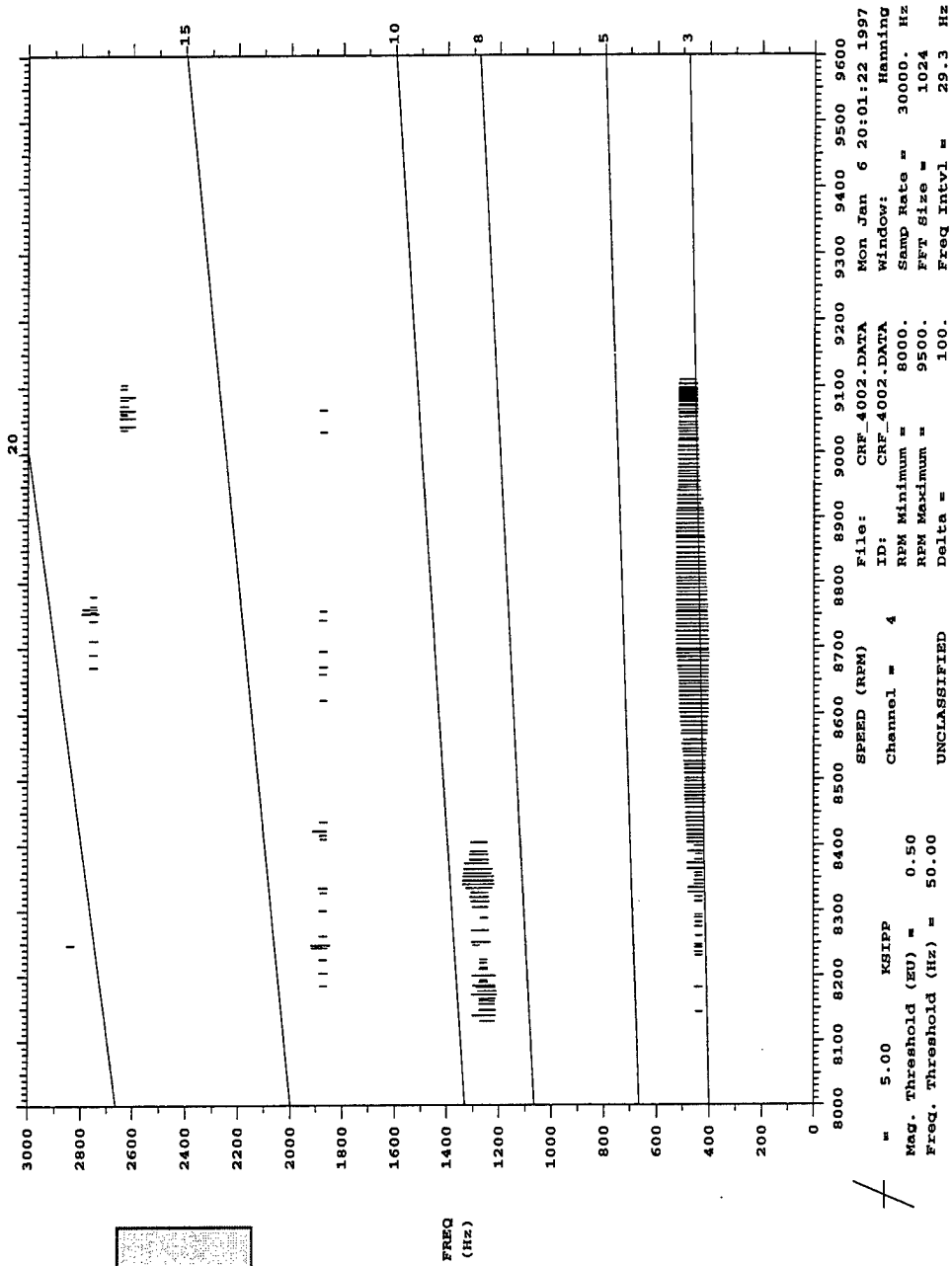


Figure C.20: Blade 4 Campbell diagram, NOL.

UNCLASSIFIED
 CRFER RUN 40, 3/Rev, NOL, No Duct, 8100-9100 rpm

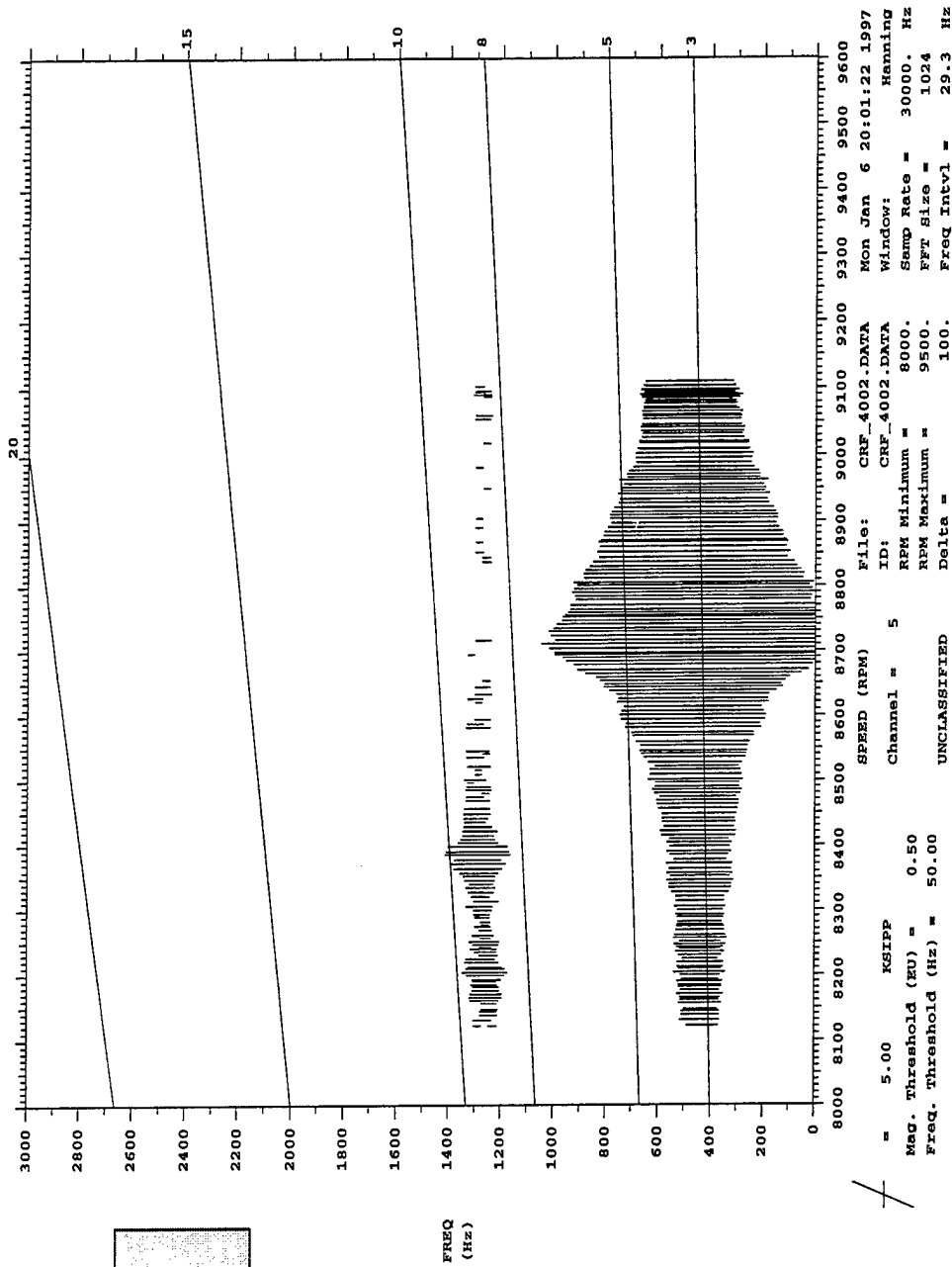


Figure C.21: Blade 5 Campbell diagram, NOL.

UNCLASSIFIED
 CRFR RUN 40, 3/rev, NOL, NO Duct, 8100-9100 rpm

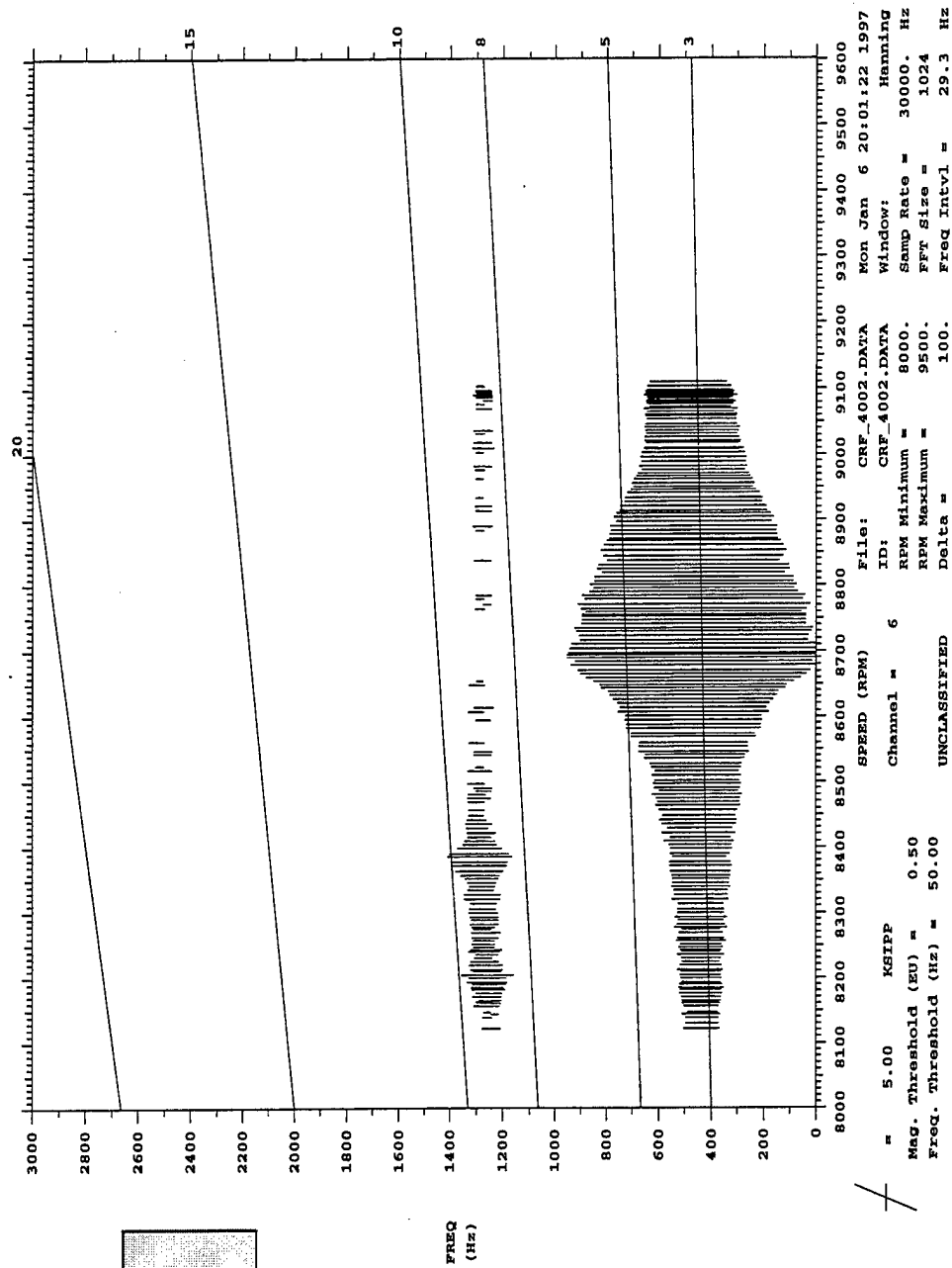


Figure C.22: Blade 6 Campbell diagram, NOL.

CRFER RUN 40, 3/Rev, NOL, No Duct, 8100-9100 rpm

UNCLASSIFIED

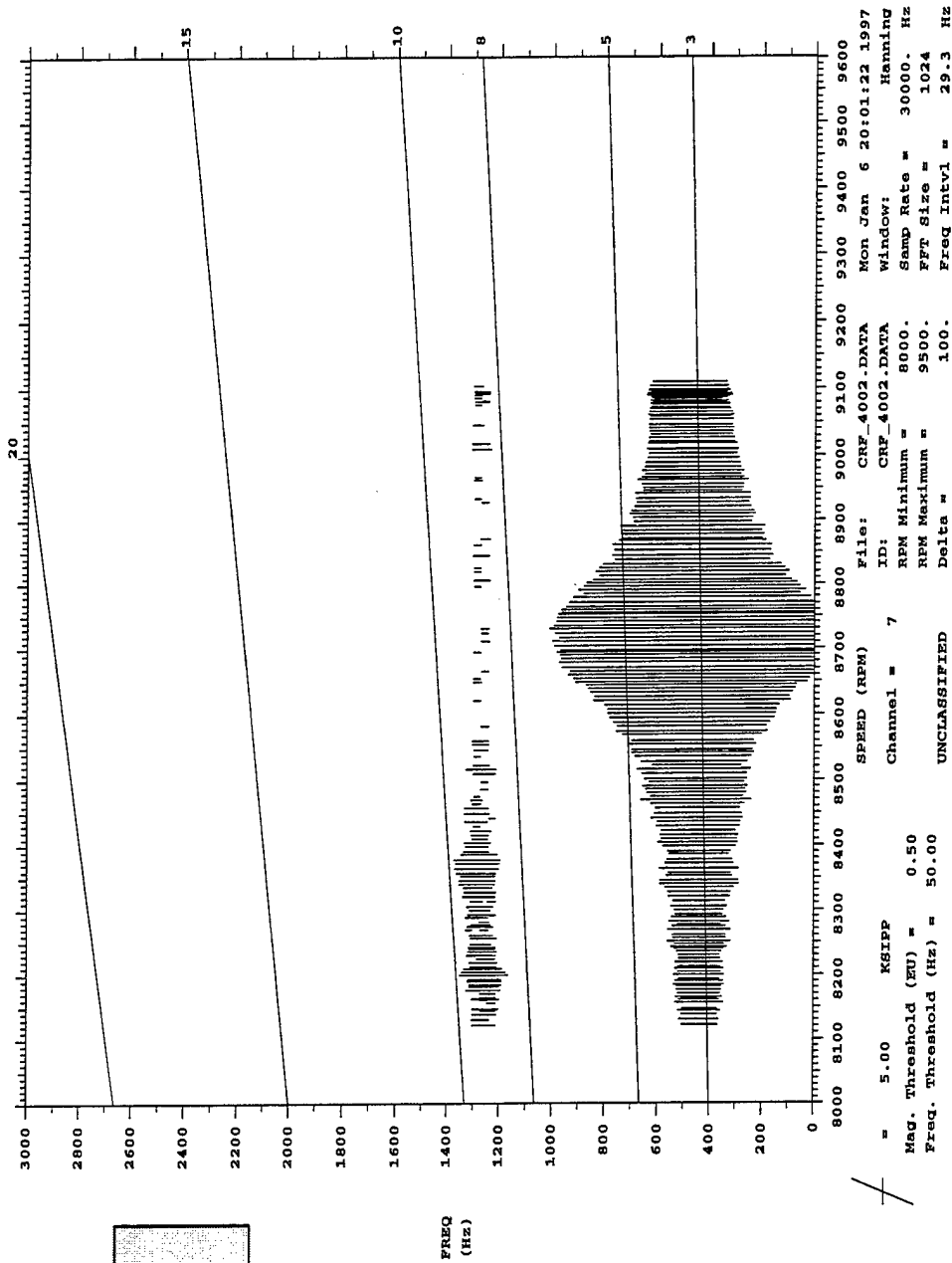


Figure C.23: Blade 7 Campbell diagram, NOL.

UNCLASSIFIED
CRFR RUN 40, 3/Rev, NOL, No Duct, 8100-9100 RPM

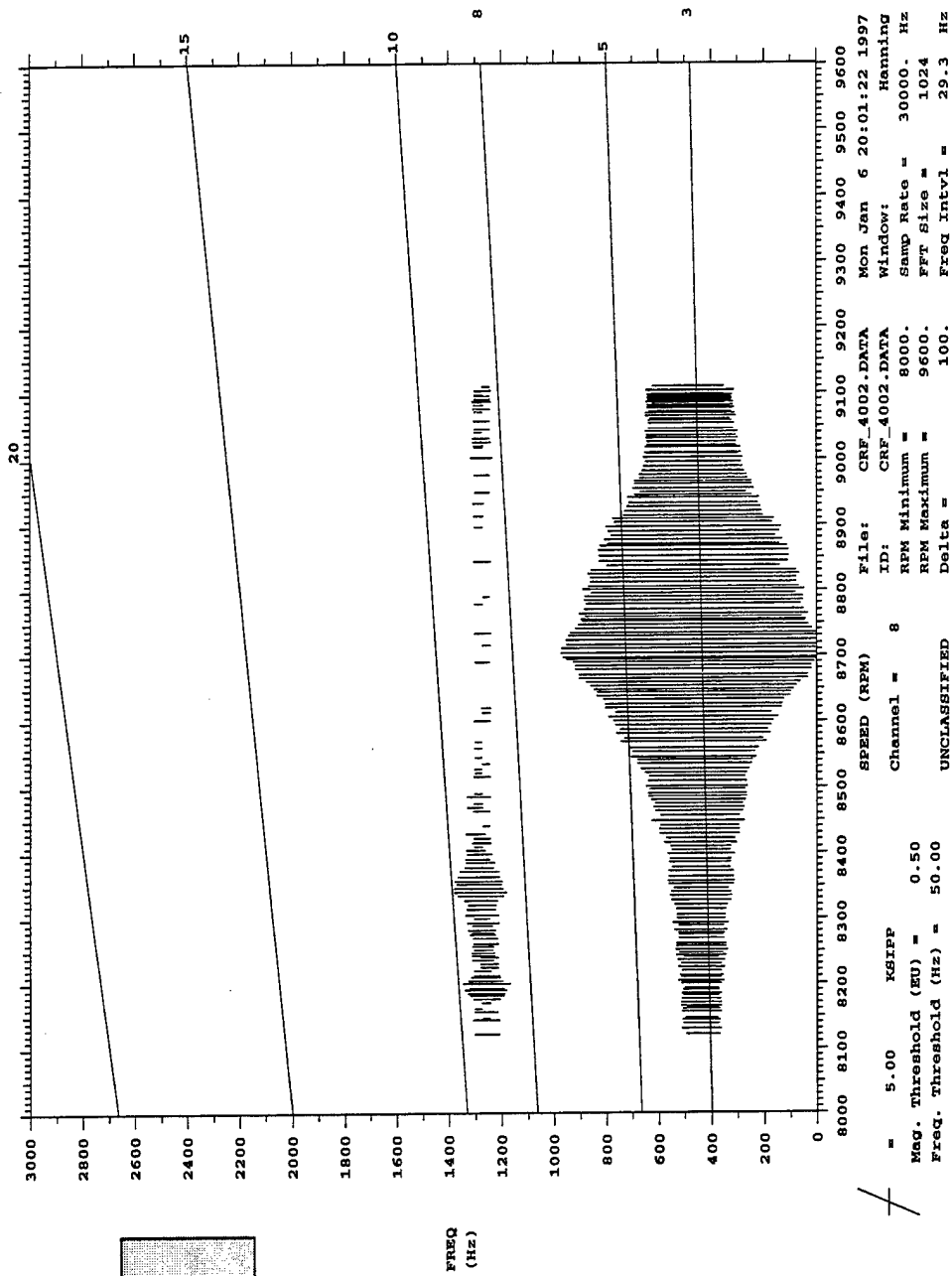


Figure C.24: Blade 8 Campbell diagram, NOL.

UNCLASSIFIED
 CRFER RUN 40, 3/Rev, NOL, No Duct, 8100-9100 rpm

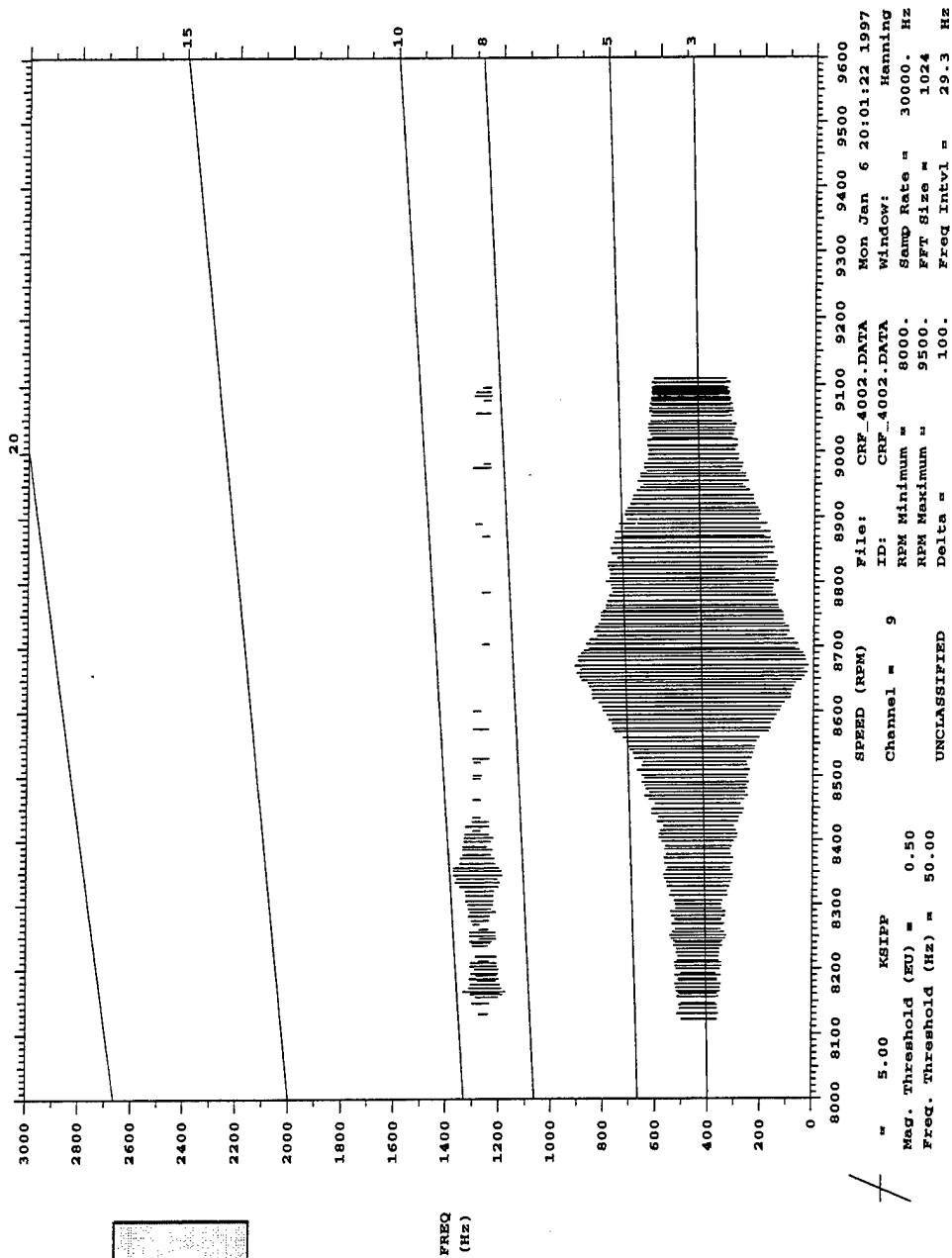


Figure C.25: Blade 9 Campbell diagram, NOL.

UNCLASSIFIED
CRFER RUN 40, 3/Rev, NOL, No Duct, 8100-9100 rpm

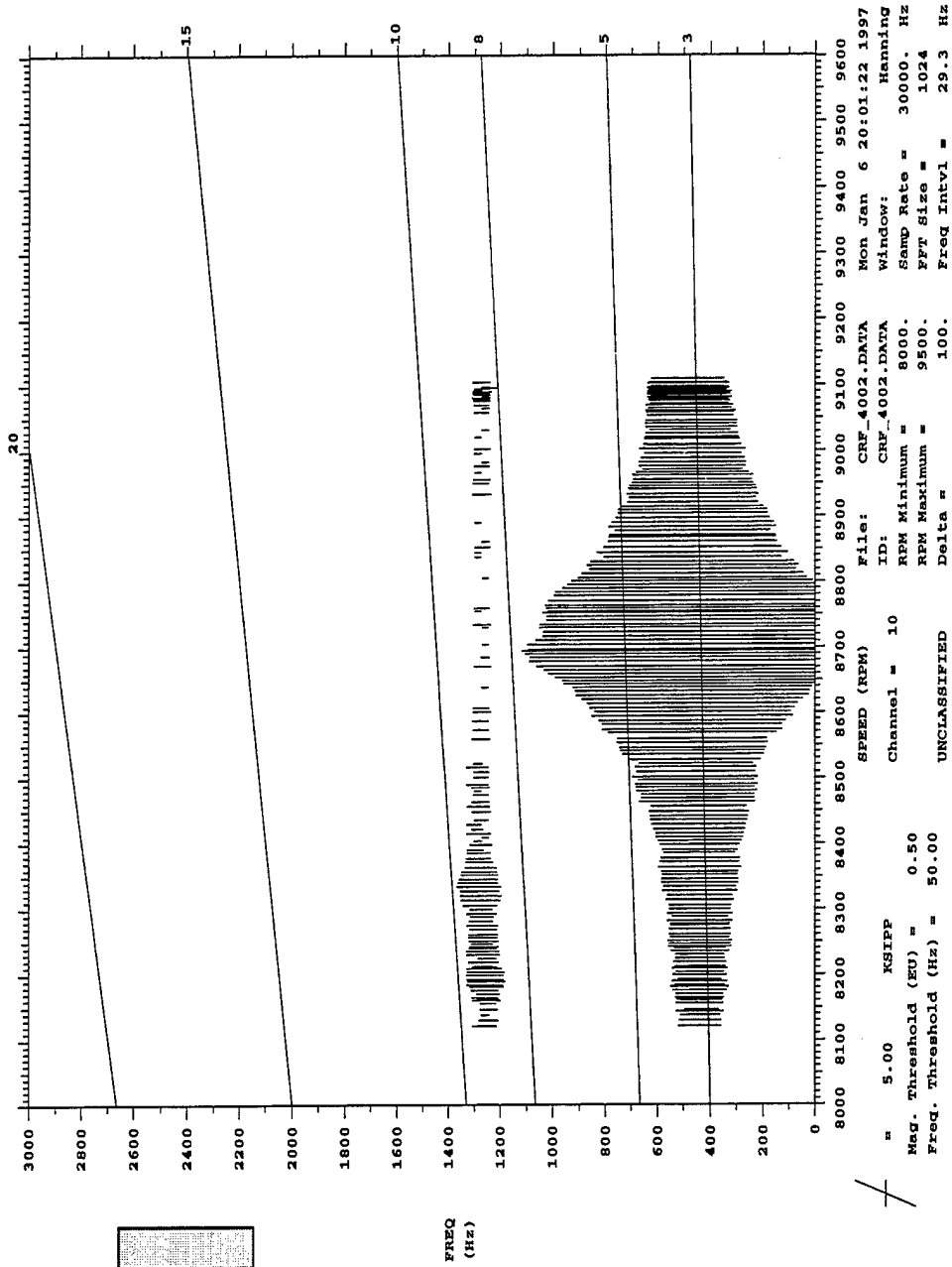


Figure C.26: Blade 10 Campbell diagram, NOL.

CEFER RUN 40, 3/Rev, NOL, No Duct, 8100-9100 rpm

UNCLASSIFIED

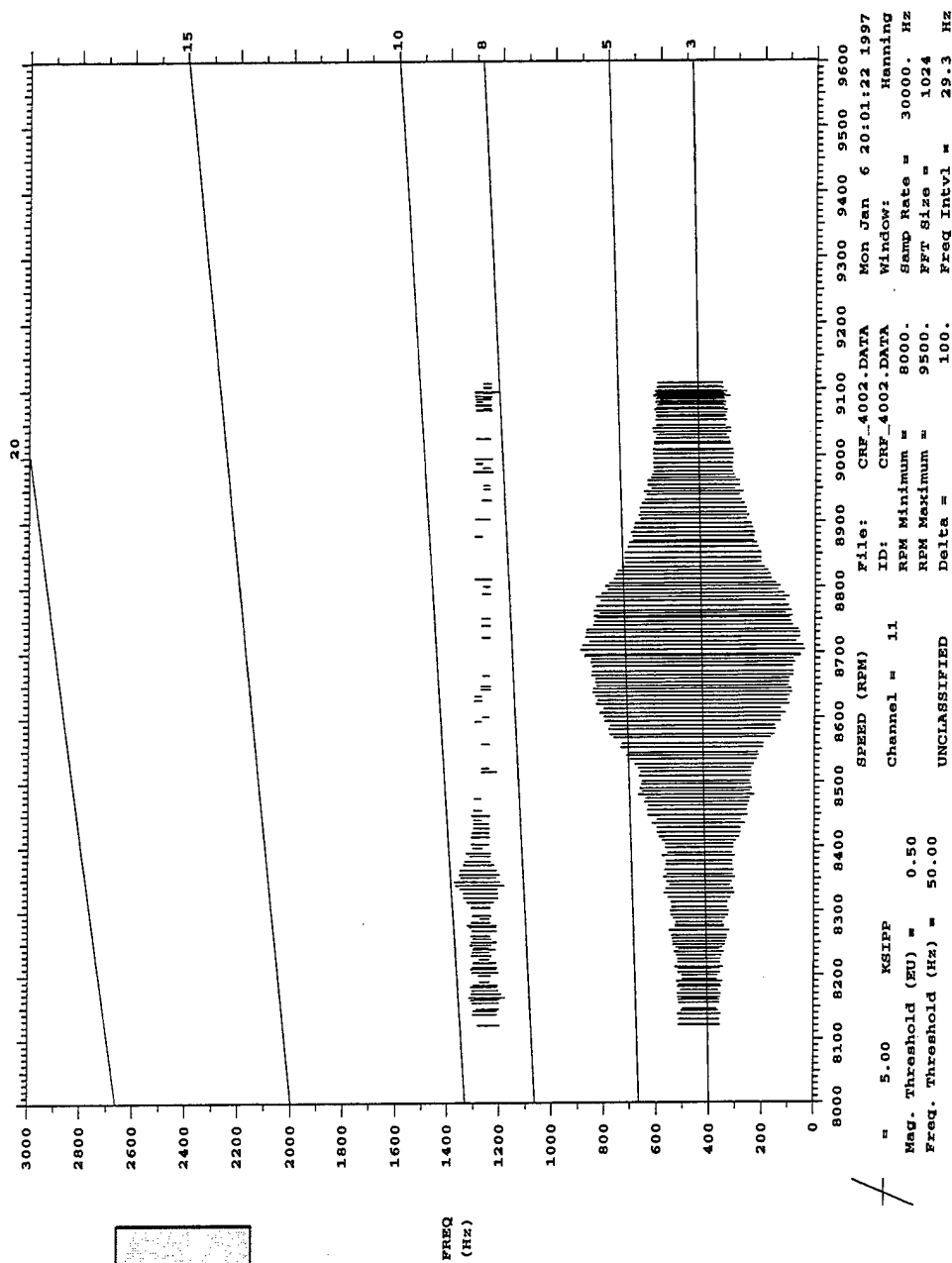


Figure C.27: Blade 11 Campbell diagram, NOL.

UNCLASSIFIED
CRPER RUN 40, 3/Rev, NOL, No Duct, 8100-9100 rpm

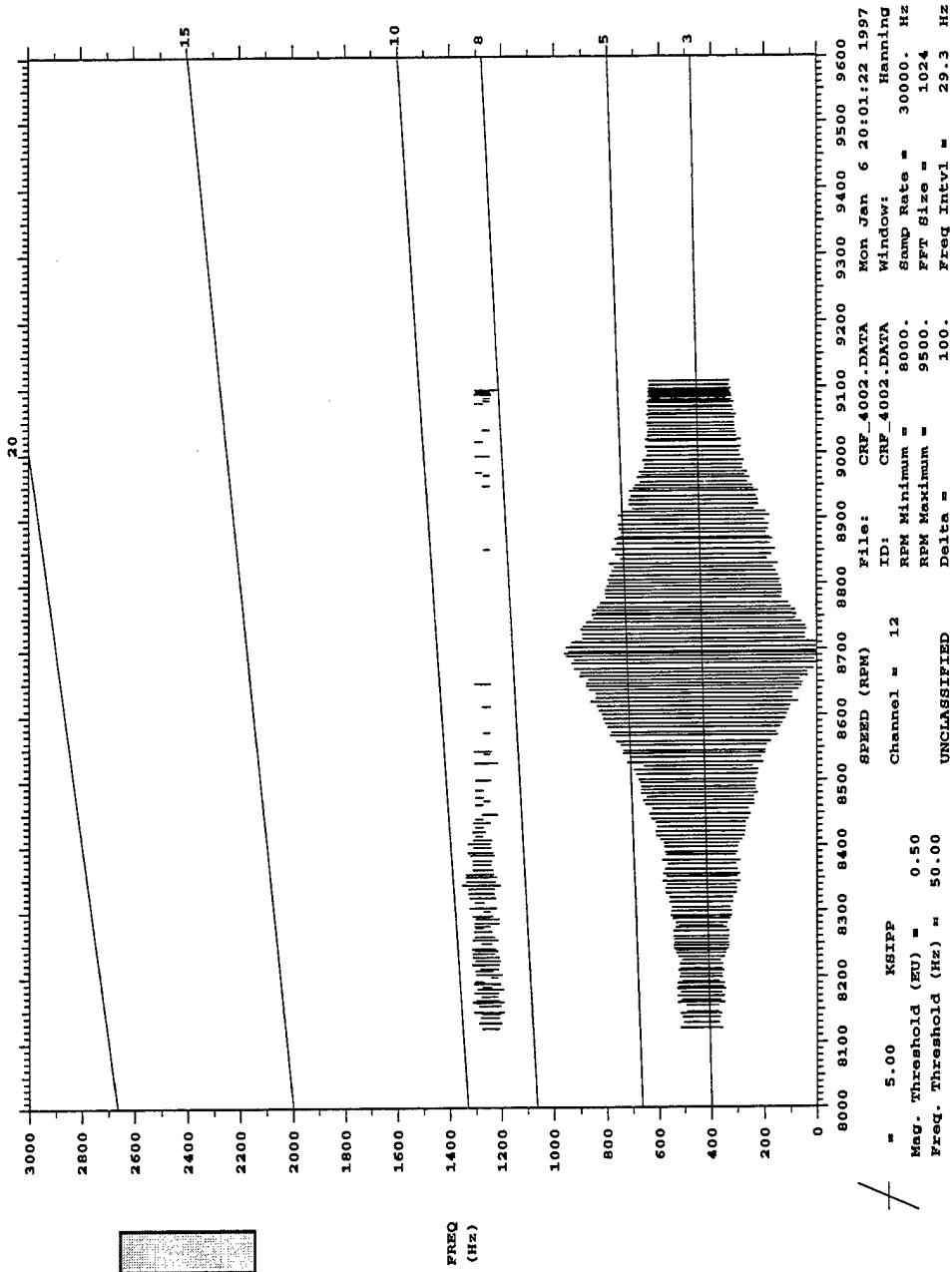


Figure C.28: Blade 12 Campbell diagram, NOL.

UNCLASSIFIED
 CRFER RUN 40, 3/Rev, NOL, No Duct, 8100-9100 rpm

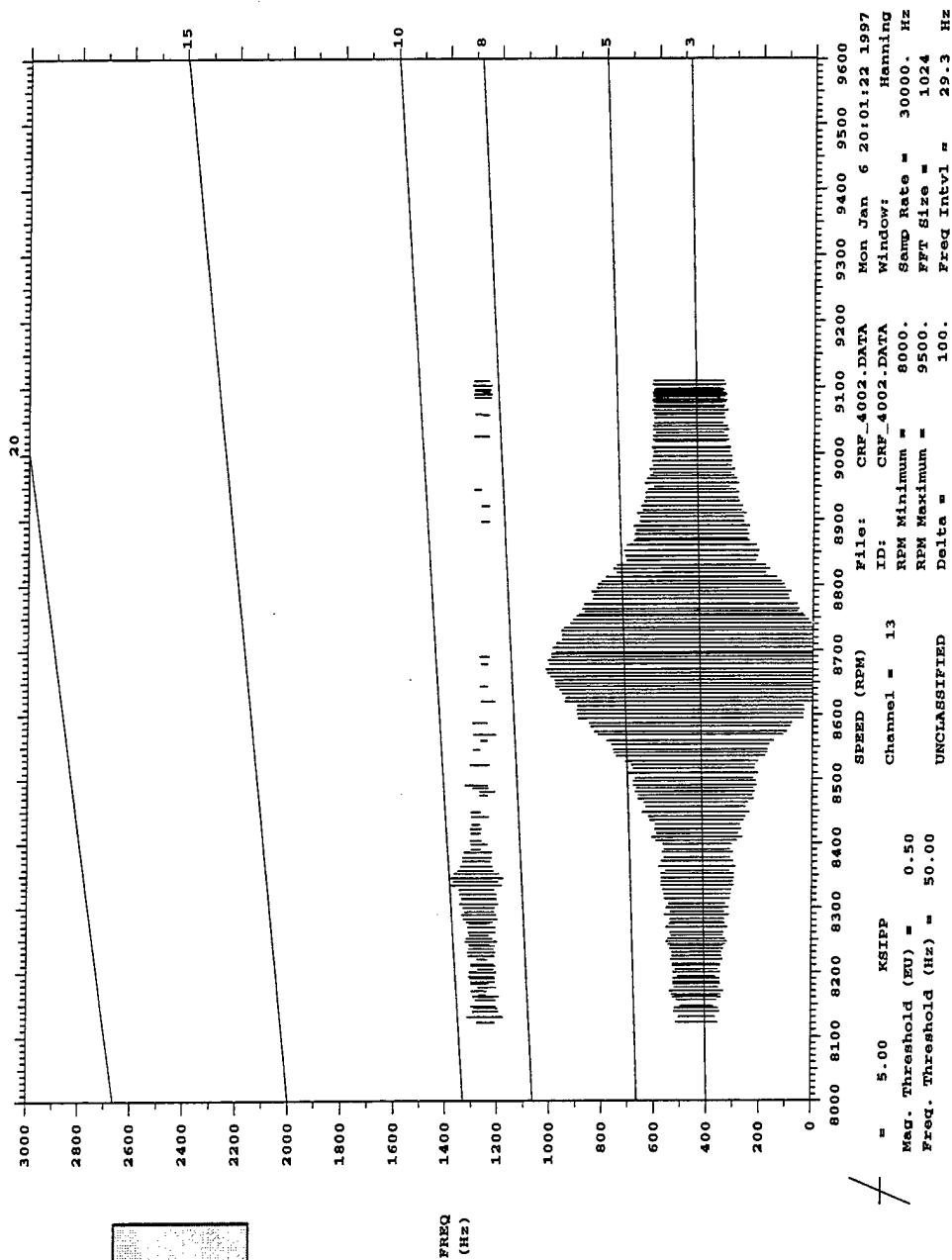


Figure C.29: Blade 13 Campbell diagram, NOL.

UNCLASSIFIED
 CRFER RUN 40, 3/rev, NOL, No Duct, 8100-9100 rpm

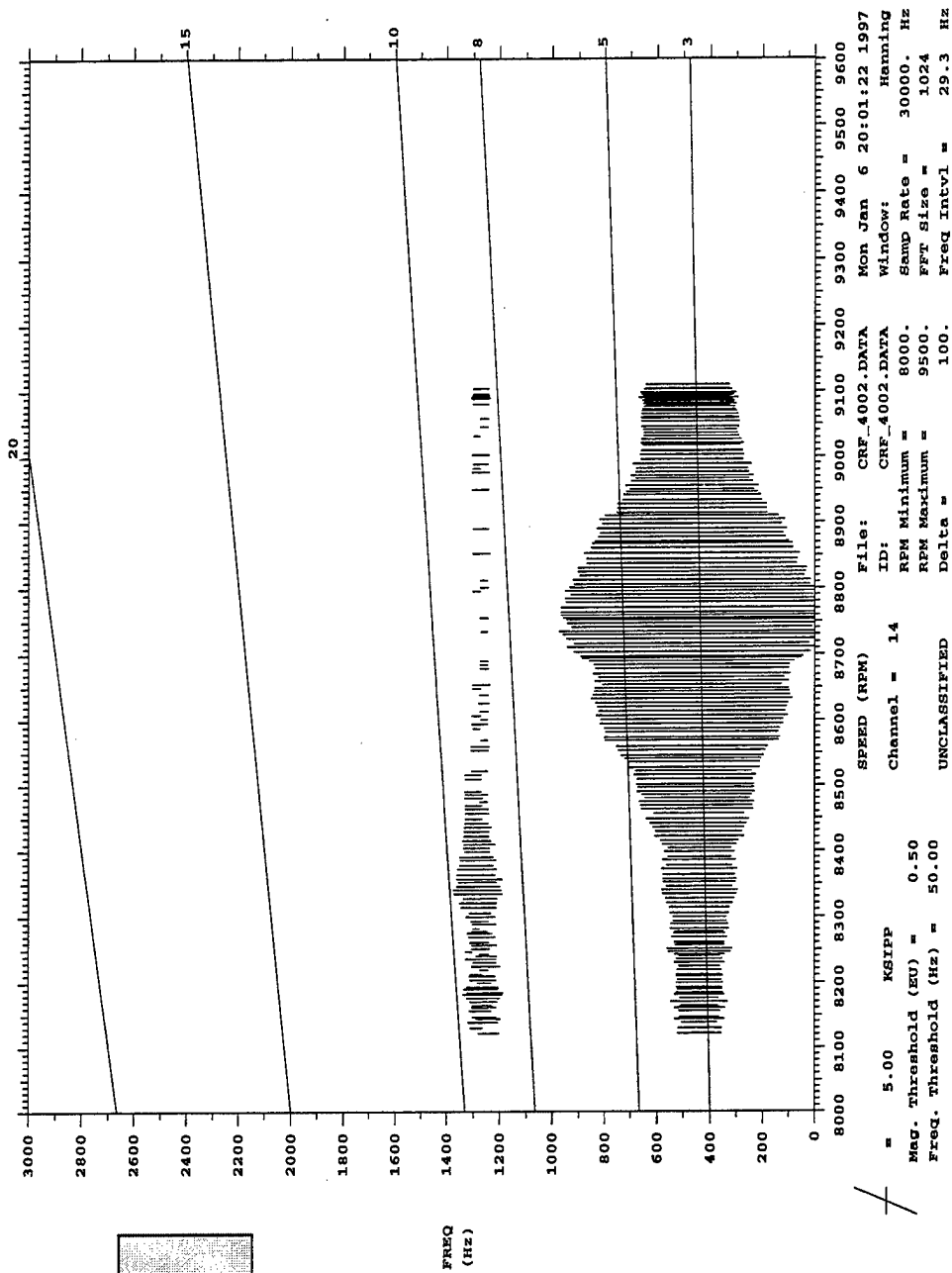


Figure C.30: Blade 14 Campbell diagram, NOL.

CRFPR RUN 40, 3/Rev, NOL, No Duct, 8100-9100 rpm

UNCLASSIFIED

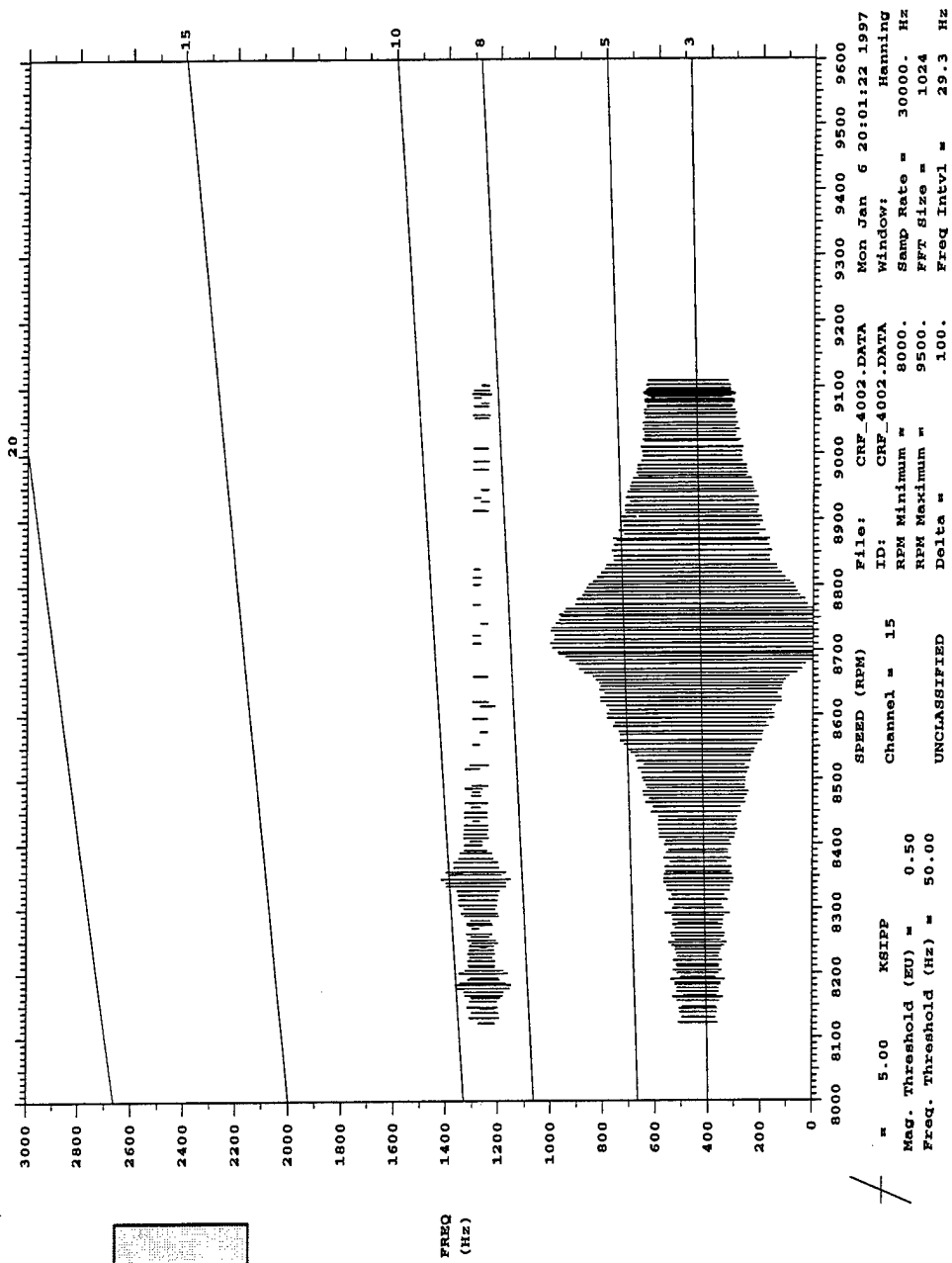


Figure C.31: Blade 15 Campbell diagram, NOL.

CRPER RUN 40, 3/Rev, NOL, No Duct, 8100-9100 RPM

UNCLASSIFIED

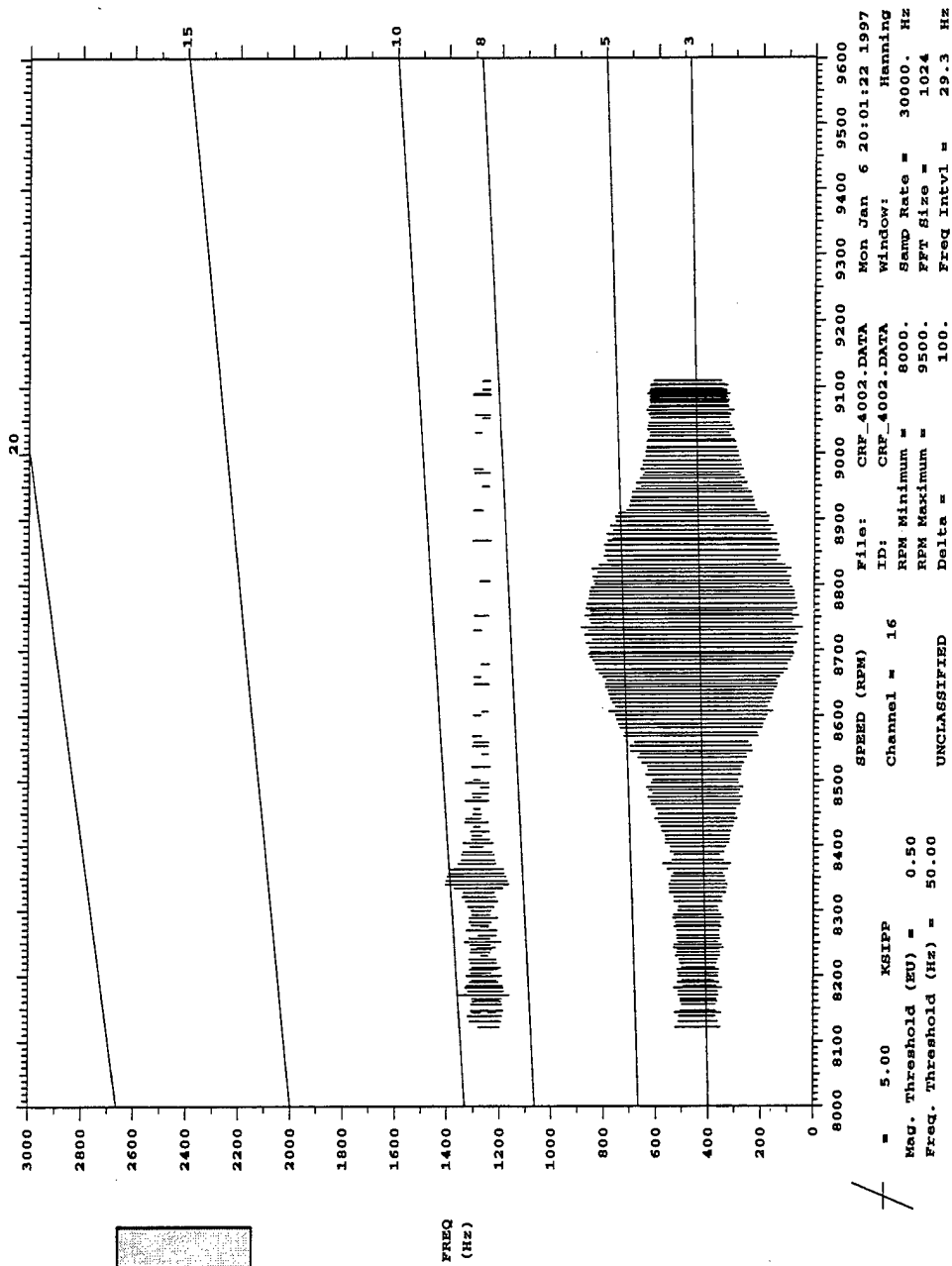


Figure C.32: Blade 16 Campbell diagram, NOL.

UNCLASSIFIED
 CRFER RUN 40, 3/Rev, PE, No Duct, 8100-9100 RPM

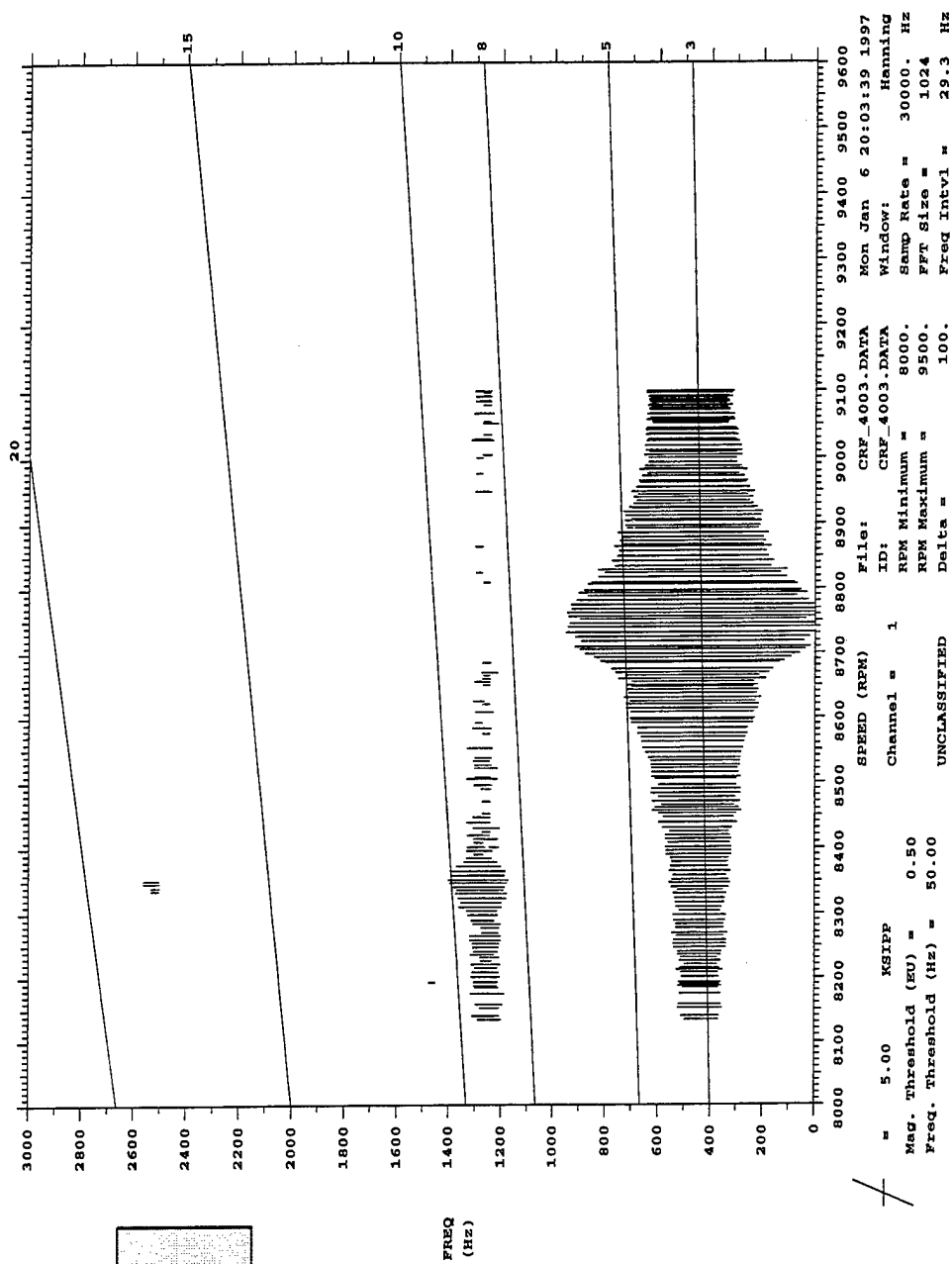


Figure C.33: Blade 1 Campbell diagram, PE.

CRPR RUN 40, 3/Rev, PE, No Duct, 8100-9100 rpm

UNCLASSIFIED

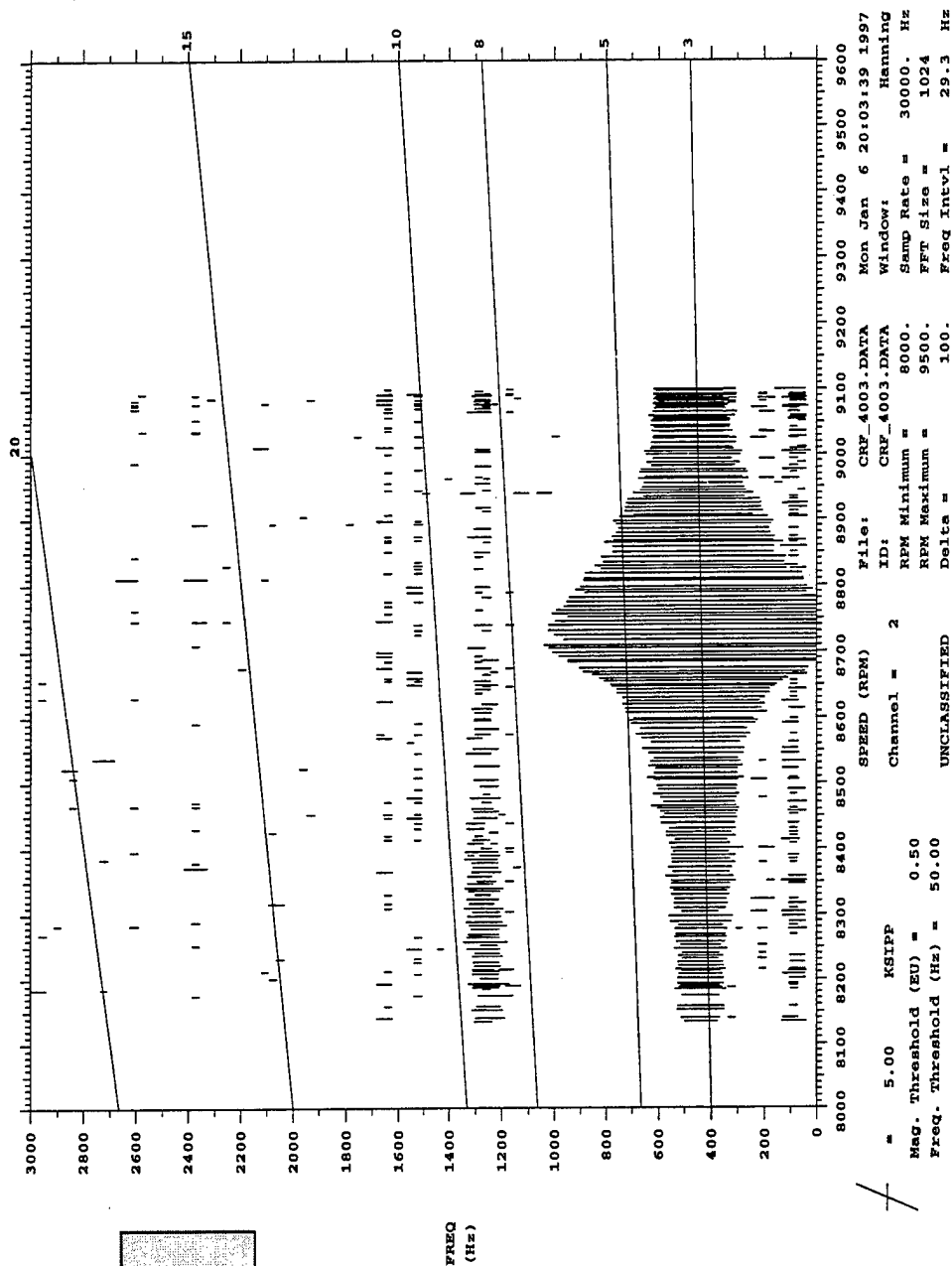


Figure C.34: Blade 2 Campbell diagram, PE.

CRFER RUN 40, 3/Rev, PE, No Duct, 8100-9100 RPM

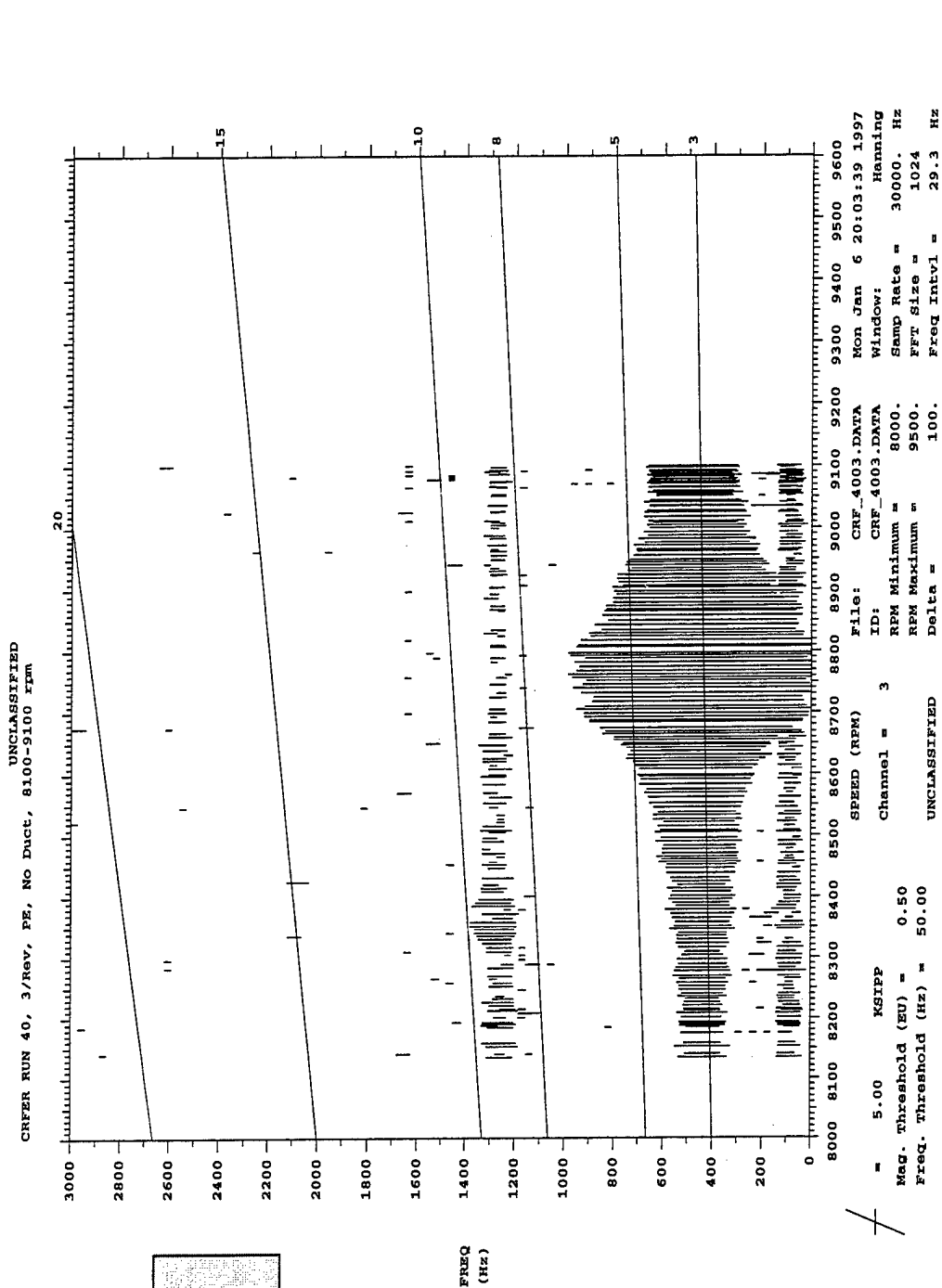


Figure C.35: Blade 3 Campbell diagram, PE.

UNCLASSIFIED
 CREER RUN 40, 3/Rev, PE, No Duct, 8100-9100 RPM

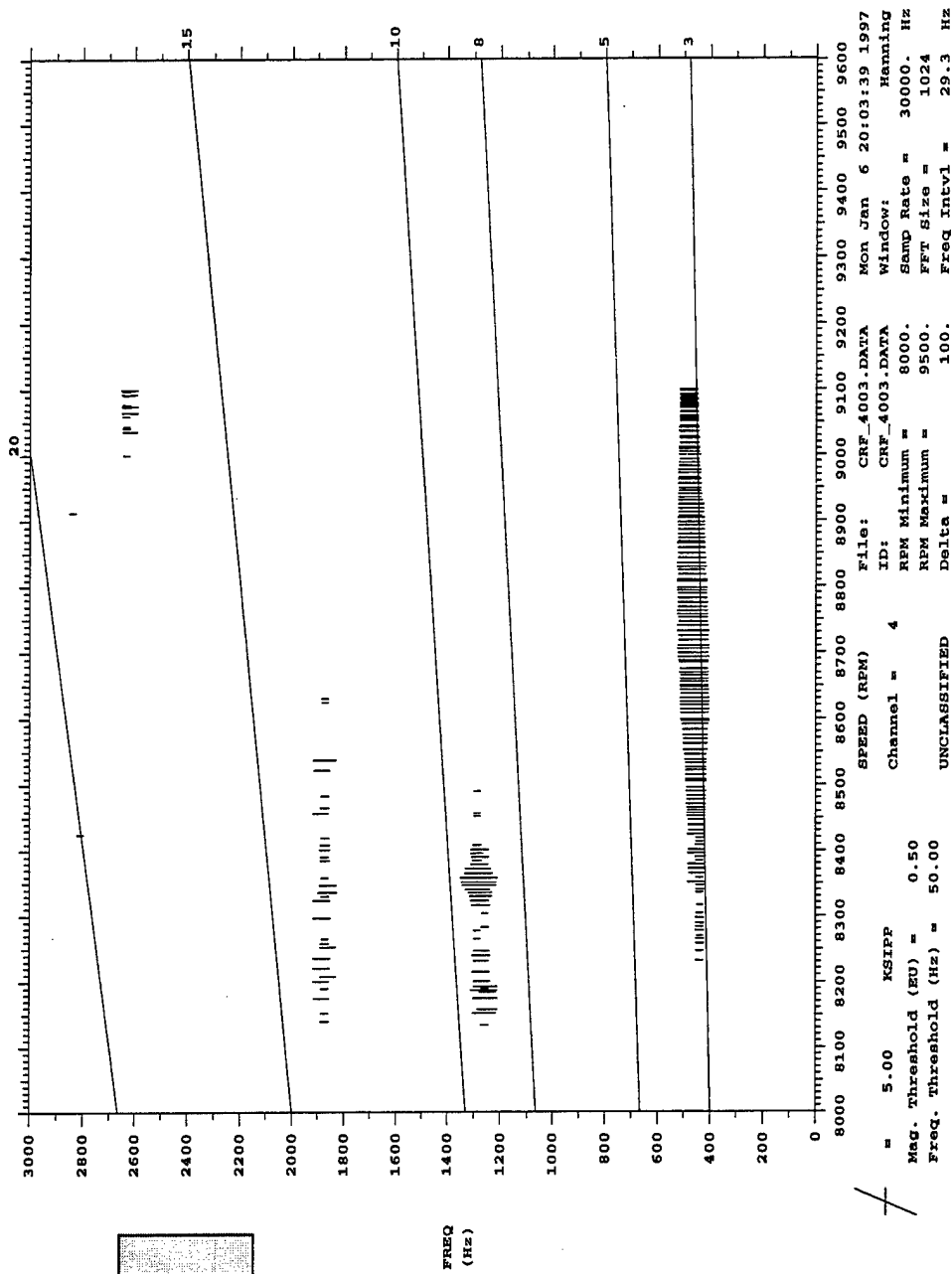


Figure C.36: Blade 4 Campbell diagram, PE.

CRFER RUN 40, 3/Rev, PE, NO Duct, 8100-9100 RPM

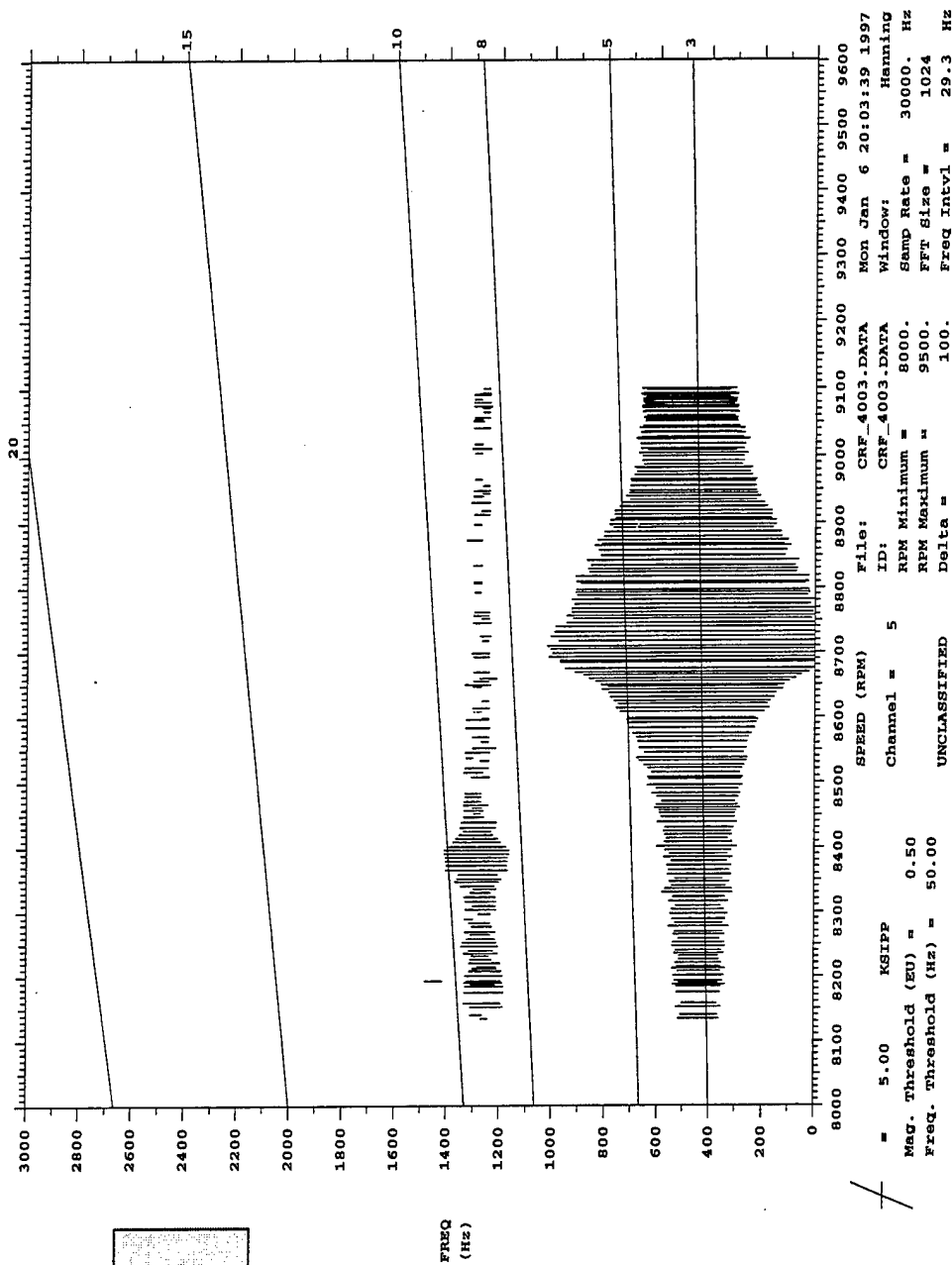


Figure C.37: Blade 5 Campbell diagram, PE.

CRFER RUN 40, 3/Rev, PE, No Duct, 8100-9100 rpm

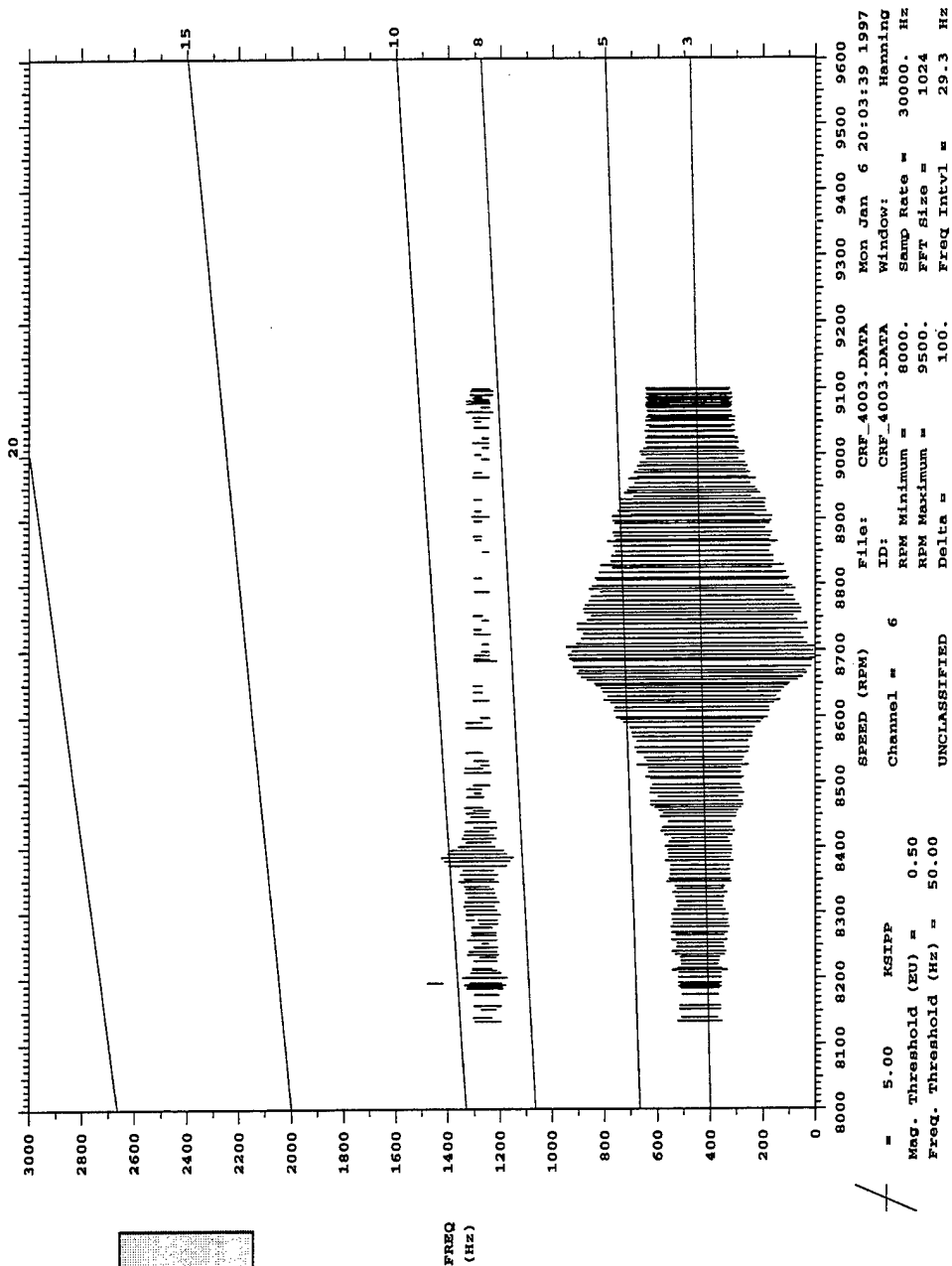


Figure C.38: Blade 6 Campbell diagram, PE.

UNCLASSIFIED
 CREPER RUN 40, 3/Rev, PE, No Duct, 8100-9100 RPM

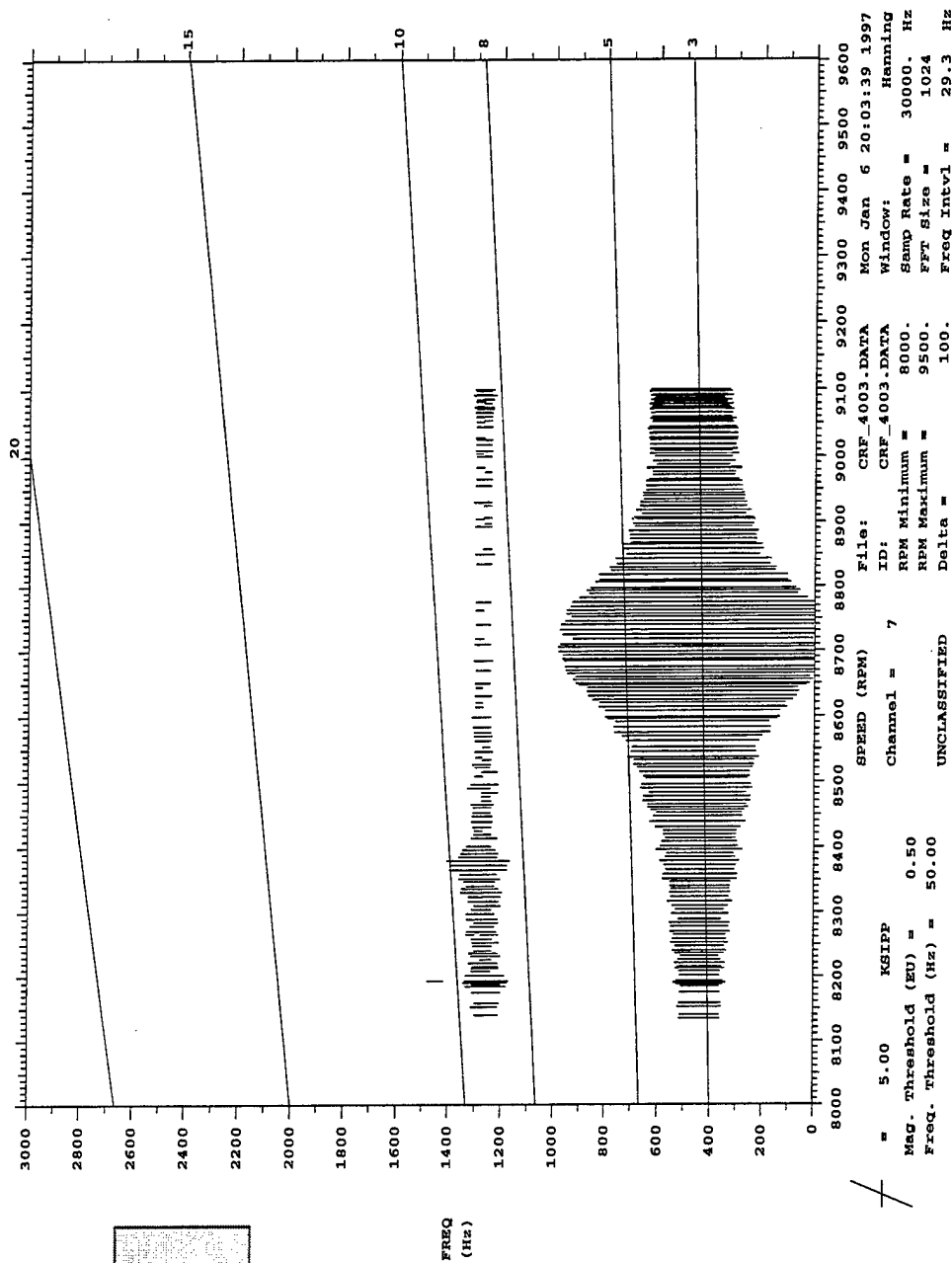


Figure C.39: Blade 7 Campbell diagram, PE.

UNCLASSIFIED
 CRFER NUN 40, 3/Rev, PE, No Duct, 8100-9100 RPM

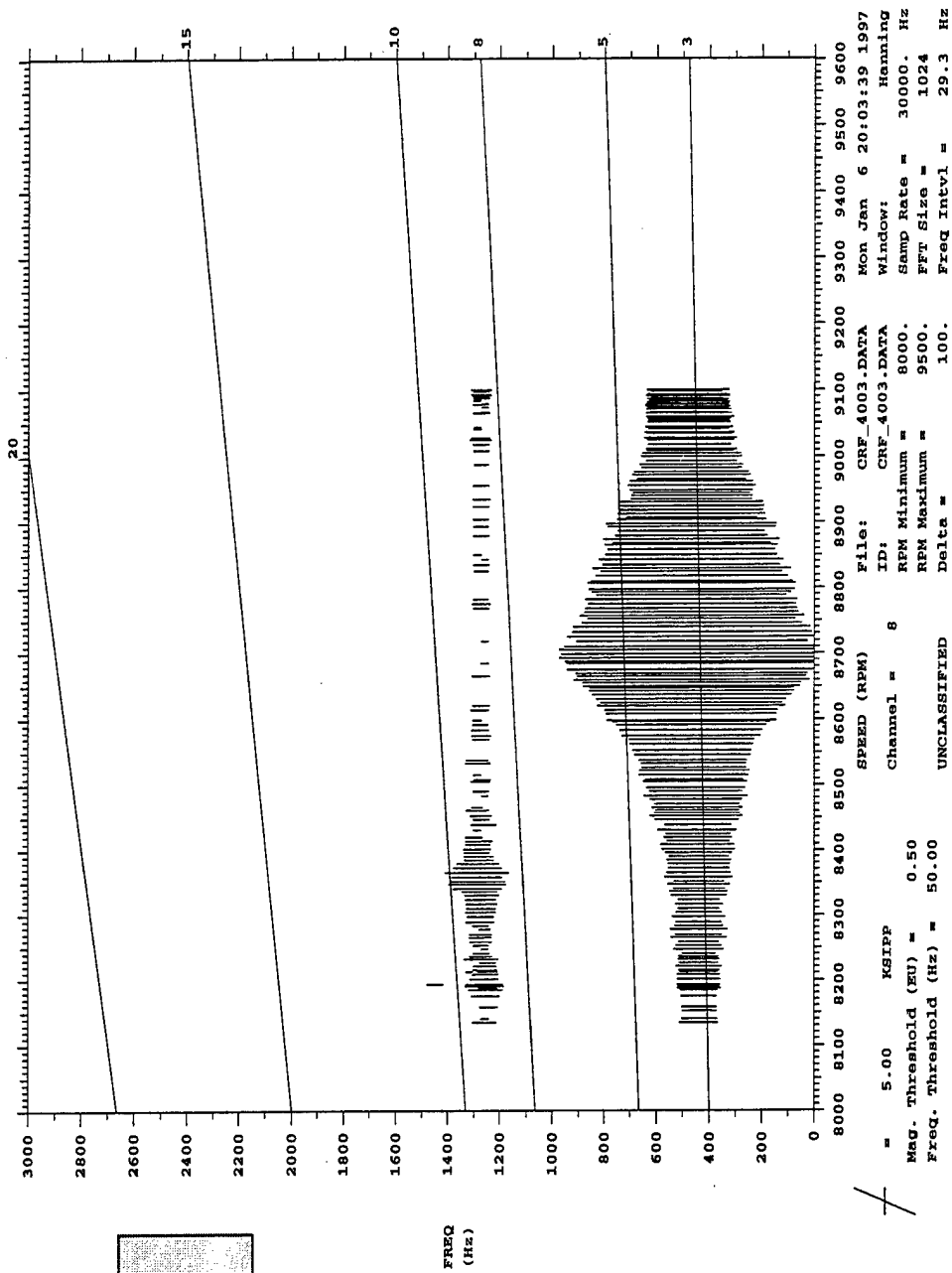


Figure C.40: Blade 8 Campbell diagram, PE.

CRFR RUN 40, 3/Rev, PE, No Duct, 8100-9100 RPM

UNCLASSIFIED

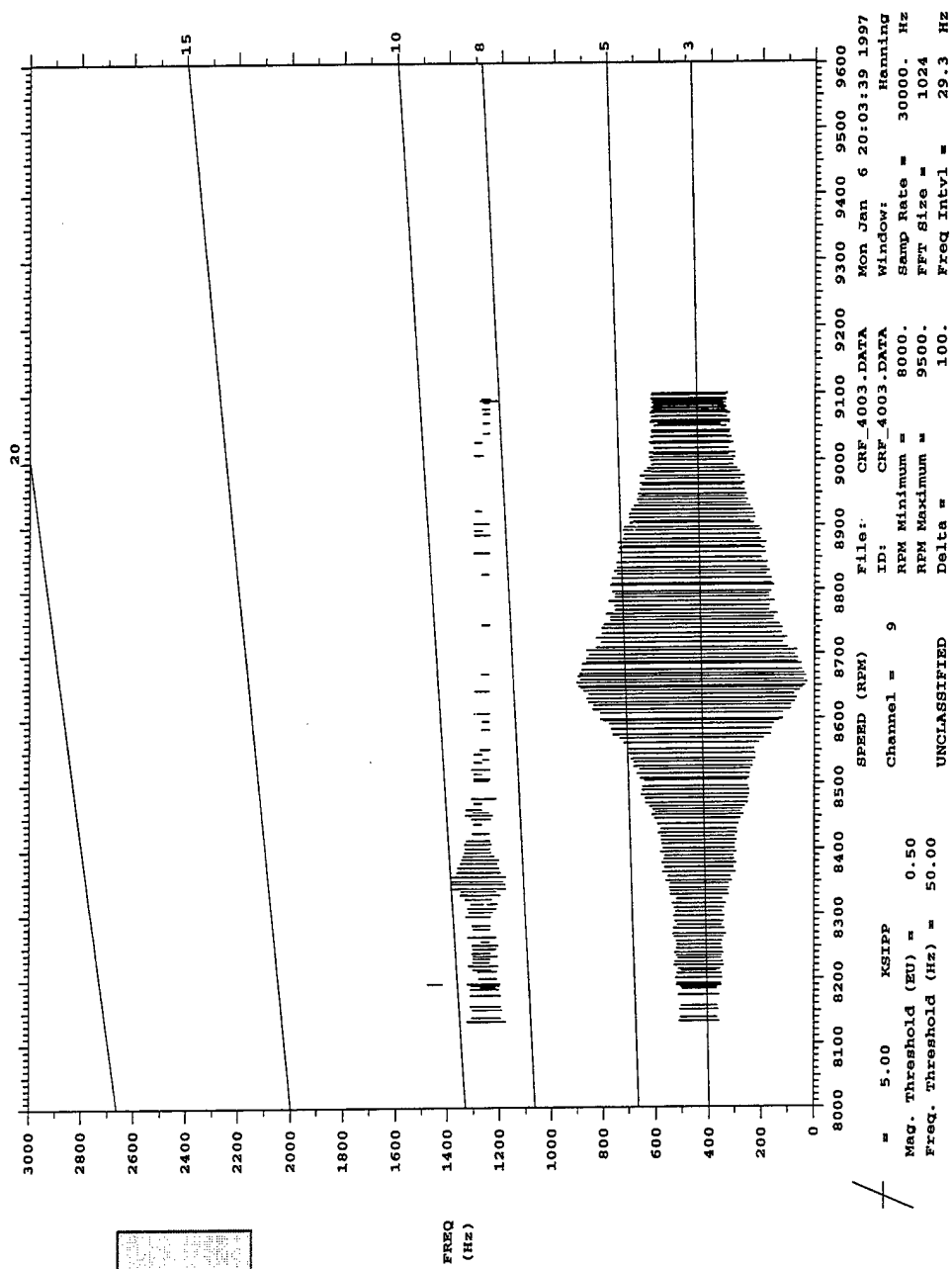


Figure C.41: Blade 9 Campbell diagram, PE.

UNCLASSIFIED
 CREPER RUN 40, 3/Rev, PE, No Duct, 8100-9100 RPM

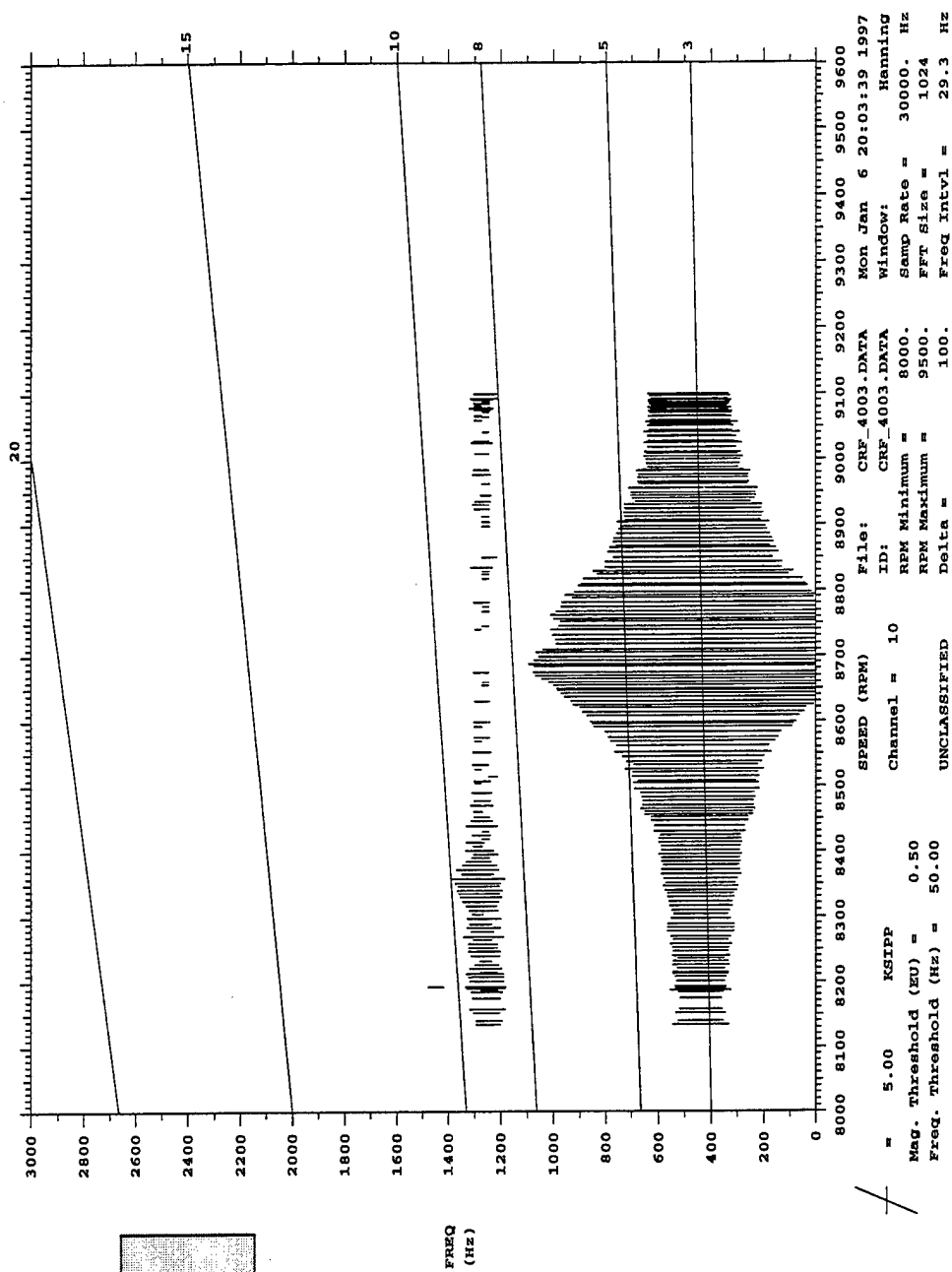


Figure C.42: Blade 10 Campbell diagram, PE.

CRFER RUN 40, 3/Rev, PE, No Duct, 8100-9100 RPM

UNCLASSIFIED

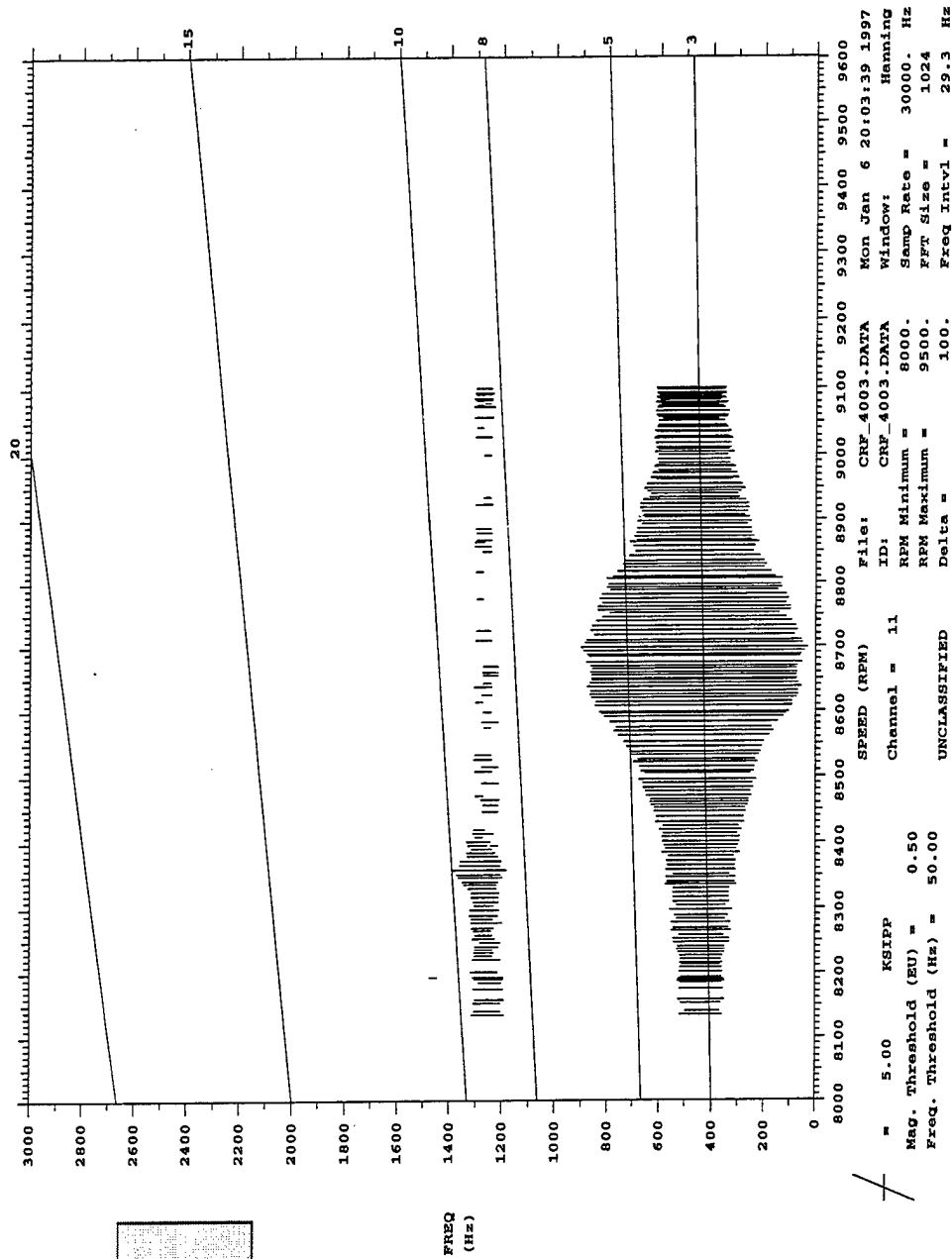


Figure C.43: Blade 11 Campbell diagram, PE.

UNCLASSIFIED
 CREER RUN 40, 3/Rev, PE, No Duct, 8100-9100 rpm

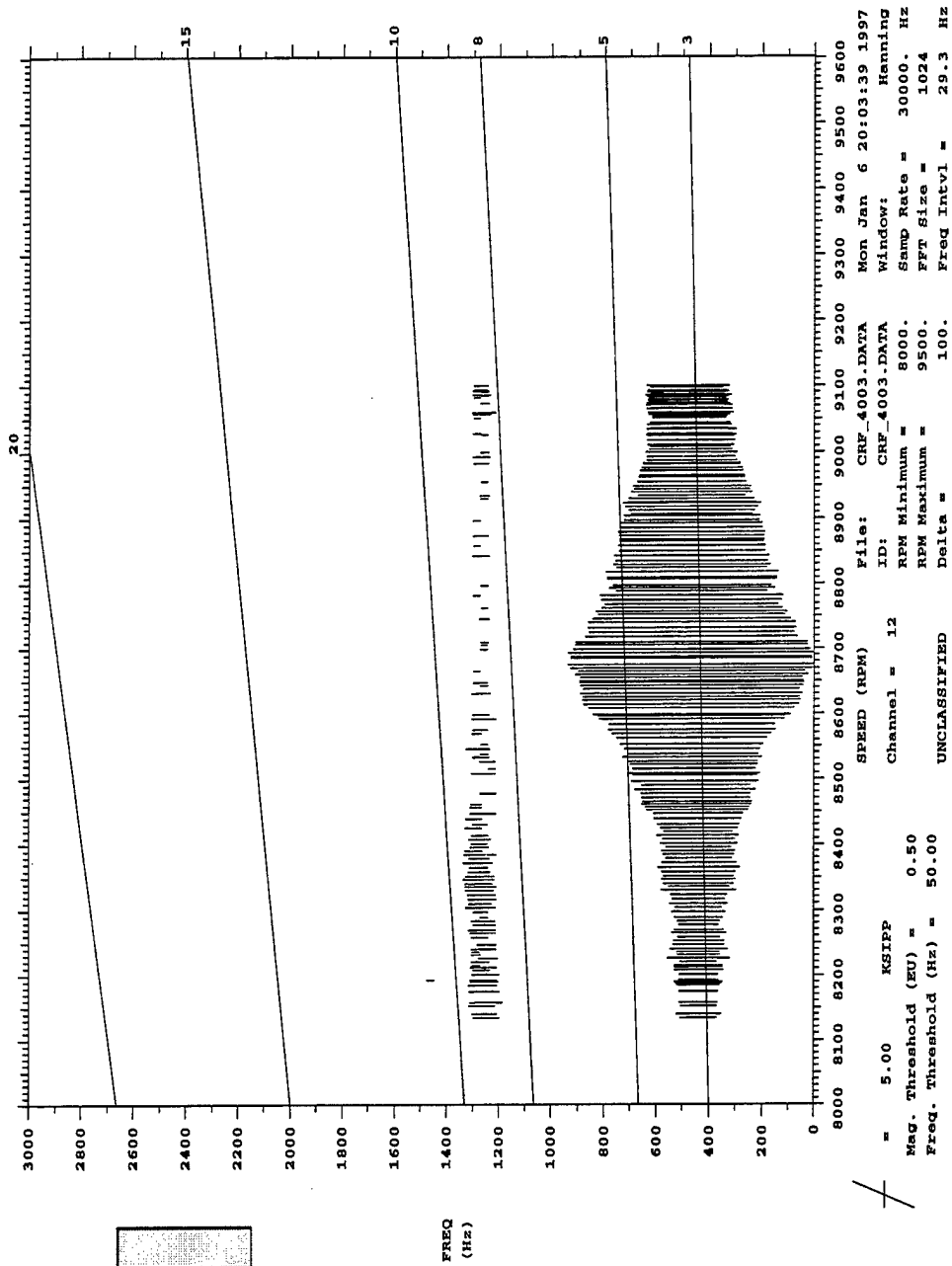


Figure C.44: Blade 12 Campbell diagram, PE.

CREFR RUN 40, 3/rev, PE, No Duct, 8100-9100 rpm

UNCLASSIFIED

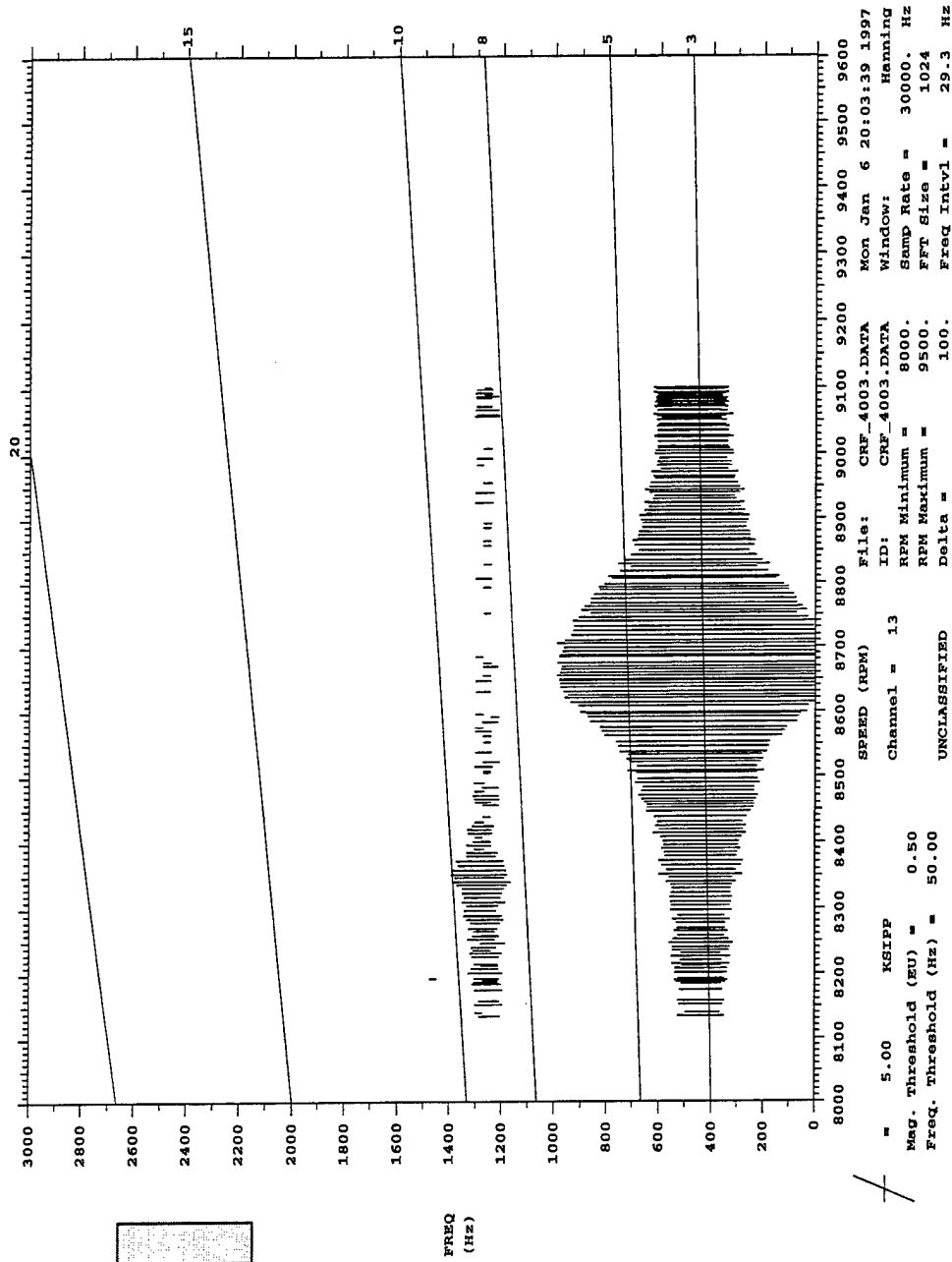


Figure C.45: Blade 13 Campbell diagram, PE.

UNCLASSIFIED
 CRFER RUN 40, 3/Rev, PE, No Duct, 8100-9100 rpm

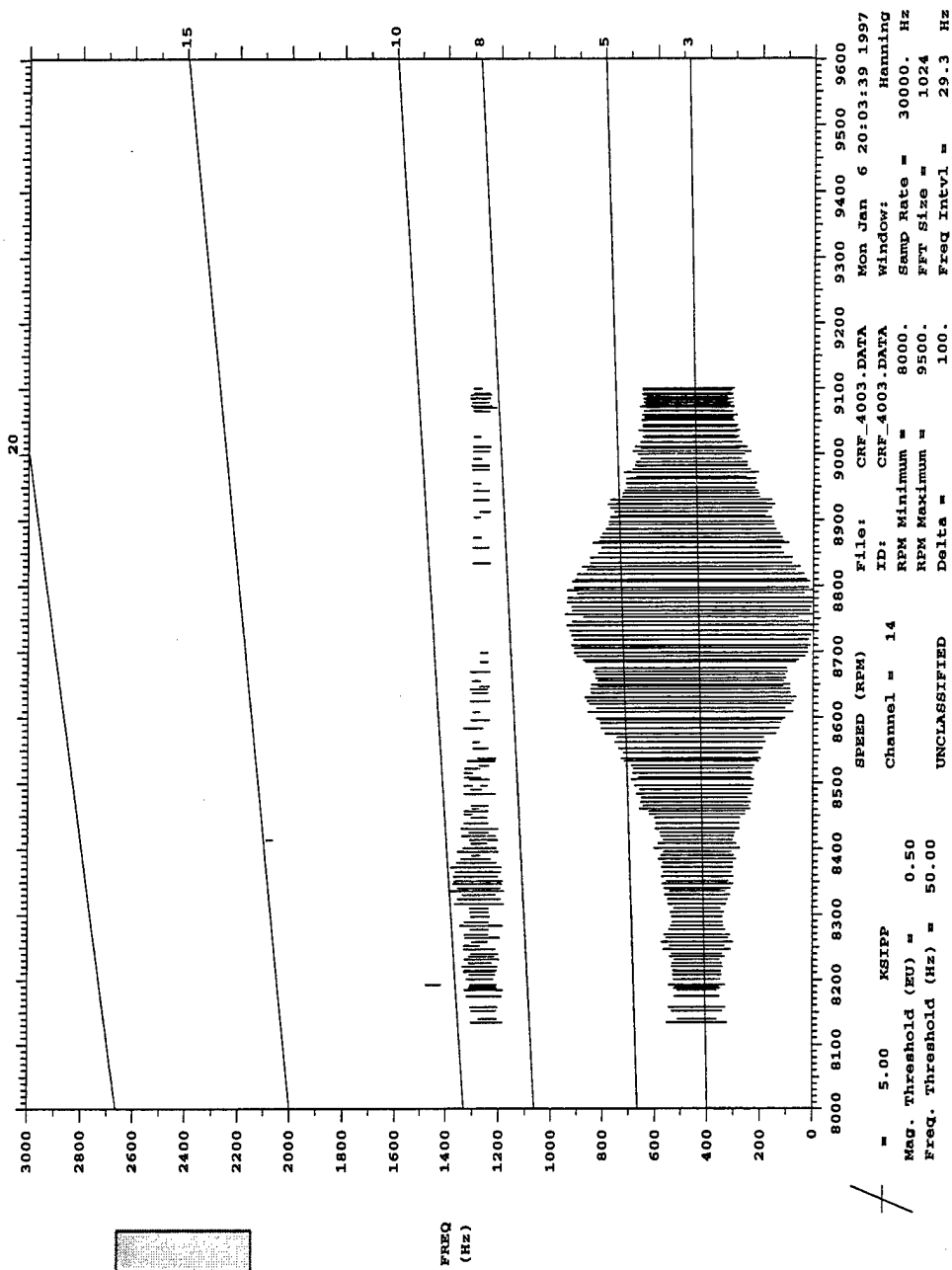


Figure C.46: Blade 14 Campbell diagram, PE.

CREER RUN 40, 3/Rev, PE, No Duct, 8100-9100 RPM

UNCLASSIFIED

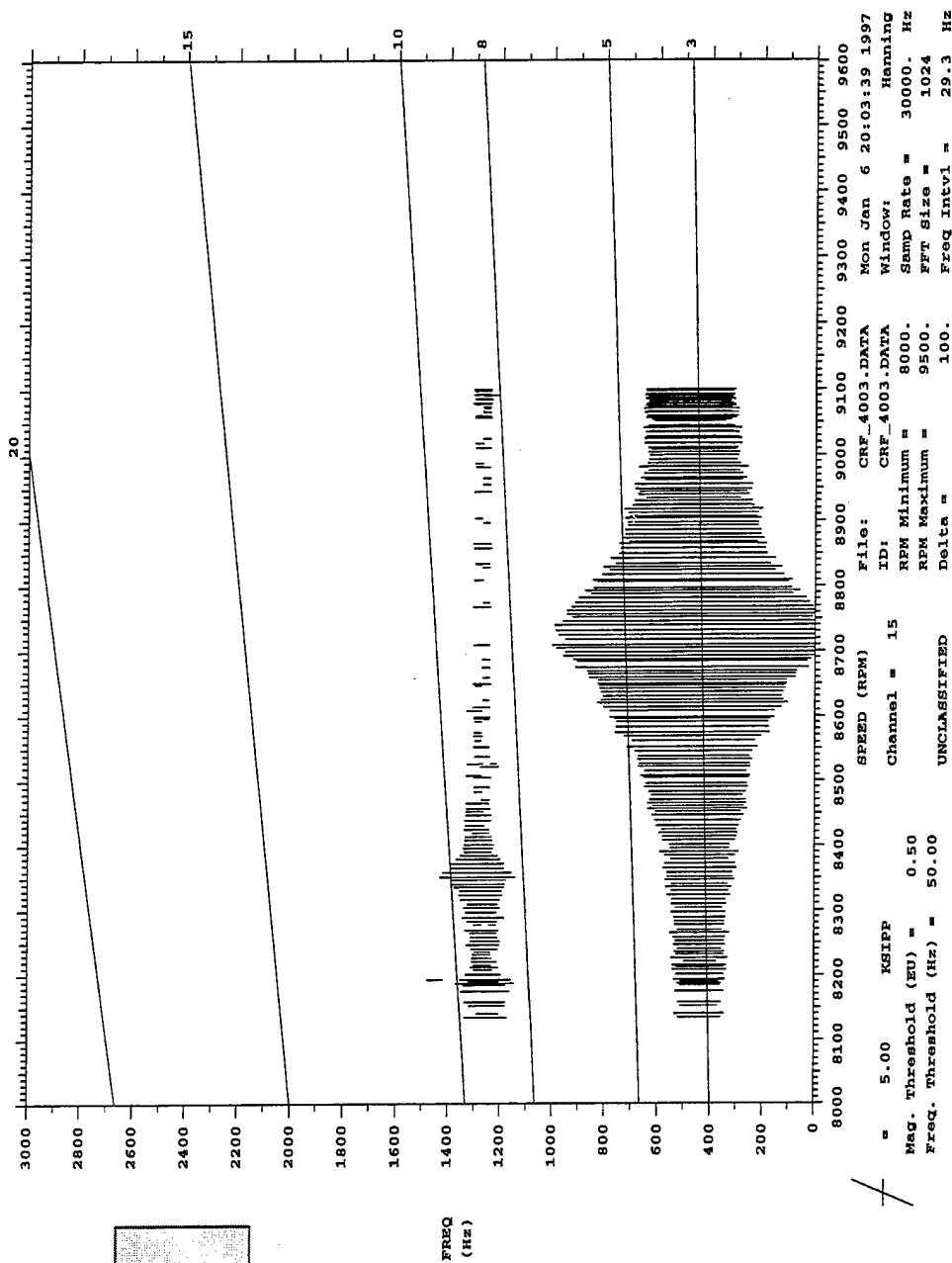


Figure C.47: Blade 15 Campbell diagram, PE.

UNCLASSIFIED
 CREER RUN 40, 3/Rev, PE, No Duct, 8100-9100 RPM

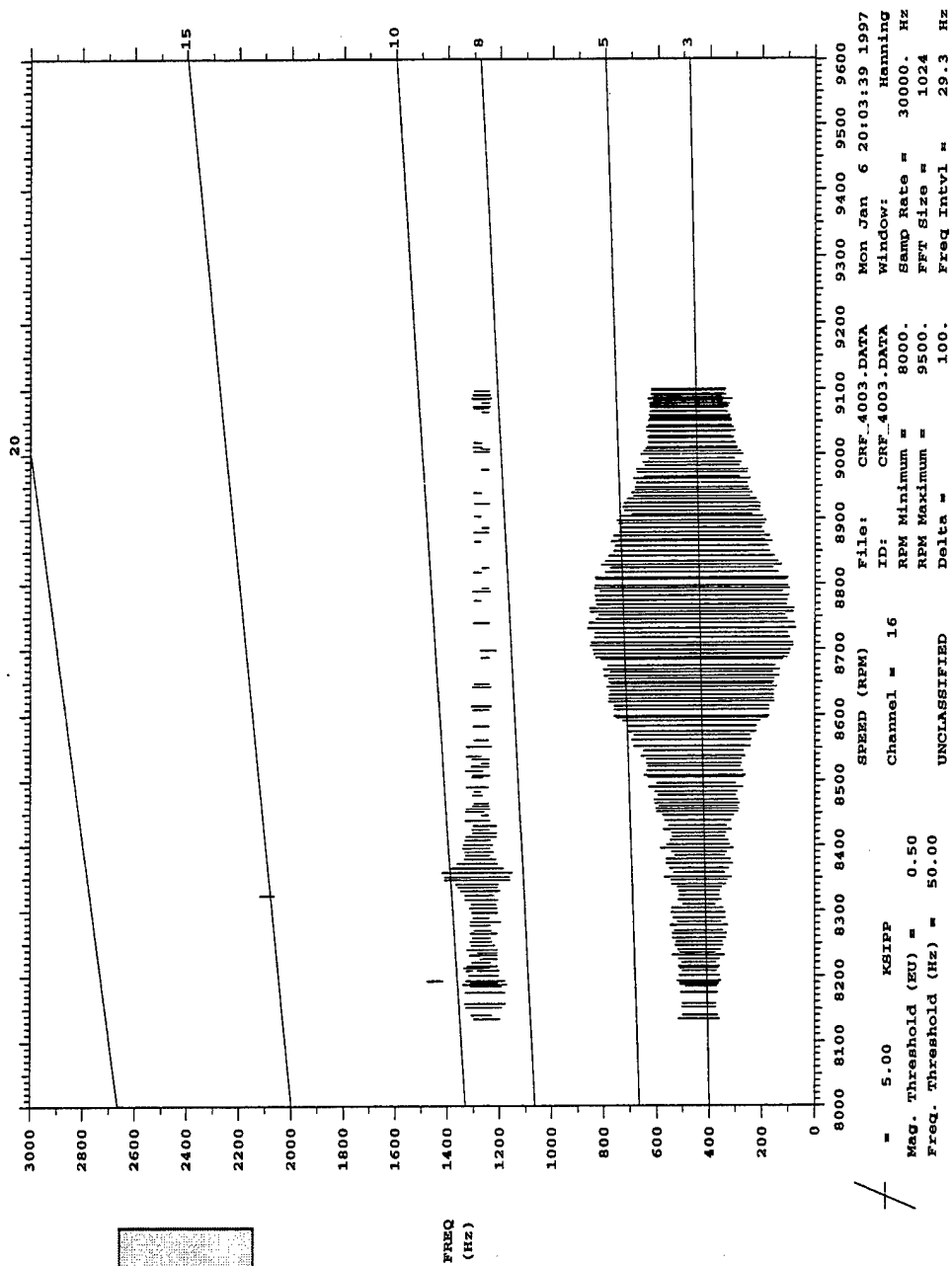


Figure C.48: Blade 16 Campbell diagram, PE.

UNCLASSIFIED
 CREER RUN 40, 3/Rev, NS, No Duct, 8100-9100 rpm

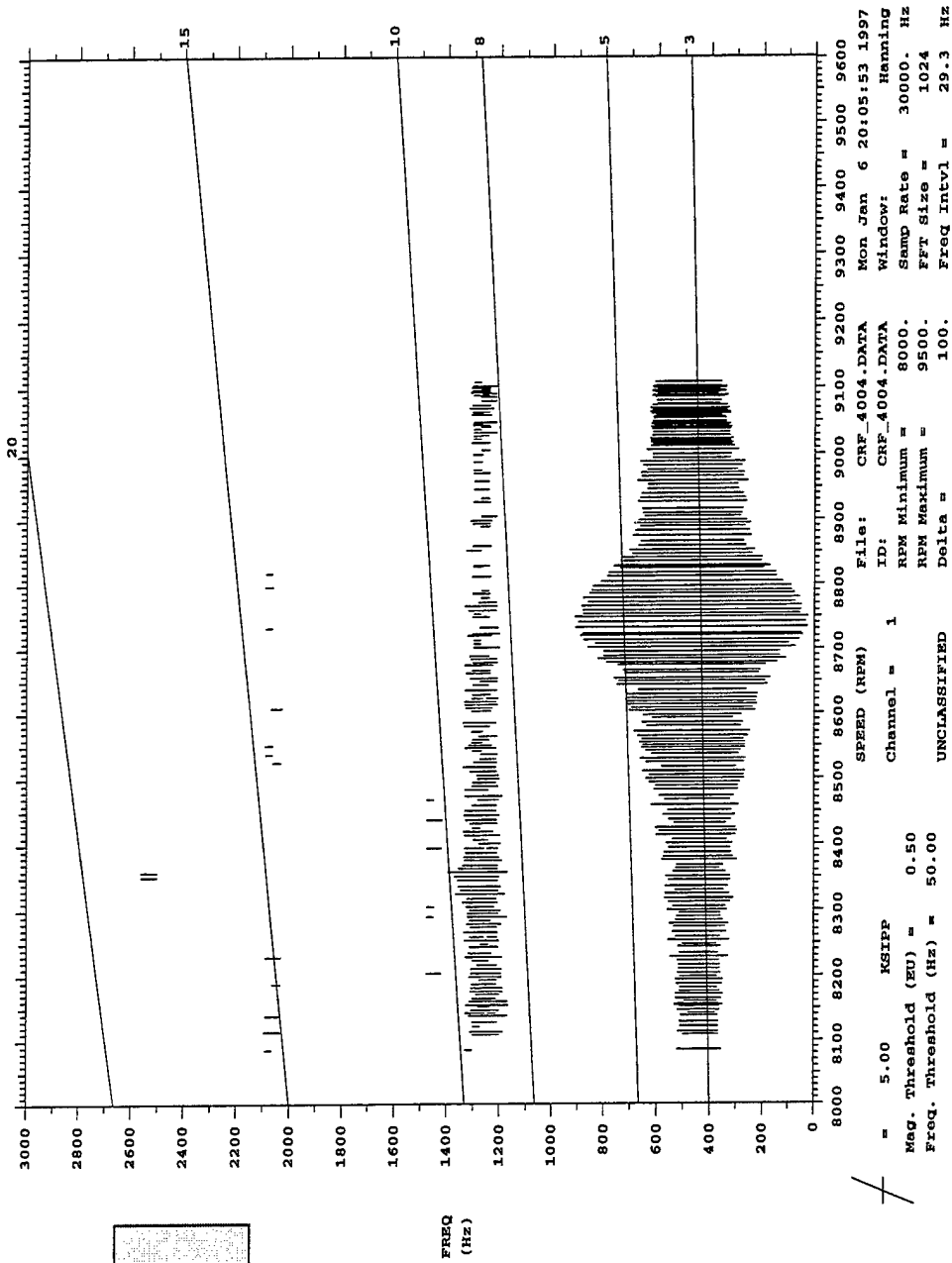


Figure C.49: Blade 1 Campbell diagram, NS.

CREPER RUN 40, 3/rev, NS, No Duct, 8100-9100 xpm

UNCLASSIFIED

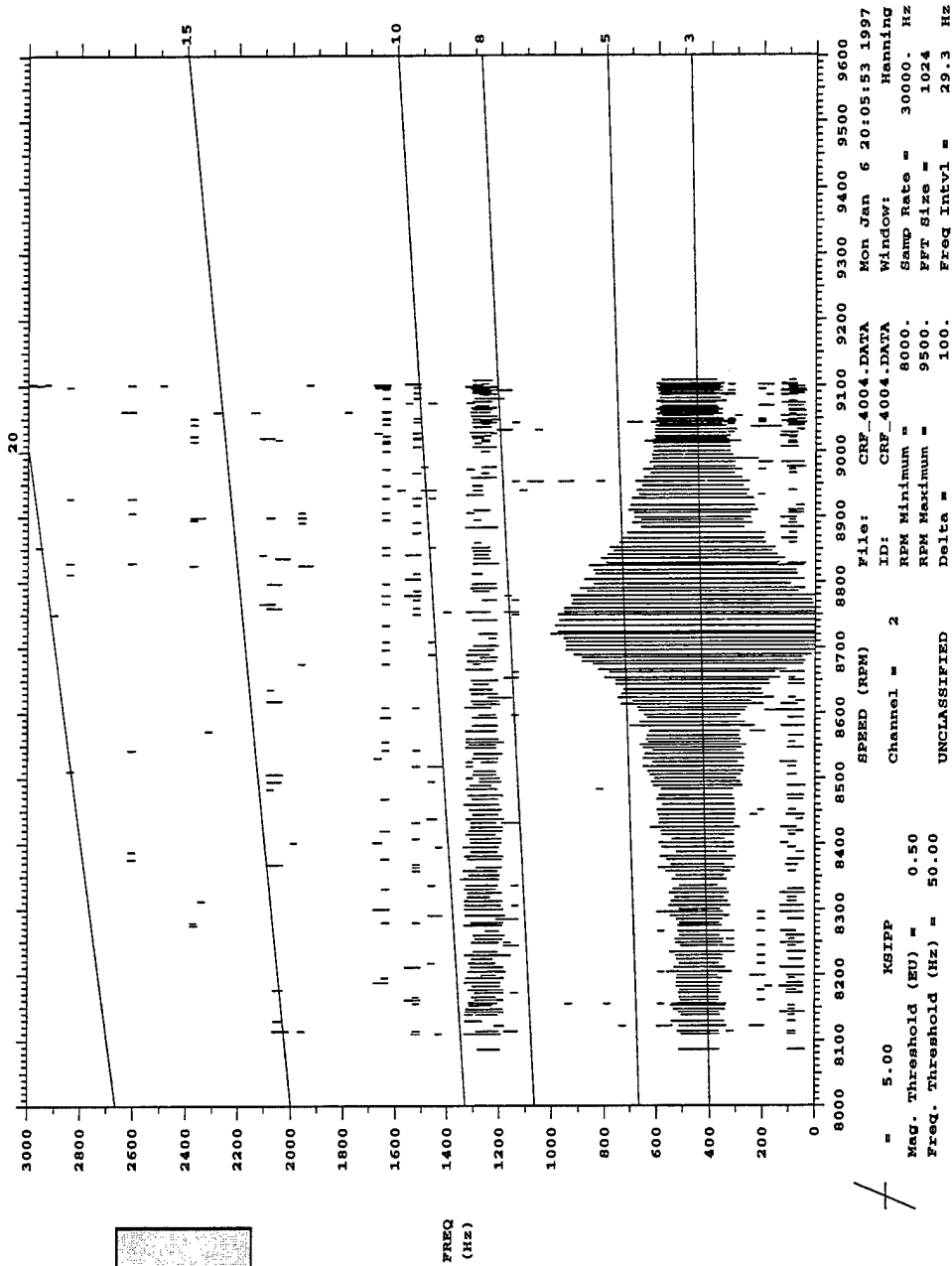


Figure C.50: Blade 2 Campbell diagram, NS.

UNCLASSIFIED
CRFR RUN 40, 3/Rev, NS, No Duct, 8100-9100 RPM

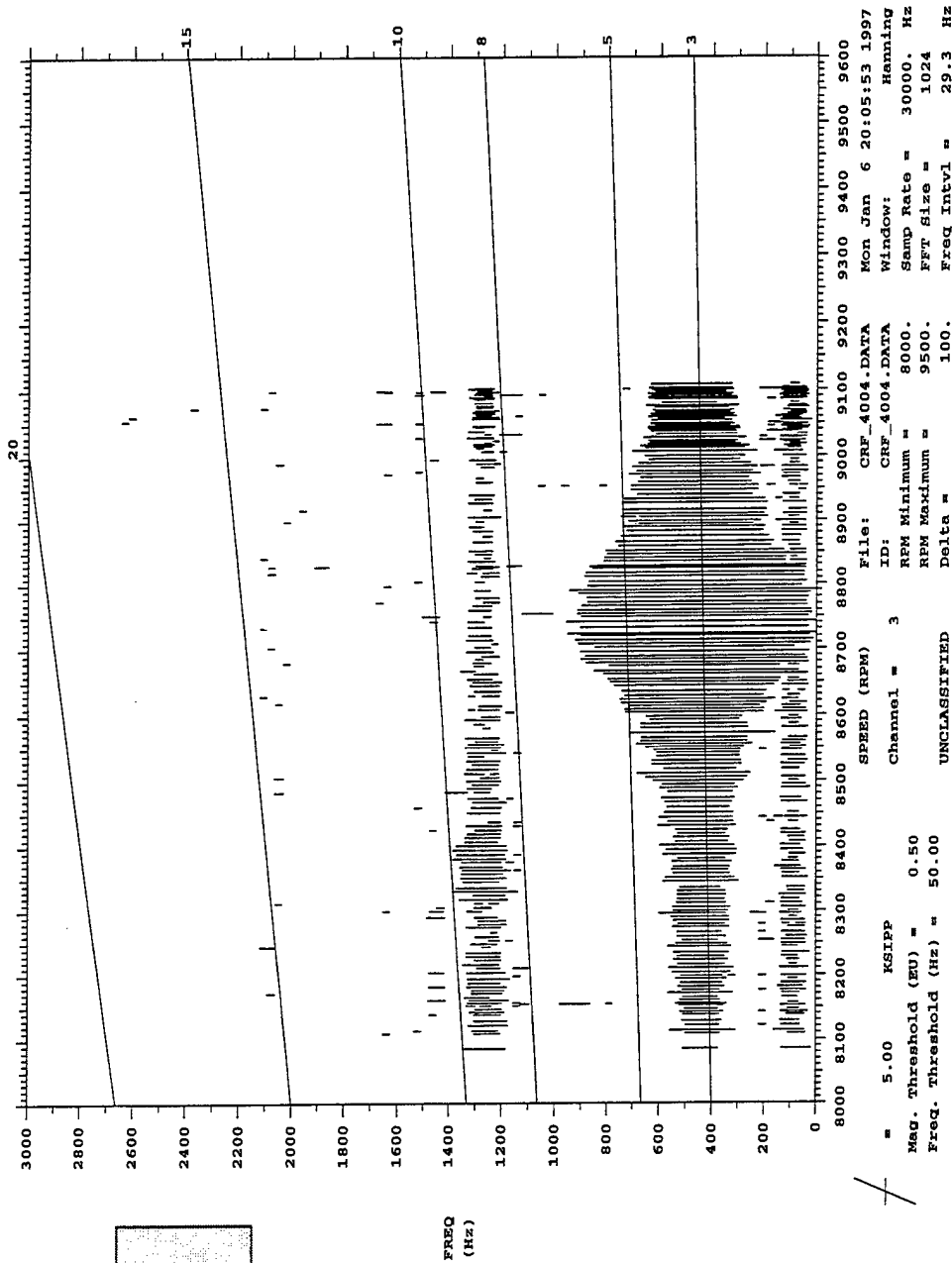


Figure C.51: Blade 3 Campbell diagram, NS.

CRFER RUN 40, 3/rev, NS, NO Duct, 8100-9100 RPM

UNCLASSIFIED

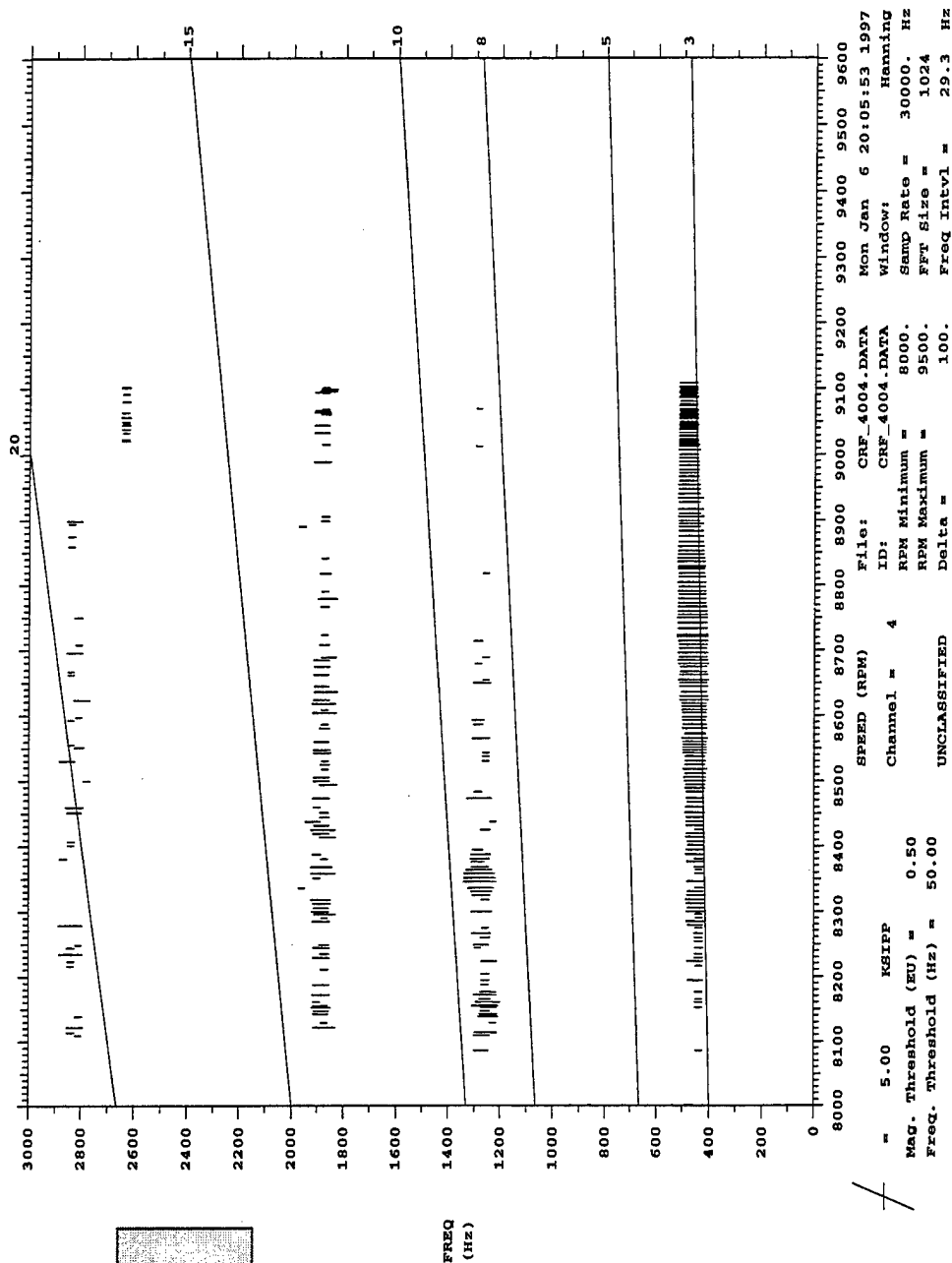


Figure C.52: Blade 4 Campbell diagram, NS.

UNCLASSIFIED
CRFR RUN 40, 3/Rev, NS, No Duct, 8100-9100 rpm

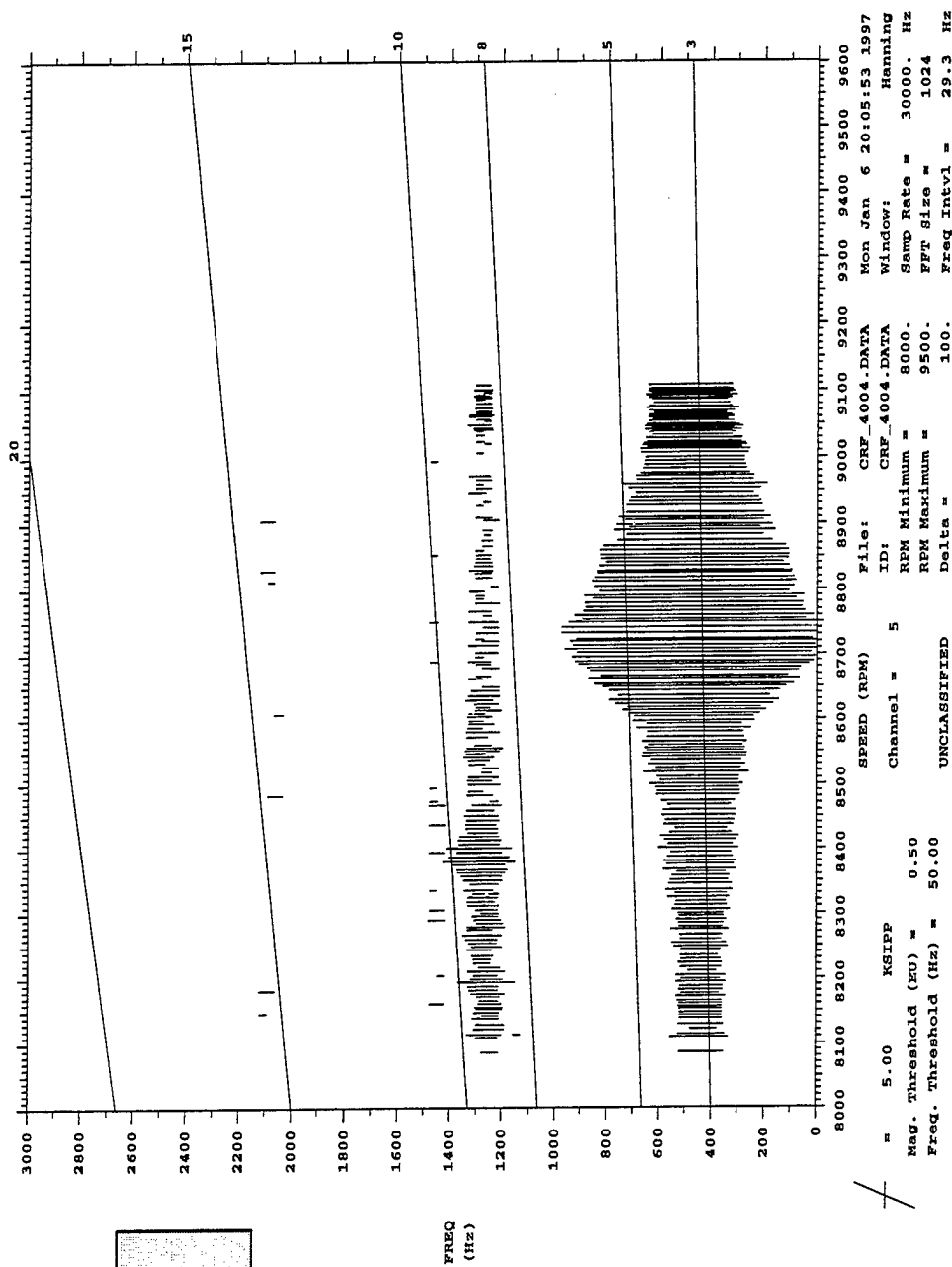


Figure C.53: Blade 5 Campbell diagram, NS.

UNCLASSIFIED
 CREER RUN 40, 3/rev, NS, No Duct, 8100-9100 rpm

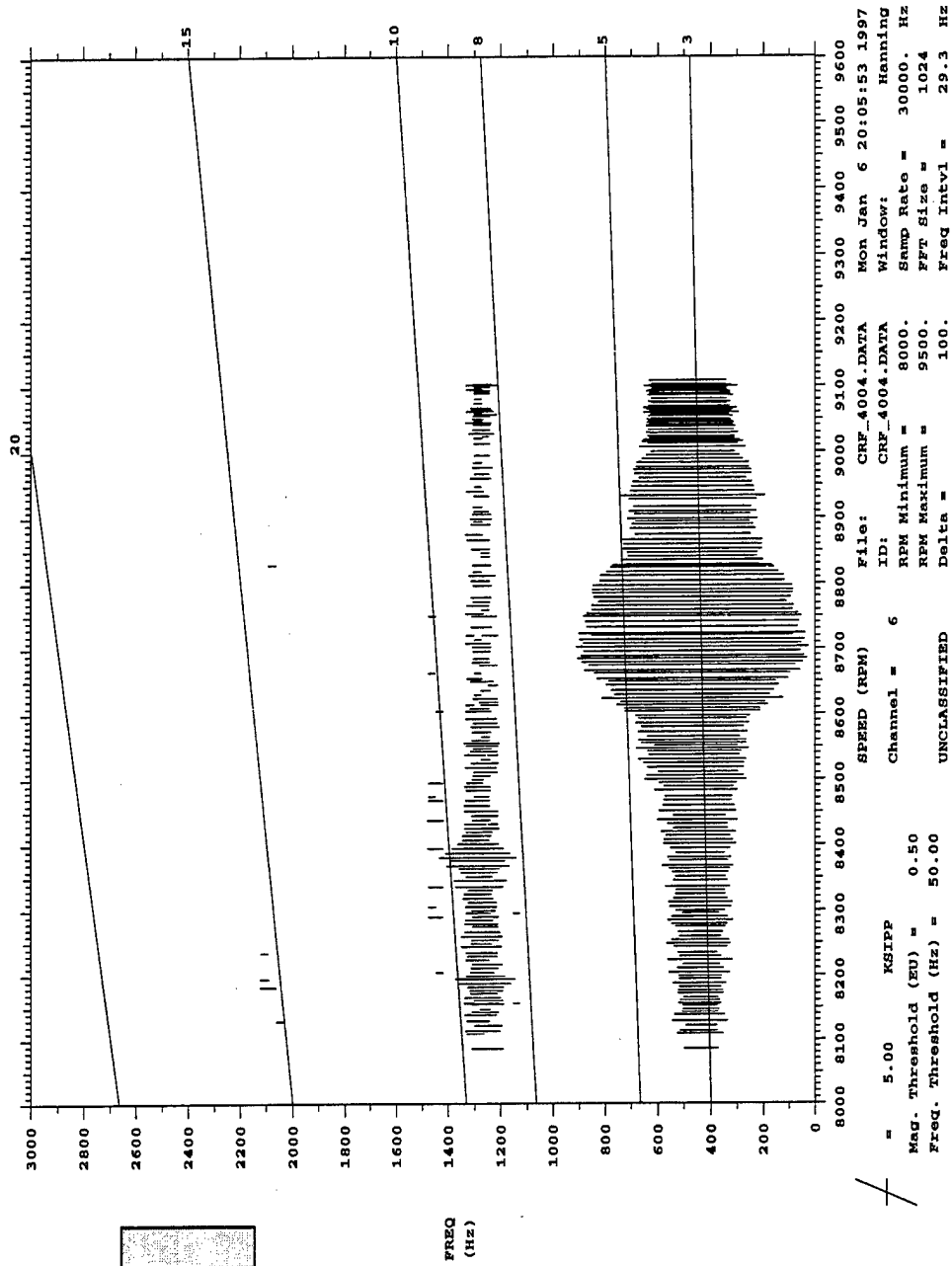


Figure C.54: Blade 6 Campbell diagram, NS.

UNCLASSIFIED
CRFR RUN 40, 3/rev, NS, No Duct, 8100-9100 RPM

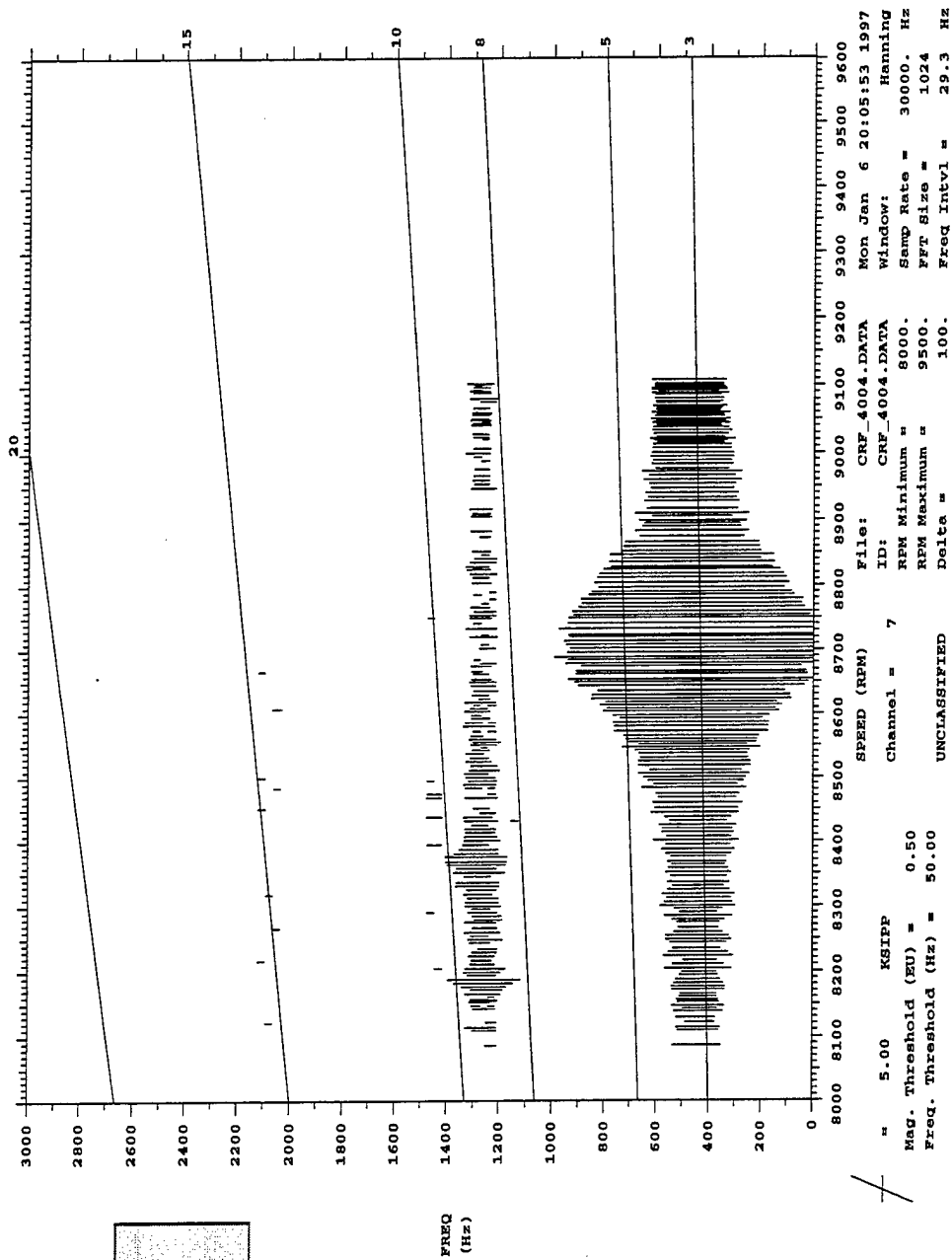


Figure C.55: Blade 7 Campbell diagram, NS.

CFRER RUN 40, 3/rev, NS, NO Duct, 8100-9100 rpm

UNCLASSIFIED

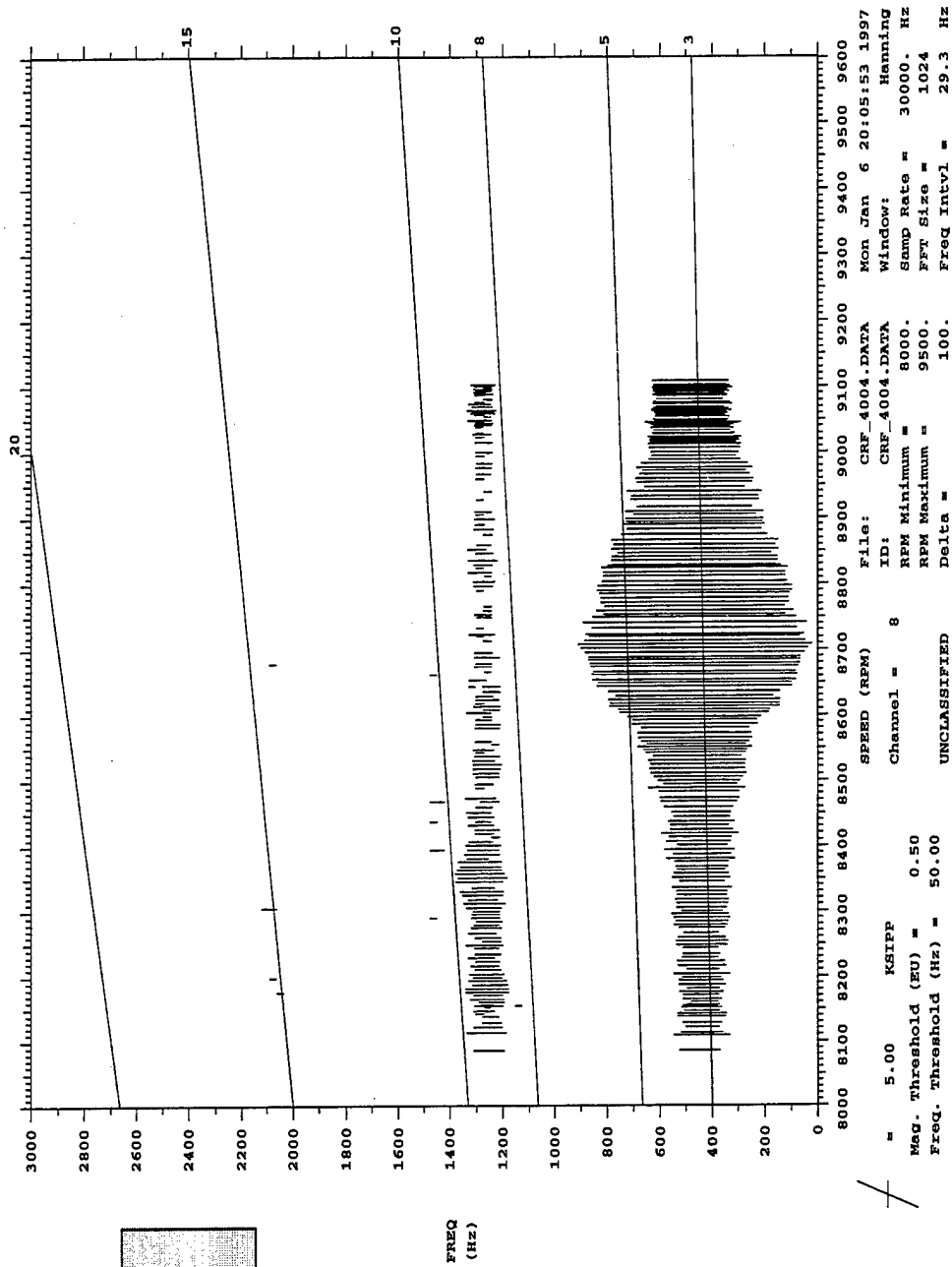


Figure C.56: Blade 8 Campbell diagram, NS.

UNCLASSIFIED
 CRFER RUN 40, 3/REV, NS, No Duct, 8100-9100 RPM

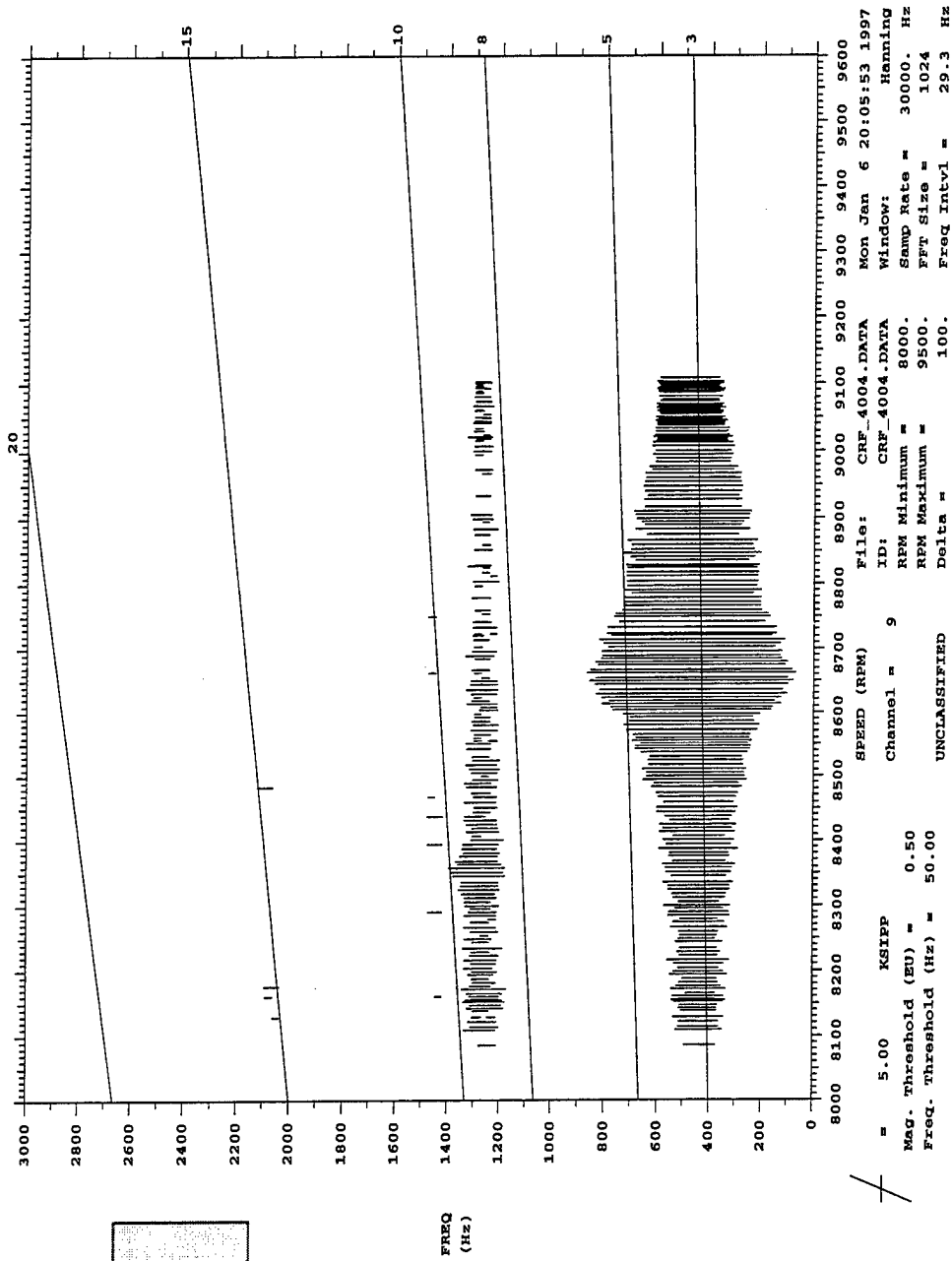


Figure C.57: Blade 9 Campbell diagram, NS.

UNCLASSIFIED
 CRFER RUN 40, 3/rev, NS, No Duct, 8100-9100 RPM

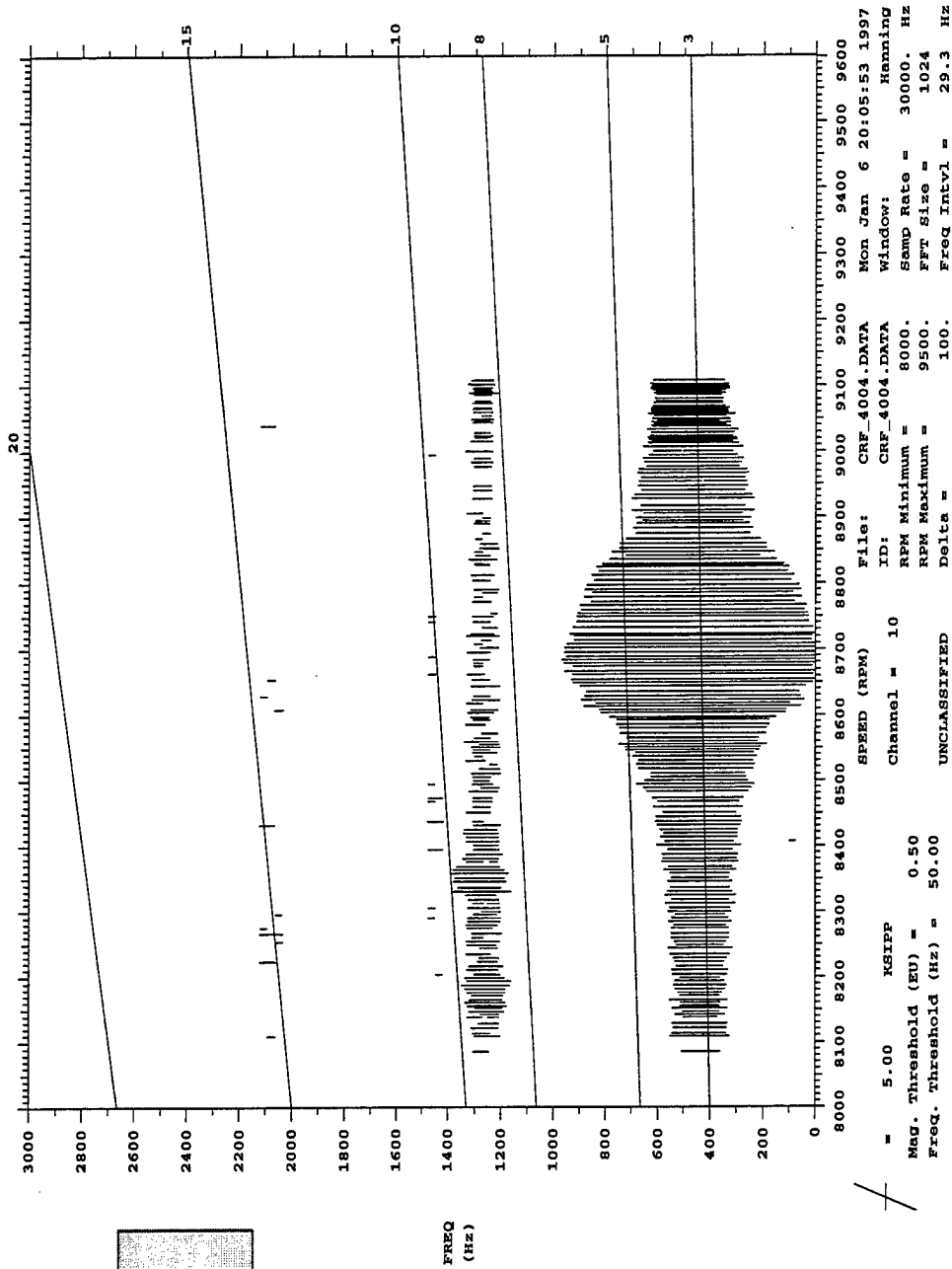


Figure C.58: Blade 10 Campbell diagram, NS.

UNCLASSIFIED
CRFPR RUN 40, 3/Rev, NS, No Duct, 8100-9100 rpm

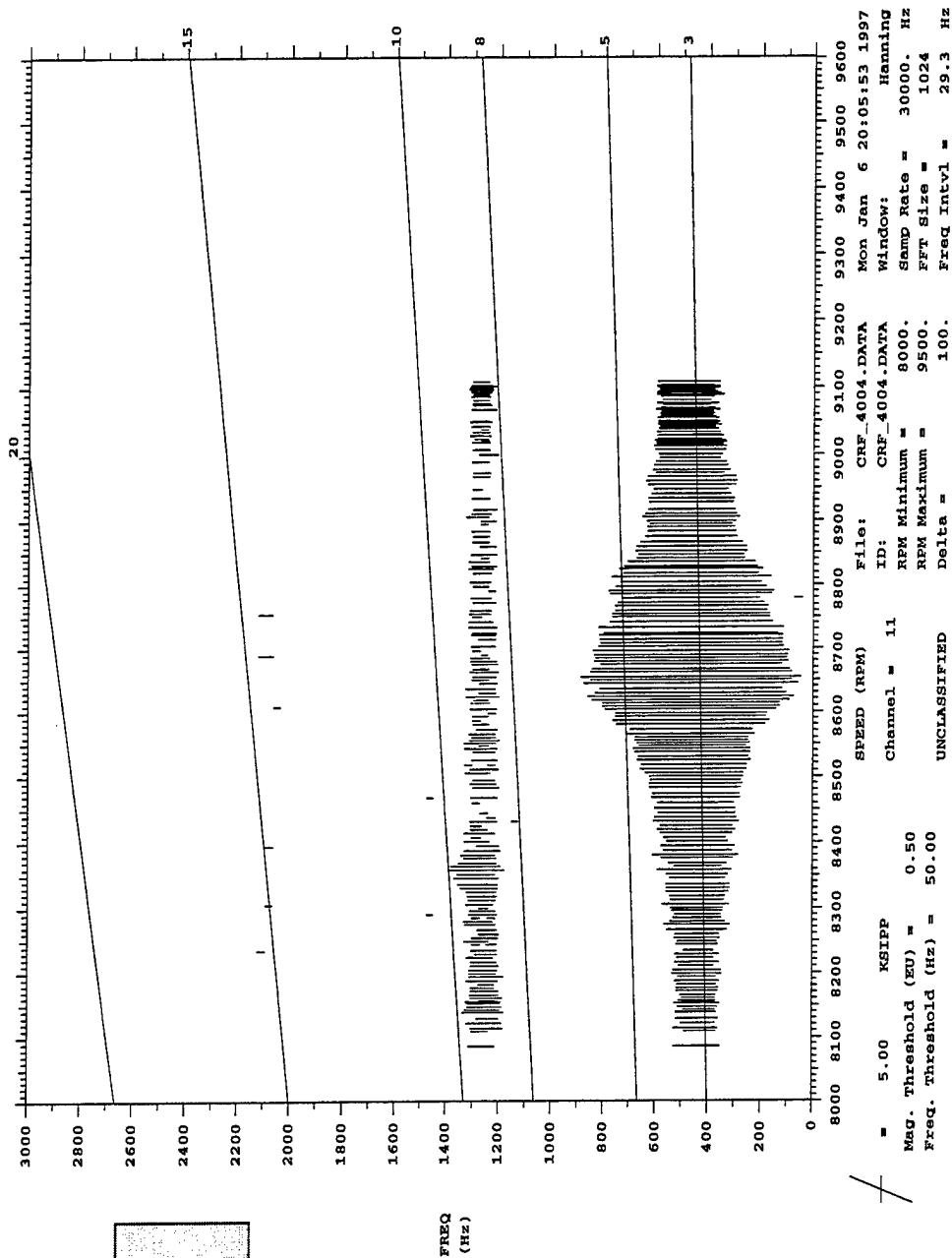


Figure C.59: Blade 11 Campbell diagram, NS.

CRFER RUN 40, 3/Rev, NS, No Duct, 8100-9100 rpm

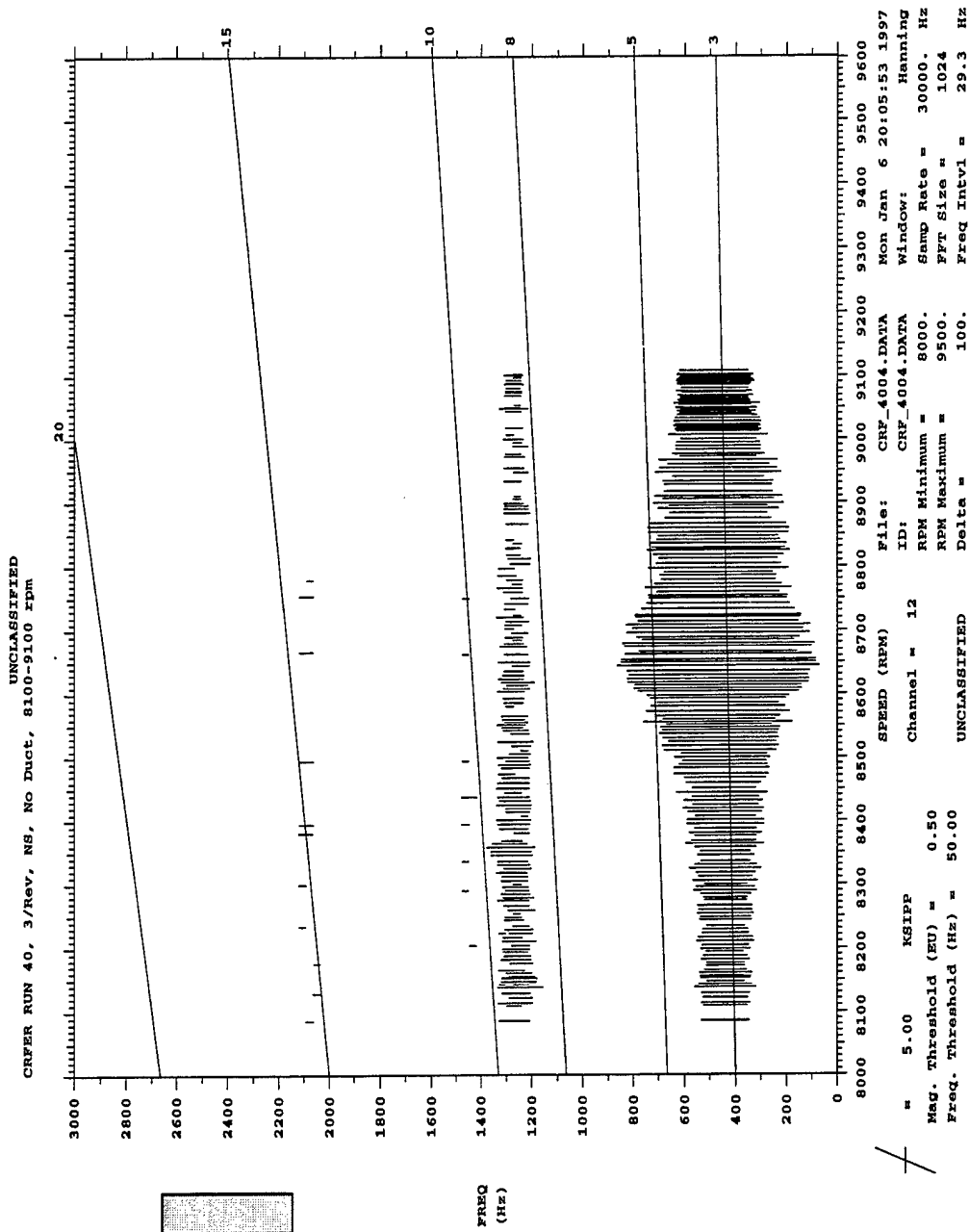


Figure C.60: Blade 12 Campbell diagram, NS.

UNCLASSIFIED
CREER RUN 40, 3/Rev, NS, No Duct, 8100-9100 rpm

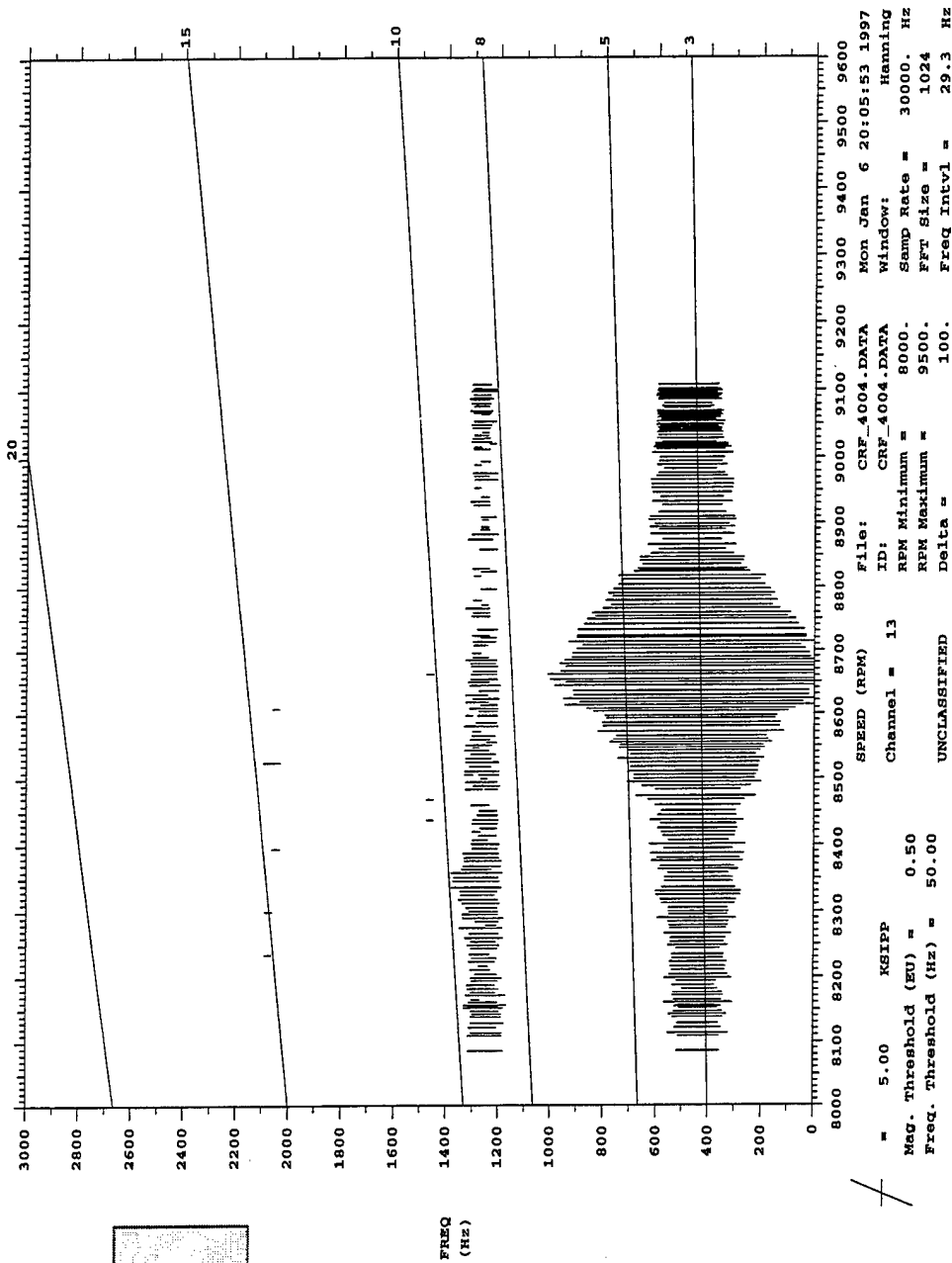


Figure C.61: Blade 13 Campbell diagram, NS.

CRPER RUN 40, 3/Rev, NS, No Duct, 8100-9100 RPM

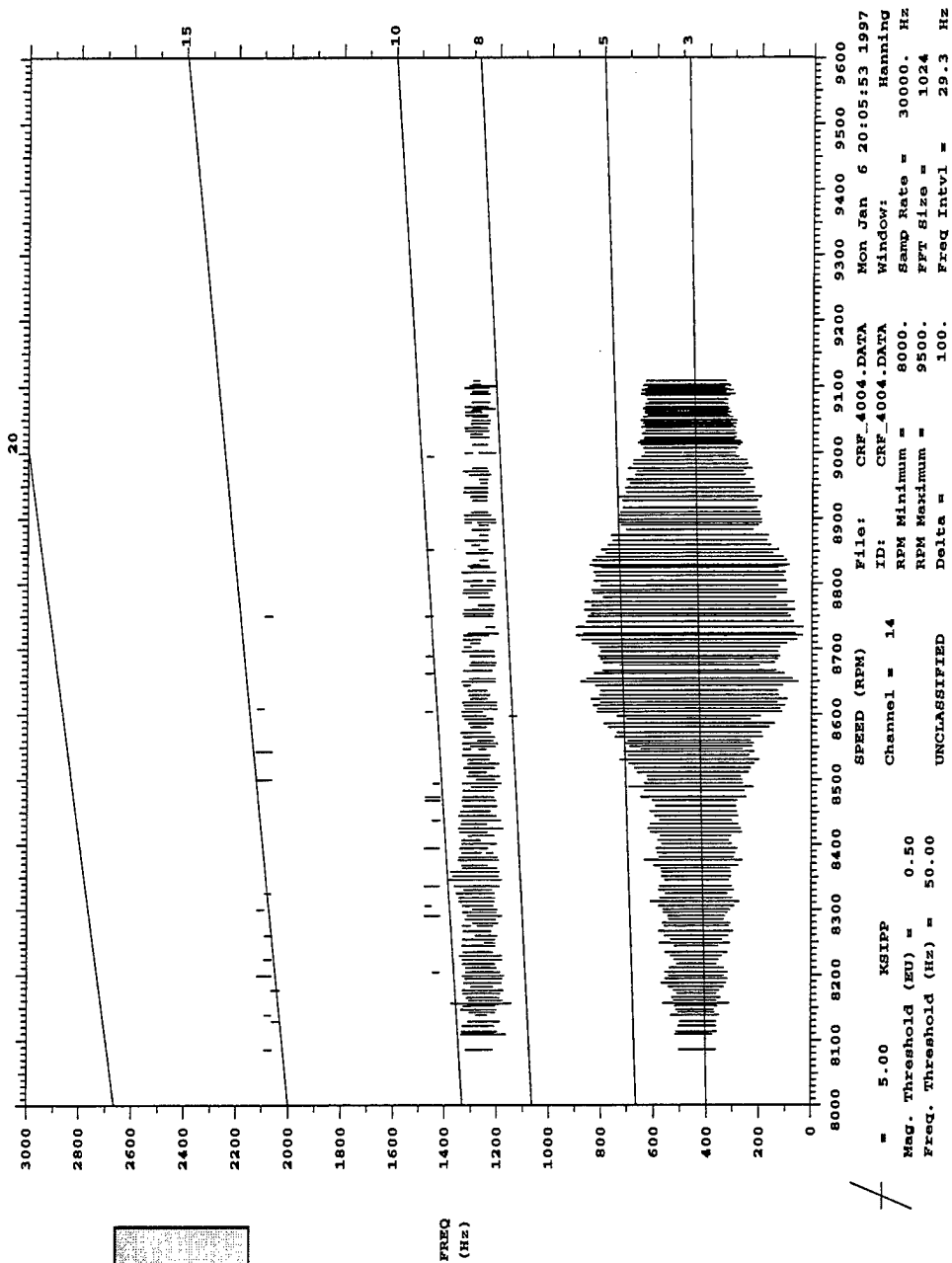


Figure C.62: Blade 14 Campbell diagram, NS.

UNCLASSIFIED
CRFER RUN 40, 3/rev, NS, No Duct, 8100-9100 rpm

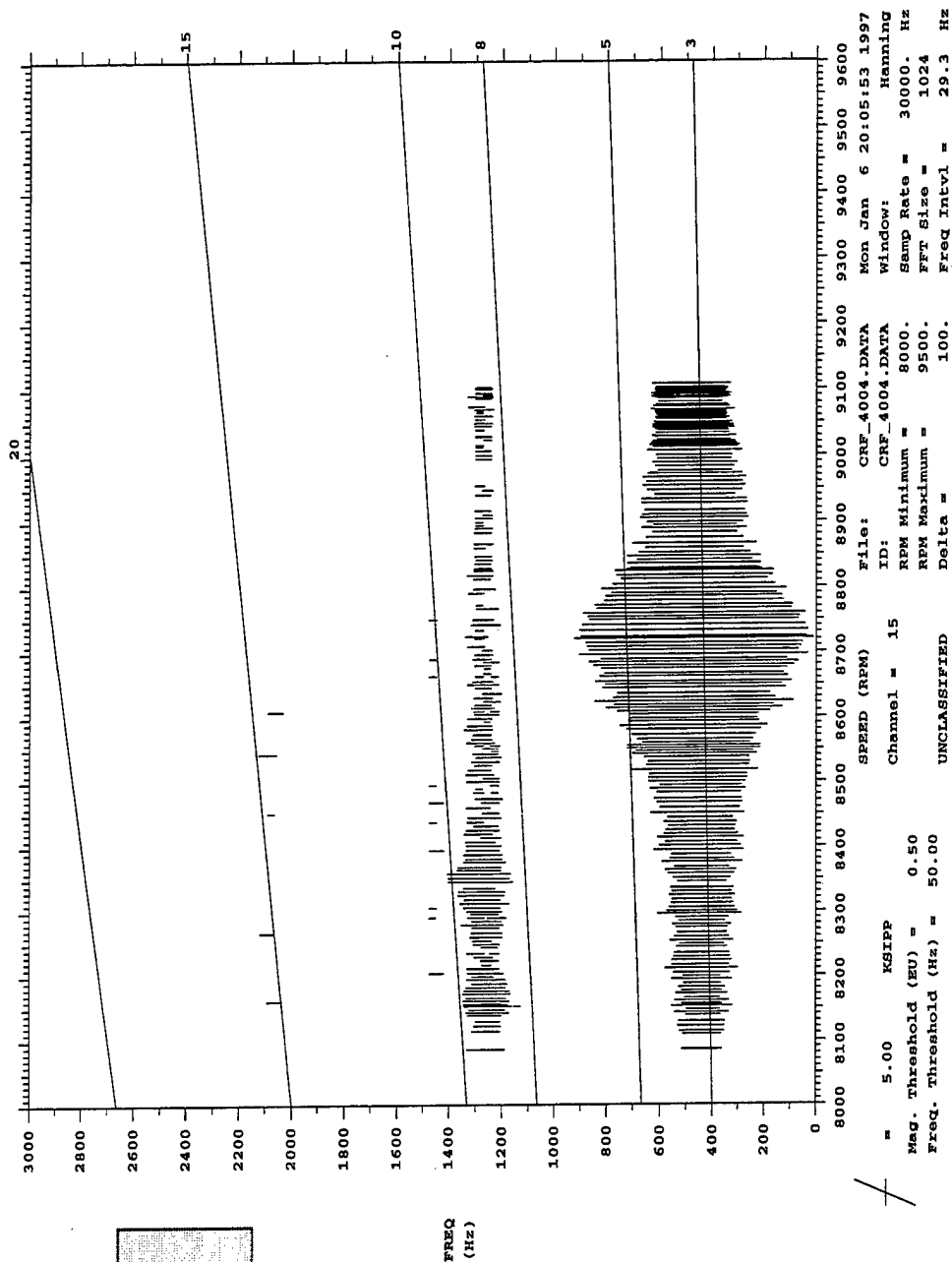


Figure C.63: Blade 15 Campbell diagram, NS.

CRFER RUN 40, 3/Rev, NS, No Duct, 8100-9100 rpm

UNCLASSIFIED

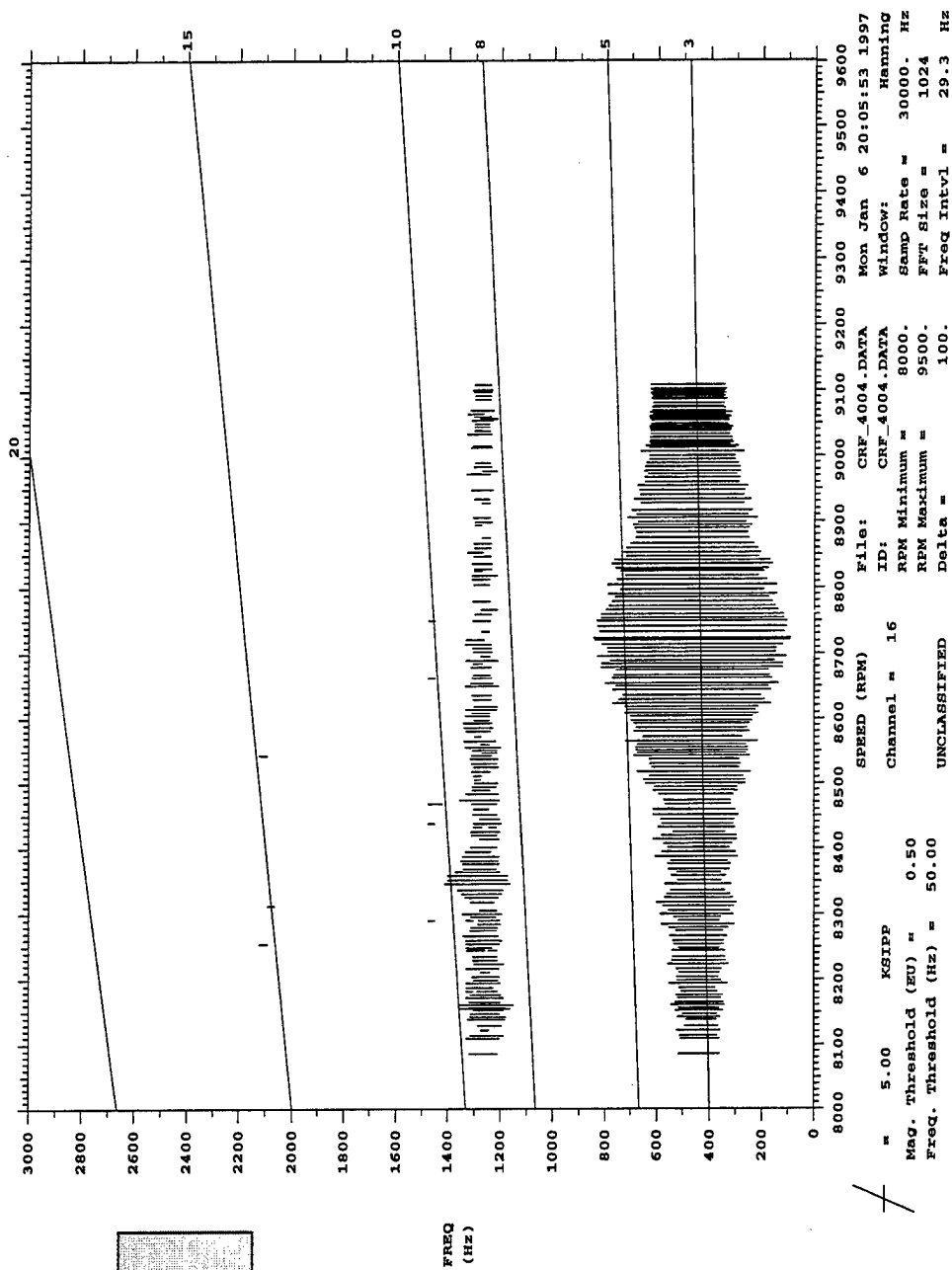


Figure C.64: Blade 16 Campbell diagram, NS.

APPENDIX D: Tabulated Experimental Data

Data were obtained during testing in the form of on-line Campbell diagrams and recorded analog signals. The Campbell diagrams were used to determine resonant frequency, peak stress amplitude, and total damping for each blade. The recorded signals were analyzed to determine off-resonant forcing frequencies and stress amplitude components at those frequencies. These results for root strain gages are provided in the tables that follow. Tables D.1 and D.2 show the results for off-resonant operation at 8100 rpm and 9100 rpm, respectively. The remaining tables, Tables D.3 through D.6, give the results at resonance for all four operating lines.

Table D.1: Off-resonant steady-state strain gage data, 8100 rpm mechanical speed.

Location	WOD		NOL		PE		NS	
	Forced Amplitude (kPa)	% Dev. from Mean	Forced Amplitude (kPa)	% Dev. from Mean	Forced Amplitude (kPa)	% Dev. from Mean	Forced Amplitude (kPa)	% Dev. from Mean
B1 Root	19406	-5.3%	15201	-2.6%	12338	-16.7%	13451	-10.2%
B2 Root	18163	-11.4%	15731	0.8%	13902	-6.1%	13417	-10.4%
B5 Root	20912	2.1%	15826	1.5%	14477	-2.2%	15164	1.2%
B6 Root	19838	-3.2%	14799	-5.1%	14865	0.4%	14064	-6.1%
B7 Root	21809	6.4%	16075	3.0%	15376	3.8%	16007	6.8%
B8 Root	19172	-6.4%	13744	-11.9%	13766	-7.0%	14007	-6.5%
B9 Root	20222	-1.3%	14988	-3.9%	14276	-3.6%	15965	6.6%
B12 Root	20579	0.4%	15629	0.2%	15198	2.6%	16341	9.1%
B13 Root	22940	12.0%	17366	11.3%	16893	14.1%	16233	8.3%
B14 Root	22569	10.1%	16930	8.5%	16779	13.3%	15505	3.5%
B15 Root	21932	7.0%	16523	5.9%	15691	6.0%	15323	2.3%
B16 Root	18343	-10.5%	14387	-7.8%	14114	-4.7%	14316	-4.4%
Mean	20490	0.0%	15600	0.0%	14806	0.0%	14983	0.0%
Max.	22940	12.0%	17366	11.9%	16893	16.7%	16341	10.4%
Std. Dev.	1589	7.8%	1050	6.7%	1292	8.7%	1082	7.2%

Table D.2: Off-resonant steady-state strain gage data, 9100 rpm mechanical speed.

Location	WOD		NOL		PE		NS	
	Forced Amplitude (kPa)	% Dev. from Mean	Forced Amplitude (kPa)	% Dev. from Mean	Forced Amplitude (kPa)	% Dev. from Mean	Forced Amplitude (kPa)	% Dev. from Mean
B1 Root	21173	1.1%	15921	4.0%	15270	2.8%	11763	-5.1%
B2 Root	19320	-7.8%	13644	-10.9%	12378	-16.6%	9884	-20.3%
B5 Root	24594	17.4%	18076	18.1%	17847	20.2%	14975	20.8%
B6 Root	22341	6.6%	16254	6.2%	15681	5.6%	13804	11.3%
B7 Root	21029	0.4%	14969	-2.2%	14630	-1.5%	11752	-5.2%
B8 Root	20773	-0.9%	15322	0.1%	14603	-1.7%	12305	-0.8%
B9 Root	17116	-18.3%	12591	-17.8%	12155	-18.2%	9895	-20.2%
B12 Root	20852	-0.5%	15414	0.7%	15468	4.2%	13200	6.5%
B13 Root	19069	-9.0%	13824	-9.7%	13309	-10.4%	10923	-11.9%
B14 Root	23347	11.4%	16851	10.1%	16397	10.4%	14944	20.5%
B15 Root	22414	7.0%	16617	8.5%	16538	11.4%	13049	5.2%
B16 Root	19392	-7.4%	14224	-7.1%	13930	-6.2%	12305	-0.8%
Mean	20952	0.0%	15309	0.0%	14851	0.0%	12400	0.0%
Max.	24594	18.3%	18076	18.1%	17847	20.2%	14975	20.8%
Std. Dev.	2057	9.8%	1557	10.2%	1710	11.5%	1699	13.7%

Table D.3: Strain gage data at resonance, WOD.

Gage Location	PSD Frequency (Hz)	% Dev. from Mean	Freq. from Campbell (Hz)	% Dev. from Mean	Stress Amplitude (kPa)	% Dev. from Mean	Damping	% Dev. from Mean
B1 Root	437	0.3%	438	0.5%	145045	-0.2%	0.008	-30.1%
B2 Root	437	0.2%	436	0.1%	163178	12.3%	0.009	-22.3%
B3 Root	NA	NA	439	0.6%	155263	6.8%	0.012	3.2%
B5 Root	437	0.3%	436	0.0%	158579	9.1%	0.010	-15.7%
B6 Root	435	-0.3%	436	0.0%	138405	-4.8%	0.011	-3.6%
B7 Root	437	0.3%	437	0.3%	151174	4.0%	0.011	-1.0%
B8 Root	435	-0.3%	436	0.0%	140446	-3.4%	0.011	-2.6%
B9 Root	435	-0.3%	433	-0.6%	122065	-16.0%	0.012	8.1%
B10 Root	NA	NA	434	-0.4%	181559	24.9%	0.011	-3.2%
B11 Root	NA	NA	436	0.0%	122830	-15.5%	0.014	26.5%
B12 Root	435	-0.3%	434	-0.4%	132531	-8.8%	0.012	7.4%
B13 Root	432	-0.8%	433	-0.6%	149133	2.6%	0.013	16.2%
B14 Root	437	0.3%	437	0.4%	145810	0.3%	0.012	6.5%
B15 Root	437	0.2%	436	0.1%	152705	5.1%	0.009	-21.8%
B16 Root	437	0.3%	436	0.1%	121299	-16.5%	0.015	32.4%
Mean	436	0.0%	436	0.0%	145335	0.0%	0.011	0.0%
Max.	437	0.8%	439	0.6%	181559	24.9%	0.015	32.4%
Std. Dev.	2	0.4%	2	0.4%	16625	11.4%	0.002	17.6%

Table D.4: Strain gage data at resonance, NOL.

Gage Location	PSD Frequency (Hz)	% Dev. from Mean	Freq. from Campbell (Hz)	% Dev. from Mean	Stress Amplitude (kPa)	% Dev. from Mean	Damping	% Dev. from Mean
B1 Root	437	0.5%	437	0.3%	138660	-2.3%	0.008	-31.4%
B2 Root	435	-0.1%	436	0.0%	155518	9.6%	0.009	-18.9%
B3 Root	NA	NA	439	0.7%	155518	9.6%	0.011	-4.4%
B5 Root	435	-0.1%	436	0.0%	158579	11.7%	0.009	-22.4%
B6 Root	435	-0.1%	435	-0.2%	134579	-5.2%	0.012	1.4%
B7 Root	437	0.5%	437	0.2%	148106	4.4%	0.011	-7.8%
B8 Root	435	-0.1%	435	-0.1%	131952	-7.0%	0.014	15.6%
B9 Root	435	-0.1%	434	-0.5%	122320	-13.8%	0.016	33.8%
B10 Root	NA	NA	435	-0.2%	178243	25.6%	0.009	-20.7%
B11 Root	NA	NA	435	-0.1%	117211	-17.4%	0.014	19.0%
B12 Root	435	-0.1%	435	-0.2%	133806	-5.7%	0.010	-13.4%
B13 Root	432	-0.7%	434	-0.5%	152195	7.2%	0.011	-9.7%
B14 Root	437	0.5%	437	0.3%	139171	-1.9%	0.017	44.6%
B15 Root	435	-0.1%	436	0.0%	147851	4.2%	0.008	-30.7%
B16 Root	435	-0.1%	437	0.3%	114915	-19.0%	0.017	45.1%
Mean	435	0.0%	436	0.0%	141908	0.0%	0.012	0.0%
Max.	437	0.7%	439	0.7%	178243	25.6%	0.017	45.1%
Std. Dev.	1	0.3%	1	0.3%	17128	12.1%	0.003	25.8%

Table D.5: Strain gage data at resonance, PE.

Gage Location	PSD Frequency (Hz)	% Dev. from Mean	Freq. from Campbell (Hz)	% Dev. from Mean	Stress Amplitude (kPa)	% Dev. from Mean	Damping	% Dev. from Mean
B1 Root	437	0.5%	437	0.3%	130745	-4.8%	0.008	-28.7%
B2 Root	437	0.5%	436	0.0%	155518	13.2%	0.009	-24.0%
B3 Root	NA	NA	438	0.7%	142239	3.6%	0.011	-2.1%
B5 Root	435	-0.1%	436	0.0%	150919	9.9%	0.010	-7.1%
B6 Root	435	-0.2%	435	0.0%	131000	-4.6%	0.011	-3.0%
B7 Root	435	-0.2%	435	0.0%	141984	3.4%	0.011	-4.5%
B8 Root	435	-0.2%	435	-0.1%	139681	1.7%	0.011	1.7%
B9 Root	435	-0.2%	433	-0.6%	119762	-12.8%	0.010	-12.1%
B10 Root	NA	NA	434	-0.2%	171603	25.0%	0.010	-8.9%
B11 Root	NA	NA	435	-0.1%	118872	-13.4%	0.014	23.7%
B12 Root	435	-0.2%	434	-0.4%	128194	-6.7%	0.011	2.0%
B13 Root	432	-0.7%	433	-0.6%	143259	4.3%	0.012	6.3%
B14 Root	437	0.5%	438	0.6%	132531	-3.5%	0.016	46.2%
B15 Root	435	-0.2%	436	0.0%	145045	5.6%	0.008	-31.1%
B16 Root	437	0.5%	437	0.3%	108654	-20.9%	0.016	41.5%
Mean	435	0.0%	435	0.0%	137334	0.0%	0.011	0.0%
Max.	437	0.7%	438	0.7%	171603	25.0%	0.016	46.2%
Std. Dev.	2	0.4%	2	0.4%	15806	11.5%	0.003	22.6%

Table D.6: Strain gage data at resonance, NS.

Gage Location	PSD Frequency (Hz)	% Dev. from Mean	Freq. from Campbell (Hz)	% Dev. from Mean	Stress Amplitude (kPa)	% Dev. from Mean	Damping	% Dev. from Mean
B1 Root	436	0.3%	437	0.4%	121044	-4.0%	0.008	-24.8%
B2 Root	436	0.3%	436	0.2%	146065	15.8%	0.009	-19.9%
B3 Root	NA	NA	437	0.5%	136619	8.3%	0.010	-10.5%
B5 Root	436	0.3%	437	0.4%	140701	11.6%	0.010	-5.6%
B6 Root	433	-0.3%	435	0.0%	120148	-4.7%	0.011	1.7%
B7 Root	436	0.3%	434	-0.1%	142749	13.2%	0.011	-1.4%
B8 Root	436	0.3%	436	0.1%	121168	-3.9%	0.015	36.3%
B9 Root	431	-0.9%	433	-0.4%	108530	-13.9%	0.009	-16.6%
B10 Root	NA	NA	434	-0.2%	136364	8.1%	0.013	17.4%
B11 Root	NA	NA	433	-0.5%	114274	-9.4%	0.010	-11.2%
B12 Root	431	-0.9%	432	-0.6%	108530	-13.9%	0.010	-9.0%
B13 Root	433	-0.3%	433	-0.4%	149644	18.7%	0.009	-20.5%
B14 Root	436	0.3%	436	0.2%	118486	-6.0%	0.016	45.2%
B15 Root	436	0.3%	436	0.2%	123974	-1.7%	0.011	1.4%
B16 Root	436	0.3%	436	0.3%	103421	-18.0%	0.013	17.4%
Mean	435	0.0%	435	0.0%	126115	0.0%	0.011	0.0%
Max.	436	0.9%	437	0.6%	149644	18.7%	0.016	45.2%
Std. Dev.	2	0.5%	2	0.4%	14829	11.8%	0.002	20.8%

APPENDIX E: Comparison of Campbell Diagrams and Recorded Data.

Natural frequencies and resonant stress amplitudes were determined from analog tape using spectral analysis techniques described in Chapter 3, but these results were not included in the mistuning study. Experimental Campbell diagrams were used for mistuning analysis because they yielded a more comprehensive data set than the recorded data. However, the recorded signals were useful for verification purposes.

Natural frequencies determined from the Campbell diagrams and the experiment are compared in Figure E.1. The results from the two data acquisition methods compare well. Both show nearly the same response frequency for each blade, and variations follow the same pattern from blade-to-blade. The agreement is confirmed in Table E.1, which tabulates the mean, standard deviation, and percent standard deviation of natural frequencies determined from the two methods. The response frequencies agreed for both methods on all operating lines in terms of all three statistical parameters.

Table E.1: Natural frequency statistical comparison.

Operating Line	Data Acquisition	Mean (Hz)	Std. Dev. (Hz)	% Std. Dev.
WOD	Recorded	436	1.3	0.29%
	Campbell Diagram	436	1.6	0.38%
NOL	Recorded	435	1.6	0.37%
	Campbell Diagram	436	1.3	0.30%
PE	Recorded	435	1.6	0.38%
	Campbell Diagram	435	1.6	0.36%
NS	Recorded	435	1.9	0.45%
	Campbell Diagram	435	1.6	0.36%

The sampling rate used in reducing the recorded data did not allow for accurate resolution of peak stress amplitudes. This is evident in Figure E.2, which consistently shows recorded peak stresses higher than those obtained from Campbell diagrams.

However, the relative stress pattern from blade-to-blade correlates well between acquisition methods. Peak stress amplitude statistics shown in Table E.2 confirm this. The mean stresses from recorded data are consistently approximately 26 percent higher than those obtained from Campbell diagrams.

Table E.2: Resonant stress statistical comparison.

Operating Line	Data Acquisition	Mean (kPa)	Std. Dev. (kPa)	% Std. Dev.
WOD	Recorded	183211	17065	9.3%
	Campbell Diagram	145335	16625	11.4%
NOL	Recorded	178076	16841	9.5%
	Campbell Diagram	141908	17128	12.1%
PE	Recorded	172930	16939	9.8%
	Campbell Diagram	137334	15806	11.5%
NS	Recorded	158829	18113	11.4%
	Campbell Diagram	126115	14829	11.8%

The Campbell diagram data agree with those obtained from the recorded signals. This shows that this data acquisition method works well for mistuning analysis at a single mode resonance.

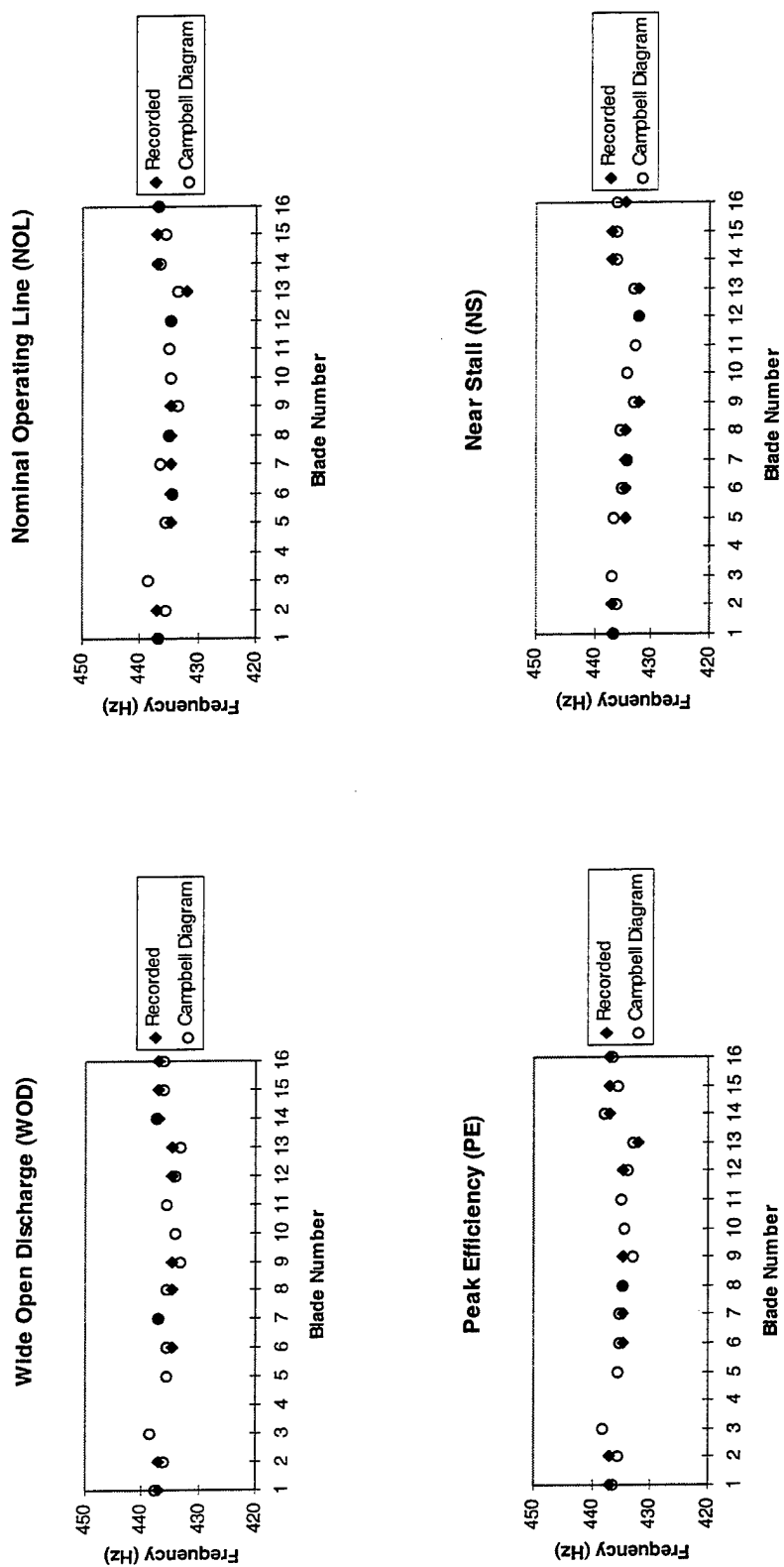


Figure E.1: Resonant frequencies from recorded signals and experimental Campbell diagrams.

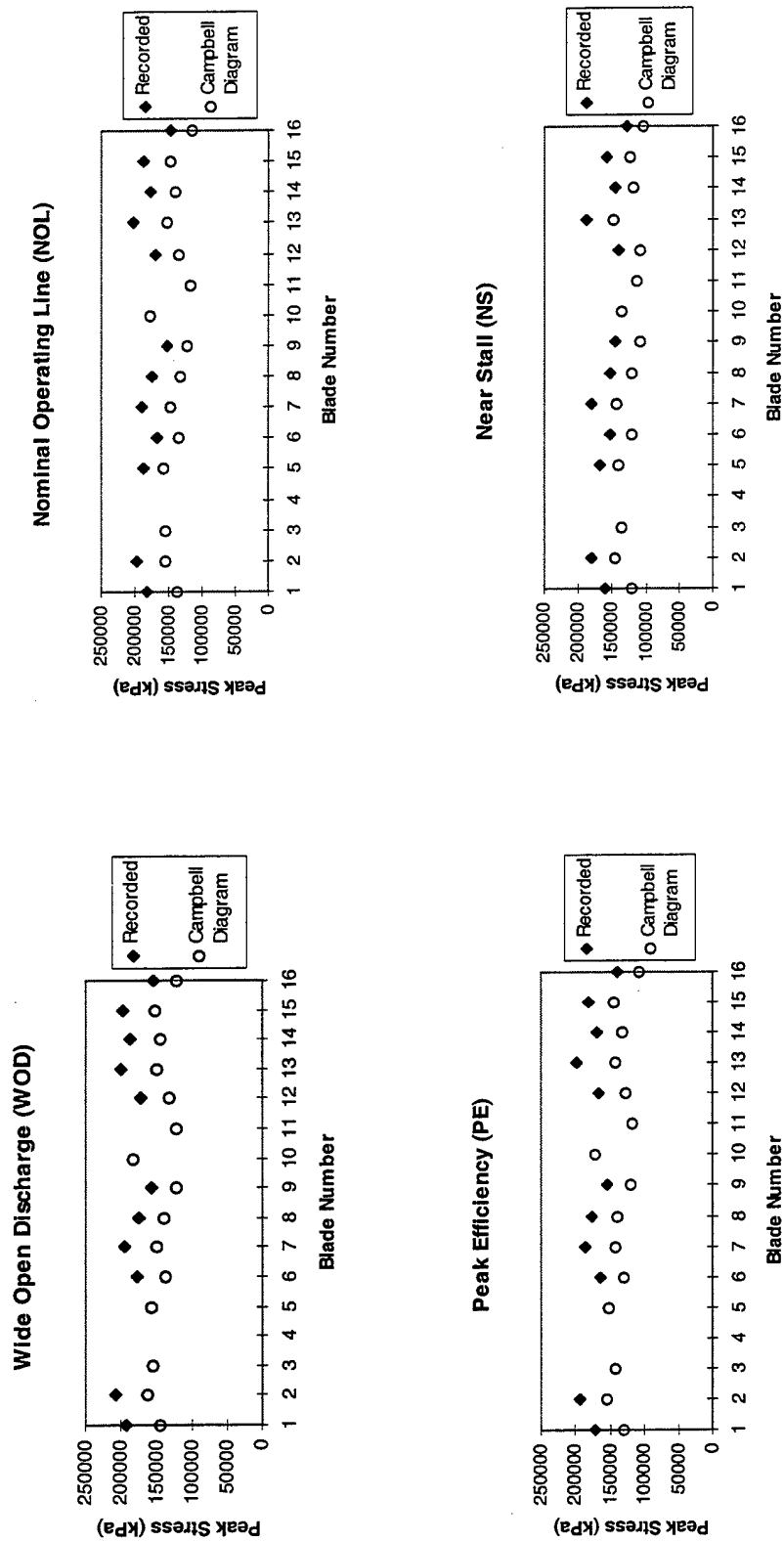


Figure E.2: Peak stress amplitudes from recorded signals and experimental Campbell diagrams.